



## Combined Chemical Looping for CO<sub>2</sub> Emissions Reduction in Energy-Intensive Industries

**Varun Singh**

Doctoral dissertation submitted to obtain the academic degree of  
Doctor of Chemical Engineering

### **Supervisors**

Prof. Mark Saeys, PhD - Prof. Vladimir Galvita, PhD

Department of Materials, Textiles and Chemical Engineering  
Faculty of Engineering and Architecture, Ghent University

May 2022



**GHENT  
UNIVERSITY**



## **Combined Chemical Looping for CO<sub>2</sub> Emissions Reduction in Energy-Intensive Industries**

**Varun Singh**

Doctoral dissertation submitted to obtain the academic degree of  
Doctor of Chemical Engineering

### **Supervisors**

Prof. Mark Saeys, PhD - Prof. Vladimir Galvita, PhD

Department of Materials, Textiles and Chemical Engineering  
Faculty of Engineering and Architecture, Ghent University

May 2022



**GHENT  
UNIVERSITY**

ISBN 978-94-6355-599-9

NUR 961, 952

Wettelijk depot: D/2022/10.500/40



## **Members of the Examination Board**

### **Chair**

Prof. Em. Luc Taerwe, PhD, Ghent University

### **Other members entitled to vote**

Prof. Angeliki Lemonidou, PhD, Aristotle University of Thessaloniki, Greece

Hilde Poelman, PhD, Ghent University

Liisa K. Rihko-Struckmann, PhD, Max-Planck-Institute for Dynamics of Complex Technical Systems, Germany

Marleen Rombouts, PhD, VITO

Prof. An Verberckmoes, PhD, Ghent University

### **Supervisors**

Prof. Mark Saeys, PhD, Ghent University

Prof. Vladimir Galvita, PhD, Ghent University



## Acknowledgments

I would like to thank the jury members for their time and suggestions. I would like to express my gratitude to my promoters, Dr. Lukas Buelens, Dr. Hilde Poelman, and Prof. Guy Marin for their valuable support. I am also grateful to my colleagues at the Laboratory for Chemical Technology at Ghent University for their company and assistance. I would also like to thank my family for their support.

Varun

May 2022

# Contents

Acknowledgments .....	i
List of figures .....	vii
List of tables.....	xxix
Glossary and list of abbreviations, symbols, and sub- and super-scripts...	xxxiii
Glossary .....	xxxiii
Abbreviations .....	xxxvii
Symbols .....	xl
Subscripts .....	xliv
Superscripts .....	xlvi
Summary.....	xlvi
Samenvatting.....	liv
Chapter 1 .....	1
Introduction.....	1
1.1 <i>Low grade</i> resources as feedstock for chemical looping.....	3
1.2 <i>Low grade</i> gaseous fuels .....	8
1.3     Scope of this thesis .....	13
Chapter 2 .....	16
Methodology .....	16
3.1     Material synthesis .....	16
3.2     Material characterisation .....	19
3.2.1     N <sub>2</sub> physisorption .....	19
3.2.2     Energy dispersive x-ray spectroscopy.....	20
3.2.3     X-ray diffraction .....	20
3.2.4     Temperature programmed reactions.....	21
3.2.5     Scanning transmission electron microscopy and elemental mapping	22
3.3     Material testing .....	23

Chapter 3 .....	25
Carbon capture from steel mill gases.....	25
4.1    Introduction.....	27
4.2    Conception of the process.....	32
4.2.1    Energy and mass flows .....	33
4.2.2    Selection of the oxygen carrier for chemical looping combustion.....	34
4.2.3    Selection of the oxygen carrier for chemical looping air separation.....	38
4.3    Methods .....	40
4.3.1    Process simulation.....	41
4.3.2    Process and experimental performance metrics .....	50
4.4    Results and discussion .....	51
4.4.1    Process simulations .....	52
4.4.2    Experimental proof of concept.....	62
4.4.3    Material characterisation .....	73
4.5    Conclusions and perspectives .....	79
Chapter 4.....	82
CO <sub>2</sub> capture and conversion from the blast furnace gas.....	82
5.1    Introduction.....	84
5.2    Methods .....	89
5.2.1    Experimental proof of concept.....	89
5.3    Process calculations.....	91
5.3.1    Process simulation.....	91
5.3.2    Exergy analysis.....	97
5.3.3    Process and experimental performance indicators .....	99
5.4    Results and discussion .....	101
5.4.1    Characterisation of materials .....	101



5.4.2	Experimental proof of concept.....	111
5.4.3	Assessment of process performance indicators and cycled materials 116	
5.4.4	Process calculations.....	127
5.5	Conclusions.....	141
Chapter 5 .....		144
Auto-thermal CO production from the blast furnace gas .....		144
6.1	Introduction.....	146
6.2	Methods .....	150
6.2.1	Process simulation.....	150
6.2.2	Exergy analysis.....	157
6.2.3	Techno-economic assessment.....	161
6.2.4	Experimental proof of concept.....	165
6.3	Results and discussion .....	169
6.3.1	Process simulation.....	169
6.3.2	Exergy analysis.....	174
6.3.3	Techno-economic assessment.....	176
6.3.4	Experimental proof of concept.....	184
6.4	Conclusions.....	190
Chapter 6 .....		192
Intensified blue H <sub>2</sub> production with in situ CO <sub>2</sub> utilisation.....		192
7.1	Introduction.....	193
7.2	Methods .....	198
7.2.1	Thermodynamic calculations.....	198
7.2.2	Concept demonstration.....	198
7.2.3	Process and experimental performance metrics .....	200
7.3	Results and Discussion.....	203
7.3.1	Material characterisation .....	203

7.3.2	Thermodynamic assessment .....	207
7.3.3	Concept demonstration.....	210
7.3.4	Process and experimental performance indicators .....	216
7.4	Conclusions.....	219
Chapter 7	.....	220
Conclusions and perspectives	.....	220
Appendix A	.....	224
Appendix B.....	.....	228
Theoretical calculations.....	.....	228
Aspen Plus® simulation with a CO <sub>2</sub> /N <sub>2</sub> mixture.....	.....	228
Integrating chemical looping air separation.....	.....	230
Additional process simulations.....	.....	232
Gibbs free energy plots .....	.....	232
Experimental results and data.....	.....	234
Materials testing on a fixed bed reactor .....	.....	234
Material characterisation .....	.....	238
Appendix C.....	.....	247
Results of exergy analysis.....	.....	247
Rietveld refinement of X-ray diffraction measurements .....	.....	254
Thermodynamic analysis .....	.....	271
Additional experimental results .....	.....	281
Appendix D .....	.....	286
Calculations .....	.....	286
Thermodynamic calculations.....	.....	286
Experimental results and data.....	.....	288
Process simulations .....	.....	297
Techno-economic evaluation .....	.....	301

Estimation of the costs of fresh and spent solids and catalyst .....	301
Exergy and energy .....	310
Appendix E.....	312
Thermodynamics .....	312
Catalytic reactions .....	312
Sorption enhanced reactions .....	313
Chemical looping reverse water-gas shift reaction (CL-rWGS) .....	314
Chemical looping combustion .....	315
Experimental section .....	317
Shorter cycle (89 seconds) at 973 K .....	317
Regeneration of CO <sub>2</sub> carrier .....	318
O <sub>2</sub> post-treatment after 10 cycles .....	319
Characterisation of materials .....	320
Bibliography.....	322

List of figures

Figure 1: Process concept for decarbonisation of steel mill gases in an energy neutral chemical looping process. The final product CO<sub>2</sub> is produced in the second step. In the first step, NiO is used for fully oxidising the reductants in the steel mill gases, CaO is used for capturing CO<sub>2</sub>, and Mn<sub>3</sub>O<sub>4</sub> captures the O<sub>2</sub> for the process. In the second step, Mn<sub>2</sub>O<sub>3</sub> provides the oxygen for the exothermic oxidation of Ni to NiO while the heat is used the decarbonation of CaCO<sub>3</sub> to produce a pure CO<sub>2</sub> stream. .... xlviii

Figure 2: Combined chemical looping applying calcium and iron looping breaks down the reverse water-gas shift reaction into two steps to produce a CO-rich stream from the blast furnace gas (BFG) of the steel industry. In the first step, FeO<sub>x</sub> oxidises the reductants in the BFG and CO<sub>2</sub> is captured by CaO. In the second step, the captured CO<sub>2</sub> is released and converted into CO while regenerating FeO<sub>x</sub> and CaO..... xlix

Figure 3: A process concept combining chemical looping reverse water-gas shift with calcium looping and chemical looping combustion. Here M<sub>1</sub> and M<sub>3</sub> are metals capable of donating or accepting lattice oxygen and M<sub>3</sub>O is a metal oxide capable of capturing and releasing CO<sub>2</sub>. Fuel can be any hydrocarbon or H<sub>2</sub> or a combination and the oxidant could be O<sub>2</sub>, NO, or N<sub>2</sub>O..... li

Figure 4: A process concept combining sorption enhanced steam reforming with chemical looping reverse water-gas shift and chemical looping combustion. In the first step, NiO is reduced by CH<sub>4</sub>, FeO is reduced by H<sub>2</sub> and/or CH<sub>4</sub>, and CaO captures CO<sub>2</sub> formed during this step. In the second step, Ni is oxidised by O<sub>2</sub>, CaCO<sub>3</sub> decomposes to release CO<sub>2</sub>, and Fe is oxidised to FeO by the release CO<sub>2</sub>..... liii

Figuur 5: Procesconcept voor decarbonisatie van staalfabrieksgassen in een energieneutraal chemisch kringproces. In de eerste stap wordt NiO gebruikt voor het volledig oxideren van de reductanten in de staalfabrieksgassen, CaO wordt gebruikt voor het afvangen van CO<sub>2</sub> en Mn<sub>3</sub>O<sub>4</sub> vangt O<sub>2</sub> op. In de tweede stap levert Mn<sub>2</sub>O<sub>3</sub> zuurstof voor de exotherme oxidatie van Ni tot NiO, terwijl de warmte wordt gebruikt om CaCO<sub>3</sub> te ontbinden en een zuivere CO<sub>2</sub>-stroom als eindproduct te produceren. lvi

Figuur 6: Een gecombineerd chemisch calcium- en ijzerkringproces splitst de omgekeerde water-gasverschuivingsreactie in twee stappen om een CO-rijke stroom te produceren uit het hoogovengas (BFG) van de staalindustrie. In de eerste stap oxideert  $\text{FeO}_x$  de reductanten in het BFG en wordt  $\text{CO}_2$  opgevangen door  $\text{CaO}$ . In de tweede stap wordt het opgevangen  $\text{CO}_2$  vrijgegeven en omgezet in CO, terwijl  $\text{FeO}_x$  en  $\text{CaO}$  worden geregenereerd. ....lviii

Figuur 7: Een procesconcept dat de omgekeerde water-gasverschuivingsreactie in chemische kring combineert met het calciumkringproces en chemische kringverbranding. Hier zijn  $\text{M}_1$  en  $\text{M}_3$  metalen die roosterzuurstof kunnen doneren of accepteren en  $\text{M}_3\text{O}$  is een metaaloxide dat in staat is om  $\text{CO}_2$  op te vangen en af te geven. Brandstof kan een koolwaterstof zijn, of  $\text{H}_2$  of een combinatie, en als oxidatiemiddel kan  $\text{O}_2$ , NO of  $\text{N}_2\text{O}$  gebruikt worden. ....lix

Figuur 8: Een procesconcept dat stoomreforming verbetert door sorptie te combineren met de omgekeerde water-gasverschuivingsreactie in chemische kring en chemische kringverbranding. In de eerste stap wordt NiO gereduceerd met  $\text{CH}_4$ , FeO wordt gereduceerd met  $\text{H}_2$  en/of  $\text{CH}_4$  en  $\text{CaO}$  vangt het tijdens deze stap gevormde  $\text{CO}_2$  op. In de tweede stap wordt Ni geoxideerd door  $\text{O}_2$ ,  $\text{CaCO}_3$  ontbindt om  $\text{CO}_2$  vrij te maken en Fe wordt geoxideerd tot FeO door het vrijkomen van  $\text{CO}_2$ . ....lxi

Figure 9: Schematic displaying the chemical looping approach for producing chemical feedstocks, energy carriers, and  $\text{CO}_2$  sequestration. .... 2

Figure 10: A selection of chemical looping approaches. For example,  $\text{CO}_2$  sequestration (A1 using an oxygen carrier  $\text{MO}_x$  via chemical looping combustion and B1 using a  $\text{CO}_2$  carrier MO via calcium looping), chemical reforming for syngas production (A2),  $\text{CO}_2$  utilisation or clean  $\text{H}_2$  production by oxygen uncoupling (A3), selective oxidation applicable to catalytic reactions proceeding via the Mars-van-Krevelen mechanism (A4) for production of organic compounds such as alkenes, a combined chemical looping approach using two or more different types of solid intermediates (B2), for desulphuration of industrial or effluent streams by means of a sulphur carrier (B3), and highly selective  $\text{NH}_3$  synthesis by applying a nitrogen carrier



(B4). Note that for the oxidation reactions,  $x < y$  for the oxygen carrier pair ( $MO_x/MO_y$ ).  
 Figure adapted from [2]. Other catalyst-assisted chemical looping approaches can be  
 found in [12]. ..... 4

Figure 11: The energetic value of resources vs. their respective price in 2020 EUR. The  
 size of the points indicates the production volumes of the resources and the colour  
 codes indicate their source. EFB: empty fruit bunch, HDPE: (end-of-life) high density  
 polyethylene, LDPE: (end-of-life) low density polyethylene, MSW: municipal solid  
 waste, PET: (end-of-life) polyethylene terephthalate, PMR: palm mill residue, POME:  
 palm oil mill effluent, PP: polypropylene, PSA: pressure swing adsorption, and SMR:  
 steam methane reforming. Further details of the data and their sources can be found  
 in Appendix A. Note that these data points are obtained from several different sources  
 in literature (cited in Appendix A) and should, thus, be treated as indicative. .... 5

Figure 12: Gas compositions (molar basis) of four identified low grade industrial gas  
 streams. Note that the small amount of methane ( $<0.2$  mol%) in carbon black tail gas  
 is not shown. More information about the gas streams can be found in Appendix  
 A ..... 12

Figure 13: Schematic illustration for the physical wet mixing synthesis route used for  
 creating 83%  $CaO/CeO_2$  and Ca-Ni-Ce based materials. .... 18

Figure 14: Micromeritics Autochem II apparatus for performing temperature-  
 programmed reactions with a schematic representation of the furnace and U-tube  
 reactor. Figure from [61]. ..... 22

Figure 15: Fixed bed reactor used for material testing. Overview of the fixed bed  
 reactor with indication of feed, reactor and analytical (mass spectrometer, MS)  
 section. .... 24

Figure 16: Blast furnace – basic oxygen furnace steelmaking process. .... 27

Figure 17: Schematic of the developed process concept which combines chemical  
 looping combustion using  $NiO/Ni$  redox pair and calcium looping ( $CaO/CaCO_3$ ) to form  
 a combined chemical loop (Ni-Ca loop), which is coupled to CLAS comprising the

Mn <sub>2</sub> O <sub>3</sub> /Mn <sub>3</sub> O <sub>4</sub> redox pair via the CO <sub>2</sub> -rich stream of the combined Ni-Ca loop. BFG: blast furnace gas and COG: coke oven gas. ....	32
Figure 18: Standard enthalpy of oxidation of common reduced oxygen carriers depicted by red bars and of CH <sub>4</sub> , CO, and H <sub>2</sub> depicted by grey bars. ....	35
Figure 19: Schematic of CLAS driven by recycled CO <sub>2</sub> from the decarbonator. Me <sub>2</sub> /Me <sub>2</sub> O is a generic oxygen carrier that is capable of uncoupling oxygen at temperatures below the decarbonation temperature of the calcium looping cycle and is chemically unaffected by CO <sub>2</sub> at given conditions. ....	39
Figure 20: A block flow diagram displaying the simple heat integration used for process calculations. Note that the steam exiting the turbines is not recycled to maintain the simplicity of the simulation. Grey dashed lines indicate the flow of the circulating solids. RC stands for reduction-carbonation, OD for oxidiser-decarbonator, R for reducer, and O for oxidiser. Dark blue solid and dashed lines indicate the flow of water and steam, light blue lines represent flow of air, purple lines represent the flow of O <sub>2</sub> depleted air, red lines indicate the flow of O <sub>2</sub> and CO <sub>2</sub> from the CLAS loop, green lines indicate the flow of quasi-pure CO <sub>2</sub> , light pink lines indicate the flow of the flue gas from the reducer-carbonator. ....	46
Figure 21: Block diagram of the process concept combining chemical looping combustion and calcium looping in the Ni-Ca loop and integrating chemical looping air separation (CLAS) for utilising blast furnace gas (BFG) and coke oven gas (COG) from steel mills. R-C and O-D stand for reduction-carbonation and oxidation-decarbonation of the Ni-Ca loop. For sake of visual brevity, the circulation of CeO <sub>2</sub> is not shown. The mass and exergy flows are indicated next to the arrows. Exergy output is also indicated in the top section of the process blocks. Red coloured streams indicate the primary energy sources driving the desired chemical reactions to achieve pure CO <sub>2</sub> production for storage and/or utilisation. A: inlet gas streams BFG and COG carrying chemical exergy, B: N <sub>2</sub> and H <sub>2</sub> O rich stream leaving the process, C: CO <sub>2</sub> product with 99.9% purity, D: fraction of hot CO <sub>2</sub> (1173 K) diverted to the CLAS loop, E: O <sub>2</sub> and CO <sub>2</sub> stream	

from the CLAS loop to supply heat for the production of pure CO <sub>2</sub> , F: air fed to the CLAS loop, and G: O <sub>2</sub> -depleted air. ....	52
Figure 22: Sankey diagrams for the exergy (a) and active mass (b) flows in the process for the base case simulation. R-C and O-D stand for reduction-carbonation and oxidation-decarbonation of the Ni-Ca loop. ....	54
Figure 23: Influence of excess material in the Ni-Ca loop on (a) carbon capture and corresponding temperature in the reducer-carbonator, (b) recycled CO <sub>2</sub> , (c) material utilisation, and (d) surplus heat in the CLAS loop. The total inlet flow of gases (BFG and COG) is 105 t/h.....	57
Figure 24: Influence of the temperature in the CLAS loop on (a) carbon capture and the surplus heat in the CLAS loop (dashed orange line serves as a guide to the eye to mark zero surplus heat), (b) concentration of O <sub>2</sub> in the mixed CO <sub>2</sub> -O <sub>2</sub> stream sent to the oxidiser-decarbonator of the Ni-Ca loop, (c) recycled CO <sub>2</sub> , and (d) temperature of the reducer-carbonator of the Ni-Ca loop. A solids flow rate of 310 t/h in the NI-Ca loop, corresponding to 10% excess material, is assumed and the total inlet flow of gases (BFG and COG) is 105 t/h. ....	59
Figure 25: Influence of the available COG used in the proposed process on (a) carbon capture and corresponding temperature in the reducer-carbonator, (b) carbon capture and equivalent CO <sub>2</sub> emissions, (c) material utilisation, and (d) surplus heat in the CLAS loop.....	60
Figure 26: Evolution of the material utilisation and the difference between the maximum temperatures of the two half-cycles over 30 cycles. Synthetic BFG (molar composition: 23.8% CO, 24.1% CO <sub>2</sub> , 5.1% H <sub>2</sub> , 7% He, and 40% Ar) was used during the reduction-carbonation half-cycle and 50% O <sub>2</sub> /Ar during the oxidation-decarbonation half-cycle. The flow rates of all inlet gases were kept constant at $41 \cdot 10^{-6}$ mol/s, corresponding to a GHSV of about 3700 h <sup>-1</sup> , throughout the experimental run.....	65
Figure 27: Measured outlet flow rates and temperature versus time over one cycle when synthetic BFG is used and the GHSV is kept constant for the inlet gas streams at (a) 1500 h <sup>-1</sup> , (b) 3700 h <sup>-1</sup> , and (c) 5000 h <sup>-1</sup> and when a mixture containing 20% CH <sub>4</sub> and	

80% synthetic BFG is tested at a constant GHSV of $6200 \text{ h}^{-1}$ while the reactor furnace temperature is fixed at (d) 873 K, (e) 923 K, and (f) 1023 K. ....	70
Figure 28: XRD of (a) as prepared and (b) the material after 50 cycles. Only peaks with intensities larger than 2% and 5% of the maximum intensity have been marked for (a) and (b). HAADF-STEM imaging for the (c) as prepared material and (e) the cycled material and their EDX mapping in (d) and (f). (g) $\text{CO}_2$ -TPCD of the as prepared and the cycled materials using 20% $\text{CO}_2$ in Ar (h) $\text{H}_2$ -TPR and $\text{O}_2$ -TPO of the as prepared and the cycled materials using 5% $\text{H}_2/\text{Ar}$ and 5% $\text{O}_2/\text{Ar}$ .....	78
Figure 29: Blast furnace – basic oxygen furnace steelmaking process. The schematic inside the dashed lines in the top section of the figure illustrates the scope of this work within its broader context. ....	85
Figure 30: Process schematic for the combined chemical looping approach to produce CO from the BFG. ....	86
Figure 31: Specifications of the experimental design for the proof of concept. ....	90
Figure 32: Aspen Plus V10 process flowsheet. ....	92
Figure 33: Process flowsheet used in the exergy analysis of isothermal and temperature-programmed CO production. Notations for the different sections were harmonised with those of the Aspen Plus simulation. The sections in red pertain to the temperature-programmed CO production process and the ones in blue are exclusively for the isothermal CO production process. ....	98
Figure 34: Nitrogen sorption isotherm of the oxygen carrier at 77 K. $p_0$ on the x-axis represents atmospheric pressure and p the pressure during the measurement. All 69 measured points were interpolated to provide 22 common points at regular pressure intervals for the assessment of the standard deviation depicted by the error bars. ....	102
Figure 35: Nitrogen sorption isotherm of the $\text{CO}_2$ carrier at 77 K. $p_0$ on the x-axis represents atmospheric pressure and p the pressure during the measurement. All 69 measured points were interpolated to provide 22 common points at regular pressure intervals for the assessment of the standard deviation depicted by the error bars. ....	103

Figure 36: X-ray diffractogram (XRD) of the calcined (a) OC and (b) CC and their STEM-EDX maps in (c) and (d), respectively. Peaks which have an intensity higher than 5% and 1% of the maximum peak intensity are marked and identified on the plot for the calcined OC (a) and CC (b), respectively. The indexes in (a) and (b) display the crystallite sizes and phase fraction estimated by Rietveld refinement. ....	106
Figure 37: Temperature-programmed reactions (TPRe) with a temperature ramp of 10 K/min up to 1173 K and a total flow rate of $45 \cdot 10^{-6}$ mol/s. (a): H <sub>2</sub> -TPR under a flow of 5 mol% H <sub>2</sub> in Ar for the determination of exchangeable oxygen atoms in the calcined OC; (b) CO <sub>2</sub> -TPO under a flow of 100% CO <sub>2</sub> for the determination of replenish-able oxygen atoms in the fully reduced OC; (c) H <sub>2</sub> -TPR under a flow of 5 mol% H <sub>2</sub> in Ar for the determination of exchangeable oxygen atoms in the OC oxidised by CO <sub>2</sub> ; (d) CO <sub>2</sub> -TPCD under a flow of 25% CO <sub>2</sub> in He for the determination of the total CO <sub>2</sub> capture and release capacity. ....	110
Figure 38: Outlet flow rates and temperature versus time during the 1 <sup>st</sup> (top; (a) for isothermal cycles and (d) for temperature-programmed cycles) and the 10 <sup>th</sup> (middle; (b) for isothermal and (e) for temperature-programmed cycles) cycles. Average CO STY over 10 cycles during the decarbonation-oxidation half-cycles (bottom; (c) for isothermal cycles and (f) for temperature-programmed cycles). Inlet gas flow rate during reduction-carbonation: $41 \cdot 10^{-6}$ mol/s ( $10 \cdot 10^{-6}$ mol/s CO; $10 \cdot 10^{-6}$ mol/s CO <sub>2</sub> ; $2 \cdot 10^{-6}$ mol/s H <sub>2</sub> ; rest: Ar and He). Inlet gas flow rate during decarbonation-oxidation: $41 \cdot 10^{-6}$ mol/s Ar. Error bars indicate the standard deviation from 3 independent experiments. ....	112
Figure 39: Instantaneous CO space time yield during the decarbonation-oxidation half-cycle for the isothermal and temperature-programmed CO production routes for the 1 <sup>st</sup> and 10 <sup>th</sup> cycles. Error bars represent standard deviation obtained from 3 independent experiments. ....	116
Figure 40: Utilisation of fuel (CO and H <sub>2</sub> ) in the reduction and carbonation half-cycle for the isothermal (grey circles) and temperature-programmed (red circles) CO production. ....	117



Figure 41: Experimental results of the 10 <sup>th</sup> cycle of isothermal CO production with shortened reduction-carbonation half-cycle time (20 seconds). Inlet gas flow rate during reduction-carbonation: 41 • 10 <sup>-6</sup> mol/s (10 • 10 <sup>-6</sup> mol/s CO; 10 • 10 <sup>-6</sup> mol/s CO <sub>2</sub> ; 2 • 10 <sup>-6</sup> mol/s H <sub>2</sub> ; rest: Ar and He). Inlet gas flow rate during decarbonation-oxidation: 41 • 10 <sup>-6</sup> mol/s Ar.....	118
Figure 42: Experimental results of the 10 <sup>th</sup> cycle of temperature-programmed CO production with shortened reduction-carbonation half-cycle time (20 seconds). Inlet gas flow rate during reduction-carbonation: 41 • 10 <sup>-6</sup> mol/s (10 • 10 <sup>-6</sup> mol/s CO; 10 • 10 <sup>-6</sup> mol/s CO <sub>2</sub> ; 2 • 10 <sup>-6</sup> mol/s H <sub>2</sub> ; rest: Ar and He). Inlet gas flow rate during decarbonation-oxidation: 41 • 10 <sup>-6</sup> mol/s Ar.....	119
Figure 43: Carbon recovery over 10 cycles in isothermal (grey filled circles) and temperature-programmed (red filled circles) CO production. ....	120
Figure 44: Utilisation of the oxygen carrier for isothermal (grey) and temperature-programmed (red) processes for CO production. Open and filled circles indicate decarbonation-oxidation and reduction-carbonation half-cycles. ....	122
Figure 45: Utilisation of the CO <sub>2</sub> carrier for isothermal (grey) and temperature-programmed (red) open circles) CO production. Open and filled circles indicate decarbonation-oxidation and reduction-carbonation half-cycles. ....	124
Figure 46: Experimental results of the post-treatment of the oxygen carrier and the CO <sub>2</sub> carrier after 10 cycles of isothermal CO production. Inlet gas flow rate during post-treatment: 41 • 10 <sup>-6</sup> mol/s Ar. ....	126
Figure 47: Block flow diagram with mass flows generated from simulation of the temperature-programmed CO production at 1013 K and 121 kPa. ....	129
Figure 48: Effect of temperature in the reduction-carbonation half-cycle on the carbon recovery and fuel efficiency of the process with the corresponding influence on the CO:CO <sub>2</sub> ratio of the process (secondary axis). ....	132
Figure 49: Effect of temperature during the reduction-carbonation half-cycle on the conversion of CO into CO <sub>2</sub> and H <sub>2</sub> into H <sub>2</sub> O. ....	133

Figure 50: Effect of temperature in the reduction-carbonation half-cycle on the minimum required temperature in the decarbonation-oxidation half-cycle for fully regenerating the materials. The secondary axis depicts the corresponding temperature difference between the two half-cycles.....	134
Figure 51: Block flow diagram for the exergy analysis of the process. Exergy of feedstock or products comprises of chemical exergy and the exergy of mixing of different components in the feedstock or products.....	136
Figure 52: Additional theoretical separation step considered for the exergy analysis to compare the chemical looping processes (isothermal and temperature-programmed). The greyed words represent components not present in the product stream of the temperature-programmed chemical looping process.....	136
Figure 53: The variation of the thermodynamic equilibrium partial pressure of CO <sub>2</sub> against temperature at a pressure of 101.3 kPa. Data for CaO and CO <sub>2</sub> from NIST[118] and of CaCO <sub>3</sub> from FactSage (FactPS database) [119]. .....	147
Figure 54: The variation of the thermodynamic equilibrium partial pressure of O <sub>2</sub> against temperature at a pressure of 101.3 kPa. Note that FeO is unstable below 843 K. Data for Fe <sub>3</sub> O <sub>4</sub> , Fe, and O <sub>2</sub> from NIST[118] and of FeO, Mn <sub>3</sub> O <sub>4</sub> , and MnO from FactSage (FactPS database) [119]. .....	147
Figure 55: General concept [137] of a two-step process wherein a feed gas containing fuel(s) and CO <sub>2</sub> (see black arrows) come into contact with metal oxide pairs that can oxidise fuel(s) partially (M <sub>1</sub> O/M <sub>1</sub> ) and almost completely (M <sub>3</sub> O/M <sub>3</sub> ) and a metal oxide (M <sub>2</sub> O) that is capable of capturing the produced CO <sub>2</sub> in the form of a carbonate (M <sub>2</sub> CO <sub>3</sub> ) under the process conditions of the first step. When the feed gas is switched to an oxidising gas (see blue arrows), at least one of the 2 redox pairs is capable of being oxidised by CO <sub>2</sub> while the other is readily oxidised by O <sub>2</sub> , releasing heat and decreasing the partial pressure of CO <sub>2</sub> such that the release of the captured CO <sub>2</sub> and its conversion to CO are favoured. ....	149
Figure 56: Block flow diagram of the process concept with mass flow rates. Labels: A: BFG feed for producing a CO/CO <sub>2</sub> product stream (C), B: additional BFG feed for	

generating the heat via chemical looping combustion to fulfil the heat demand in the decarbonator-oxidiser, D: recycled portion of product stream as a sweep or fluidising gas, E: CO<sub>2</sub> released by combusting additional BFG and partly oxidised BFG (F) via chemical looping combustion (CLC), G: air fed to replenish the lattice oxygen consumed during CLC, and H: O<sub>2</sub> depleted air. The compositions of the gas streams are given on a mass basis. Note that, for brevity and simplicity sake, the flows of inert solids MgAl<sub>2</sub>O<sub>4</sub>, and CeO<sub>2</sub> that are used for imparting stability to the oxygen carriers (FeO<sub>x</sub> and Mn<sub>3</sub>O<sub>4</sub>) and CO<sub>2</sub> carrier (CaCO<sub>3</sub>) and of the make-up flows are not displayed. Details are mentioned in Table 20 and in Figure D13..... 150

Figure 57: Laboratory reactor bed to carry out the proof of concept experiments and experimental specifications. The scale bar on the right indicates the length in cm. Gas flow:  $41 \cdot 10^{-6}$  mol/s. Size fraction of solids: 355 – 500 µm. Top bed (manganese oxide and calcium oxide): 1.1 g. Bottom bed (iron oxide and calcium oxide): 0.5 g. .... 166

Figure 58: Exergy analysis of the proposed chemical looping process (in blue) and conventional rWGS with downstream purification (in red). For the sake of brevity, the negligible exergy required for separation of H<sub>2</sub>O is not displayed. The displayed values represent the exergy content in different streams/processes normalised to the total exergy input. .... 176

Figure 59: Breakdown of the contribution to the costs constituting the CAPEX, OPEX, and revenue for the proposed chemical looping (CL) process and rWGS process with downstream separation. A, C, and E (in blue) show the breakdown of the CAPEX, OPEX, and revenue generated for the proposed chemical looping process (total CAPEX: 122 EUR<sub>2020</sub>/tonne<sub>product</sub> and OPEX: 100 EUR<sub>2020</sub>/tonne<sub>product</sub>), whereas B, D, and F (in red) show the corresponding breakdown for the rWGS (total CAPEX: 99 EUR<sub>2020</sub>/tonne<sub>product</sub> and OPEX: 136 EUR<sub>2020</sub>/tonne<sub>product</sub>). O&M stands for operation and maintenance. .... 178

Figure 60: Sensitivity analysis to examine the effect of A: CAPEX estimation, B: Cost of natural gas and electricity, C: Costs of solids: oxygen carriers and CO<sub>2</sub> carrier, or catalyst, and D: their lifetime on the net income defined as the difference between

the revenue and the production costs, i.e., CAPEX and OPEX. Abbreviations used in the figure legends: CL – chemical looping, NG – natural gas, El. – electricity, CC – Ca-based CO<sub>2</sub> carrier, Fe-OC – iron based oxygen carrier, Mn-OC – manganese based oxygen carrier, and Cat-rWGS – Ni/Al<sub>2</sub>O<sub>3</sub> catalyst for the reverse water-gas shift reaction..... 181

Figure 61: Anti-clockwise from top to bottom – A: the 6<sup>th</sup> cycle of the proposed chemical looping process showcasing its capabilities to use/store the chemical energy from synthetic BFG in stage 1 to produce CO (in stages 2 to 4) while completely using the fed O<sub>2</sub> in stage 3 to create heat for the decarbonation of CaCO<sub>3</sub>, B – utilisation of Mn in the top portion of the bed and its maximum possible utilisation based on reaction stoichiometry, C – utilisation of Ca as CaO in the top and bottom beds of the reactor and its maximum possible utilisation based on reaction stoichiometry, and D – utilisation of Fe in the bottom bed and its maximum possible utilisation based on the transitions of its redox pairs Fe/FeO, Fe/Fe<sub>3</sub>O<sub>4</sub>, or FeO/Fe<sub>3</sub>O<sub>4</sub>..... 185

Figure 62: Schematic representations of the process with the left half depicting a first step for H<sub>2</sub> production and the right half depicting CO production in a second step. The blue and red shading at the peripheries of the solid intermediates (represented by circles) indicate heat uptake or release in that step. Steam is added to the feed gas in step 1 to shift reaction equilibrium towards H<sub>2</sub> production in the top half of the bed and create conditions less favourable for coke formation. For the sake of simplicity, an equimolar ratio of H<sub>2</sub>O and CH<sub>4</sub> in step 1 of 2 is shown. .... 197

Figure 63. Fixed bed reactor configuration for the production of an H<sub>2</sub> and CO-rich stream in a 2-step chemical looping process. Percentages for solids and gases are displayed in mass% and mol%. .... 200

Figure 64: X-ray diffractograms of A: 40% NiO – 40% CaO – 20% CeO<sub>2</sub>, B: 50% Fe<sub>2</sub>O<sub>3</sub>/MgAl<sub>2</sub>O<sub>4</sub>, and C: 83% CaO/CeO<sub>2</sub>. .... 205

Figure 65: TPre with a temperature ramp of 10 K/min up to 1173 K and a total flow rate of  $45 \cdot 10^{-6}$  mol/s for the multifunctional material, 40% NiO – 40% CaO – 20% CeO<sub>2</sub>. A: H<sub>2</sub>-TPR under a flow of 5 mol% H<sub>2</sub> in Ar for the determination of exchangeable

oxygen atoms; B: CO <sub>2</sub> -TPCD under a flow of 20% CO <sub>2</sub> in Ar for the determination of the CO <sub>2</sub> capture and release capacity.....	206
Figure 66: Thermodynamic analyses to examine the influence of temperature (A) and total pressure (B) on H <sub>2</sub> purity and CH <sub>4</sub> conversion. In sub-figure A, the pressure was kept constant at 101 kPa and the H <sub>2</sub> O:CH <sub>4</sub> molar ratio was kept constant at 1. In sub-figure B, only the H <sub>2</sub> O:CH <sub>4</sub> molar ratio was kept constant at 1. In sub-figure C, the temperature was kept constant at 973 K and the pressure was kept constant at 101 kPa. ....	209
Figure 67. Proof-of-concept experiment for the 2-step chemical looping process to produce an H <sub>2</sub> -rich stream in step 1 and a CO-rich stream in step 2, performed at different temperatures and 120 kPa. The experimental results shown here were A) at 923 K (cycle#24 in Figure 69), B) at 973 K (cycle#26 in Figure 69), and C) at 998 K (cycle#25 in Figure 69). ....	213
Figure 68: Experiment to prove that the carbon content of CH <sub>4</sub> is captured by CaO (cycle#21 in Figure 69). Total gas flow rate: $55 \cdot 10^{-6}$ mol/s. Duration of the first step: 169 seconds. ....	215
Figure 69. Process and materials performance over multiple cycles wherein the symbols represent experimental values. Colour codes on top indicate the conditions used during the cycles. A: utilisation of Ni based on the O <sub>2</sub> uptake in the second step, B: utilisation of Ca based on the outlet flow of carbon containing gases – CO, CO <sub>2</sub> , and CH <sub>4</sub> , C: utilisation of Fe based on CO produced (equation (107)). D: concentrations of H <sub>2</sub> and CO in the first and second step of the process compared to the equilibrium concentrations calculated by FactSage for catalytic partial oxidation of methane (CPO), assuming no coke is formed. E: productivity of the process and the minimum productivity for sustainable industrial production recommended by Lange [154, 165]. F: conversion of CH <sub>4</sub> in the first step and of CO <sub>2</sub> in the second step of the process. In A, B, and C, the dotted or dashed lines indicate the maximum utilisation of the materials in the bed, whereas the dot-dashed line indicates the maximum	



experimental utilisation possible based on reaction stoichiometry and gas feed (see equations (113) to (118)).....	218
Figure B1: Block diagram of the Aspen Plus simulation used for estimating the minimum concentration of CO <sub>2</sub> required to achieve adiabatic operation of the carbonator. ....	228
Figure B2: Block flow diagram to assess the minimum reversible work to produce O <sub>2</sub> via (a) cryogenic distillation of air and (b) CLAS loop.....	230
Figure B3: Influence of CeO <sub>2</sub> in the Ni-Ca loop on the CO <sub>2</sub> capture of the process..	232
Figure B4: Standard Gibbs free energy against temperature for typical reactions involving C1 molecules that cause coking. ....	232
Figure B5: Standard Gibbs free energy against temperature for typical reforming reactions of CH <sub>4</sub> . ....	233
Figure B6: Evolution of the utilisation of the materials over multiple cycles, Ni oxidised and CaCO <sub>3</sub> decarbonated during the oxidation-decarbonation half-cycle and NiO reduced and CaO carbonated during the reduction-carbonation half-cycle.....	234
Figure B7: Maximum and average temperatures recorded during the two half-cycles of the multiple cycle test (on the primary y-axis on the left). Difference between the maximum temperatures of the half-cycles and between the average temperatures of the half-cycles (on the secondary y-axis on the right).....	235
Figure B8: Outlet flow rates and temperature vs time during: (a) the reduction-carbonation half-cycle of the 1 <sup>st</sup> cycle, (b) the oxidation-decarbonation half-cycle of the 1 <sup>st</sup> cycle, (c) the reduction-carbonation half-cycle of the 2 <sup>nd</sup> cycle, and (d) the oxidation- decarbonation half-cycle of the 2 <sup>nd</sup> cycle. In the oxidation-decarbonation half-cycle of the 1 <sup>st</sup> cycle, 21% O <sub>2</sub> /Ar was used instead of 50% O <sub>2</sub> /Ar. Synthetic BFG (molar composition: 5.1% H <sub>2</sub> , 23.8% CO, 24.1% CO <sub>2</sub> , 40% Ar, and 7% He) was used during the reduction-carbonation half-cycles. The inlet gases had a constant flow rate of $41 \cdot 10^{-6}$ mol/s.....	236

Figure B9: Measured outlet flow rates and temperature versus time over one cycle when synthetic BFG is used and the GHSV is kept constant at 3700 h <sup>-1</sup> while the reactor furnace temperature is fixed at (a) 873 K, (b) 923 K, and (c) 1023 K. During reduction-carbonation, synthetic BFG (molar composition: 5.1% H <sub>2</sub> , 23.8% CO, 24.1% CO <sub>2</sub> , 40% Ar, and 7% He) was fed and during oxidation-decarbonation, 21% O <sub>2</sub> /Ar was fed. The total inlet gas feed was kept constant at 41 • 10 <sup>-6</sup> mol/s.....	237
Figure B10: Measured isotherms of the as prepared (fresh) material and of the material after being cycled more than 50 times. ....	239
Figure B11: Pore size distribution based on incremental volume calculated using BJH theory applied on the desorption branch of the isotherm of the as prepared material and the material after being subjected to more than 50 cycles.....	240
Figure B12: XRD of the as prepared material (in red, centre) with the XRD generated by Rietveld refinement (in black, top) and the difference between the observed and fitted diffractogram (in grey, bottom). Only peak intensities greater than 5% of the maximum intensity have been marked. ....	241
Figure B13: XRD of the material cycled 50 times (in red, centre) with the XRD generated by Rietveld refinement (in black, top) and the difference between the observed and fitted diffractogram (in grey, bottom). Only peak intensities greater than 2% of the maximum intensity have been marked. ....	242
Figure B14: STEM-EDX mapping of the as prepared material: (a) overlay of Ca, Ni, and Ce mapping, (b) Ca mapping, (c) Ni mapping, and (d) Ce mapping. ....	245
Figure B15: STEM-EDX mapping of the material after 50 cycles: (a) overlay of Ca, Ni, and Ce mapping, (b) Ca mapping, (c) Ni mapping, and (d) Ce mapping. ....	246
Figure C1: X-ray diffractogram of the calcined oxygen carrier (in red, center) with the X-ray diffractogram generated by Rietveld refinement (in black, top) and the difference between the observed and fitted diffractogram (in grey, bottom). Peaks which have an intensity greater than 5% of the maximum peak intensity are marked and identified on the plot. ....	255

Figure C2: X-ray diffractogram of the calcined CO <sub>2</sub> carrier (in red, center) with the X-ray diffractogram generated by Rietveld refinement (in black, top) and the difference between the observed and fitted diffractogram (in grey, bottom). Peaks which have an intensity greater than 1% of the maximum peak intensity are marked and identified on the plot. ....	256
Figure C3: X-ray diffractogram of the oxygen carrier after being fully oxidised by CO <sub>2</sub> (in red, center) with the X-ray diffractogram generated by Rietveld refinement (in black, top) and the difference between the observed and fitted diffractogram (in grey, bottom). Peaks which have an intensity greater than 5% of the maximum peak intensity are marked and identified on the plot. ....	257
Figure C4: X-ray diffractogram of the oxygen carrier and the CO <sub>2</sub> carrier cycled 10 times for temperature-programmed production of CO (in red, center) with the X-ray diffractogram generated by Rietveld refinement (in black, top) and the difference between the observed and fitted diffractogram (in grey, bottom). Peaks which have an intensity higher than 2% of the maximum peak intensity are marked and identified on the plot. ....	258
Figure C5: X-ray diffractogram of the oxygen carrier and the CO <sub>2</sub> carrier cycled once for isothermal production of CO (in red, center) with the X-ray diffractogram generated by Rietveld refinement (in black, top) and the difference between the observed and fitted diffractogram (in grey, bottom). Peaks which have an intensity higher than 1% of the maximum peak intensity are marked and identified on the plot. ....	259
Figure C6: X-ray diffractogram of the oxygen carrier and the CO <sub>2</sub> carrier cycled 5 times for isothermal production of CO (in red, center) with the X-ray diffractogram generated by Rietveld refinement (in black, top) and the difference between the observed and fitted diffractogram (in grey, bottom). Peaks which have an intensity higher than 1% of the maximum peak intensity are marked and identified on the plot. ....	260

Figure C7: X-ray diffractogram of the oxygen carrier and the CO<sub>2</sub> carrier cycled 10 times for isothermal production of CO (in red, center) with the X-ray diffractogram generated by Rietveld refinement (in black, top) and the difference between the observed and fitted diffractogram (in grey, bottom). Peaks which have an intensity higher than 5% of the maximum peak intensity are marked and identified on the plot.

..... 261

Figure C8: X-ray diffractogram of the oxygen carrier and the CO<sub>2</sub> carrier cycled once for temperature-programmed production of CO (in red, center) with the X-ray diffractogram generated by Rietveld refinement (in black, top) and the difference between the observed and fitted diffractogram (in grey, bottom). Peaks which have an intensity higher than 3% of the maximum peak intensity are marked and identified on the plot. .... 262

Figure C9: X-ray diffractogram of the oxygen carrier and the CO<sub>2</sub> carrier cycled 5 times for temperature-programmed production of CO (in red, center) with the X-ray diffractogram generated by Rietveld refinement (in black, top) and the difference between the observed and fitted diffractogram (in grey, bottom). Peaks which have an intensity higher than 3% of the maximum peak intensity are marked and identified on the plot. .... 263

Figure C10: X-ray diffractograms displaying the evolution of the crystal structures of the materials upon being cycled in isothermal conditions to produce CO..... 264

Figure C11: X-ray diffractograms displaying the evolution of the crystal structures of the materials upon being cycled in temperature-programmed conditions to produce CO. .... 265

Figure C12: X-ray diffractogram of the oxygen carrier and the CO<sub>2</sub> carrier cycled 9 times for temperature-programmed production of CO and after the reduction-carbonation half-cycle of the 10<sup>th</sup> cycle. Peaks which have an intensity higher than 3% of the maximum peak intensity are marked and identified on the plot..... 266

Figure C13: Reaction quotient and equilibrium constants in the 10 <sup>th</sup> reduction-carbonation half-cycle of isothermal CO production. Error bars indicate the standard deviation obtained from three independent experiments.....	274
Figure C14: Reaction quotient and equilibrium constants in the 1 <sup>st</sup> reduction-carbonation half-cycle of isothermal CO production. Error bars indicate the standard deviation obtained from three independent experiments.....	275
Figure C15: Reaction quotient and equilibrium constants in the 1 <sup>st</sup> reduction-carbonation half-cycle of temperature-programmed CO production. Error bars indicate the standard deviation obtained from three independent experiments. ..	276
Figure C16: Reaction quotient and equilibrium constants in the 1 <sup>st</sup> decarbonation-oxidation half-cycle of isothermal CO production. Error bars indicate the standard deviation obtained from three independent experiments.....	277
Figure C17: Reaction quotient and equilibrium constants in the 10 <sup>th</sup> reduction-carbonation half-cycle of temperature-programmed CO production. Error bars indicate the standard deviation observed in three different experiments. ....	278
Figure C18: Reaction quotient and equilibrium constants in the 1 <sup>st</sup> decarbonation-oxidation half-cycle of temperature-programmed CO production. Error bars indicate the standard deviation obtained from three independent experiments. ....	279
Figure C19: Experimental results of temperature-programmed CO production with shortened reduction-carbonation half-cycle time (20 seconds) and reduction-carbonation carried out at 923 K. Inlet gas flow rate during reduction-carbonation: 41 • 10 <sup>-6</sup> mol/s (10 • 10 <sup>-6</sup> mol/s CO; 10 • 10 <sup>-6</sup> mol/s CO <sub>2</sub> ; 2 • 10 <sup>-6</sup> mol/s H <sub>2</sub> ; rest: Ar and He). Inlet gas flow rate during decarbonation-oxidation: 41 • 10 <sup>-6</sup> mol/s Ar. Materials were cycled 48 times (isothermally and in temperature-programmed conditions) before the experiment.....	281
Figure C20: Experimental results of temperature-programmed CO production with shortened reduction-carbonation half-cycle time (180 seconds) and reduction-carbonation carried out at 923 K. Inlet gas flow rate during reduction-carbonation: 41 • 10 <sup>-6</sup> mol/s (10 • 10 <sup>-6</sup> mol/s CO; 10 • 10 <sup>-6</sup> mol/s CO <sub>2</sub> ; 2 • 10 <sup>-6</sup> mol/s H <sub>2</sub> ; rest: Ar and	

He). Inlet gas flow rate during decarbonation-oxidation: $41 \cdot 10^{-6}$ mol/s Ar. Materials were cycled 49 times (isothermally and in temperature-programmed conditions) before the experiment.....	282
Figure C21: Photos of the reactor containing the solids used for the experiments. The red particles are those of the OC and the white particles are either the CC or the solid diluent, $\alpha\text{-Al}_2\text{O}_3$ . The ruler has a cm based scale. ....	284
Figure D1: The variation of the thermodynamic equilibrium partial pressure of $\text{O}_2$ against temperature at a pressure of 101.3 kPa. Note that FeO is unstable below 843 K. Data for $\text{Fe}_3\text{O}_4$ , Ni, Fe, and $\text{O}_2$ from NIST [118] and of FeO and NiO from FactSage (FactPS database) [119]. ....	286
Figure D2: Bauer-Glaessner diagram generated using data from NIST [118] and FactSage (for FeO only). ....	287
Figure D3: X-ray diffractogram of the fresh oxygen carrier 80% $\text{Mn}_2\text{O}_3/\text{MgAl}_2\text{O}_4$ (in red circles) with the X-ray diffractogram generated by Rietveld refinement (in black) and the difference between the observed and fitted diffractogram (in grey, bottom). Peaks which have an intensity higher than 5% of the maximum peak intensity are marked and identified on the plot. ....	290
Figure D4: Temperature-programmed reactions (TPRe) with a temperature ramp of 10 K/min up to 1173 K and a total flow rate of $45 \cdot 10^{-6}$ mol/s for the 80% $\text{Mn}_2\text{O}_3/\text{MgAl}_2\text{O}_4$ . A: $\text{H}_2$ -TPR under a flow of 5 mol% $\text{H}_2$ in Ar for the determination of exchangeable oxygen atoms; B: $\text{O}_2$ -TPO under a flow of 5% $\text{O}_2$ in Ar for the determination of replenishable oxygen atoms in the fully reduced material. ....	293
Figure D5: The first of the 30 redox cycles executed for the proof of concept experiments involving $\text{Mn}_3\text{O}_4$ , CaO, and $\text{FeO}_x$ as active materials. Compared to the last 25 cycles, the reduction step lasted 180 seconds instead of 240 cycles to determine the time required for complete decarbonation of the $\text{CaCO}_3$ in the given conditions. The vertical dashed lines indicate the change of stage (from left to right: stages 1 to 4 marked by numbers in circles). ....	293

Figure D6: The second of the 30 redox cycles executed for the proof of concept experiments involving $\text{Mn}_3\text{O}_4$ , $\text{CaO}$ , and $\text{FeO}_x$ as active materials. Compared to the last 25 cycles, the reduction step lasted 180 seconds instead of 240 seconds. The vertical dashed lines indicate the change of stage (from left to right: stages 1 to 4 marked by numbers in circles).....	294
Figure D7: The third of the 30 redox cycles executed for the proof of concept experiments involving $\text{Mn}_3\text{O}_4$ , $\text{CaO}$ , and $\text{FeO}_x$ as active materials. Compared to the last 25 cycles, the reduction step lasted 180 seconds instead of 240 seconds. The vertical dashed lines indicate the change of stage (from left to right: stages 1 to 4 marked by numbers in circles).....	295
Figure D8: The fourth of the 30 redox cycles executed for the proof of concept experiments involving $\text{Mn}_3\text{O}_4$ , $\text{CaO}$ , and $\text{FeO}_x$ as active materials. Compared to the last 25 cycles, the reduction step lasted 180 seconds instead of 240 seconds. The vertical dashed lines indicate the change of stage (from left to right: stages 1 to 4 marked by numbers in circles).....	295
Figure D9: The fifth of the 30 redox cycles executed for the proof of concept experiments involving $\text{Mn}_3\text{O}_4$ , $\text{CaO}$ , and $\text{FeO}_x$ as active materials. Compared to the last 25 cycles, the reduction step lasted 180 seconds instead of 240 seconds. The vertical dashed lines indicate the change of stage (from left to right: stages 1 to 4 marked by numbers in circles).....	296
Figure D10: Experimental results showing the outlet flow rates of different components when gases were fed to an empty reactor. Total inlet flow rate during all 4 stages: $41 \cdot 10^{-6} \text{ mol/s}$ . ....	297
Figure D11: Block flow diagram of the process involving steady-state catalytic rWGS and downstream separation with mass flow rates. Labels: A: BFG feed to the catalytic reverse water-gas shift reaction (rWGS) block for producing a $\text{CO}/\text{CO}_2$ product stream (E), B: a hypothetical $\text{H}_2\text{O}$ separator (for example, a knockout drum), C: an $\text{H}_2$ pressure swing adsorption (PSA) column for creating a 100% pure $\text{H}_2$ stream partly for sale and partly for providing heat to the rWGS block (F), D: a pure $\text{N}_2$ stream generated from	

the product stream via cryogenic distillation, G: air fed for H <sub>2</sub> combustion, and H: outlet gas from H <sub>2</sub> combustion.....	298
Figure D12: Aspen Plus flowsheet of rWGS with downstream separation. The alphabetical blue labels correspond to those from Figure D11.....	299
Figure D13: Aspen Plus flowsheet of the proposed chemical looping process. The alphabetical blue labels correspond to those from Figure 2 of the main text. ....	300
Figure D14: Fit of retail pricing data obtained from Sigma-Aldrich (Belgium), Carl Roth (Belgium), and Alfa Aesar (Germany) on 04/06/2021 and 05/06/2021 for A: iron nitrate nonahydrate, B: magnesium nitrate hexahydrate, C: aluminium nitrate nonahydrate, and D: 28% NH <sub>4</sub> OH in H <sub>2</sub> O, precursors for the synthesis of 50% Fe <sub>2</sub> O <sub>3</sub> /MgAl <sub>2</sub> O <sub>4</sub> . The purity of precursors was higher than 98% for all considered data points. ....	303
Figure D15: Fit of retail pricing data obtained from Sigma-Aldrich (Belgium), Carl Roth (Belgium), and Alfa Aesar (Germany) on 04/06/2021 and 05/06/2021 for manganese nitrate hexahydrate, precursor for the synthesis of 80% Mn <sub>2</sub> O <sub>3</sub> /MgAl <sub>2</sub> O <sub>4</sub> . The purity of the precursor was higher than 98% for all considered data points. ....	304
Figure D16: Fit of retail pricing data obtained from Sigma-Aldrich (Belgium), Carl Roth (Belgium), and Alfa Aesar (Germany) on 04/06/2021 and 05/06/2021 for A: calcium gluconate monohydrate and B: cerium nitrate hexahydrate, precursor for the synthesis of 83% CaO/CeO <sub>2</sub> . The purity of precursors was higher than 98% for all considered data points. ....	305
Figure E1: Standard enthalpy of several reactions that are typically catalysed during steam methane reforming using data from NIST webbook [118] and FactSage [119] for C (graphite).....	312
Figure E2: Standard Gibbs free energy of several reactions that are typically catalysed during steam methane reforming using data from NIST webbook [118] and FactSage [119] for C (graphite). ....	313



Figure E3: Standard enthalpy of the sorption enhanced reactions using data from NIST webbook [118] and FactSage [119] for $\text{CaCO}_3$ , Ni, and NiO. ....	313
Figure E4: Standard Gibbs free energy of the sorption enhanced reactions using data from NIST webbook [118] and FactSage [119] for $\text{CaCO}_3$ , Ni, and NiO. ....	314
Figure E5: Standard enthalpy of the reduction and oxidation half-cycle of CL-rWGS using data from NIST webbook [118] and FactSage [119] for FeO. ....	314
Figure E6: Standard Gibbs free energy for the reduction and oxidation half-cycle of CL-rWGS using data from NIST webbook [118] and FactSage [119] for FeO. ....	315
Figure E7: Standard enthalpy of chemical looping combustion half-cycles of $\text{CH}_4$ with NiO with data from NIST webbook [118] and FactSage [119] for NiO and Ni. ....	315
Figure E8: Standard Gibbs free energy of chemical looping combustion half-cycles of $\text{CH}_4$ with NiO with data from NIST webbook [118] and FactSage [119] for NiO and Ni. ....	316
Figure E9: Shorter cycle (89 seconds) for the two-step chemical looping process to produce an $\text{H}_2$ -rich stream in step 1 (45 seconds) and a CO-rich stream in step 2 (44 seconds) at 973 K. ....	317
Figure E10: Decarbonation of the $\text{CO}_2$ carrier, $\text{CaCO}_3$ , in Ar gas flow ( $55 \cdot 10^{-6}$ mol/s) upon imposing a temperature ramp after the second step of the process carried out at three different temperatures (923 K – dashed lines, 973 K – dotted lines, and 998 K – solid lines). ....	318
Figure E11: Outlet flow of gases during $\text{O}_2$ feed (21% $\text{O}_2$ in Ar at $55 \cdot 10^{-6}$ mol/s) at 1073 K. The $\text{O}_2$ feed was temporarily suspended to avoid extremely high temperatures in the reactor (from 140 to 240 seconds). Note that the thermocouple is placed between the two beds. The remaining consumption of $\text{O}_2$ from 240 s onwards till its breakthrough is likely caused by the oxidation of $\text{FeO}_x$ ( $x = 0$ to 1.3) to $\text{Fe}_2\text{O}_3$ . ....	319
Figure E12: Temperature programmed reactions (TPRe) with a temperature ramp of 10 K/min up to 1173 K and a total flow rate of $45 \cdot 10^{-6}$ mol/s for the multifunctional material, 40% NiO – 40% CaO – 20% $\text{CeO}_2$ (A and B) and 1:1 mass basis mixture of 50% $\text{Fe}_2\text{O}_3/\text{MgAl}_2\text{O}_4$ and 83% CaO/ $\text{CeO}_2$ (C and D) after the experimental campaign. A and	

C: H<sub>2</sub>-TPR under a flow of 5 mol% H<sub>2</sub> in Ar for the determination of exchangeable oxygen atoms; B and D: CO<sub>2</sub>-TPCD under a flow of 25% CO<sub>2</sub> in He (B) or 20% CO<sub>2</sub> in Ar (D) for the determination of the CO<sub>2</sub> capture and release capacity..... 321

List of tables

Table 1: List of materials, their compositions, synthesis methods, and their application within the thesis. .... 16

Table 2: Details of chemicals and reagents used during synthesis. .... 19

Table 3: Typical characteristics of steel mill gases from a modern steel production plant [42]. .... 28

Table 4: Specific oxygen transfer capacity of selected redox couples based on their capacity to fully oxidise reductants in steel mill gases and their cost. .... 37

Table 5: Specifications of the heat exchangers displayed in Figure 20. .... 42

Table 6: Aspen Plus® setup of modules, property methods, material databanks, convergence options, and models. .... 43

Table 7: Specifications and assumptions of the base case of the process simulation. .... 45

Table 8: Effect of GHSV on the solids conversion. .... 67

Table 9: Influence of the reactor furnace temperature on the conversions of the reactive components in the two half-cycles. Conversions of CH<sub>4</sub>, CO, H<sub>2</sub>, NiO, and CaO correspond to the reduction-carbonation half-cycle and the conversions of Ni and CaCO<sub>3</sub> correspond to the oxidation-decarbonation half-cycle. .... 73

Table 10: Influence of the reactor furnace temperature on the maximum temperature achieved during the two half-cycles and the difference between them. .... 73

Table 11: Textural properties of the as prepared material and the material after 50 cycles (post decarbonation-oxidation) from liquid nitrogen sorption measurements. .... 74

Table 12: Gas-solid reactions during the process with their standard reaction enthalpies and Gibbs free energies from NIST for CO, CO<sub>2</sub>, H<sub>2</sub>, H<sub>2</sub>O, Fe, Fe<sub>3</sub>O<sub>4</sub>, and CaO [118] and FactSage for CaCO<sub>3</sub> and FeO [119]. .... 88

Table 13: Aspen Plus® setup of modules, property methods, material databanks, and models. .... 93

Table 14: Specifications and assumptions of the process simulation. .... 96

Table 15: Textural properties of the as prepared materials from nitrogen sorption measurements at 77 K. ....	101
Table 16: Elemental composition obtained by energy dispersive x-ray spectroscopy (EDX) expressed in mass percentage. The error indicates the standard deviation based on four measurements. ....	104
Table 17: Comparison of process parameters (during the 10th cycle) to estimate the influence of varying the reduction-carbonation half-cycle time for reduction-carbonation carried out at 1023 K (Figure 41 and Figure 42). ....	126
Table 18: Comparison of simulation results with experimental results for the temperature-programmed CO production over 10 cycles. All values are expressed in mol%. The standard deviation was obtained from 3 independent experiments. ....	135
Table 19: Comparison of exergy losses and during isothermal, temperature-programmed CO production, and complete combustion. ....	140
Table 20: Specifications of the process simulation. Capital letters in brackets refer to the labels in Figure 56. ....	152
Table 21: Specifications of the outlet gases of the process simulation (see C, E, and H in Figure 56). Capital letters in brackets refer to the labels in Figure 56. ....	172
Table 22: Elemental composition using energy dispersive x-ray spectroscopy (EDX) expressed in mass percentage (on an oxygen-free basis) of the materials used for the experimental demonstration of the process concept. The error indicates the standard deviation based on at least four measurements. Values in brackets indicate expected values based on the nominal composition. ....	204
Table 23: Textural properties of the as prepared materials from nitrogen sorption measurements at 77 K. ....	204
Table A1: List of calorific resources from the agricultural industry. ....	224
Table A2: List of calorific resources from the biorefining industry. ....	224
Table A3: List of calorific resources from the chemicals industry. ....	225
Table A4: List of calorific resources from food waste. ....	225

Table A5: List of calorific resources from the iron and steel industry .....	225
Table A6: List of calorific resources from municipal waste. ....	226
Table A7: List of calorific resources from the petrochemical industry. ....	226
Table A8: List of calorific resources from end-of-life plastics. ....	226
Table A 9: Gas composition of <i>low grade</i> gases. ....	227
Table B1: The mass content of the different components of the synthesised materials measured using EDX. The $\pm$ sign indicates the value of one standard deviation obtained from 5 different measurements. ....	238
Table B2: Summary of the results for the Rietveld refinement of the cycled and as prepared materials. ....	244
Table C1: Details of the exergy analysis of the isothermal CO production process for 1 MMta equivalent CO <sub>2</sub> emissions from BFG. ....	248
Table C2: Details of the exergy analysis of the temperature-programmed CO production (mild temperature change) process for 1 MMta equivalent CO <sub>2</sub> emissions from BFG. ....	250
Table C3: Details of the exergy analysis of the temperature-programmed CO production (large temperature change) process for 1 MMta equivalent CO <sub>2</sub> emissions from BFG. ....	252
Table C4: Summary of the results for the Rietveld refinement of different materials and their phases. ....	267
Table C5: Comparison of process parameters to estimate the influence of varying the reduction-carbonation half-cycle time for reduction-carbonation carried out at 923 K (Figure C19 and Figure C20). ....	283
Table C6: Summary of reactor productivities at different conditions. ....	285
Table D1: Textural properties of the as prepared materials from nitrogen sorption measurements at 77 K. ....	288

Table D2: Elemental composition using energy dispersive x-ray spectroscopy (EDX) or inductively coupled plasma coupled with optical emission spectroscopy (ICP-OES) expressed in mass percentage of the materials used for the experimental demonstration of the process concept. The error indicates the standard deviation based on at least four measurements. Values in brackets indicate expected values.....	289
Table D3: Summary of the results for the Rietveld refinement of different materials and their phases. ....	292
Table D4: Aspen Plus® setup of modules, property methods, material databanks, and models. ....	297
Table D5: Cost estimation for preparing 80% $\text{Mn}_2\text{O}_3/\text{MgAl}_2\text{O}_4$ via co-precipitation. ....	306
Table D6: Cost estimation for preparing 50% $\text{Fe}_2\text{O}_3/\text{MgAl}_2\text{O}_4$ via co-precipitation..	307
Table D7: Cost estimation for preparing 83% $\text{CaO}/\text{CeO}_2$ via wet physical mixing....	308
Table D8: Price of the natural ores and the data sources.....	309
Table E1: Textural properties of the as prepared materials and materials after the experimental campaign from nitrogen sorption measurements at 77 K. ....	320

## Glossary and list of abbreviations, symbols, and sub- and super-scripts

### Glossary

As prepared material	The catalyst, oxygen carrier, CO <sub>2</sub> carrier, or a combination of these after the calcination step.
Blue hydrogen	Hydrogen produced when carbon emissions are captured and stored, or reused.
Carbonation-decarbonation cycle	A sequential process based on the carbonation and decarbonation of the CO <sub>2</sub> carrier. In the first half cycle, CO <sub>2</sub> is captured by the CO <sub>2</sub> carrier. In the second half cycle the material is regenerated while releasing captured CO <sub>2</sub> either by decreasing the partial pressure of CO <sub>2</sub> or increasing the temperature.
Catalyst	Substance or material, which through repeated cycles of elementary steps, accelerates the conversion of reagents into products. Catalysts are classified into homogeneous, which are in the

same phase with the reagents (*e.g.* acids and bases, metal complexes, etc.), and heterogeneous, which are separated from the reactants by an interface (*e.g.* metals, metal oxides, etc.).

Chemical looping process      A chemical reaction with solid intermediates that is split into multiple sub reactions and either executed in separate reactors or in an alternating manner in a single reactor.

Chemical      looping      CO<sub>2</sub>      Chemical looping process where the conversion      reduced oxygen storage material is regenerated by CO<sub>2</sub> resulting in the production of pure CO.

Chemical      looping      CO<sub>2</sub>      Chemical looping process where CO<sub>2</sub> is capture      captured by a solid CO<sub>2</sub> carrier, after which it is released in an enriched stream of CO<sub>2</sub> at elevated temperature.

CO<sub>2</sub> carrier      A material, often containing (earth) alkali metal oxides, which can periodically capture and release CO<sub>2</sub>



	by formation and decomposition of (earth) alkali metal carbonate.
Deactivation	Loss in catalyst, oxygen carrier or CO <sub>2</sub> carrier activity due to chemical, mechanical or thermal process.
Exergy	The maximum amount of useful work that can be obtained from a system.
Green hydrogen	Hydrogen produced by renewable energy sources.
Lattice oxygen	The oxygen present in the lattice of an inorganic oxide. It can act as reservoir for oxygen releasing it during reactions creating vacancies. The vacancies can be re-filled by gas phase oxidising agents such as O <sub>2</sub> , CO <sub>2</sub> or H <sub>2</sub> O.
Oxygen storage capacity	The total amount of exchangeable oxygen present in the oxygen carrier.
Oxygen carrier	A solid intermediate which can exchange oxygen during chemical looping process.
Poisoning	Refers to the partial or total deactivation of a catalyst caused by exposure to a range of chemical

	compounds. These compounds can be reactants, products or impurities.
Porosity	A measure of the void space in a material, expressed as the ratio of the volume of voids to the total volume of the material.
Redox or reduction-oxidation cycle	A sequential redox process based on the reduction oxidation of the oxygen carrier. In the first half cycle, a reducing fuel is employed to reduce the oxygen carrier. In the second half cycle the material is regenerated through reoxidation by oxidising gases such as O <sub>2</sub> or CO <sub>2</sub> .
Syngas	A variable composition mixture of hydrogen and carbon monoxide.
Used material	The recovered catalyst, oxygen carrier or CO <sub>2</sub> carrier after an activity or stability test
<i>In situ</i>	Latin phrase meaning “on site”. <i>In situ</i> materials characterization, for example, means that the material is not physically moved from one

apparatus to another between treatment and characterization.

Grey hydrogen

Hydrogen produced by fossil fuels

## Abbreviations

AMU	Atomic mass unit
ASU	Air separation unit
BET	Brunauer-Emmett-Teller
BFG	Blast furnace gas
BF-BOF	Blast furnace – basic oxygen furnace route for steelmaking
BOFG	Basic oxygen furnace gas
BJH	Barrett-Joyner-Halenda
CC	CO <sub>2</sub> carrier
CFZ	Controlled Freezing Zone – trademark of ExxonMobil
CO <sub>2,equiv</sub>	Equivalent CO <sub>2</sub> emissions when the gas is fully oxidised with O <sub>2</sub> or air
COG	Coke oven gas
CL	Chemical looping
CLAS	Chemical looping air separation
CLC	Chemical looping combustion
EFB	Empty fruit bunch
El.	Electricity
EDX	Energy dispersive x-ray spectroscopy

FEG	Field emission gun
GHSV	Gas hourly space velocity in $\text{h}^{-1}$
GSAS	General structure analysis system
HAADF	High-angle annular dark field
HDPE	High density polyethylene
ISBL	Inside battery limits
ID	Internal diameter in mm
kt	kilotonne(s)
LCV	Lower calorific value
LDPE	Low density polyethylene
MFC	Mass flow controller
MMta	Million metric tonnes per annum
MS	Mass spectrometer
MSW	Municipal solid waste
MT	Megatonne(s)
Ni-Ca loop	Combined chemical looping for $\text{CO}_2$ separation comprising $\text{NiO/Ni}$ and $\text{CaO/CaCO}_3$
NIST	National Institute of Standards and Technology, United States of America
NG	Natural gas
NTP	Normal temperature and pressure, i.e. 273.15 K and 101.3 kPa
O&M	Operation and maintenance
O-D	Oxidation-decarbonation of the Ni-Ca loop

OC	Oxygen carrier
OPEX	Operating expenses
OSBL	Outside battery limits
PET	Polyethylene terephthalate
PGM	Platinum group metals
PMR	Palm mill residue
POME	Palm oil mill effluent
PP	Polypropylene
PR-BM	Peng-Robinson cubic equation of state with the Boston Matthias alpha function
PSA	Pressure swing adsorption
R-C	Reduction-carbonation
rWGS	Reverse water-gas shift reaction
SEM	Scanning electron microscope
SMR	Steam methane reforming
STEM	Scanning transmission electron microscopy
STEAM-TA	1967 American Society of Mechanical Engineers steam tables
TPCD	Temperature-programmed carbonation and decarbonation
TPO	Temperature-programmed oxidation
TPR	Temperature-programmed reduction
TPRe	Temperature-programmed reaction
WGS	Water-gas shift reaction

XRD                      X-ray diffraction

## Symbols

$A$	Minimum reversible work required for separation or mixing in kJ/mol
$\Delta G^0$	Standard Gibbs free energy of reaction in kJ/mol
$\Delta H^0$	Standard enthalpy of reaction in kJ/mol
$\Omega$	Distillation resistance in $^{\circ}\text{C}^{-1}$
$v_j$	Molecularity of component $j$ (positive for products and negative for reactants)
$a_j$	Thermodynamic activity of component $j$
BP	Boiling point in $^{\circ}\text{C}$
$c_i$	Cost of materials or resources $i$ expressed in EUR <sub>2020</sub> /tonne <sub>product</sub>
CaCh	Capital charge in %/year.
CAPEX	Capital expenses in EUR per tonne of product
$CB$	Carbon balance in %
$CCAP$	Carbon capture in %
CCR	CO:CO <sub>2</sub> molar ratio
CCU	CO <sub>2</sub> carrier utilisation in %
CF	Carbon footprint in tonnes of CO <sub>2</sub> released to the environment per tonne of product
CI	Capital investment in million United States dollars of the year 2003

CR	Carbon recovery in moles of carbon in product per mole of carbon fed
CT	Total cycle time in hours
E	Exergy in kJ/mol
$e_{chem,i}$	Chemical exergy in kJ/mol
$E_{total}$	Total exergy in kJ/mol
$E_{physical}$	Physical exergy in kJ/mol
$E_{physical}$	Physical exergy originating from heat in kJ/mol
$E_{thermoc}$	Thermochemical exergy in kJ/mol
$\dot{E}_n$	Energy flow in MW
ET	Energy transfer duty in GJ/tonne <sub>feed</sub>
$\dot{E}_x$	Exergy flow in MW
$EXC_{Ni-C}$	Excess material in the Ni-Ca loop in mol/mol
$\eta_{exergy}$	Exergy efficiency in percentage
F	Total number of feed streams
FU	Fuel utilisation in %
FE	Fuel efficiency in %
h	Height of the fixed bed for the experimental proof of concept in m
HD	Heat duty in GJ/tonne <sub>feed</sub>
$K_e$	Equilibrium constant in Pa <sup>x</sup> where x is dependent on the reaction equation.
$MM_i$	Average molar mass of component or stream i in g/mol
$m_i$	Mass of component i in g

$\dot{m}$	Mass flow rate in tonnes/hour or kg/s
$M_{Fe}$	Mass of metallic Fe in the oxygen carrier in kg
$\dot{n}$	Molar flow rate in mol/s
$N_i$	Moles of component or compound “i” in the reactor
$\dot{n}_{CaO,min}$	Simulated minimum molar flow rate of CaO circulating in the Ni-Ca loop = 378 mol/s
$\dot{n}_{NiO,min}$	Simulated minimum molar flow rate of NiO circulating in the Ni-Ca loop = 342 mol/s
$\dot{n}_{CO_2,out}$	Molar flow rate of CO <sub>2</sub> exiting the reducer carbonator in mol/s
$\dot{n}_{x,BFG}$	Simulated flow rate of component ‘x’ in the BFG in mol/s
$\dot{n}_{x,COG}$	Simulated flow rate of component ‘x’ in the COG in mol/s
$N$	Moles of a particular element in the fixed bed
$NI$	Net income in EUR <sub>2020</sub> /tonne
$OB$	Oxygen balance in %
$OCU$	Oxygen carrier utilisation in %
$OPEX$	Operating expenses in EUR per tonne of product
$Q$	Heat released or required in MW
$p_x$	Partial pressure of gas component “x”
$P$	Total number of product streams
$PC$	Production costs in EUR per tonne of product
$p_{CO_2,eq}$	Thermodynamic equilibrium CO <sub>2</sub> partial pressure of a metal carbonate



$p_{O_2,eq}$	Thermodynamic equilibrium oxygen partial pressure of a metal oxide
$r$	Radius of the fixed bed quartz reactor for the experimental proof of concept = 3.75 mm
$\dot{r}$	Net reaction rate in mol/s
$\vec{r}$	Forward reaction rate in mol/s
$R$	Universal gas constant in kJ/mol/K
$R_{CO_2}$	Fraction of hot $CO_2$ produced in the oxidiser-decarbonator directed to the CLAS loop
RCE	Reductions in $CO_2$ emissions in % (when compared to the best available technology of combusting the steel mill gases for heat and/or electricity)
$R_{wp}$	Weighted profile R-factor
$t$	Time of half-cycle in seconds
$T_0$	Temperature at “dead state” = 298 K in K
$T$	Temperature in K
$u_{CaO}$	Utilisation of CaO in %
$u_{NiO}$	Utilisation of NiO in %
$U_{CaO,z}$	Experimental utilisation of CaO in ‘z’ half-cycle in %
$U_{NiO,z}$	Experimental utilisation of NiO in ‘z’ half-cycle in %
$v$	Volume of the packed bed in $cm^3$
$\dot{V}_{NTP}$	Volumetric gas flow in $cm^3/h$ at 273.15 K and 101.3 kPa
$w_i$	Mass fraction of component i in feed or product
$x_i$	Molar fraction of component i in feed or product

$X_y$	Conversion of a compound or element ‘y’
$\chi^2$	Goodness-of-fit

## Subscripts

0	At “dead state”: 298 K and 101 kPa
avg	Time averaged value in s
CCSU	CO <sub>2</sub> from the oxidiser-decarbonator which is captured and compressed for storage or utilisation
d-o	Of/in the decarbonation-oxidation half-cycle
eq	At equilibrium
o-d	Of/in the oxidation-decarbonation half-cycle of the Ni-Ca loop
f	“f” <sup>th</sup> feed in mol
i	“i” <sup>th</sup> component in feed or product
in	Inlet flow in mol/s
out	(Measured) outlet flow in mol/s
p	“p” <sup>th</sup> product in mol
r-c	Of/in the reduction carbonation half-cycle of the Ni-Ca loop
tot	Total flow
total	The total cycle time in seconds
X K	At X K

## Superscripts

0

Standard thermodynamic value

## Summary

Energy intensive industries such as steelmaking and  $H_2$  production contribute to more than 10% of global  $CO_2$  emissions. These sectors are considered difficult to decarbonise and the cost of applying mature technologies to decrease their emissions causes a steep increase in production costs. For example, capturing  $CO_2$  from the steel industry using mature  $CO_2$  capture technologies can hike the price of steel by 22%. Similarly, producing  $H_2$  from green electricity costs 300 – 600% more than conventional  $H_2$  production under current circumstances. Chemical looping is an emerging class of technology that can drastically reduce the cost of  $CO_2$  capture, utilisation, and  $H_2$  production. This is made possible by its improved efficiency, integrated separation, and high degree of adaptability. So far, chemical looping processes such as calcium looping and chemical looping combustion, both of which are carbon capture technologies, have been demonstrated on pilot scale, which corresponds to removal of thousands of tonnes of  $CO_2$  per year. These pilot scale demonstrations have gathered more than 11000 hours of operational time, thereby forming a large body of operational experience and technological know-how. The high degree of adaptability of chemical looping lends itself very well to combination and process intensification for accelerating reduction in  $CO_2$  emissions from the most challenging sectors. This thesis delves into the combinatorial aspect of chemical looping to

intensify processes for CO<sub>2</sub> capture and utilisation for steelmaking and H<sub>2</sub> production.

Figure 1 shows a process concept that combines three different chemical looping processes, chemical looping combustion, calcium looping, and chemical looping air separation, for capturing CO<sub>2</sub> from steel mill gases. Steel mill gases contain up to 50% N<sub>2</sub> and several valuable platform molecules such as CO, H<sub>2</sub>, and CH<sub>4</sub>. The current best available technology is to combust these gases in a power plant while co-feeding natural gas. This leads to CO<sub>2</sub> emissions of more than 1 kg of CO<sub>2</sub> per kg of steel made. The dilution of the steel mill gases makes the standalone use of chemical looping combustion less effective as the product CO<sub>2</sub> would still contain N<sub>2</sub>. Calcium looping can be applied effectively, but it suffers from high energy demand for producing O<sub>2</sub> in a cryogenic distillation column and providing an enormous proportion of energy to produce CO<sub>2</sub> while regenerating calcium oxide. The proposed concept addresses these challenges by integrating chemical looping air separation and combining chemical looping combustion with calcium looping to effectively use the residual chemical energy in the steel mill gas for producing pure CO<sub>2</sub>. The process concept was proven in a laboratory fixed bed reactor and simulations show that this strategy can eliminate up to 85% of CO<sub>2</sub> emissions caused by the blast furnace gas (BFG) and coke oven gas (COG) of the steel industry. A multifunctional material comprising NiO, CaO, and CeO<sub>2</sub> applied for the

experimental campaign remained stable for 50 cycles and thus, could be considered for future analysis and upscaling.

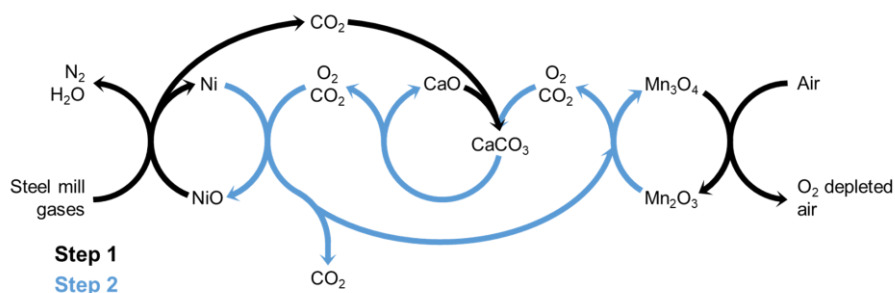


Figure 1: Process concept for decarbonisation of steel mill gases in an energy neutral chemical looping process. The final product  $CO_2$  is produced in the second step. In the first step,  $NiO$  is used for fully oxidising the reductants in the steel mill gases,  $CaO$  is used for capturing  $CO_2$ , and  $Mn_3O_4$  captures the  $O_2$  for the process. In the second step,  $Mn_2O_3$  provides the oxygen for the exothermic oxidation of  $Ni$  to  $NiO$  while the heat is used the decarbonation of  $CaCO_3$  to produce a pure  $CO_2$  stream.

BFG contains  $CO_2$  and  $H_2$  (approximately 23 and 5 mol%) and can be used for converting a small proportion of  $CO_2$  in the gas into  $CO$ , a valuable platform molecule for carbon based products. The reaction converting  $CO_2$  and  $H_2$  to  $CO$  and  $H_2O$  is called reverse water-gas shift. Typically, it is carried out at steady state at high temperature ( $> 1073$  K) with a catalyst. The product stream of the steady state catalytic process comprises unreacted  $CO_2$  and  $H_2$  along with the products, thereby necessitating complex downstream separation. The combined chemical looping approach displayed in Figure 2 breaks down the reaction in two steps using two solid mediators, iron oxide and calcium oxide, to produce a  $CO/CO_2$  product stream that can be used for making polyols

applied in polyurethane production or for the production of synthetic fuels. Calcium oxide captures  $\text{CO}_2$ , whereas iron oxide, after its reduction by  $\text{H}_2$ , converts the captured  $\text{CO}_2$  to  $\text{CO}$ . The process can be operated either by feeding an inert stream (such as  $\text{N}_2$  or  $\text{He}$ ) in step 2 or increasing the temperature of step 2. Experimental results and exergy analysis indicate that changing temperature in step 2 results in superior performance and improved exergy efficiency. Changing the temperature and the utilisation of the solid mediators provides optimisation opportunities to maximise  $\text{H}_2$  utilisation and  $\text{CO}_2$  capture. The proximity of the process to a steel mill facilitates disposal of the solid mediators once they reach the end of their life-time because both iron and calcium oxide are raw materials necessary for iron and steelmaking.

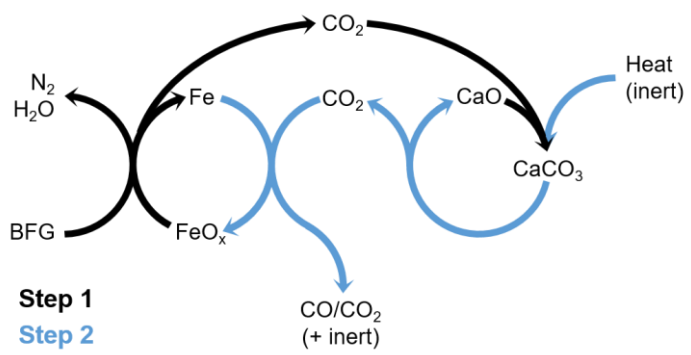


Figure 2: Combined chemical looping applying calcium and iron looping breaks down the reverse water-gas shift reaction into two steps to produce a  $\text{CO}$ -rich stream from the blast furnace gas (BFG) of the steel industry. In the first step,  $\text{FeO}_x$  oxidises the reductants in the BFG and  $\text{CO}_2$  is captured by  $\text{CaO}$ . In the second step, the captured  $\text{CO}_2$  is released and converted into  $\text{CO}$  while regenerating  $\text{FeO}_x$  and  $\text{CaO}$ .

Reverse water-gas shift reaction is endothermic and thus, requires constant heat supply at fairly high temperatures ( $>923\text{ K}$ ). A new process concept integrating chemical looping combustion displayed in Figure 3 was developed to address this and provide the energy to run the process concept in Figure 2.  $M_1$ ,  $M_2$ , and  $M_3$  here can, for example, be Fe, Ca, and MnO. The process concept can make use of any gas stream containing fuel and  $\text{CO}_2$ . Optimal conditions for a given feed stream can be arrived at by changing the metals used and the operating conditions, i.e. temperature and pressure. This process concept was applied to BFG and an experimental proof of concept was obtained in a laboratory fixed bed reactor. Techno-economic assessment showed that BFG can be processed at a cost of approximately 50 EUR<sub>2020</sub>/tonne. Comparison with a combination of mature technologies confirmed that the proposed process concept is far more viable and its primary cost savings come from its integrated separation. Analyses suggest that the profitability of the process concept is highly sensitive to the cost and the life-time of the  $\text{CO}_2$  carrier ( $\text{M}_2\text{O}$ ). Thus, future efforts need to be directed to address these aspects and quantify the cost and life-time of the  $\text{CO}_2$  carrier accurately.



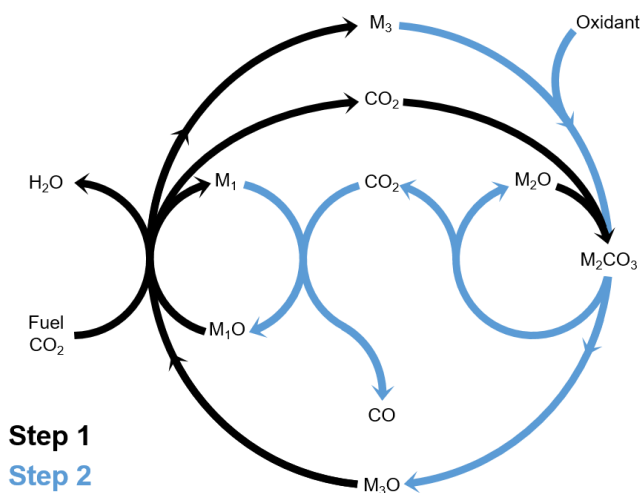


Figure 3: A process concept combining chemical looping reverse water-gas shift with calcium looping and chemical looping combustion. Here  $\text{M}_1$  and  $\text{M}_3$  are metals capable of donating or accepting lattice oxygen and  $\text{M}_3\text{O}$  is a metal oxide capable of capturing and releasing  $\text{CO}_2$ . Fuel can be any hydrocarbon or  $\text{H}_2$  or a combination and the oxidant could be  $\text{O}_2$ ,  $\text{NO}$ , or  $\text{N}_2\text{O}$ .

95% of  $\text{H}_2$  production currently relies on fossil fuels and for every kg of  $\text{H}_2$  produced by natural gas, 10 kg of  $\text{CO}_2$  is emitted. The endothermic character of  $\text{H}_2$  production and the complex downstream processing are significant challenges that limit decreasing the carbon footprint of  $\text{H}_2$  production via thermochemical routes. By combining reverse water-gas shift and sorption-enhanced steam reforming, a new concept displayed in Figure 4 was developed. This process concept produces so-called blue hydrogen in step 1 and in step 2 converts the captured  $\text{CO}_2$  into  $\text{CO}$  at the expense of one out of three  $\text{H}_2$  molecules produced in the first step. The overall reaction is partial oxidation and by using a combination of solid intermediates, the equilibrium is shifted

as per Le Chatelier's principle towards  $H_2$  production or  $CO_2$  utilisation. As the overall reaction is partial oxidation, the developed process is mildly exothermic and thus, does not require external heating. Compared to conventional technologies for producing  $H_2$ , the developed process runs at an operating temperature lower by 150 – 300 K, mitigates carbon deposition, improves safety by avoiding direct mixing of  $O_2$  and fuel, and finally produces  $H_2$  and CO as two separate streams. The developed process was tested in a laboratory scale fixed bed reactor. The experimental results showed that the process can achieve a reactor productivity of more than  $100 \text{ kg}_{\text{product}}/\text{m}^3_{\text{reactor}}/\text{h}$ , which is necessary for the process to have commercial relevance. Experimental results achieved up to 80% conversion of the captured  $CO_2$  and  $H_2$  purity that was higher than that in commercial auto-thermal reforming reactors operating at far higher temperatures. The process concept can be extended to any type of fuel such as glycerol, waste vegetable oil, complex hydrocarbon mixtures, etc. instead of  $CH_4$ .

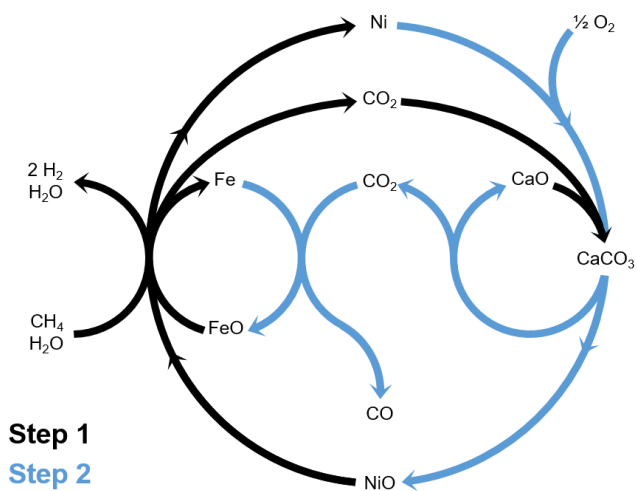


Figure 4: A process concept combining sorption enhanced steam reforming with chemical looping reverse water-gas shift and chemical looping combustion. In the first step, NiO is reduced by CH<sub>4</sub>, FeO is reduced by H<sub>2</sub> and/or CH<sub>4</sub>, and CaO captures CO<sub>2</sub> formed during this step. In the second step, Ni is oxidised by O<sub>2</sub>, CaCO<sub>3</sub> decomposes to release CO<sub>2</sub>, and Fe is oxidised to FeO by the release CO<sub>2</sub>.

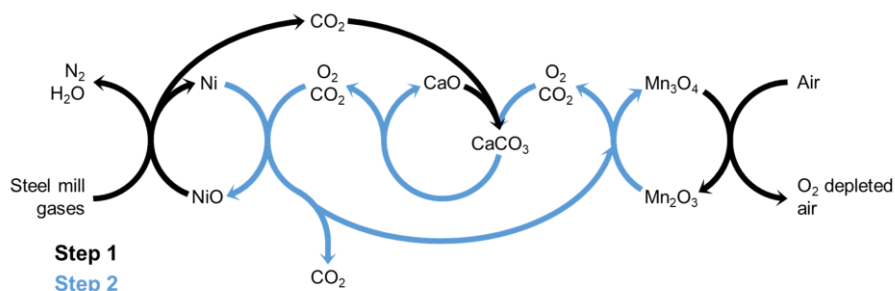
## Samenvatting

Energie-intensieve industrieën zoals staal- en H<sub>2</sub>-productie veroorzaken meer dan 10% van de wereldwijde CO<sub>2</sub>-emissies. Deze sectoren worden beschouwd als moeilijk koolstofvrij te maken en het toepassen van technieken om hun emissies te verminderen gaat gepaard met een sterke stijging van de productiekosten. Zo kan het afvangen van CO<sub>2</sub> uit de staalindustrie met behulp van bewezen CO<sub>2</sub>-afvangtechnologieën de prijs van staal met 22% doen stijgen. Evenzo kost de productie van H<sub>2</sub> uit groene stroom 300 – 600% meer dan conventionele H<sub>2</sub>-productie in de huidige omstandigheden. Chemische kringprocessen vormen een opkomende technologieklasse die de kosten van CO<sub>2</sub>-afvang, CO<sub>2</sub>-gebruik en H<sub>2</sub>-productie drastisch kan verlagen. Dit wordt mogelijk gemaakt door de verbeterde efficiëntie, geïntegreerde scheiding en een hoge mate van flexibiliteit. Tot dusver zijn twee chemische kringprocessen gedemonstreerd, het calciumkringproces en chemische kringverbranding, twee technologieën voor het afvangen van koolstof dioxide met een verwerkingscapaciteit van duizenden ton CO<sub>2</sub> per jaar. Deze demonstraties op pilotschaal hebben meer dan 11000 uur aan operationele tijd verzameld en leveren zo een grote hoeveelheid operationele ervaring en technologische knowhow. Door hun hoge graad van aanpasbaarheid en de mogelijkheid om chemische kringprocessen te combineren, leent dit soort chemische processen zich uitstekend voor procesintensivering en het aanpakken van de

enorme uitdagingen die gepaard gaan met het verminderen van de CO<sub>2</sub>-emissies van deze sectoren. Dit proefschrift gaat in op het combinatorisch aspect van chemische kringprocessen met het oog op de intensifiëring van CO<sub>2</sub>-afvang en -gebruik voor staal- en H<sub>2</sub>-productie.

Figuur 5 toont een procesconcept dat drie verschillende chemische kringprocessen combineert: chemische kringverbranding, calciumkringproces en chemische kring voor luchtscheiding, voor het afvangen van CO<sub>2</sub> uit staalfabrieksgassen. Staalfabrieksgassen bevatten tot 50% N<sub>2</sub> en verschillende waardevolle moleculen zoals CO, H<sub>2</sub> en CH<sub>4</sub>. De huidige, best beschikbare technologie voor hun verwerking is om deze gassen in een elektriciteitscentrale te verbranden met aardgas. Dit leidt tot een CO<sub>2</sub>-uitstoot van meer dan 1 kg CO<sub>2</sub> per kg gemaakt staal. De verdunning van de staalfabrieksgassen maakt het op zichzelf staand gebruik van chemische kringverbranding minder effectief omdat het product CO<sub>2</sub> nog steeds N<sub>2</sub> zal bevatten. Het calciumkringproces kan wel worden toegepast, maar dat gaat enerzijds gepaard met een hoge energiebehoefte voor de productie van O<sub>2</sub> in een cryogene destillatiekolom, en anderzijds met een enorme hoeveelheid energie om CO<sub>2</sub> te produceren en calciumoxide te regenereren. Het hier voorgestelde concept pakt deze uitdagingen aan door chemische luchtscheiding in een lus te integreren en chemische kringverbranding te combineren met het calciumkringproces om de resterende chemische energie in het staalfabrieksgas effectief te gebruiken voor de

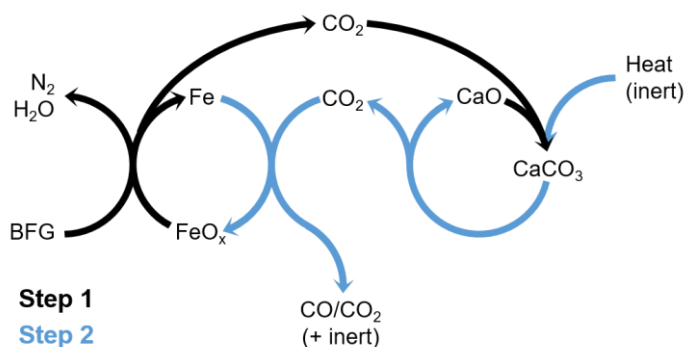
productie van zuiver  $\text{CO}_2$ . Het procesconcept werd gevalideerd in een vastbedreactor op laboschaal en simulaties tonen aan dat deze strategie tot 85% van de  $\text{CO}_2$ -uitstoot, veroorzaakt door het hoogovengas (BFG) en cokesovengas (COG) van de staalindustrie, kan elimineren. Een multifunctioneel materiaal bestaande uit  $\text{NiO}$ ,  $\text{CaO}$  en  $\text{CeO}_2$ , toegepast in de experimentele campagne, bleef 50 cycli stabiel en kan dus worden overwogen voor toekomstige analyse en opschaling.



Figuur 5: Procesconcept voor decarbonisatie van staalfabrieksgassen in een energieneutraal chemisch kringproces. In de eerste stap wordt  $\text{NiO}$  gebruikt voor het volledig oxideren van de reductanten in de staalfabrieksgassen,  $\text{CaO}$  wordt gebruikt voor het afvangen van  $\text{CO}_2$  en  $\text{Mn}_3\text{O}_4$  vangt  $\text{O}_2$  op. In de tweede stap levert  $\text{Mn}_2\text{O}_3$  zuurstof voor de exotherme oxidatie van  $\text{Ni}$  tot  $\text{NiO}$ , terwijl de warmte wordt gebruikt om  $\text{CaCO}_3$  te ontbinden en een zuivere  $\text{CO}_2$ -stroom als eindproduct te produceren.

BFG bevat  $\text{CO}_2$  en  $\text{H}_2$  (ongeveer 23 en 5 mol%) en kan worden gebruikt om een deel van  $\text{CO}_2$  in het gas om te zetten in  $\text{CO}$ , een waardevolle platformmolecule voor de aanmaak van producten gebaseerd op koolstof. De reactie die  $\text{CO}_2$  en  $\text{H}_2$  omzet in  $\text{CO}$  en  $\text{H}_2\text{O}$  wordt de omgekeerde water-gasverschuivingsreactie genoemd. Gewoonlijk wordt die met behulp van een katalysator uitgevoerd in

stationaire toestand bij hoge temperatuur ( $> 1073$  K). De productstroom van het stationair katalytisch proces omvat niet-gereageerd  $\text{CO}_2$  en  $\text{H}_2$  samen met de producten, waardoor een complexe productscheiding noodzakelijk is. De gecombineerde chemische kringbenadering weergegeven in Figuur 6 splitst de reactie op in twee stappen met behulp van twee vaste mediators, ijzeroxide en calciumoxide, om een  $\text{CO}/\text{CO}_2$  product te produceren dat gebruikt kan worden voor het maken van polyolen, die op hun beurt worden gebruikt bij de productie van polyurethaan of van synthetische brandstoffen. Calciumoxide vangt  $\text{CO}_2$  af, terwijl ijzeroxide, na reductie met  $\text{H}_2$ , het opgevangen  $\text{CO}_2$  omzet in  $\text{CO}$ . Het proces kan worden uitgevoerd door ofwel een inerte stroom (zoals  $\text{N}_2$  of  $\text{He}$ ) toe te voeren in stap 2 of door de temperatuur in stap 2 te verhogen. Experimentele resultaten en exergieanalyse geven aan dat het veranderen van de temperatuur in stap 2 resulteert in betere prestaties en verbeterde exergie-efficiëntie. Het veranderen van de temperatuur en het gebruik van de vaste mediators biedt optimalisatiemogelijkheden om het  $\text{H}_2$ -gebruik en de  $\text{CO}_2$ -afvang te maximaliseren. Indien geïnstalleerd nabij een staalfabriek vergemakkelijkt dit proces de verwijdering van de vaste mediators zodra ze het einde van hun levensduur hebben bereikt, omdat zowel ijzeroxide als calciumoxide grondstoffen zijn, nodig voor de productie van ijzer en staal.

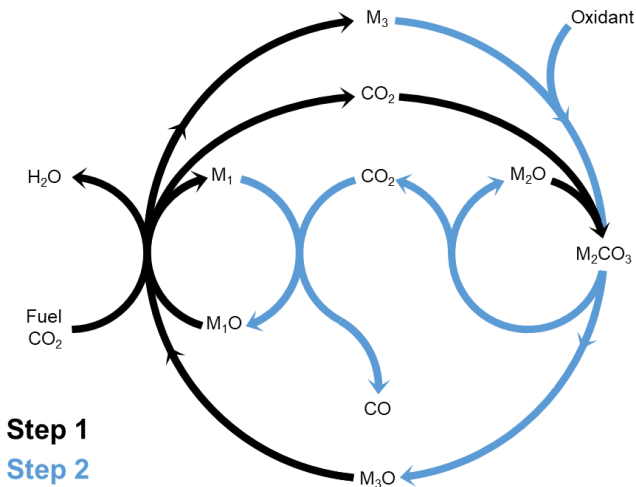


Figuur 6: Een gecombineerd chemisch calcium- en ijzerkringproces splitst de omgekeerde water-gasverschuivingsreactie in twee stappen om een CO-rijke stroom te produceren uit het hoogovensgas (BFG) van de staalindustrie. In de eerste stap oxideert  $\text{FeO}_x$  de reductanten in het BFG en wordt  $\text{CO}_2$  opgevangen door  $\text{CaO}$ . In de tweede stap wordt het opgevangen  $\text{CO}_2$  vrijgegeven en omgezet in CO, terwijl  $\text{FeO}_x$  en  $\text{CaO}$  worden geregenereerd.

De omgekeerde water-gasverschuivingsreactie is endotherm en vereist dus een constante warmtetoevoer bij vrij hoge temperatuur ( $> 923 \text{ K}$ ). Om dit aan te pakken en de energie te leveren om het proces in Figuur 6 uit te voeren, is een nieuw concept ontwikkeld dat chemische verbranding in de lus integreert, zoals weergegeven in Figuur 7. Hier kunnen  $M_1$ ,  $M_2$  en  $M_3$  bijvoorbeeld Fe, Ca en  $\text{MnO}$  zijn. Dit procesconcept werd toegepast op BFG en een experimenteel conceptbewijs werd verkregen in een laboratoriumreactor met vast bed. Een techno-economische studie toonde aan dat BFG kan worden verwerkt tegen een kostprijs van ongeveer  $50 \text{ EUR}_{2020}/\text{ton}$ . Vergelijking met een combinatie van bestaande technologieën bevestigde dat het voorgestelde procesconcept veel rendabeler is en dat de belangrijkste kostenbesparingen te danken zijn aan de geïntegreerde



productscheiding. Analyses suggereren dat het profijt van het procesconcept zeer gevoelig is voor de kosten en de levensduur van de CO<sub>2</sub>-drager (M<sub>2</sub>O). Daarom moeten toekomstige onderzoeksinspanningen gericht zijn op het aanpakken van deze aspecten en het nauwkeurig kwantificeren van de kosten en de levensduur van de CO<sub>2</sub>-drager.

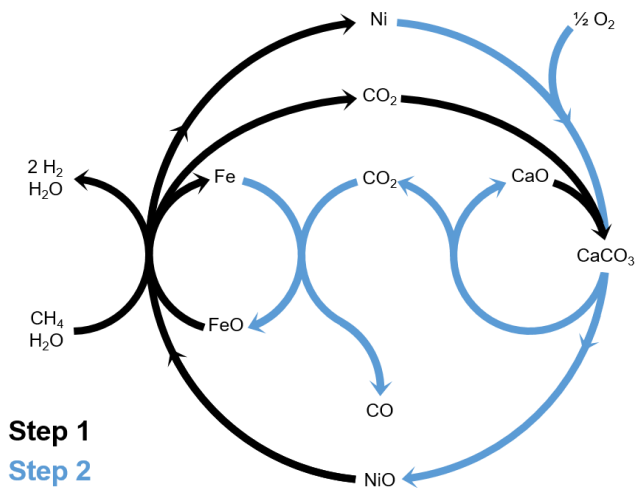


Figuur 7: Een procesconcept dat de omgekeerde water-gasverschuivingsreactie in chemische kring combineert met het calciumkringproces en chemische kringverbranding. Hier zijn M<sub>1</sub> en M<sub>3</sub> metalen die roosterzuurstof kunnen doneren of accepteren en M<sub>3</sub>O is een metaaloxide dat in staat is om CO<sub>2</sub> op te vangen en af te geven. Brandstof kan een koolwaterstof zijn, of H<sub>2</sub> of een combinatie, en als oxidatiemiddel kan O<sub>2</sub>, NO of N<sub>2</sub>O gebruikt worden.

95% van de waterstofproductie is momenteel afhankelijk van fossiele brandstoffen en elke kg H<sub>2</sub>, die uit aardgas wordt geproduceerd, gaat gepaard met een uitstoot van 10 kg CO<sub>2</sub>. Het endotherme karakter van H<sub>2</sub>-productie en de complexe naverwerking

zijn belangrijke uitdagingen die het verminderen van de koolstofvoetafdruk van  $H_2$ -productie via thermochemische routes beperken. Door een combinatie van omgekeerde water-gasverschuivingsreactie en stoomreforming, versterkt door sorptie, werd een nieuw concept ontwikkeld, weergegeven in Figuur 8. Dit procesconcept produceert in stap 1 zogenaamde blauwe waterstof en zet in stap 2 het opgevangen  $CO_2$  om in CO ten koste van één op de drie geproduceerde  $H_2$ -moleculen. De algemene reactie komt overeen met de gedeeltelijke oxidatie van methaan en door een combinatie van vaste tussenproducten te gebruiken wordt het evenwicht volgens het principe van Le Châtelier verschoven naar  $H_2$ -productie of  $CO_2$ -gebruik. Aangezien de algemene reactie gedeeltelijke oxidatie is, is het ontwikkelde proces licht exotherm en vereist het dus geen externe verwarming. Vergeleken met conventionele technologieën voor de productie van  $H_2$  werkt het ontwikkelde proces bij een bedrijfstemperatuur die 150 – 300 K lager is, vermindert het de koolstofafzetting, verbetert het de veiligheid door directe vermenging van  $O_2$  en brandstof te vermijden, en produceert het uiteindelijk  $H_2$  en CO als twee afzonderlijke stromen. Het ontwikkelde proces werd getest in een vastbedreactor op laboratoriumschaal. De experimentele resultaten tonen aan dat het proces een reactorproductiviteit van meer dan  $100 \text{ kg}_{\text{product}}/\text{m}^3_{\text{reactor}}/\text{u}$  kan bereiken, wat nodig is voor een commercieel relevant proces. De experimenten bereikten een omzetting tot 80% van de opgevangen  $CO_2$  en een  $H_2$ -zuiverheid die

hoger was dan in commerciële autothermische reformingsreactoren, die bij veel hogere temperaturen werken. Het procesconcept kan worden uitgebreid tot elk type brandstof zoals glycerol, plantaardige afvalolie, complexe koolwaterstofmengsels, enz. in plaats van CH<sub>4</sub>.



Figuur 8: Een procesconcept dat stoomreforming verbetert door sorptie te combineren met de omgekeerde water-gasverschuivingsreactie in chemische kring en chemische kringverbranding. In de eerste stap wordt NiO gereduceerd met CH<sub>4</sub>, FeO wordt gereduceerd met H<sub>2</sub> en/of CH<sub>4</sub> en CaO vangt het tijdens deze stap gevormde CO<sub>2</sub> op. In de tweede stap wordt Ni geoxideerd door O<sub>2</sub>, CaCO<sub>3</sub> ontbindt om CO<sub>2</sub> vrij te maken en Fe wordt geoxideerd tot FeO door het vrijkomen van CO<sub>2</sub>.



# Chapter I

## Introduction

Our accelerated consumption of natural resources threatens the survivability of diverse life on Earth. Thus, we urgently need to seek and implement efficient technologies to use the limited materials and resources available to us. In the last three decades, chemical looping has been gaining renewed attention as an efficient and clean technology that could play a pivotal role in mitigating anthropogenic environmental harm [1-3]. Chemical looping makes use of an intermediate, typically a solid, to bring about chemical transformation(s) in multiple steps, which are operated under most optimal conditions [4]. Figure 9 shows schematised examples of solid intermediates, also known as looping materials, with the capability to exchange oxygen, nitrogen, CO<sub>2</sub>, and energy from the environment to create useful products for humanity. The chemical looping approach to utilising resources provides several advantages such as: improved selectivity towards desired chemical transformations, simplified downstream separation, higher exergy efficiency, a high degree of adaptability, and combinatorial synergy (Figure 9) [5].

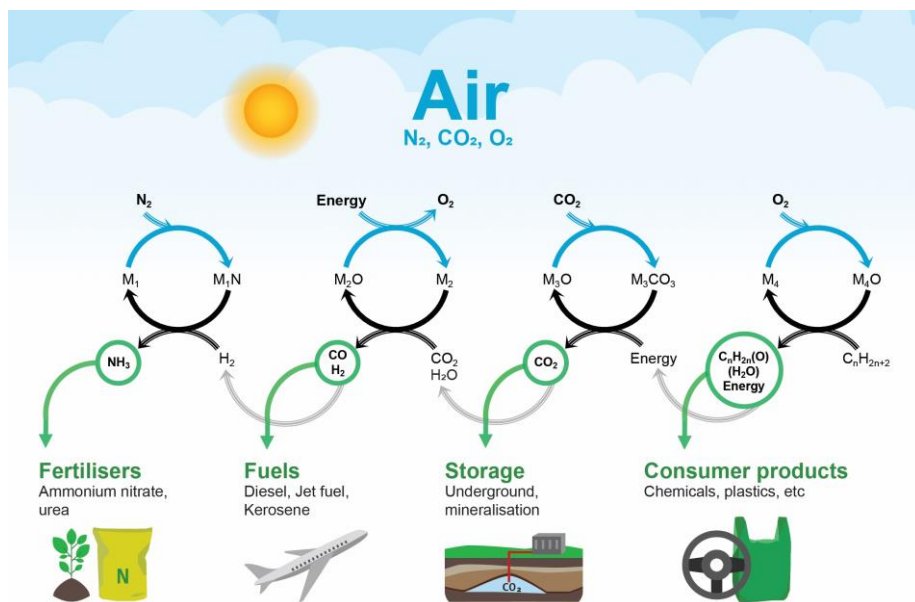


Figure 9: Schematic displaying the chemical looping approach for producing chemical feedstocks, energy carriers, and CO<sub>2</sub> sequestration.

Chemical looping has been thoroughly covered in literature through several excellent review articles. The interested reader is referred to reviews on the versatility of the chemical looping approach [2] (Figure 10), the path to its commercialisation [6, 7], its role in CO<sub>2</sub> capture and utilisation [1, 8], the importance of looping materials' properties [9, 10], and its environmental footprint [11]. Despite this wide coverage, the potential of chemical looping in utilising *low grade* resources as fuels and/or looping materials has not yet been fully grasped by the wider scientific community. This thesis focuses on the untapped potential of chemical looping as a technology that can be applied to rigorously realise circularity in our society.

## 1.1 *Low grade* resources as feedstock for chemical looping

With a focus on utilising resources via chemical looping, *low grade* resources are defined based on their energetic content. Resources which have an energetic content, measured by their net calorific value, lower than 10 GJ/tonne or 20% of the calorific value of methane, are defined as *low grade* and can potentially serve as feedstocks to be upgraded or treated by chemical looping. Once these resources are mapped, their potential valorisation impact is characterised by their availability and economic value. Using quantified characteristics of *low grade* resources, opportunities are highlighted for their upcycling or their utilisation via chemical looping.

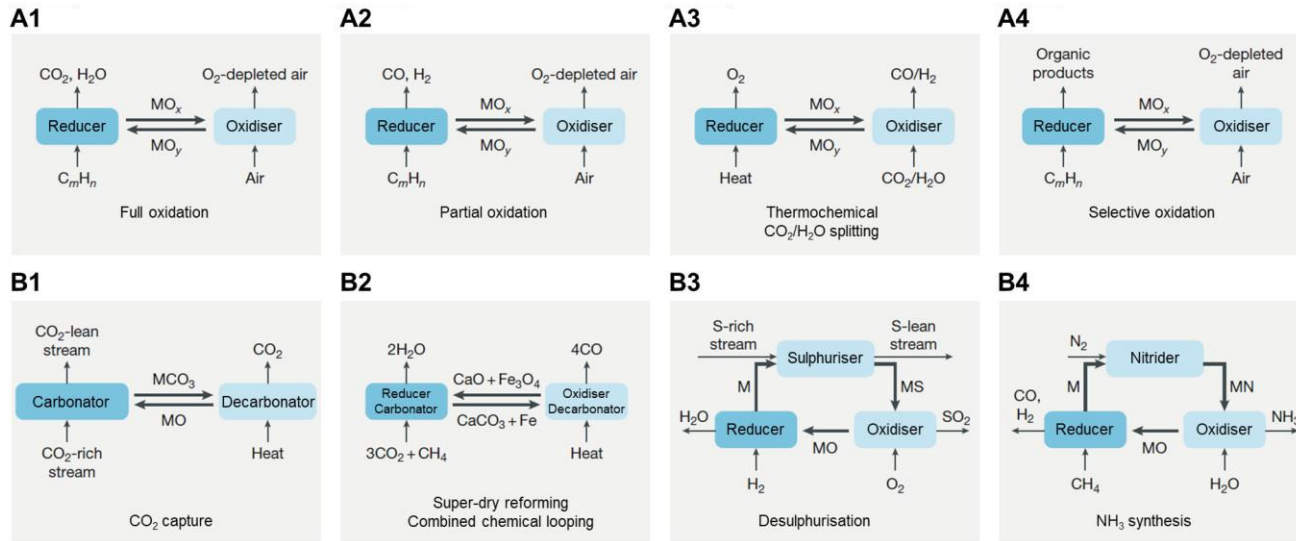


Figure 10: A selection of chemical looping approaches. For example,  $CO_2$  sequestration (A1 using an oxygen carrier  $MO_x$  via chemical looping combustion and B1 using a  $CO_2$  carrier  $MO$  via calcium looping), chemical reforming for syngas production (A2),  $CO_2$  utilisation or clean  $H_2$  production by oxygen uncoupling (A3), selective oxidation applicable to catalytic reactions proceeding via the Mars-van-Krevelen mechanism (A4) for production of organic compounds such as alkenes, a combined chemical looping approach using two or more different types of solid intermediates (B2), for desulphurisation of industrial or effluent streams by means of a sulphur carrier (B3), and highly selective  $NH_3$  synthesis by applying a nitrogen carrier (B4). Note that for the oxidation reactions,  $x < y$  for the oxygen carrier pair ( $MO_x/MO_y$ ). Figure adapted from [2]. Other catalyst-assisted chemical looping approaches can be found in [12].



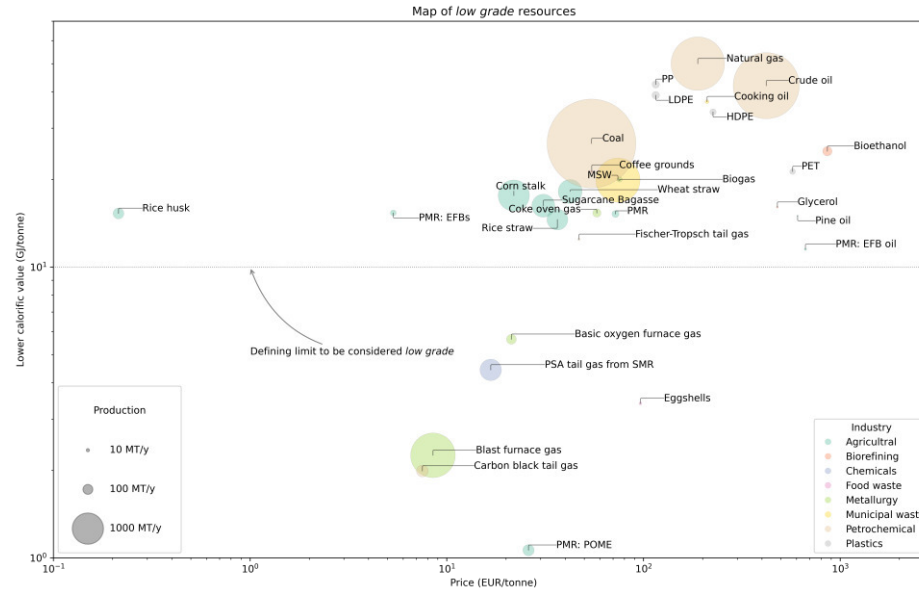


Figure 11: The energetic value of resources vs. their respective price in 2020 EUR. The size of the points indicates the production volumes of the resources and the colour codes indicate their source. EFB: empty fruit bunch, HDPE: (end-of-life) high density polyethylene, LDPE: (end-of-life) low density polyethylene, MSW: municipal solid waste, PET: (end-of-life) polyethylene terephthalate, PMR: palm mill residue, POME: palm oil mill effluent, PP: polypropylene, PSA: pressure swing adsorption, and SMR: steam methane reforming. Further details of the data and their sources can be found in Appendix A. Note that these data points are obtained from several different sources in literature (cited in Appendix A) and should, thus, be treated as indicative.

Figure 11 shows a non-exhaustive overview of resources available, both fossil and renewable, which have a non-zero energetic content. Solid biomass resources such as corn stalk, rice straw, etc. have a slightly lower price than their fossil counterpart, coal, but an energetic content in the same order of magnitude. This makes them excellent candidates for negative emissions via carbon capture and storage through chemical looping, albeit with their own specific challenges covered in the review by Zhao and co-workers [3]. Considering 10 GJ/tonne as the cut-off limit for classifying a resource as *low grade*, the only solids that can be classified as such are eggshells [13]. The limited energetic content comes from the membrane still found in disposed eggshells [14]. Because of the high calcium content of eggs, they are a far more interesting looping material for CO<sub>2</sub> capture in calcium looping (Figure 10 B1) than a source of energy [15-17]. Similarly, for liquids, only the palm oil mill effluent stream (POME) is identified as a *low grade* resource, far less expensive and energetic than its fossil counterpart, crude oil. POME is produced in large quantities (1 kg of crude palm oil produces approximately 3 kg of POME [18]) but difficult to use because of its high water content (more than 90 mass% [19]). Currently, POME is treated using the ponding system, which causes direct emissions of greenhouse gases CH<sub>4</sub> and CO<sub>2</sub> to the environment along with energy losses [20]. Using biochemical reactors to produce a mixture of H<sub>2</sub> and CH<sub>4</sub> from POME is seen as an efficient and environmentally friendlier alternative for utilising POME. This route has been demonstrated on a

pilot scale [21] and is expected to grow further [22]. Compared to biochemical routes, the well-established thermochemical catalytic route, i.e. steam reforming to produce  $H_2$  from POME has the advantages of faster kinetics and higher reactor productivity [23]. So far, it has been studied on the basis of thermodynamic calculations [24] and proven in preliminary experiments [25, 26]. Significant drawbacks of this route are the large energy demand necessary for vaporising the feedstock and catalyst deactivation caused by coking [23]. These drawbacks can be adequately tackled by means of sorption-enhanced steam reforming, i.e. co-feeding POME with other renewables such as bio-methane, and co-application of chemical looping combustion to provide energy for hydrogen production. However, to the best of our knowledge, such approaches have not yet been studied in literature and therefore, represent sizeable opportunities to intensify the use of renewable resources such as POME for producing clean energy (and water) to satisfy our increasing energy demands. The remaining *low grade* gaseous resources are indirectly derived from fossil sources. For example, the blast furnace gas and the basic oxygen furnace gas are produced during steel production when iron ore is reduced by carbon from coal and excess carbon is removed by pure  $O_2$  respectively. This route for iron and steelmaking, wherein production of 1 kg of steel emits approximately 2 kg of  $CO_2$ , constitutes roughly 70% of global iron and steel production [27] and causes up to 9% of global  $CO_2$  emissions [28]. Similarly, carbon black tail gas is produced when crude oil and

natural gas are partially combusted [29]. This route constitutes approximately 95% of global carbon black production and emits approximately 3 kg of CO<sub>2</sub> for every kg of carbon black produced [30]. Another carbon-intensive process is conventional H<sub>2</sub> production via steam reforming of fossil fuels, which emits 10 kg of CO<sub>2</sub> for every kg of H<sub>2</sub> produced [31]. More than 95% of H<sub>2</sub> produced currently is derived from fossil resources, mainly natural gas, causing up to 3% of global CO<sub>2</sub> emissions [32]. Pure H<sub>2</sub> (>99% purity) from the process is obtained by applying pressure swing adsorption (PSA) to the outlet gases of the reformer and water-gas shift reactor. The PSA unit is incapable of fully separating H<sub>2</sub> from the process and thus, produces a CO<sub>2</sub>-rich tail gas which is conventionally combusted to provide energy for the endothermic H<sub>2</sub> production process. The industries emitting *low grade* gases cause roughly 10% of all global CO<sub>2</sub> emissions and therefore present impactful opportunities for intensified processes such as chemical looping.

## 1.2 *Low grade gaseous fuels*

The composition of the four identified *low grade* gas streams is presented in Figure 12. Blast furnace gas (BFG) from the steel industry contributes around 70% of all CO<sub>2</sub> emissions from steel manufactured via the blast furnace - basic oxygen furnace route and is the largest of the *low grade* gas stream. Chemical looping is especially suited for dilute gas streams such as the blast furnace gas and thus, several studies have explored different routes to efficiently utilise the chemical

energy in the blast furnace gas (composition in Figure 12, top-left) without causing additional CO<sub>2</sub> emissions. For example, Tian et al. [33] modified by-product solids from the iron and steel industry for developing a process to capture CO<sub>2</sub> by combining calcium looping with chemical looping combustion. Other studies have investigated producing H<sub>2</sub> from BFG by using a CO<sub>2</sub> sorbent to effectively shift the reaction equilibrium towards H<sub>2</sub> production via the water-gas shift reaction. Although this process has been demonstrated on a pilot scale [34], its product is a mixed H<sub>2</sub>/N<sub>2</sub> stream that requires substantial downstream separation processes for obtaining pure H<sub>2</sub> (>95% purity) or significant addition of H<sub>2</sub> for the stream to be used for ammonia synthesis. The captured CO<sub>2</sub> can be recovered as a pure CO<sub>2</sub> stream at the cost of energy input, either in the form of combustion of fuel [35] or from mechanical work to switch pressure while creating conditions to thermodynamically favour the desired reactions [36]. Another approach that has been recently investigated is the use of the steam-iron process to fully combust the blast furnace gas at a high temperature (923 K) while reducing iron oxide (Fe<sub>2</sub>O<sub>3</sub>) to produce a ~50 mol% CO<sub>2</sub> in N<sub>2</sub> stream and then to split water while oxidising reduced iron (Fe) to Fe<sub>3</sub>O<sub>4</sub> at a lower temperature (~723 K) for producing nearly pure H<sub>2</sub> [37]. In a third step, air is used to regenerate Fe<sub>2</sub>O<sub>3</sub>. The authors conclude that the application of a molten liquid layer on iron (oxides) is key for the performance of the process concept. However, a molten layer on a solid material poses several practical

problems such as corrosion of reactor wall and infeasibility of using fluidised bed reactors, which are typical for operations requiring a significant change in temperature ( $>150$  K). Moreover, the  $\text{CO}_2$  produced via the proposed route would require further processing for separating  $\text{N}_2$ .

The next most abundant stream is the PSA tail gas from  $\text{H}_2$  production. Steam methane reforming (SMR) produces a syngas mixture comprising  $\text{CO}$ ,  $\text{H}_2$ ,  $\text{CO}_2$ ,  $\text{H}_2\text{O}$ , and other trace components which goes through catalytic water-gas shift reactors to improve the  $\text{H}_2$  yield before being sent to a PSA column for producing a high purity  $\text{H}_2$  stream. From stoichiometry, around 5.5 kg of  $\text{CO}_2$  per kg of  $\text{H}_2$  should be available downstream in the PSA tail gas. Thus, this stream (see composition in Figure 12, top-right) is highly relevant for minimising the  $\text{CO}_2$  emissions of  $\text{H}_2$  production. Some approaches that have been studied in literature are combusting the PSA tail gas via chemical looping combustion, thereby providing heat for the endothermic steam methane reforming reaction while producing an outlet gas stream with high  $\text{CO}_2$  purity [38]. Using chemical looping combustion improves energy efficiency of the steam reforming reactor and minimises production of export (excess) steam. Other approaches of using the PSA tail gas include combusting it for integrated production of ammonia [39] or methanol [40].

Carbon black tail gas is especially well suited for chemical looping applications such as sorption enhanced steam reforming and

water-gas shift due to its high water vapour content, which eliminates the requirement to spend energy on vaporising water. However, to the best of our knowledge, there have been no studies related to the use of carbon black tail gas as a feedstock for either  $H_2$  production or energy via sorption-enhanced processes or chemical looping combustion. Rather, carbon black, along with activated carbon, has been used as a catalyst and carbon carrier for hydrogen production via chemical looping mediated methane cracking [41]. For decarbonising the carbon black industry, research efforts have explored replacing fossil fuels with other renewable carbon sources such as pyrolysis oil or synthetic natural gas derived from biomass and electrification by means of plasma. However, the narrow specifications of carbon black required in the end application, the requirement to overhaul existing facilities, or lack of industrial demonstration hamper progress of these decarbonisation options [30].

Like carbon black tail gas, basic oxygen furnace gas also has a low inert content, which facilitates recovery of  $CO$ ,  $H_2$ , and  $CO_2$ . The high  $CO$  content ( $> 50$  mol%) makes this gas very relevant for sorption-enhanced water-gas shift and further processing to useful compounds such as methanol [42] and/or urea [43].

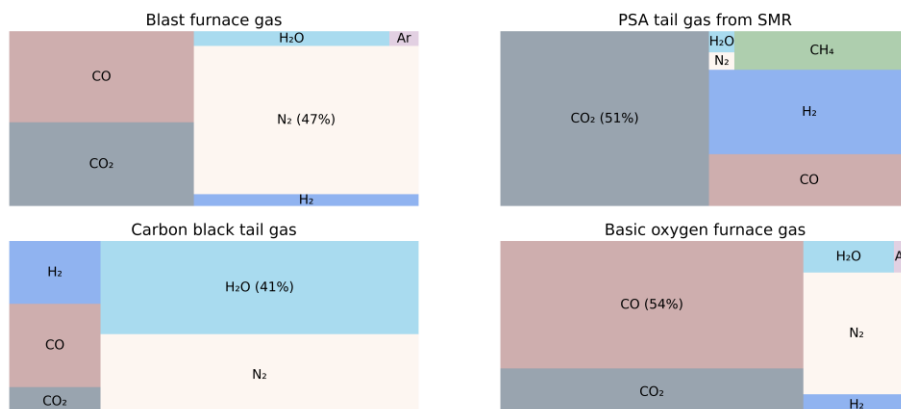


Figure 12: Gas compositions (molar basis) of four identified low grade industrial gas streams. Note that the small amount of methane (<0.2 mol%) in carbon black tail gas is not shown. More information about the gas streams can be found in Appendix A.

The chemicals and petrochemical industry produces several other *low grade* streams from production processes which are internally used, flared, or emitted. Chemical looping can play a key role in efficiently using these *low grade* streams [44]. For example, flaring of shale gas can be mitigated by application of chemical looping to produce ethylene, thereby producing a valuable polymer precursor, minimising loss of resources, and facilitating the transport of energy stored in shale gas [45]. Another example is nitrous oxide emitted from the production of nitric acid, adipic acid, and caprolactam, which amounts to 100 MT/year of CO<sub>2</sub> equivalent emissions [46]. These emissions not only contribute to climate change because of their greenhouse effect but also to ozone depletion [47]. Recently, Hu et al. have shown how these emissions can be used to intensify the utilisation of CO<sub>2</sub> in dry reforming of methane, thereby using three greenhouse



gases for facilitating the production of useful commodities [48]. Apart from the *low grade* industrial resources described above, industrial processes such as glass- and steel-making also produce waste heat. Haribal et al. show how chemical looping can provide an effective pathway to use this waste heat combined with methane and CO<sub>2</sub> to produce chemicals such as methanol and acetic acid [49]. The inherent versatility of chemical looping can open up new pathways to efficiently utilise a wide range of *low grade* resources while creating useful products.

### 1.3 Scope of this thesis

Pilot scale demonstrations of various chemical looping processes were initiated with gaseous fuels and a vast amount of process know-how exists for upscaling the technology [50]. Thus, *low grade* gaseous fuels represent an exciting opportunity to further develop chemical looping, while promoting sustainability and efficient usage of these oft-overlooked resources.

Given the magnitude of CO<sub>2</sub> emissions from the iron and steel industry and from H<sub>2</sub> production, these industries are focused on in this PhD thesis. H<sub>2</sub> production is taken into account also because of its potential to enable large scale CO<sub>2</sub> utilisation at gigatonne scale. The thesis has been divided into the following chapters to elaborate on the investigations performed.

- Chapter 2 deals primarily with the methods used to carry out the experimental investigation, perform modelling

studies, analyse mass and energy balances, and assess the techno-economics of proposed processes.

- Chapter 3 introduces a process concept for capturing CO<sub>2</sub> emissions from the steel mill gases by fully exploiting the chemical energy stored in these gases. The process concept is proven experimentally and its performance is assessed via process simulations.
- Chapter 4 introduces a process concept to break down the reverse water-gas shift reaction that converts CO<sub>2</sub> to CO in a two-step chemical looping process using the blast furnace gas of the iron and steel industry. CO is a platform molecule that can be effectively used for the production of chemicals and fuels, thereby enabling a circular carbon economy. The concept is demonstrated experimentally, wherein two different operation modes to drive the process are compared. A preliminary exergy analysis based on process simulations is described to compare the two implementation modes with combustion of the blast furnace gas, the current best available technology.
- Chapter 5 extends the process concept introduced in Chapter 4 to produce CO auto-thermally using three metal oxides. The chapter further analyses the process via a techno-economic evaluation and exergy analysis. A comparison of the proposed technology is made with a

combination of mature technologies and proof-of-principle experiments are shown.

- Chapter 6 presents a new process for producing blue  $H_2$ , which is intensified by *in situ* utilisation of the captured  $CO_2$  by converting it into CO. A thermodynamic assessment is shown to highlight the potential of the process concept with experimental results in a laboratory fixed bed reactor.
- Chapter 7 presents the conclusion and perspectives of the technologies developed in this thesis.

# Chapter 2

## Methodology

This chapter describes the common methods used in the rest of the thesis.

### 3.1 Material synthesis

The list of materials synthesised for the thesis is shown in Table 1.

Table 1: List of materials, their compositions, synthesis methods, and their application within the thesis.

Nominal composition in mass%	Synthesis route	Used in
50% Fe <sub>2</sub> O <sub>3</sub> /MgAl <sub>2</sub> O <sub>4</sub>	Co-precipitation	Chapters 4, 5, and 6
83% CaO/CeO <sub>2</sub>	Physical wet mixing	Chapters 4, 5, and 6
35% CaO – 45% NiO – 20% CeO <sub>2</sub>	Physical wet mixing	Chapter 3
80% Mn <sub>2</sub> O <sub>3</sub> /MgAl <sub>2</sub> O <sub>4</sub>	Co-precipitation	Chapter 5
40% CaO – 40% NiO – 20% CeO <sub>2</sub>	Physical wet mixing	Chapter 6

50% Fe<sub>2</sub>O<sub>3</sub>/MgAl<sub>2</sub>O<sub>4</sub> and 80% Mn<sub>2</sub>O<sub>3</sub>/MgAl<sub>2</sub>O<sub>4</sub>, were synthesized via co-precipitation using the procedure described by Dharanipragada et al. [51]. The Fe-based material, 50% Fe<sub>2</sub>O<sub>3</sub>/MgAl<sub>2</sub>O<sub>4</sub>, has proven stability for chemical looping [52-54]. The calcium based materials were synthesised via a wet physical mixing route based on the work by Liu et al. [55]. This synthesis route is described in further detail in the paragraph below. The calcium precursor was selected based on a

previous study that indicated that CaO-based CO<sub>2</sub> carriers made using the selected precursor show high retention of their capacity upon repeated cycling [56]. The CaO loading was selected based on a study by Liu et al., which showed that optimal CaO loading is around 80% to maximise CO<sub>2</sub> capture capacity and stability[57].The support material CeO<sub>2</sub> was chosen to impart resistance against trace quantities of sulphurous compounds [58, 59]. Apart from that, the support material CeO<sub>2</sub> provides stability to CaO by preventing sintering [59] and facilitates total oxidation of reductants such as CH<sub>4</sub> by NiO [60]. The details of the chemical reagents used are described in Table 2.

The different steps involved in the wet mixing synthesis procedure are elaborated below and illustrated in Figure 13:

### **1. Preparation of the aqueous solution of calcium d-gluconate monohydrate**

An excess quantity of deionised water (based on the solubility of the calcium precursor) was heated to 80°C and stirred at 300 rpm with a magnetic stirrer. A measured amount of the calcium precursors was added slowly under constant stirring and the mixture was stirred till it became visibly clear.

### **2. Preparation of the aqueous solution of cerium and/or nickel precursors**

An excess of deionised water (based on the solubility of the precursor) was used to dissolve the cerium and/or nickel precursor(s) at room

temperature and stirred manually till the resulting solution became visibly clear.

### 3. Mixing of solutions

The aqueous solution of the cerium and/or nickel precursors was added to the hot aqueous solution of the calcium precursor. The mixture was kept at 353 K under constant stirring at 300 rpm with a magnetic stirrer till a wet, viscous paste was left.

### 4. Drying of solids

The wet, viscous paste was dried at 383 K overnight in a drying oven.

### 5. Calcination of solids

The dried solids were crushed and calcined in a constant air flow at 1173 K. The temperature was increased from ambient temperature to 1173 K at 2 K/min and then kept at 1173 K for 90 minutes.

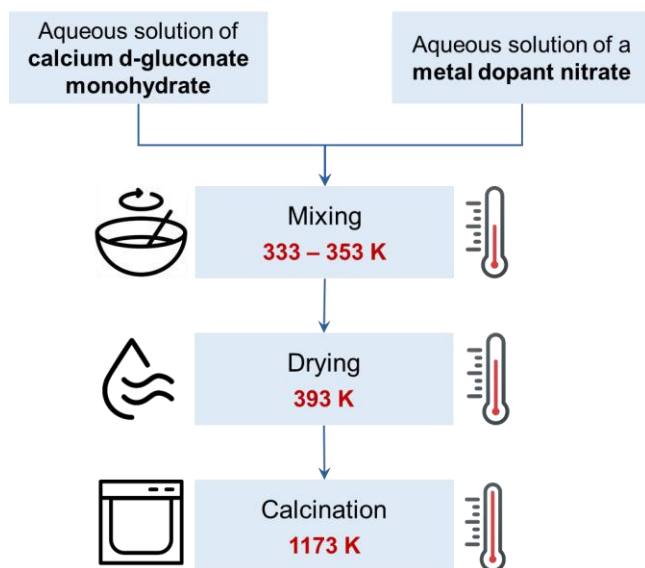


Figure 13: Schematic illustration for the physical wet mixing synthesis route used for creating 83% CaO/CeO<sub>2</sub> and Ca-Ni-Ce based materials.

Table 2: Details of chemicals and reagents used during synthesis.

Chemical	Formula	Purity	Supplier
Iron nitrate nonahydrate	$\text{Fe}(\text{NO}_3)_3 \cdot 9\text{H}_2\text{O}$	98	Sigma-Aldrich
Magnesium nitrate hexahydrate	$\text{Mg}(\text{NO}_3)_2 \cdot 6\text{H}_2\text{O}$	99	Sigma-Aldrich
Manganese nitrate hydrate	$\text{Mn}(\text{NO}_3)_2 \cdot x\text{H}_2\text{O}$	98	Sigma-Aldrich
Aluminium nitrate nonahydrate	$\text{Al}(\text{NO}_3)_3 \cdot 9\text{H}_2\text{O}$	98	Sigma-Aldrich
Calcium d-gluconate monohydrate	$\text{C}_{12}\text{H}_{22}\text{CaO}_{14} \cdot \text{H}_2\text{O}$	98	Sigma-Aldrich
Cerium nitrate hexahydrate	$\text{Ce}(\text{NO}_3)_3 \cdot 6\text{H}_2\text{O}$	99	Sigma-Aldrich
Nickel nitrate hexahydrate	$\text{Ni}(\text{NO}_3)_2 \cdot 6\text{H}_2\text{O}$	99.999	Sigma-Aldrich
Ammonium hydroxide	$\text{NH}_4\text{OH}$	28	Sigma-Aldrich
Water	$\text{H}_2\text{O}$	18.2 M $\Omega$ .cm (resistivity)	ThermoScientific GenPure Pro UV

## 3.2 Material characterisation

A detailed description of the characterisation techniques can be found in the PhD thesis of Buelens [61]. In the text below, a brief description of the techniques is given.

### 3.2.1 $\text{N}_2$ physisorption

Textural properties of the materials were analysed by sorption measurements with  $\text{N}_2$  at 77 K in a Micromeritics Tristar II apparatus.

Prior to the measurements, the materials were degassed overnight under an N<sub>2</sub> flow at 623 K in a Micromeritics SmartPrep apparatus. At least 69 points of relative pressure between 0.01 and 0.99 were measured to develop an adsorption-desorption isotherm. IUPAC guidelines were applied for estimating the specific surface area based on the Brunauer-Emmett-Teller theory [62]. Pore volume was measured at the highest relative pressure (approximately 0.99) during the adsorption phase. Average pore size was estimated using the Barrett-Joyner-Halenda (BJH) analysis applied to the desorption isotherm. Particle size was calculated using the relation described in the work by Wohlleben et al. [63] and assuming that the particles were spherical and without internal pores. 100 to 400 mg of the samples were used for the measurements.

### 3.2.2 Energy dispersive x-ray spectroscopy

SEM-EDX was performed on the as prepared OC and the CC to obtain their composition using a SEM JEOL JSM 5400 setup equipped with an INCA x-act extension (Oxford instruments) for Energy Dispersive X-ray spectrometry (EDX) measurements.

### 3.2.3 X-ray diffraction

Powder X-ray diffraction (XRD) measurements using Cu-K $\alpha$  radiation (wavelength = 0.15406 nm) were performed with a Siemens Diffractometer Kristalloflex D5000. Diffractograms were collected between 2 $\theta$  angles of 5° and 110° with a step of 0.02° and 10 s collection time at each angle. The Rietveld refinement of the diffractogram was



performed using GSAS [64] and EXPGUI [65] to estimate the crystallite size and material composition. For quantification of the instrumental width, a reference LaB<sub>6</sub> (660a from NIST) measurement was used. The degree of crystallinity (DoC) in vol% was estimated using equation (1) upon obtaining its constituent terms from Rietveld refinement.

$$\text{DoC} = \frac{A_{\text{dp}}}{A_{\text{bg}} + A_{\text{dp}}} * 100$$

### 3.2.4 Temperature programmed reactions

Temperature-programmed reactions were performed in a Micromeritics Autochem II apparatus. For the temperature-programmed reduction (TPR) and temperature-programmed oxidation (TPO), 5% H<sub>2</sub> in Ar and 100% CO<sub>2</sub> or 2.5 to 5% O<sub>2</sub> in Ar were used respectively. For the temperature-programmed carbonation/decarbonation, 25% CO<sub>2</sub> in He or 20% CO<sub>2</sub> in Ar was used. About 100-150 mg of sample was tested for each material.

Before each experiment, the sample was pre-treated in an inert flow at 623 K to remove adsorbates (for example, water) and then cooled to 323 K. For the temperature-programmed carbonation and decarbonation, the sample was pre-treated in an inert flow at 1173 K to decompose CaCO<sub>3</sub> and Ca(OH)<sub>2</sub>. During the experiments, the temperature was ramped at a rate of 10 K/min. The flow rate was kept constant at  $4.5 \cdot 10^{-5}$  mol/s and the pressure was close to 101 kPa. The built-in thermal conductivity detector (TCD) of the setup was used to quantify the amount of gas converted, captured, or released. The TCD

was calibrated with a binary gas mixture using 11 different ratios of the two components.

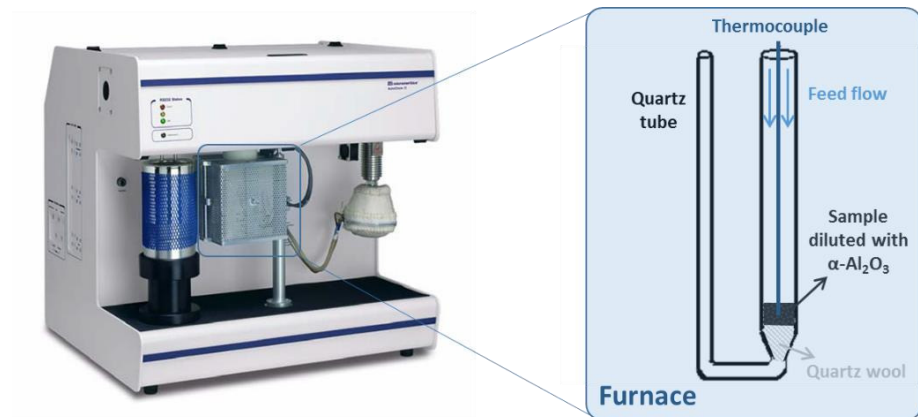


Figure 14: Micromeritics Autochem II apparatus for performing temperature-programmed reactions with a schematic representation of the furnace and U-tube reactor. Figure from [61].

### 3.2.5 Scanning transmission electron microscopy and elemental mapping

The nanoscale morphology of the as prepared materials was probed with high-angle annular dark field scanning transmission electron microscopy (HAADF-STEM) using a JEOL JEM-2200 FS apparatus operated at 200 kV, equipped with a Schottky-type field-emission gun (FEG) and a JEOL JED-2300D EDX for elemental mapping. Sample preparation consisted of immersing a lacey carbon film, supported on a copper grid, in the sample powder. After blowing off large particles, the remaining smaller particles adhering to the carbon film were studied.

### 3.3 Material testing

For the experiments related to the proof of the concept, a 7.5 mm ID quartz fixed bed reactor (Figure 15) with a length of 470 mm and wall thickness of 1 mm was used. A type K thermocouple was axially placed inside the material bed to measure the temperature at the centre of the bed. The reactor was enclosed in an electrically operated oven with three heating zones equipped with three thermocouples to provide feedback for control. Mass flow controllers (MFCs) (Bronkhorst EL-Flow) were used to control the inlet gases and a fast switching pneumatic valve allowed to change the inlet feed gas to the fixed bed. The outlet of the reactor was connected to a sampling port with an on-line mass spectrometer (MS) (Pfeiffer Vacuum OmniStar QMS 301). Depending on the process studied, the product gases were analysed by tracking H<sub>2</sub>, He, CH<sub>4</sub>, H<sub>2</sub>O, CO, O<sub>2</sub>, Ar, and CO<sub>2</sub> signals at 2 AMU (atomic mass unit), 4 AMU, 15 AMU, 18 AMU, 28 AMU, 32 AMU, 40 AMU, and 44 AMU respectively. Fragmentation patterns were taken into account and Ar was used as the internal standard. The MS was regularly calibrated with reference gases flowing through an empty reactor at room temperature under the assumption that reactions would not occur either because of very slow kinetics and/or unfavourable thermodynamics.

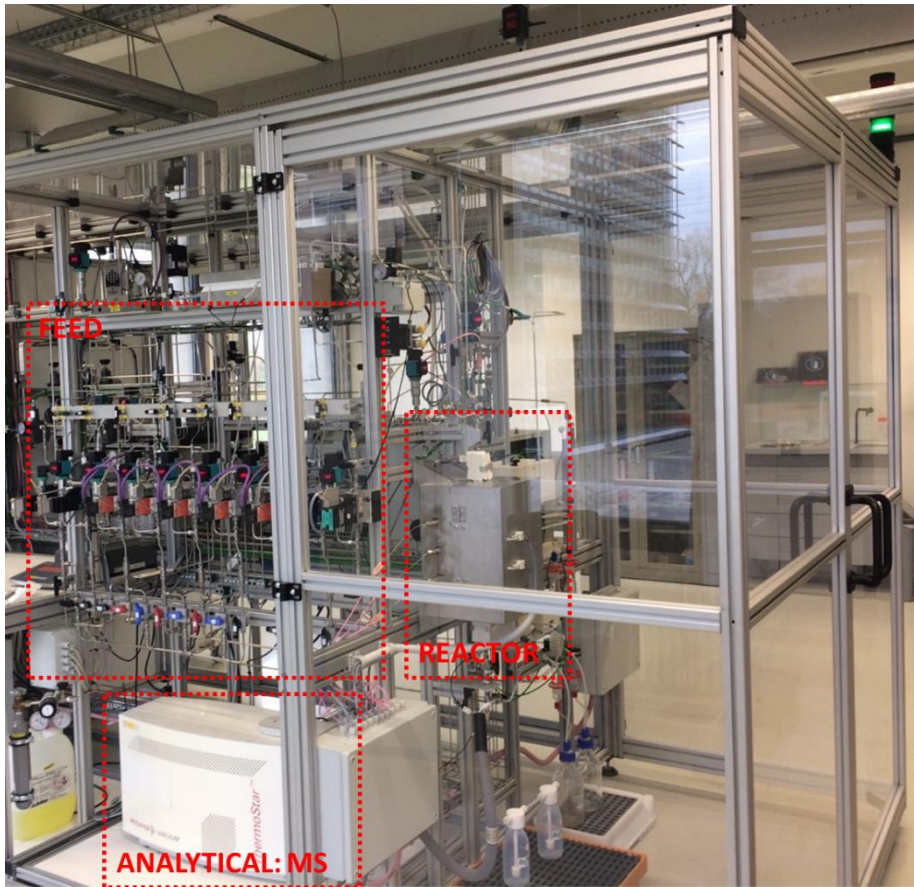


Figure 15: Fixed bed reactor used for material testing. Overview of the fixed bed reactor with indication of feed, reactor and analytical (mass spectrometer, MS) section.

## Chapter 3

### Carbon capture from steel mill gases

#### Abstract

The iron and steel industry is the largest industrial carbon dioxide emitter. More than 70% of their emissions originate from conventional combustion of steel mill gases. In this work, a strategy for carbon capture from the steel mill gases is laid out, using a combination of emerging technologies employing oxygen carrying nickel oxide, carbon dioxide accepting calcium oxide, and dioxygen uncoupling manganese(III) oxide. The process combination was simulated and analysed using Aspen Plus. By applying the proposed strategy, up to 85% of carbon dioxide emitted from the combustion of blast furnace gas and coke oven gas can be captured and compressed for storage or utilisation without external heat and electricity supply. The chemical energy in the steel mill gases is used for the reduction of nickel oxide to nickel and the exothermic capture of carbon dioxide by calcium oxide to form calcium carbonate. Auto-thermal conditions for the energy-intensive carbon dioxide release by the endothermic decomposition of calcium carbonate at 1173 K are achieved by combining it with the exothermic oxidation of nickel by dioxygen, thereby regenerating nickel oxide and calcium oxide for another cycle while efficiently using the chemical energy stored in the steel mill gases.

The dioxygen necessary for nickel oxidation to nickel oxide is produced by using a fraction of the product carbon dioxide stream at 1173 K for the endothermic manganese(III) oxide reduction to manganese(II,III) oxide, operated between 1100 to 1140 K, making use of the sensible heat of the carbon dioxide product stream and shifting the equilibrium towards dioxygen uncoupling of manganese(III) oxide. Air is used to re-oxidise manganese(II,III) oxide to manganese(III) oxide and complete the process cycle. Self-sufficiency of electrical power for carbon dioxide compression is obtained by recovering high temperature heat and converting it into electricity via high pressure steam in a steam turbine assembly. A proof of concept is obtained in a laboratory scale fixed bed reactor and the effect of operating conditions is experimentally explored.

**This chapter was published as**

V. Singh, L.C. Buelens, H. Poelman, M. Saeys, G.B. Marin, V.V. Galvita. Decarbonisation of steel mill gases in an energy-neutral chemical looping process. *Energy Conversion and Management*. 254 (2022) 115248.

4.1 Introduction

The iron and steel industry is one of the largest industrial sources of carbon dioxide (CO<sub>2</sub>) emissions, contributing up to 9% of global CO<sub>2</sub> emissions [28]. These emissions are caused by the high temperature necessary for iron and steelmaking (1373 to 1773 K [66]), reliance on coal as a reducing agent [67], and high consumer demand for steel (projected to increase at 0.5 to 1.8% per year up till 2050 [68]). In order to meet the European Union’s 2050 greenhouse gas emissions reduction target of 85 – 95% [69] while tackling an increasing demand for steel, the adoption of innovative technologies to drastically reduce this sector’s CO<sub>2</sub> emissions is necessary [70]. The use of green dihydrogen (H<sub>2</sub>) as a reductant instead of coal is an example receiving widespread attention, but the consistent production, storage, and transport of green H<sub>2</sub>, i.e. from water using renewable energy, remains challenging [71].

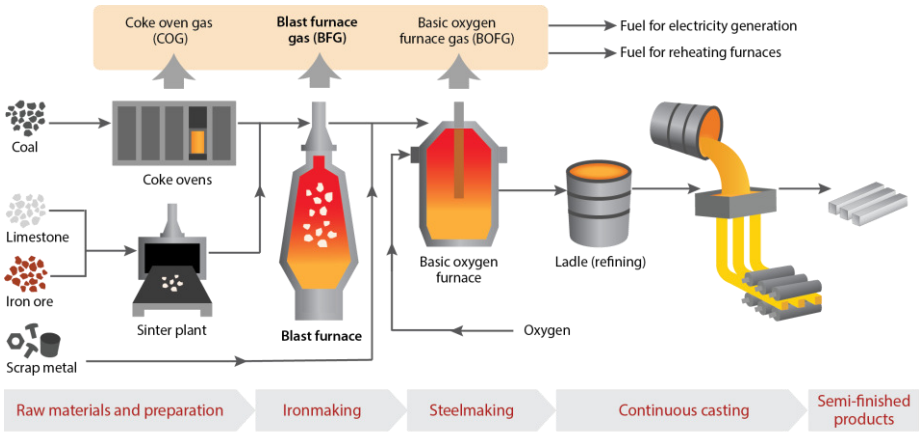


Figure 16: Blast furnace – basic oxygen furnace steelmaking process.

The blast furnace - basic oxygen furnace (BF-BOF) iron and steel production route is currently the most common, constituting more than 70% of the global steel production [72]. The steel mill gases (schematic displayed in Figure 16) produced in this route, namely the blast furnace gas (BFG), coke oven gas (COG), and basic oxygen furnace gas (BOFG), are responsible for the large majority of CO<sub>2</sub> emissions ( $1 \pm 0.2$  kg<sub>CO<sub>2</sub></sub>/kg<sub>steel</sub>) [73]. These calorific gases (Table 3) are typically used in a power plant [58] to generate electricity with an average efficiency of 32% [27]. Post-combustion carbon capture of the flue gases is expected to play a significant role in reducing the CO<sub>2</sub> emissions from steel industry using the BF-BOF route [69]. Although post-combustion CO<sub>2</sub> capture technologies such as amine scrubbing are fairly mature, the associated cost of CO<sub>2</sub> capture in the range of 50 - 80 EUR/tonne could increase the cost of steel by 22% [74].

Table 3: Typical characteristics of steel mill gases from a modern steel production plant [42].

	COG	BFG	BOFG
Volume fraction	0.05	0.91	0.04
Energy fraction	0.18	0.74	0.08
Lower heating value [kJ/Nm <sup>3</sup> ]	15660	3365	7163
Carbon dioxide (CO <sub>2</sub> ) [mol%]	1.2	21.6	20.0
Carbon monoxide (CO) [mol%]	4.1	23.5	54.0
Methane (CH <sub>4</sub> ) [mol%]	22.0	0.0	0.0



Dihydrogen (H <sub>2</sub> ) [mol%]	60.7	3.7	3.2
Hydrocarbons (C <sub>x</sub> H <sub>y</sub> ) [mol%]	2.0	0.0	0.0
Dinitrogen (N <sub>2</sub> ) [mol%]	5.8	46.6	18.1
Water (H <sub>2</sub> O) [mol%]	4.0	4.0	4.0
Argon (Ar) and/or dioxygen (O <sub>2</sub> ) [mol%]	0.2	0.6	0.7

One option for post-combustion CO<sub>2</sub> capture is calcium looping, an emerging technology that has been demonstrated on a megawatt scale (corresponding to 1 tonne of CO<sub>2</sub> capture per hour) [75] and is capable of CO<sub>2</sub> capture at almost half the cost of amine scrubbing [76]. A key challenge for capturing CO<sub>2</sub> via calcium looping is the heat required at high temperatures (1123 to 1223 K) to release the captured CO<sub>2</sub> for subsequent storage or utilisation. Tian et al. [77] have shown that calcium looping is especially relevant for capturing post-combustion CO<sub>2</sub> from the steel industry because (i) calcium oxide (CaO) used as solid intermediate in calcium looping can be re-used for ironmaking and (ii) the proposed process requires less additional capital expenses. To provide heat for producing a high purity CO<sub>2</sub> stream for storage or utilisation, they propose combustion of a hydrocarbon fuel with pure dioxygen (O<sub>2</sub>) obtained from an air separation unit (ASU). In another publication [33], Tian et al. proposed applying chemical looping combustion using reduced iron oxide and pure O<sub>2</sub> from an ASU as a means to provide heat for producing a high purity CO<sub>2</sub> stream in the

decarbonation step of calcium looping. An ASU is capital and energy-intensive, constituting 30 – 60 % of the energy required to drive the conventional calcium looping cycle [78]. Consequently, O<sub>2</sub> production has been identified as a major source of energy penalty for calcium looping [79]. The approach outlined by Manovic and Anthony avoids the necessity of obtaining pure O<sub>2</sub> from an ASU by combining chemical looping combustion of copper oxide (CuO) with decarbonation of calcium carbonate (CaCO<sub>3</sub>) [80]. However, their approach requires the additional use of methane (CH<sub>4</sub>) to generate the necessary heat (from the reduction of CuO to copper (Cu) by CH<sub>4</sub>) for producing a high purity CO<sub>2</sub> stream. Applying a similar approach involving CuO/CaO composites, Martinez et al. [35] proposed co-producing H<sub>2</sub> from steel mill gases via combined chemical looping in fluidised bed reactors. This concept was further investigated in packed bed reactors by Fernandez et al. [81]. The co-produced H<sub>2</sub> in this process concept is diluted with dinitrogen (N<sub>2</sub>) (N<sub>2</sub> content more than 50 mol%), thereby making commercial use of the co-produced H<sub>2</sub> challenging. H<sub>2</sub> production via iron oxide based chemical looping water splitting with CH<sub>4</sub> as fuel was suggested by Bahzad et al. as a means to decarbonise the iron and steel industry [82], but the use of H<sub>2</sub> in steelmaking via direct reduction of iron would require additional expenses for building new infrastructure and will make the existing BF-BOF route for iron and steelmaking obsolete [70]. To overcome these drawbacks, the present contribution avoids the use of an ASU and additional fuel by combining calcium

looping and chemical looping combustion driven by pure  $O_2$  generated by chemical looping air separation to produce a high purity  $CO_2$  stream (>99%), thereby optimally using the chemical energy stored in the steel mill gases from the BF-BOF route for pure compressed  $CO_2$  production.

Figure 17 displays the described process concept schematically. In the first half-cycle of the process (called “reduction-carbonation”), BFG and COG are oxidised by nickel oxide (NiO) producing  $CO_2$ , water ( $H_2O$ ), and reduced nickel (Ni). Together with  $CO_2$  already present in BFG and COG, the produced  $CO_2$  during reduction of NiO is captured by CaO through the carbonation of CaO to  $CaCO_3$ . A stream of  $O_2$  mixed with  $CO_2$  is obtained from a separate loop applying chemical looping air separation (CLAS) and is used to release the captured  $CO_2$  as a high purity stream in the second half-cycle (called “oxidation-decarbonation”). The obtained  $O_2$  is used for the oxidation of Ni to NiO, which provides sufficient heat to decarbonate  $CaCO_3$  and produce pure  $CO_2$ . A fraction of the produced  $CO_2$  is recycled for  $O_2$  production in the CLAS loop by manganese(III) oxide ( $Mn_2O_3$ ) reduction to manganese(II,III) oxide ( $Mn_3O_4$ ). The oxygen lost in the CLAS loop is replenished by using air to oxidise  $Mn_3O_4$  back to  $Mn_2O_3$ , thereby completing the process cycle.

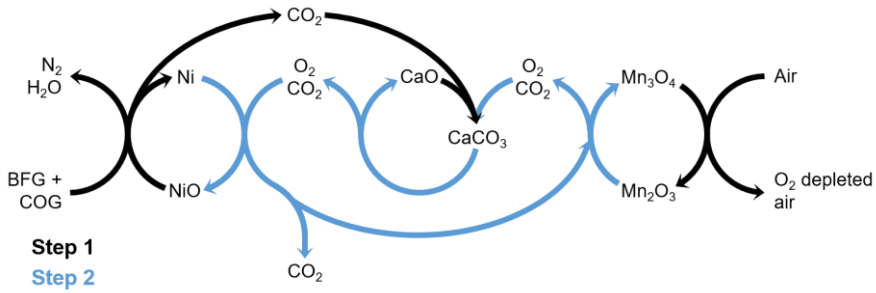
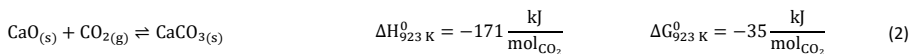


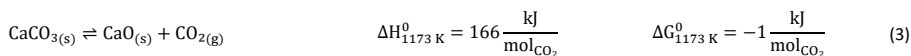
Figure 17: Schematic of the developed process concept which combines chemical looping combustion using NiO/Ni redox pair and calcium looping (CaO/CaCO<sub>3</sub>) to form a combined chemical loop (Ni-Ca loop), which is coupled to CLAS comprising the Mn<sub>2</sub>O<sub>3</sub>/Mn<sub>3</sub>O<sub>4</sub> redox pair via the CO<sub>2</sub>-rich stream of the combined Ni-Ca loop. BFG: blast furnace gas and COG: coke oven gas.

## 4.2 Conception of the process

The approach presented in Figure 17 exploits the chemical energy present in the steel mill gases in an exergetically efficient manner due to the reversibility of the chemical looping processes involved [83]. Depending on the reaction kinetics, such a process can either be operated in fluidised beds or in periodically operated multiple fixed bed reactors.

Central to the proposed process concept is calcium looping, a cyclic process involving two steps, carbonation and decarbonation (equations (2) and (3)), using CaO as the CO<sub>2</sub> carrier. These reactions are typically carried out at 923 and 1173 K, at which they are thermodynamically and kinetically favourable [6].





While CO<sub>2</sub> capture is strongly exothermic, the release of CO<sub>2</sub> is endothermic and requires supply of heat at a temperature of 1173 K to drive the process for producing pure CO<sub>2</sub> at ambient pressure. It is, thus, desirable to use the heat from the exothermic carbonation reaction as efficiently as possible. The process of separating CO<sub>2</sub> from a gas mixture leads to inevitable losses of useful energy, in the form of reversible work to overcome the increase in entropy due to mixing and heat to provide the necessary work for separation. Adequate heat management allows to minimise these losses.

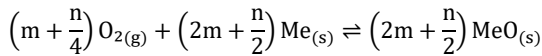
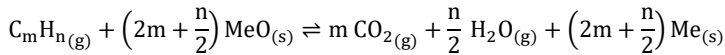
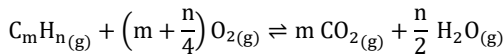
#### 4.2.1 Energy and mass flows

The combination of calcium looping with chemical looping combustion increases the CO<sub>2</sub> content of the BFG to up to 50 mol% by oxidising the CO in BFG to CO<sub>2</sub>, which is subsequently captured by CaO (Figure 17, left-hand side) in the exothermic carbonation reaction (see equation (2)). As CaO carbonation is favoured at lower temperatures, it is necessary to remove heat for maintaining temperatures favourable for carbonation to maximise CO<sub>2</sub> capture. To put this into perspective, an adiabatic temperature rise from ambient temperature to 923 K, at which kinetics of carbonation are sufficiently fast, can be reached when the flue gas from which CO<sub>2</sub> is captured has around 10 mol% CO<sub>2</sub> and is fed at ambient temperature (Appendix B 0). Chemical looping combustion can potentially be deployed for removing the excess heat by coupling an endothermic reduction reaction of a suitable oxygen

carrier with the exothermic carbonation of CaO. The next section examines the suitability of some commonly applied oxygen carriers for the given process.

#### 4.2.2 Selection of the oxygen carrier for chemical looping combustion

A general combustion reaction is presented in equation (4). In chemical looping combustion (CLC), this target reaction is broken down into two steps, reduction and oxidation (equations (5) and (6)), by the oxygen carrier. The oxygen carrier is typically a metal oxide (MeO) that is reduced to a metal or an oxygen deficient metal oxide (Me) and regenerated in a cyclic operation.



The heat of the overall target reaction (equation (4)) is distributed over the 2 steps depending on the type of oxygen carrier employed in CLC. Potential oxygen carriers with their standard enthalpy of oxidation are listed in Figure 18. They are selected for their capability to fully oxidise the steel mill gases at a temperature between 923 K and 1023 K (i.e. at favourable temperatures for the carbonation reaction (equation (2))).  $H_2$ , CO, and  $CH_4$  are chosen as reductants since they are present in different proportions in the steel mill gases, BFG, COG, and BOFG (Table 3). Note that, in Figure 18, the heat of combustion of a reductant gas is the sum of an oxygen carrier's heat of reduction by that reductant gas

and the heat of its oxidation reaction with O<sub>2</sub>. Thus, the heat liberated during the reduction step of CLC is the difference between the heat of combustion of a reductant gas and the heat of oxidation of an oxygen carrier by O<sub>2</sub>.

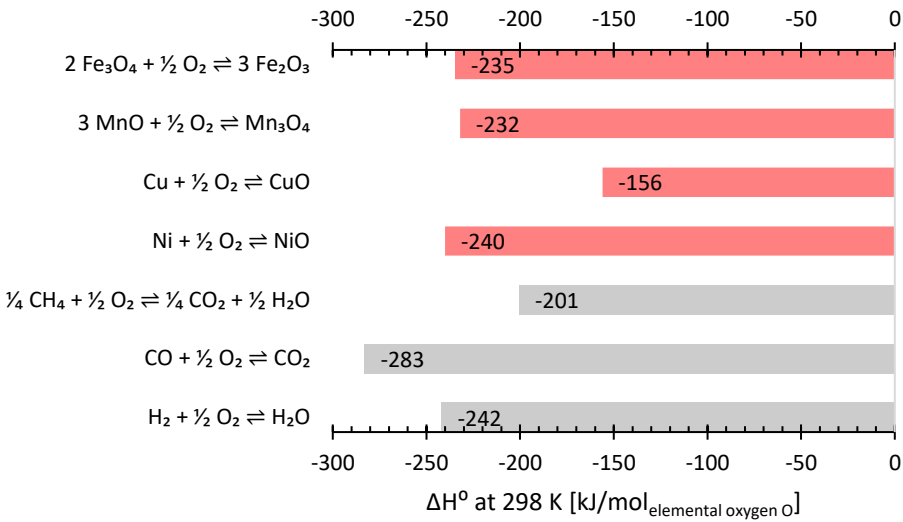
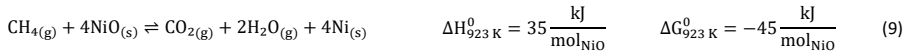
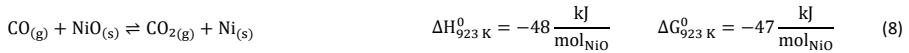
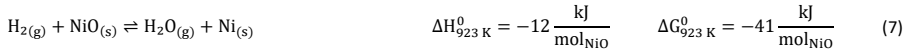


Figure 18: Standard enthalpy of oxidation of common reduced oxygen carriers depicted by red bars and of CH<sub>4</sub>, CO, and H<sub>2</sub> depicted by grey bars.

For managing the heat in the combined chemical looping process for separating CO<sub>2</sub> from BFG, it is desirable to shift the excess heat from the carbonation (and reduction) step to the decarbonation (and oxidation) step, which is the most energy-consuming step. This can be achieved by coupling the exothermic carbonation reaction (equation (2)) with the endothermic reduction of chemical looping combustion. From Figure 18, Ni produces the most heat upon oxidation. Thus,

among the oxygen carriers considered, the NiO/Ni pair is the most suitable choice for the desired objective.

At 923 K, a commonly used temperature for carbonation, the standard enthalpies of reduction and change in Gibbs free energy of NiO with H<sub>2</sub>, CO, and CH<sub>4</sub>, are as follows:



The endothermic reduction of NiO by CH<sub>4</sub> (equation (9)) is, among the reductant fuels available at a steel mill, the most suitable match for the exothermic carbonation reaction (equation (2)) from a heat management point of view. CH<sub>4</sub> is not present in BFG, but it can be sourced from COG (Table 1). Although the addition of COG to the process will result in a slight addition of exothermicity in the reduction-carbonation step due to CO and H<sub>2</sub> oxidation (see equations (7) and (8)), it does not come with a large penalty of additional energy required to release CO<sub>2</sub> associated with its use in the oxidation-decarbonation step. This is because COG predominantly comprises H<sub>2</sub>, which acts as a clean energy carrier to form H<sub>2</sub>O in the outlet flow of the reduction-carbonation step and shift more than 99% of its heat of combustion to the oxidation-decarbonation step.

Apart from favourable thermodynamic redox properties, an oxygen carrier is also characterised by its oxygen transfer capacity on a mass basis. Higher oxygen storage capacities minimise the solids



circulation rate in fluidised bed reactors that are typically used for calcium looping and chemical looping combustion. Among the oxygen carriers considered, the NiO/Ni redox couple has the highest specific oxygen transfer capacity (Table 4), almost 7 times higher than Fe<sub>2</sub>O<sub>3</sub>/Fe<sub>3</sub>O<sub>4</sub>. Moreover, Ni is catalytically active for methane activation and can catalyse its reforming with H<sub>2</sub>O and CO<sub>2</sub> (equations (10) and (11)) in the steel mill gases to facilitate carbon capture by producing H<sub>2</sub> and CO, which readily reduce NiO (see equations (7) and (8)).

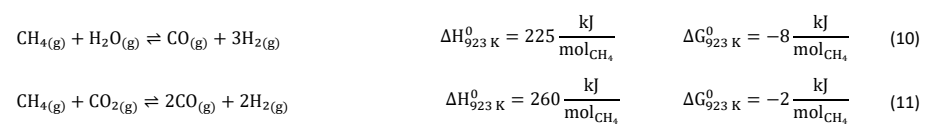


Table 4: Specific oxygen transfer capacity of selected redox couples based on their capacity to fully oxidise reductants in steel mill gases and their cost.

Oxygen couple	carrier redox	Specific oxygen transfer capacity [g/g <sub>oc</sub> ]	Cost of metal* [USD/tonne]
Fe <sub>2</sub> O <sub>3</sub> /Fe <sub>3</sub> O <sub>4</sub>		0.03	102
Mn <sub>3</sub> O <sub>4</sub> /MnO		0.07	4**
CuO/Cu		0.20	6800
NiO/Ni		0.21	15300

\* based on 10-year average metal price from London Metal Exchange between 2010 and 2020.

\*\* from [tradingeconomics.com](https://tradingeconomics.com) [84].

Based on this analysis, NiO was chosen as the oxygen carrier for chemical looping combustion. It is noteworthy that although NiO

possesses the most suitable chemical and thermodynamic properties, it is also the most expensive metal among the oxygen carriers that were compared. Handling metallic Ni and some Ni compounds also poses toxicity risks [85]. Thus, the process developed in this work could benefit from new oxygen carriers which have similar or better thermodynamic redox properties than NiO/Ni but which are cheaper and non-toxic.

#### 4.2.3 Selection of the oxygen carrier for chemical looping air separation

The proposed process requires an O<sub>2</sub> inlet stream to the combined chemical loop in the oxidation-decarbonation step. Typically, the O<sub>2</sub> required for oxyfuel combustion to drive the decarbonation of CaCO<sub>3</sub> is obtained from an air separation unit (ASU), in which liquid O<sub>2</sub> is produced via cryogenic air distillation [86].

In the given context of capturing CO<sub>2</sub> from steel mill gases, it is noteworthy that an ASU is already present in a steel mill and thus, capital costs can be limited [58]. However, this does not eliminate the energy penalty associated with producing and feeding additional O<sub>2</sub> [78]. In this work, chemical looping air separation for O<sub>2</sub> production (Figure 19) partly driven by the sensible heat of the high temperature reactions of this process is proposed.

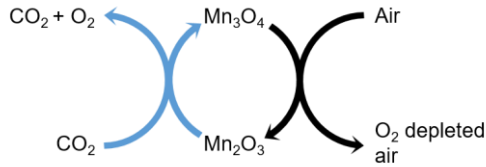
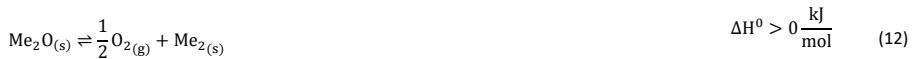


Figure 19: Schematic of CLAS driven by recycled  $\text{CO}_2$  from the decarbonator.  $\text{Me}_2/\text{Me}_2\text{O}$  is a generic oxygen carrier that is capable of uncoupling oxygen at temperatures below the decarbonation temperature of the calcium looping cycle and is chemically unaffected by  $\text{CO}_2$  at given conditions.

Equations (12) and (13) represent the reduction and oxidation of the oxygen carrier ( $\text{Me}_2\text{O} / \text{Me}_2$ ) in the CLAS loop. Reduction is typically endothermic and favoured by a low partial pressure of  $\text{O}_2$ . Taking a fraction of the  $\text{CO}_2$  stream at 1173 K from the oxidiser-decarbonator and sending it to the CLAS loop (right hand side of Figure 17) can not only provide the heat of reduction for CLAS (equation (12)) but also decrease the  $\text{O}_2$  partial pressure to facilitate the reduction via Le Chatelier's principle. The oxygen carrier should thus, be capable of releasing  $\text{O}_2$  at temperatures below 1173 K to make use of the sensible heat from the recycled  $\text{CO}_2$  stream and should be chemically inert towards  $\text{CO}_2$  [87].



In order to compare the proposed addition of CLAS with conventional  $\text{O}_2$  production via cryogenic distillation in an ASU, the minimum work required for separation in a reversible process is assessed for both cases (Appendix B section 0 with schematics in Figure

B2). This thermodynamic analysis shows that CLAS is exergetically more favourable than ASU. Several redox materials are candidates for CLAS, e.g. CuO/Cu, Mn<sub>2</sub>O<sub>3</sub>/Mn<sub>3</sub>O<sub>4</sub>, and Co<sub>3</sub>O<sub>4</sub>/CoO [88]. The Mn<sub>2</sub>O<sub>3</sub>/Mn<sub>3</sub>O<sub>4</sub> redox couple (equation (14)) is most suitable due to its favourable operating regime, i.e. the thermodynamic equilibrium partial pressure of O<sub>2</sub> between 1130 to 1170 K varies from 10 to 21 kPa. Within this operating window, the CLAS loop can be operated isothermally and isobarically by swinging the O<sub>2</sub> partial pressure; using CO<sub>2</sub> during the reduction step and air during the oxidation step. Isothermal operation, as suggested above, is preferred to avoid irreversible losses due to cyclic heating and cooling of the solids [89].



Apart from its favourable operating regime, manganese oxide is also the cheapest metal oxide with proven stability [90]. Thus, it is selected as the redox couple of choice for CLAS.

### 4.3 Methods

The described process concept was simulated in Aspen Plus® to analyse the influences of (i) unreacted solids in the Ni-Ca combined chemical loop, (ii) the temperature in the CLAS loop, and (iii) the proportion of available COG added to the process. Addition of BOFG to the process was not considered because its high CO concentration and low N<sub>2</sub> dilution (Figure 12) make it a valuable feedstock that can be readily used in the chemicals industry without extensive processing [42]. The experimental proof of concept explored the effects of (i) gas

hourly space velocities (GHSVs), (ii) addition of CH<sub>4</sub> at 3 different temperatures, and (iii) exposure to multiple cycles. To mimic BFG, a synthetic mixture was used with the following composition: 5.1 mol% H<sub>2</sub>, 23.8 mol% CO, 24.1 mol% CO<sub>2</sub>, 7 mol% He, and 40 mol% Ar. The pressure was kept at 120 kPa by means of a back pressure regulator. For a typical experiment, 1 g of the synthesised material (pelletised, crushed, and sieved to obtain aggregates in the range of 355-500 µm) was loaded in the reactor on a quartz wool plug. The CLAS loop was not experimentally tested as long-term tests in several reactor setups have proven the stability of Mn-based oxygen carriers for CLAS [91]. The materials, as prepared and after 50 cycles, were characterised by means of XRD, TPre, STEM-EDX, N<sub>2</sub> sorption measurements at 77 K, and EDX. The methods used to carry out simulations, obtain the experimental proof of concept, and evaluate the performance metrics of the process and experiments in this section.

#### 4.3.1 Process simulation

Table 7 displays the specifications of the process simulation of the base case performed in Aspen Plus® V10, while Table 5 lists the setup of the flowsheet for the process simulation. For the sake of simplicity, the process was simulated with solids being transported from one reactor block to another, which is physically similar to fluidised or moving bed operation. Nevertheless, the global mass and energy balances derived with this approach will remain relevant for any other reactor type. The difference in the densities of NiO and CaO makes the

use of a multifunctional material comprising both NiO and CaO recommended in fluidised beds. Using a single material comprising the necessary functionalities allows fluidisation conditions to be met for a single solid phase.

Unless mentioned otherwise, other specifications were the default values in Aspen Plus® V10. A block flow diagram for the entire process simulation with simple heat integration is displayed in Figure 20. Further details related to heat exchangers are described in Table 5. As the objective of this work was to quantify the influence of the operating conditions on the process performance, a rigorous heat integration, such as the one reported by Saqline et al. [92], was deemed to be outside the scope of this contribution.

Table 5: Specifications of the heat exchangers displayed in Figure 20.

ID	Specification	
(1) exchange	Heat	Outlet temperature of the flue gas stream from reducer-carbonator = 383 K
(2) exchange	Heat	Temperature difference between hot outlet (CO <sub>2</sub> ) and cold inlet (CO <sub>2</sub> + O <sub>2</sub> ) = 10 K
(3) exchange	Heat	Temperature difference between hot outlet (CO <sub>2</sub> ) and cold inlet (air) = 10 K
(4) exchange	Heat	Outlet temperature and pressure of steam = 873 K and 13 MPa
(5) exchange	Heat	Temperature difference between hot inlet (CO <sub>2</sub> ) and cold outlet (steam) = 10 K and outlet pressure of steam (cold outlet) = 13 MPa
(6) exchange	Heat	Temperature difference between hot inlet (CO <sub>2</sub> ) and cold outlet (steam) = 10 K and outlet pressure of steam (cold outlet) = 13 MPa

(7) exchange	Heat	Temperature difference between hot outlet (O <sub>2</sub> depleted air) and cold inlet (air) = 10 K
Cooler		Outlet temperature of vent stream = 298 K

Table 6: Aspen Plus® setup of modules, property methods, material databanks, convergence options, and models.

Flowsheet setup	
Property method	PR-BM and STEAM-TA for free water method
Databank	PURE36, INORGANIC, SOLIDS
Solid components	C (graphite), NiO, Ni, CaO, CaCO <sub>3</sub> , Ca(OH) <sub>2</sub> , Mn <sub>2</sub> O <sub>3</sub> , Mn <sub>3</sub> O <sub>4</sub> , MnO, Mn, CeO <sub>2</sub>
Fluid components	CO, CO <sub>2</sub> , H <sub>2</sub> , H <sub>2</sub> O, CH <sub>4</sub> , O <sub>2</sub> , N <sub>2</sub>
Stream class	MIXCISLD
Unit operation models	
Reactors	RGIBBS (product distribution achieved by minimisation of Gibbs free energy of selected solids and gases i.e. all possible components)
Gas-solid separators	SSplit for solids and gases
Fluid flow splitting	FSplit
Heat exchangers	HeatX (Shortcut method, Countercurrent flows, 10 K minimum temperature approach) and Heater
Mechanical operation models	
Compression	MCompr for CO <sub>2</sub> compressions (5 stage, intercooling temperature = 298 K, isentropic efficiency = 72%, equal pressure ratio = 2.5, Final pressure = 11 MPa (liquefied CO <sub>2</sub> ))

Turbine		Compr (72% isentropic efficiency & 100% mechanical efficiency)
Flowsheet convergence options		
Maximum flowsheet evaluations		250
Tear streams calculation	Wegstein  Wegstein acceleration parameters: upper bound: 0, lower bound: -20	

**Other design specifications:** the amount of fresh deionised water used for generating steam is varied such that the heat from the reducer-carbonator of the Ni-Ca loop is sufficient to create stream with 100% vapour fraction.



Table 7: Specifications and assumptions of the base case of the process simulation.

	Reducer-carbonator	Oxidiser-decarbonator	CLAS reducer	CLAS oxidiser
Temperature [K]	1010	1173	1132	1132
Pressure [kPa]	101	101	101	101
Inlet gas flow [kg/s]	29.2	97.7	67.9	41.8
	(BFG and COG)	(CO <sub>2</sub> and O <sub>2</sub> )	(CO <sub>2</sub> )	(Air)
Inlet gas composition [mass basis]	2.5% H <sub>2</sub> O 21.7% CO 31.1% CO <sub>2</sub> 0.5% H <sub>2</sub> 43.6% N <sub>2</sub> 0.6% CH <sub>4</sub> 0% O <sub>2</sub>	92.5% CO <sub>2</sub>	99.9% CO <sub>2</sub>	77% N <sub>2</sub>
Inlet solid flow [kg/s]	86.3	97.7	789.4	783.9
Inlet solids composition [mass basis]	32.6% NiO 27.5% CaO 39.9% ceria (CeO <sub>2</sub> )*	2.9% NiO 2.4% CaO 35.2% CeO <sub>2</sub> * 20.4% Ni 39.1% CaCO <sub>3</sub>	100% Mn <sub>2</sub> O <sub>3</sub>	80.2% Mn <sub>2</sub> O <sub>3</sub> 19.8% Mn <sub>3</sub> O <sub>4</sub>
Design specifications	Temperature is varied such that the net heat duty is $0 \pm 1$ W, i.e. there is auto-thermal operation	Fraction of CO <sub>2</sub> diverted to the CLAS loop varied such that the purity of product CO <sub>2</sub> stream is $99.9 \pm 0.01$ mol%	-	Inlet air flow varied such that partial pressure of O <sub>2</sub> in outlet steam = $0.5 \pm 0.1$ kPa + thermodynamic equilibrium O <sub>2</sub> partial pressure

\* CeO<sub>2</sub> acts as a structural promoter typically used to extend the lifetime of the materials.

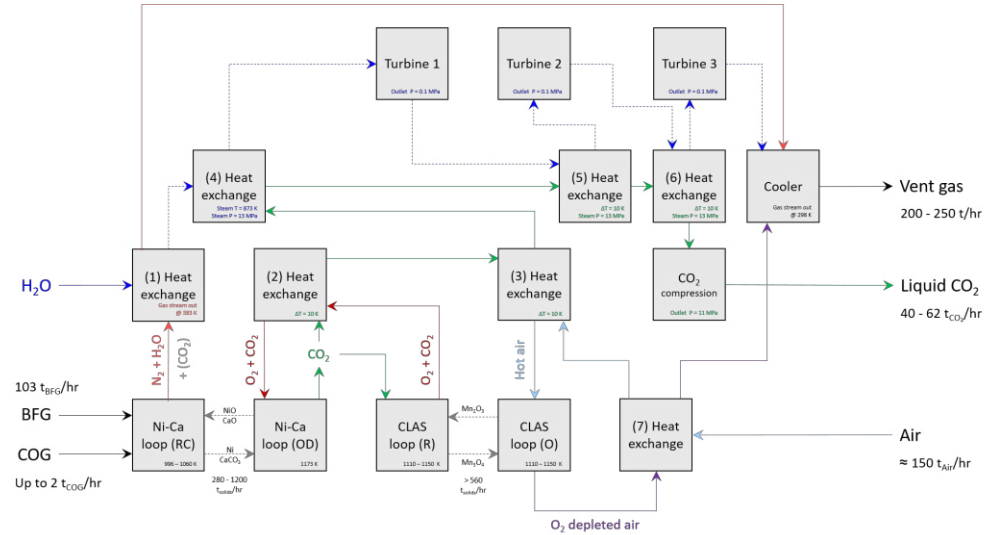


Figure 20: A block flow diagram displaying the simple heat integration used for process calculations. Note that the steam exiting the turbines is not recycled to maintain the simplicity of the simulation. Grey dashed lines indicate the flow of the circulating solids. RC stands for reduction-carbonation, OD for oxidiser-decarbonator, R for reducer, and O for oxidiser. Dark blue solid and dashed lines indicate the flow of water and steam, light blue lines represent flow of air, purple lines represent the flow of O<sub>2</sub> depleted air, red lines indicate the flow of O<sub>2</sub> and CO<sub>2</sub> from the CLAS loop, green lines indicate the flow of quasi-pure CO<sub>2</sub>, light pink lines indicate the flow of the flue gas from the reducer-carbonator.

An exergy analysis was carried out using the results of the process simulation. Exergy of a system is defined as the maximum shaft work that can be done by the composite of the system and a specified reference environment [93]. The total exergy ( $E_{\text{tot}}$ ) of a stream is defined as the sum of its physical and thermochemical exergy (equation (68)).

$$E_{\text{tot}} = E_{\text{physical}} + E_{\text{thermochemical}}$$

The physical exergy ( $E_{\text{physical}}$ ) was calculated by Aspen Plus via equation (16) with 298 K and 101.3 kPa (the so-called “dead state”) as the reference state. In equation (16),  $H$  and  $S$  are the enthalpy and entropy of the mixture at given conditions, whereas  $H_0$  and  $S_0$  are the enthalpy and entropy at reference temperature ( $T_0$ ) and pressure.

$$E_{\text{physical}} = (H - H_0) - T_0 * (S - S_0)$$

The thermochemical exergy of the streams was calculated using equation (69), where  $\dot{n}$  is the total molar flow rate of the stream,  $x_i$  the molar fraction of the  $i^{\text{th}}$  component,  $e_{\text{chem},i}^0$  the standard chemical exergy of the  $i^{\text{th}}$  component from Szargut [94],  $R$  the universal gas constant, and  $T_0$  the reference temperature, i.e. 298 K. The latter term of equation (69) associated with mixing exergy is not applicable to solids.

$$E_{\text{thermochemical}} = \dot{n} \sum x_i e_{\text{chem},i}^0 + \dot{n} \sum x_i T_0 R \ln(x_i)$$

The physical exergy from a heat source  $E_{\text{physical},Q}$  at a temperature  $T$  is given by equation (18), where  $Q$  is the amount of heat released and  $T_0$  is the reference temperature, i.e. 298 K.

$$E_{\text{physical},Q} = Q * \left(1 - \frac{T_0}{T}\right)$$

The exergy efficiency of the process,  $\eta_{\text{exergy}}$ , is defined by equation (71).

$$\eta_{\text{exergy}} = \frac{E_{\text{tot,out}}}{E_{\text{tot,in}}} * 100$$

Apart from the exergy efficiency, other assessed performance metrics and process variables are elaborated on in the text below.

A small fraction of carbon from the steel mill gases is not captured and leaves the process through the exit stream (stream B in Figure 21) of the reducer-carbonator  $\dot{n}_{\text{CO}_2, \text{out r-c}}$  as  $\text{CO}_2$ . An increase of this loss leads to a decrease of the carbon capture (CCAP). Carbon capture of the process is favoured at lower reducer-carbonator temperatures.

$$\text{CCAP} = \frac{\dot{n}_{\text{CO}_2, \text{BFG}} + \dot{n}_{\text{CO}, \text{BFG}} + \dot{n}_{\text{CH}_4, \text{COG}} + \dot{n}_{\text{CO}_2, \text{COG}} + \dot{n}_{\text{CO}, \text{COG}} - \dot{n}_{\text{CO}_2, \text{out r-c}}}{\dot{n}_{\text{CO}_2, \text{BFG}} + \dot{n}_{\text{CO}, \text{BFG}} + \dot{n}_{\text{CH}_4, \text{COG}} + \dot{n}_{\text{CO}_2, \text{COG}} + \dot{n}_{\text{CO}, \text{COG}}} * 100$$

The minimum mass of NiO circulating in the Ni-Ca loop is the stoichiometric amount required for oxidation of the reductants. Their oxidation is thermodynamically less sensitive to temperature and hence, near complete oxidation can be achieved over a large range of temperatures. Carbonation of CaO, unlike NiO reduction, is highly temperature-sensitive. As the temperature in the reduction-carbonation step is varied to ensure auto-thermal conditions for the oxidiser-decarbonator, the minimum flow rate of CaO is, for the sake of simplicity, assumed to be 378 mol/s corresponding to 100% conversion of CaO.

After multiple cycles, deactivation phenomena occur for CaO carbonation, causing lower material utilisation [76] and thus, leading to

unreacted material, considered “excess”, circulating in the beds. Consequently, excess material in the Ni-Ca loop ( $EXC_{Ni-Ca \text{ loop}}$ ) is defined by equation (21).

$$EXC_{Ni-Ca \text{ loop}} = \frac{(\dot{n}_{NiO} + \dot{n}_{CaO}) - (\dot{n}_{NiO,min} + \dot{n}_{CaO,min})}{\dot{n}_{NiO,min} + \dot{n}_{CaO,min}}$$

The flow ratio of NiO and CaO is kept constant for all simulations at 0.887, based on the preliminary optimisation wherein stoichiometric NiO was input for combusting 114.1 t/h of BFG and 1.9 t/h of COG. Varying the excess material in the Ni-Ca loop, thus changes both NiO and CaO flow rates simultaneously.

$$R_{CO_2} = 1 - \frac{\dot{n}_{CO_2,CCSU}}{\dot{n}_{CO_2,out \text{ o-c}}}$$

$R_{CO_2}$  (equation (22)) represents the fraction of hot  $CO_2$  produced in the oxidiser-decarbonator that is directed to the CLAS loop.

In order to assess the surplus heat in this loop ( $Q_{s,CLAS}$ ) using equation (23), the energy consumption by the endothermic  $O_2$  uncoupling ( $Q_{red,CLAS}$ ) and the energy released by the exothermic oxidation with air ( $Q_{ox,CLAS}$ ) are determined. A negative value indicates the necessity to provide more energy to the CLAS loop.

$$Q_{s,CLAS} = |Q_{ox,CLAS}| - |Q_{red,CLAS}|$$

NiO and CaO utilisation ( $u_{NiO}$  and  $u_{CaO}$ ) are calculated using equations (24) and (25) by taking into account their molar flow rate entering and leaving the reduction-carbonation step.

$$u_{NiO} = \frac{\dot{n}_{NiO,in \text{ r-c}} - \dot{n}_{NiO,out \text{ r-c}}}{\dot{n}_{NiO,in \text{ r-c}}} * 100$$

$$u_{\text{CaO}} = \frac{\dot{n}_{\text{CaO},\text{in } r-c} - \dot{n}_{\text{CaO},\text{out } r-c}}{\dot{n}_{\text{CaO},\text{in } r-c}} * 100$$

### 4.3.2 Process and experimental performance metrics

The gas hourly space velocity (GHSV) was calculated using the equation displayed in (26). The volume occupied by the bed was calculated by measuring the height of the bed after the experiment and assuming that the reactor bed had a cylindrical geometry.

$$\text{GHSV} = \frac{\dot{V}_{\text{NTP}}}{V}$$

The total amount of moles of NiO ( $N_{\text{NiO}}$ ) and CaO ( $N_{\text{CaO}}$ ) in the reactor were calculated using equations (27) and (28).

$$N_{\text{NiO}} = \frac{m * w_{\text{NiO}}}{MM_{\text{NiO}}}$$

$$N_{\text{CaO}} = \frac{m * w_{\text{CaO}}}{MM_{\text{CaO}}}$$

The utilisation of the oxygen transfer capacity and the CO<sub>2</sub> carrying capacity in both half-cycles were calculated using equations (29) to (88):

$$U_{\text{NiO},r-c} = \frac{\int_0^{t_{r-c}} \left( (\dot{n}_{\text{H}_2,\text{in}} - \dot{n}_{\text{H}_2,\text{out}}) + (\dot{n}_{\text{CO},\text{in}} - \dot{n}_{\text{CO},\text{out}}) + 4 * (\dot{n}_{\text{CH}_4,\text{in}} - \dot{n}_{\text{CH}_4,\text{out}}) \right) dt}{N_{\text{NiO}}} * 100$$

$$U_{\text{Ni},o-d} = \frac{\int_0^{t_{o-d}} \left( 2 * (\dot{n}_{\text{O}_2,\text{in}} - \dot{n}_{\text{O}_2,\text{out}}) \right) dt}{N_{\text{NiO}}} * 100$$

$$U_{\text{CaO},r-c} = \frac{\int_0^{t_{r-c}} \left( (\dot{n}_{\text{CO}_2,\text{in}} - \dot{n}_{\text{CO}_2,\text{out}}) + (\dot{n}_{\text{CO},\text{in}} - \dot{n}_{\text{CO},\text{out}}) + (\dot{n}_{\text{CH}_4,\text{in}} - \dot{n}_{\text{CH}_4,\text{out}}) \right) dt}{N_{\text{CaO}}} * 100$$

$$U_{\text{CaCO}_3,o-d} = \frac{\int_0^{t_{o-d}} (\dot{n}_{\text{CO}_2,\text{out}} + \dot{n}_{\text{CO},\text{out}}) dt}{N_{\text{CaO}}} * 100$$

For the calculations of material utilisation, it was assumed that the fresh material placed in the reactor consists exclusively of NiO, CaO, and CeO<sub>2</sub>. The contribution of CeO<sub>2</sub> for oxidation of reductants was

neglected since, under the applied reaction conditions, only a small fraction of its lattice oxygen atoms can be removed during its reduction to non-stoichiometric  $\text{CeO}_{2-\delta}$  ( $\delta < 0.1$ ) [95].

The conversion (x) of the reductants (or fuel) during the reduction and carbonation was calculated using equations (33) to (35).

$$X_{\text{CH}_4} = \frac{\int_0^{t_{r-c}} (\dot{n}_{\text{CH}_4,\text{in}} - \dot{n}_{\text{CH}_4,\text{out}}) dt}{\int_0^{t_{r-c}} \dot{n}_{\text{CH}_4,\text{in}} dt} * 100$$

$$X_{\text{H}_2} = \frac{\int_0^{t_{r-c}} (\dot{n}_{\text{H}_2,\text{in}} - \dot{n}_{\text{H}_2,\text{out}}) dt}{\int_0^{t_{r-c}} \dot{n}_{\text{H}_2,\text{in}} dt} * 100$$

$$X_{\text{CO}} = \frac{\int_0^{t_{r-c}} (\dot{n}_{\text{CO},\text{in}} - \dot{n}_{\text{CO},\text{out}}) dt}{\int_0^{t_{r-c}} \dot{n}_{\text{CO},\text{in}} dt} * 100$$

The carbon and oxygen balance (CB and OB) were computed using equations (92) and (93).

$$\text{CB} = \frac{\int_0^{t_{\text{total}}} (\dot{n}_{\text{CH}_4,\text{out}} + \dot{n}_{\text{CO}_2,\text{out}} + \dot{n}_{\text{CO},\text{out}}) dt - \int_0^{t_{\text{total}}} (\dot{n}_{\text{CH}_4,\text{in}} + \dot{n}_{\text{CO}_2,\text{in}} + \dot{n}_{\text{CO},\text{in}}) dt}{\int_0^{t_{\text{total}}} (\dot{n}_{\text{CH}_4,\text{in}} + \dot{n}_{\text{CO}_2,\text{in}} + \dot{n}_{\text{CO},\text{in}}) dt} * 100$$

$$\text{OB} = \frac{\int_0^{t_{\text{total}}} 2 * (\dot{n}_{\text{O}_2,\text{in}} - \dot{n}_{\text{O}_2,\text{out}}) dt - \int_0^{t_{\text{total}}} (4 * (\dot{n}_{\text{CH}_4,\text{in}} - \dot{n}_{\text{CH}_4,\text{out}}) + (\dot{n}_{\text{CO},\text{in}} - \dot{n}_{\text{CO},\text{out}}) + (\dot{n}_{\text{H}_2,\text{in}} - \dot{n}_{\text{H}_2,\text{out}})) dt}{\int_0^{t_{\text{total}}} 2 * (\dot{n}_{\text{O}_2,\text{in}} - \dot{n}_{\text{O}_2,\text{out}}) dt} * 100$$

## 4.4 Results and discussion

In what follows, the base case process simulations derived from the thermodynamics of the system are shown and discussed (section 4.4.1). Herein, the influence of key variables on the carbon capture performance of the process concept is assessed. Thereafter, an experimental proof of concept and an experimental investigation of the influence of process variables are shown and discussed in section 4.4.2.

Finally, the characteristics of the material used in the experimental campaign, before and after testing, are presented in section 4.4.3.

#### 4.4.1 Process simulations

Based on process simulations, the influences of excess unreacted solids in the Ni-Ca loop, the temperature in the CLAS loop, and addition of COG to the process are quantified and presented. In all the studied cases, the electrical output from the turbines was higher than the electrical demand for CO<sub>2</sub> compression. The simulations were performed such that certain process specifications such as CO<sub>2</sub> purity and auto-thermal operation of the oxidiser-decarbonator were always met (Table 7 section 4.3.1). The results of the base case simulation with material and exergy flows are presented in the form of a block flow diagram in Figure 21.

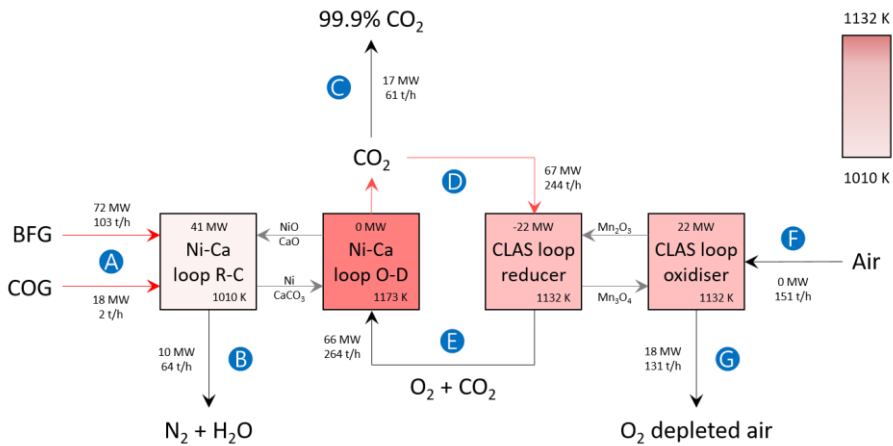


Figure 21: Block diagram of the process concept combining chemical looping combustion and calcium looping in the Ni-Ca loop and integrating chemical looping air separation (CLAS) for utilising blast furnace gas (BFG) and coke oven gas (COG) from



steel mills. R-C and O-D stand for reduction-carbonation and oxidation-decarbonation of the Ni-Ca loop. For sake of visual brevity, the circulation of  $\text{CeO}_2$  is not shown. The mass and exergy flows are indicated next to the arrows. Exergy output is also indicated in the top section of the process blocks. Red coloured streams indicate the primary energy sources driving the desired chemical reactions to achieve pure  $\text{CO}_2$  production for storage and/or utilisation. A: inlet gas streams BFG and COG carrying chemical exergy, B:  $\text{N}_2$  and  $\text{H}_2\text{O}$  rich stream leaving the process, C:  $\text{CO}_2$  product with 99.9% purity, D: fraction of hot  $\text{CO}_2$  (1173 K) diverted to the CLAS loop, E:  $\text{O}_2$  and  $\text{CO}_2$  stream from the CLAS loop to supply heat for the production of pure  $\text{CO}_2$ , F: air fed to the CLAS loop, and G:  $\text{O}_2$ -depleted air.

In order to maintain auto-thermal operation of the decarbonator-oxidiser, the reducer-carbonator temperature was set to 1010 K. At this temperature, the corresponding carbon capture is 86%. Although a lower temperature in the reducer-carbonator would result in improved carbon capture, it would come at the cost of external energy demand for the decarbonator-oxidiser. The CLAS loop is operated isothermally and thus, the solids circulation rate does not influence the energy balances of the process concept. The isothermal operation of the CLAS loop simplifies the choice of reactor type and allows the reactions to be carried out in a simple fixed bed reactor.

The Sankey diagrams for the simulated base case displayed in Figure 22 show that the majority of the exergy and mass is concentrated in the Ni-Ca and CLAS solid loops and the gas loop comprising  $\text{CO}_2$  and  $\text{O}_2$  connecting the solid loops. The exergy of heat generated by the CLAS oxidiser is recycled back to the CLAS reducer, which is possible and

efficient due to the isothermal operation of both steps of CLAS. Compared to the BFG, the COG contributes to a very small fraction of mass and exergy input. Analysis of exergy flows indicates that high exergetic efficiencies of up to 96% are achievable in the process.

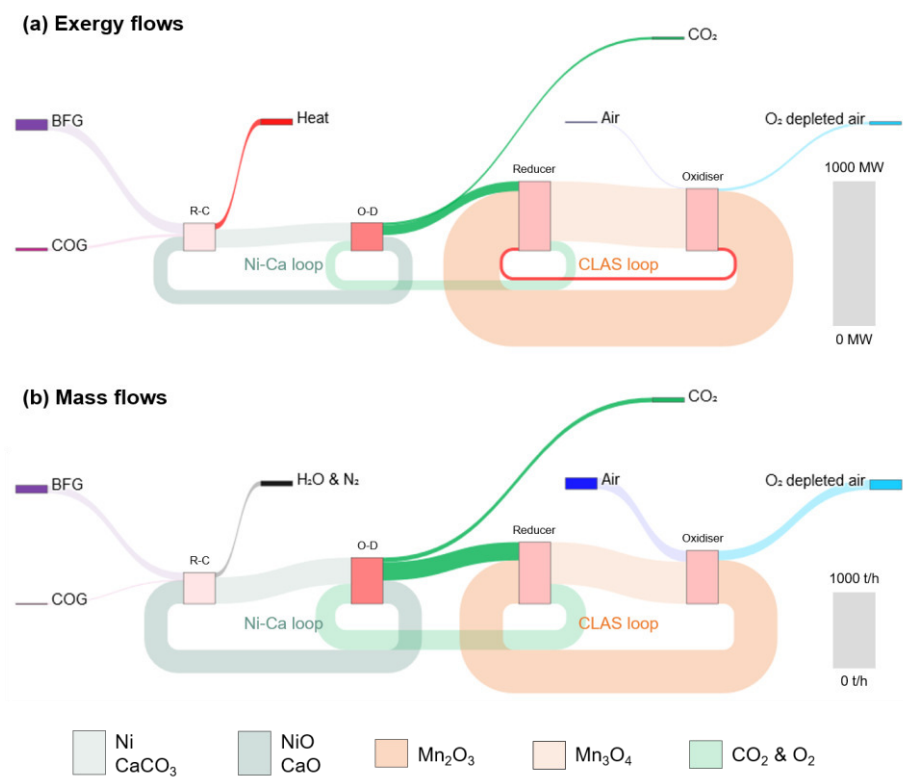


Figure 22: Sankey diagrams for the exergy (a) and active mass (b) flows in the process for the base case simulation. R-C and O-D stand for reduction-carbonation and oxidation-decarbonation of the Ni-Ca loop.

#### 4.4.1.1 Influence of excess unreacted material

While maintaining auto-thermal conditions in the oxidiser-decarbonator, an increase in unreacted material in the Ni-Ca loop

results in a decrease in the amount of carbon captured during the process because of the increased reduction-carbonation temperature (Figure 23 (a)). An increase in the reduction-carbonation temperature has two effects. Firstly, lower production of  $\text{CaCO}_3$ , meaning lower carbon capture and thus, less heat required to completely decarbonate  $\text{CaCO}_3$  in the strongly endothermic decarbonation reaction. Secondly, lower temperature difference between the reducer-carbonator and the oxidiser-decarbonator, which helps to minimise the heat required to raise the temperature of the solids exiting the reducer-carbonator to 1173 K in the oxidiser-decarbonator.

As the total amount of  $\text{CO}_2$  produced becomes lower due to less carbon capture ((C) in Figure 21), a higher fraction of the produced  $\text{CO}_2$  is necessary for operating the CLAS loop ((D) in Figure 21). This isothermal loop requires dilution by  $\text{CO}_2$  to facilitate uncoupling of  $\text{O}_2$  from  $\text{Mn}_2\text{O}_3$ . The  $\text{O}_2$  required in the oxidiser-decarbonator ((E) in Figure 21) does not vary with excess material in the Ni-Ca loop since reductants are quasi-fully oxidised. Thus, the fraction of  $\text{CO}_2$  recycled from the oxidiser-decarbonator increases with an increasing amount of excess material in the Ni-Ca loop (Figure 23 (b)).

The material utilisation of both NiO and CaO decreases when materials are used in excess (Figure 23 (c)). The utilisation of CaO diverges from the trend observed for NiO because the conversion of CaO to  $\text{CaCO}_3$  is sensitive to the reducer-carbonator temperature, as it determines the thermodynamic equilibrium partial pressure of  $\text{CO}_2$ . A

higher temperature in the reducer-carbonator results in a higher thermodynamic equilibrium partial pressure of  $\text{CO}_2$ , which translates in less carbon capture in the reducer-carbonator. Thus, despite the availability of  $\text{CaO}$  in excess of the stoichiometric requirement to capture  $\text{CO}_2$ , the increased temperature does not permit full carbon capture due to thermodynamic constraints.

The produced  $\text{CO}_2$  (i.e. the fraction that is not recycled) directed to the compression unit is used to pre-heat the air entering the oxidiser of the CLAS loop (Figure 20). This helps to create surplus heat in the CLAS loop that can provide a thermal buffer in case of unintended heat losses. As both steps in the CLAS loop are operated isothermally, heat from the oxidation reaction can be transferred to the reducer of the CLAS loop for the endothermic reduction. The heat input to the CLAS reducer is partly provided by the sensible heat of the hot recycled  $\text{CO}_2$  at 1173 K, whereas the heat generated from the oxidiser is partly used for increasing the temperature of air (and subsequently  $\text{O}_2$  deficient air) that is fed to the oxidiser. Pre-heating the air fed to the oxidiser of the CLAS loop ((F) in Figure 21) minimises the heat demand for reaching the CLAS operating temperature. When the amount of  $\text{CO}_2$  capture decreases, the heat associated with the produced  $\text{CO}_2$  also decreases. Thus, additional heat becomes necessary to drive the CLAS loop to maintain auto-thermal conditions in the oxidiser-decarbonator of the Ni-Ca loop. When the excess material in the Ni-Ca loop is higher than

4.2, additional heat supply to the CLAS loop becomes necessary (Figure 23 (d)).

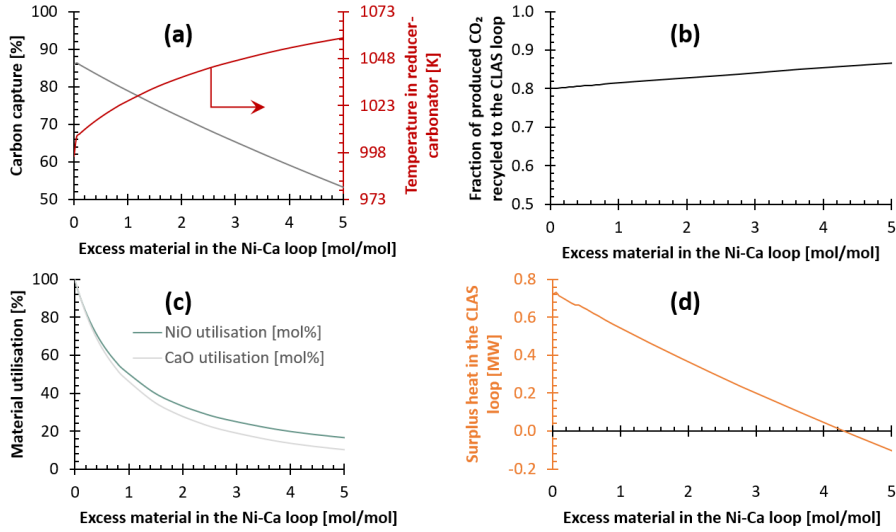


Figure 23: Influence of excess material in the Ni-Ca loop on (a) carbon capture and corresponding temperature in the reducer-carbonator, (b) recycled CO<sub>2</sub>, (c) material utilisation, and (d) surplus heat in the CLAS loop. The total inlet flow of gases (BFG and COG) is 105 t/h.

#### 4.4.1.2 Influence of temperature on chemical looping air separation

In order to estimate the influence of the temperature in the CLAS loop on the overall process performance, 10% excess materials were used in the Ni-Ca loop (equation (21)) corresponding to a solids circulation rate of 1 kmol/s or approximately 310 t/h. The ratio of solids circulation rate to the feed in the proposed process is approximately 3 kg/kg, which is comparable to that of a commercial fluid catalytic cracking (FCC) process (between 5 to 7 kg/kg) [96].

Increasing the temperature in the CLAS loop improves the carbon capture of the process (Figure 24 (a)). The temperature increase causes an increase in the thermodynamic equilibrium  $O_2$  partial pressure of  $Mn_2O_3$ , resulting in a higher  $O_2$  concentration of the  $O_2/CO_2$  stream ((E) in Figure 21) fed to the oxidiser-decarbonator to oxidise Ni (Figure 24 (b)). As the required dilution by  $CO_2$  decreases, the fraction of the  $CO_2$  produced in the oxidiser-decarbonator that is sent to the reducer of the CLAS loop also decreases (Figure 24 (c)). Thus, less heat is required in the oxidiser-decarbonator because its inlet stream has lower dilution (i.e. the mass flow rate of this inlet stream is lower) and it enters the oxidiser-decarbonator at a higher temperature. To maintain auto-thermal conditions in the oxidiser-decarbonator, an increase in the temperature of the CLAS loop allows the temperature in the reducer-carbonator to be further decreased (Figure 24 (d)), thereby resulting in higher carbon capture.

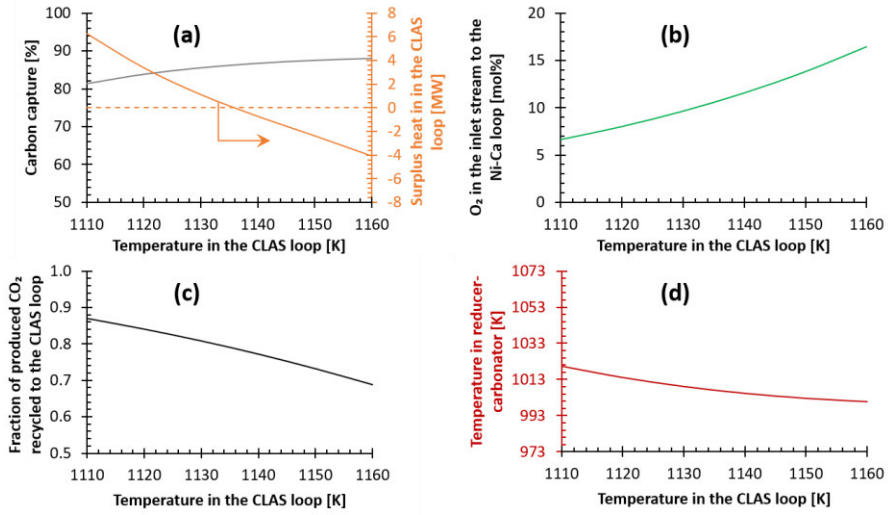


Figure 24: Influence of the temperature in the CLAS loop on (a) carbon capture and the surplus heat in the CLAS loop (dashed orange line serves as a guide to the eye to mark zero surplus heat), (b) concentration of O<sub>2</sub> in the mixed CO<sub>2</sub>-O<sub>2</sub> stream sent to the oxidiser-decarbonator of the Ni-Ca loop, (c) recycled CO<sub>2</sub>, and (d) temperature of the reducer-carbonator of the Ni-Ca loop. A solids flow rate of 310 t/h in the Ni-Ca loop, corresponding to 10% excess material, is assumed and the total inlet flow of gases (BFG and COG) is 105 t/h.

The higher carbon capture comes at the cost of lower surplus heat in the CLAS loop, implying the necessity of additional heat to drive the process when there is net deficiency of heat above 1140 K in the CLAS loop (Figure 24 (a)). This additional heat may be supplied by combusting carbonaceous fuels, which would lead to additional CO<sub>2</sub> emissions (not shown in Figure 24) or it may be sourced from renewable energy. Since the goal of this process concept is to improve energetic self-sufficiency for carbon capture in the context of steel mill gases, a temperature of 1132 K in the CLAS loop offers a good compromise

between the CO<sub>2</sub> capture of the process and the surplus heat in the CLAS loop.

#### 4.4.1.3 Influence of addition of coke oven gas to the process

Due to its low inert content and high concentrations of CH<sub>4</sub> and H<sub>2</sub>, COG is a valuable gas that can easily be valorised for a plethora of applications [42]. Thus, minimisation of its use in the proposed process to capture CO<sub>2</sub> is of interest. To study the influence of COG addition, the circulation of solids in the Ni-Ca loop was kept constant at 1 kmol/s or 310 t/h corresponding to a 10% excess (equation (21)).

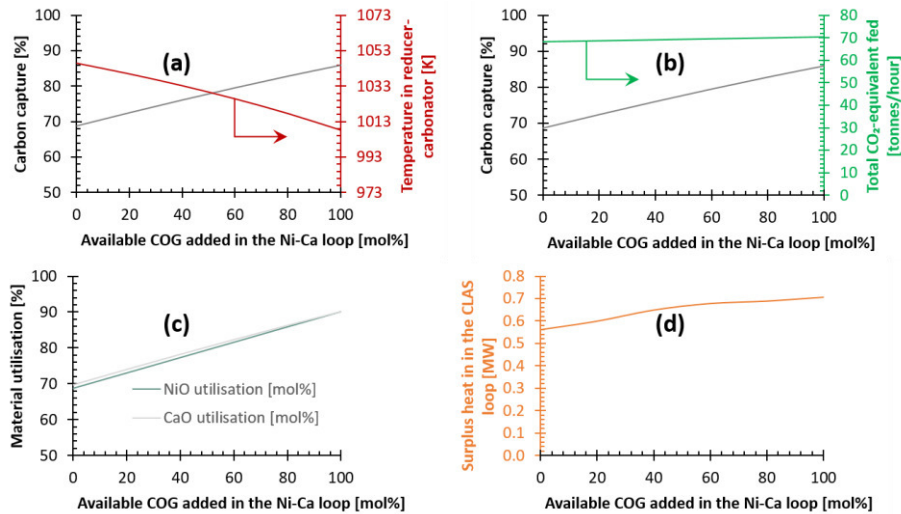


Figure 25: Influence of the available COG used in the proposed process on (a) carbon capture and corresponding temperature in the reducer-carbonator, (b) carbon capture and equivalent CO<sub>2</sub> emissions, (c) material utilisation, and (d) surplus heat in the CLAS loop.

The addition of COG has a significant impact on the carbon capture of the process (Figure 25 (a)). NiO and CH<sub>4</sub> (in COG) help to



redistribute the heat of oxidation of  $\text{CH}_4$  such that a large proportion of this heat becomes available for oxidation-decarbonation. Moreover, utilisation of  $\text{H}_2$ , as a carbon-free reductant, in COG also liberates a substantial portion of heat of  $\text{H}_2$  oxidation in the oxidiser-decarbonator of the Ni-Ca loop. The available COG is much smaller in quantity than BFG (50 times smaller mass flow, Figure 22 (b)) and contains mostly  $\text{H}_2$  (Table 3). Thus, the addition of COG and its combustion does not particularly lead to a significant increase in  $\text{CO}_{2,\text{equiv}}$  emissions, but it certainly results in substantially higher carbon capture (Figure 25 (b)). Thus, maximum use of COG (ideally, 100%) is desirable to improve carbon capture in the process.

For a constant flow rate of circulating solids in the Ni-Ca loop, adding less COG results in lower utilisation of  $\text{NiO}$  and  $\text{CaO}$  (Figure 25 (c)). The decrease in  $\text{NiO}$  utilisation is slightly steeper because for oxidising one mole of  $\text{CH}_4$  in the COG, 4 moles of  $\text{NiO}$  are required, whereas only one mole of  $\text{CaO}$  is required to capture the resulting  $\text{CO}_2$ . The addition of COG also benefits the CLAS loop by increasing its surplus heat (Figure 25 (d)), caused by the increased production of  $\text{CO}_2$  in the decarbonator-oxidiser and the associated heat content.

For application of  $\text{NiO}$  and  $\text{CaO}$  in chemical looping processes, it is typical to use a structural promoter such as  $\text{CeO}_2$  [97]. The role of  $\text{CeO}_2$  for the solids circulating in the Ni-Ca loop is two-fold: it provides structural stability and high oxygen mobility, which improves redox kinetics. Without  $\text{CeO}_2$  circulating in the Ni-Ca loop, the carbon capture

can be improved by 2.5% points from 85.8% to 88.3% (Figure B3). Thus, the proportion of  $\text{CeO}_2$  circulating the Ni-Ca loop has minimal effects on the carbon capture of the process.

#### 4.4.2 Experimental proof of concept

To demonstrate that chemical looping and calcium looping can be combined to form an  $\text{O}_2$ -free  $\text{CO}_2$  stream using a gas that resembles the BFG of a steel mill, experiments were performed in a fixed bed reactor. The fixed bed reactor was an open system allowing transfer of energy (in the form of heat) and matter (in the form of inlet and outlet gases) over its boundaries. Although the transfer of matter in the form of inlet gases and heat input was well-controlled, the reactor was susceptible to heat losses. Addition of COG was simulated by adding pure methane to the synthetic BFG. The minimum amount of  $\text{CH}_4$  that could be experimentally added while maintaining stable flows, reasonable GHSV values, and limited pressure drop over the bed was such that it contributed to 20% of the total gas flow, far higher than expected from the addition of COG to BFG (around 1% of  $\text{CH}_4$  in the total gas flow). In order to facilitate quantitative analysis of the effluent gas streams,  $\text{CO}_2$  was replaced by Ar in the gas stream sent during the oxidation-decarbonation half-cycle.

##### 4.4.2.1 Multiple cycles using synthetic blast furnace gas

In order to assess the stability of the materials and to provide the proof of concept, 30 cycles were executed to demonstrate (1)  $\text{CO}_2$  capture during reduction-carbonation using NiO and CaO and (2)

subsequent release of pure  $\text{CO}_2$  without  $\text{O}_2$  contamination despite feeding  $\text{O}_2$  at the inlet during the oxidation-decarbonation half-cycle. The CLAS loop was not experimentally tested because this would require at least 2 reactors in parallel (one for the Ni-Ca loop and the other for the CLAS loop). Synthetic BFG was used during the reduction-carbonation half-cycle and 50%  $\text{O}_2/\text{Ar}$  during the oxidation-decarbonation half-cycle. The latter was used to enable rapid heating of the solids and maximise the heat produced from the oxidation of Ni for the endothermic decarbonation reaction, thus limiting the heat loss from the reactor. Between the reduction-carbonation half-cycle and the oxidation-decarbonation half-cycles, Ar was used as sweep gas to avoid direct contact between the synthetic BFG and  $\text{O}_2$ . The reduction-carbonation half-cycle lasted for 480 s, whereas the oxidation-decarbonation half-cycle lasted for 120 s to maximise the utilisation of the materials. Except for the first cycle (Figure B8 (a) and (b)), the temperature of the furnace enclosing the reactor was kept constant at 973 K. The flow rates of all inlet gases were kept constant at  $41 \cdot 10^{-6} \text{ mol/s}$ , corresponding to a GHSV of about  $3700 \text{ h}^{-1}$ , throughout the experimental run.

The conversion of Ni to NiO and of  $\text{CaCO}_3$  to CaO during the oxidation-decarbonation half-cycles (equations (87) and (88)) over multiple cycles is displayed in Figure 26. On the secondary axis, the difference in the maximum temperature achieved during the two half-cycles is plotted. Based on Figure 26, the utilisation of Ni is almost

unaffected by the redox cycles. Due to the high reactivity and thus, fast kinetics of reduction, NiO can remain active despite being sintered [98]. The utilisation of  $\text{CaCO}_3$  for producing  $\text{CO}_2$ , on the other hand, increased until cycle 16 and then decreases. Interestingly, the difference in the maximum temperature of the 2 half-cycles roughly follows a mirrored trend when compared to the utilisation of  $\text{CaCO}_3$ . This suggests that the heat produced by the oxidation of Ni was effectively used to sustain the endothermic decarbonation until cycle 16, beyond which it was used to increase the solids' temperature instead of providing heat for decarbonation. This may have been caused by structural rearrangement due to sintering of Ni/NiO and/or CaO/ $\text{CaCO}_3$ . . Repeated cycling of redox materials [99] and CaO/ $\text{CaCO}_3$  [100] is known to cause sintering, leading to decreased reactivity of the materials. Antzaras et al. have shown that an intimate physical contact between Ni and  $\text{CaCO}_3$  is important to effectively decarbonate  $\text{CaCO}_3$  using the heat released during Ni oxidation [101]. Over 30 cycles, the loss in the  $\text{CO}_2$  production capacity of the material relative to its initial capacity was less than 13%, which is comparable to  $\text{CO}_2$  sorbents synthesised using more sophisticated techniques [97]. The carbon and oxygen balances (equations (92) and (93)) over the entire experiment were -3.8 and -7.7 mol%. Figure B6 shows further details about the active materials' utilisation in both half-cycles over multiple cycles and Figure B7 shows the corresponding maximum and average temperatures recorded.

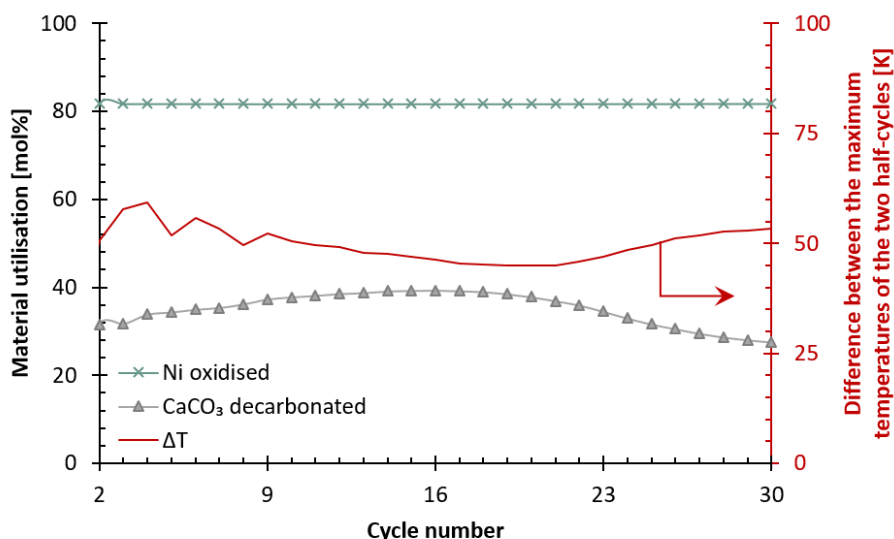


Figure 26: Evolution of the material utilisation and the difference between the maximum temperatures of the two half-cycles over 30 cycles. Synthetic BFG (molar composition: 23.8% CO, 24.1% CO<sub>2</sub>, 5.1% H<sub>2</sub>, 7% He, and 40% Ar) was used during the reduction-carbonation half-cycle and 50% O<sub>2</sub>/Ar during the oxidation-decarbonation half-cycle. The flow rates of all inlet gases were kept constant at  $41 \cdot 10^{-6}$  mol/s, corresponding to a GHSV of about 3700 h<sup>-1</sup>, throughout the experimental run.

In the first cycle, the temperature of the furnace enclosing the reactor was set at 923 K, the reduction-carbonation and oxidation-decarbonation half-cycle times were 318 and 219 s and 21% O<sub>2</sub>/Ar was fed during the oxidation-decarbonation half-cycle instead of 50% O<sub>2</sub>/Ar that was used for the rest of the cycles. The experimental results of the first and second cycles are displayed in Figure B8. The first cycle was run differently compared to the remaining 29 cycles to estimate the optimal operating conditions for the subsequent cycles.

#### 4.4.2.2 Influence of space velocity

In order to study the influence of GHSV, the inlet flow rate was maintained constant at three different values of  $21 \cdot 10^{-6}$  mol/s,  $41 \cdot 10^{-6}$  mol/s, and  $80 \cdot 10^{-6}$  mol/s corresponding to GHSVs of 1900, 3700, and  $5000 \text{ h}^{-1}$ . The range covers the GHSVs typical for ethylene production via ethane steam cracking ( $1880 \text{ h}^{-1}$ ) [102], industrial  $\text{H}_2$  production via steam methane reforming ( $3000 \text{ h}^{-1}$ ) [102], and methanol synthesis ( $5000 \text{ h}^{-1}$ ) [103]. The duration of both cycles was chosen such that the amounts of synthetic BFG fed in the reduction-carbonation half-cycle and of  $\text{O}_2$  in the oxidation-decarbonation half-cycle for each GHSV case were equal. The temperature of the furnace was set to 923 K. During oxidation-decarbonation half-cycle, 21%  $\text{O}_2/\text{Ar}$  was used to more closely mimic the simulation conditions, i.e. 10%  $\text{O}_2$ . After this half-cycle, the temperature was increased to 1173 K in Ar to decarbonate the  $\text{CaCO}_3$  completely.

Experimental results of the variation in GHSV (Figure 27 (a, b, and c)) show that CO and  $\text{H}_2$  were fully oxidised during the reduction-carbonation half-cycle. Lower GHSVs favoured  $\text{CO}_2$  capture whereas higher GHSVs favoured decarbonation. Thus, at a GHSV of  $1500 \text{ h}^{-1}$ , the fraction of  $\text{CaCO}_3$  decarbonated was as low as 0.4%. At a higher GHSV of  $5000 \text{ h}^{-1}$ , the amount of  $\text{CaCO}_3$  decarbonated increases to around 14%. The principal reason for the observed trends can be the heat losses to the surroundings that are higher at lower GHSVs. As low temperature favours carbonation, heat loss during the reduction-

carbonation keeps the reactor temperature low i.e. closer to the set-point of 923 K, and thus, leads to higher CaO conversion. Thus, higher GHSVs cause a more rapid increase in temperature that causes CO<sub>2</sub> capture during reduction-carbonation to be thermodynamically unfavourable. Conversely, decarbonation benefits from high temperatures and when the heat provided by oxidation of Ni is not lost to the surroundings, it can be used for decarbonation. Interestingly, the variation of GHSV had little to no effect on redox reactions of NiO/Ni, probably due to the fast kinetics of NiO reduction and Ni oxidation. A summary of the conversions of CaO/CaCO<sub>3</sub> and NiO/Ni in the 2 half-cycles using equations (29) to (88) at different GHSVs is presented in Table 8. The discrepancy in NiO/Ni utilisation during the 2 half-cycles is most likely due to the measurement inaccuracies of the MS.

Table 8: Effect of GHSV on the solids conversion.

GHSV [h <sup>-1</sup> ]	CaO carbonated [mol%]	CaCO <sub>3</sub> decarbonated [mol%]	NiO reduced [mol%]	Ni oxidised [mol%]
1500	100	0.41	62.8	62.7
3700	92.5	7.85	62.6	56.3
5000	75.5	13.7	62.4	56.1

#### 4.4.2.3 Influence of methane addition and temperature in the reducer-carbonator

As shown in section 4.4.1.3 and discussed in section 2 of SI, heat management can be improved by co-feeding  $\text{CH}_4$  and using  $\text{NiO}$  as oxygen carrier. In order to limit the heat released during reduction-carbonation and further increase the heat from oxidation-decarbonation, experiments were performed by mixing synthetic BFG with  $\text{CH}_4$ . Experimental results were obtained by setting and maintaining the reactor furnace at three different temperatures, 823 K, 923 K, and 1023 K. A GHSV value of  $6200 \text{ h}^{-1}$  (corresponding to an inlet flow rate of  $67 \cdot 10^{-6} \text{ mol/s}$ ), chosen to minimise heat losses, was kept constant over the entire cycle for all the experiments. Between the two half-cycles, an inert purge step lasting approximately 15 s was introduced to avoid direct contact between the reductants (80 mol% BFG + 20 mol%  $\text{CH}_4$ ) and oxidants (21 mol%  $\text{O}_2/\text{Ar}$ ). After each oxidation-decarbonation half-cycle, the temperature was increased to 1173 K in Ar to decarbonate  $\text{CaCO}_3$  completely.

At a reactor temperature of 873 K (Figure 27 (d)), not all  $\text{CH}_4$  was oxidised at the start of the reduction-carbonation half-cycle (0 to 20 s). Towards the end (72 to 87 s), the measured outlet flow rate of CO and  $\text{H}_2$  increased along with a steep temperature increase. A combination of methane cracking (equation (38)), Boudouard reaction (equation (39)), and carbonation could explain the observed phenomenon.



$$\text{CH}_4(\text{g}) \rightleftharpoons \text{C}(\text{s}) + 2\text{H}_2(\text{g}) \quad \Delta H_{923 \text{ K}}^0 = 89 \frac{\text{kJ}}{\text{mol}_{\text{CH}_4}} \quad \Delta G_{923 \text{ K}}^0 = -11 \frac{\text{kJ}}{\text{mol}_{\text{CH}_4}} \quad (38)$$

$$2\text{CO}(\text{g}) \rightleftharpoons \text{C}(\text{s}) + \text{CO}_2(\text{g}) \quad \Delta H_{923 \text{ K}}^0 = -171 \frac{\text{kJ}}{\text{mol}_{\text{C}}} \quad \Delta G_{923 \text{ K}}^0 = -88 \frac{\text{kJ}}{\text{mol}_{\text{C}}} \quad (39)$$

Formation of coke or carbon species on the Ni surface can effectively hinder the diffusion and subsequent oxidation of CO and H<sub>2</sub> by bulk NiO, which would cause an increase in the CO and H<sub>2</sub> flow. Upon switching the inlet gas to pure Ar, a continuous flow of CO was measured between 88 to 116 s, further corroborating this hypothesis. Finally, when the inlet flow was switched to 21% O<sub>2</sub>/Ar, a continued flow of H<sub>2</sub> and CO was observed which dropped to zero after 80 s (from 117 s to 196 s). However, the breakthrough of O<sub>2</sub> in the oxidation-decarbonation half-cycle was gradual rather than sharp as in the case when only synthetic BFG was used, suggesting that the temperature may not be sufficiently high to cause fast oxidation of stable graphitic or semi-graphitic coke. The phenomenon of coking was possibly caused by the high CH<sub>4</sub> content of the inlet gas, which created conditions that thermodynamically favour coke formation (Figure B4 for Gibbs free energy plots of reactions (38) and (39)). The actual addition of COG to the BFG will lead to a much smaller content of CH<sub>4</sub> in the feed mixture (about 1 mol%), making coke formation thermodynamically unfavourable. The presence of excess oxidants (H<sub>2</sub>O and traces of CO<sub>2</sub>) would favour steam gasification (equation (40)) and reverse Boudouard reaction (reverse of equation (39)). With increasing temperature, the Gibbs free energy ( $\Delta G^0$ ) of steam gasification becomes increasingly negative and thus, favourable (Figure B4). Note that the inlet gases used

for the experiments were dry, whereas the steel mill gases are typically saturated with H<sub>2</sub>O (approximately, 4 mol%).

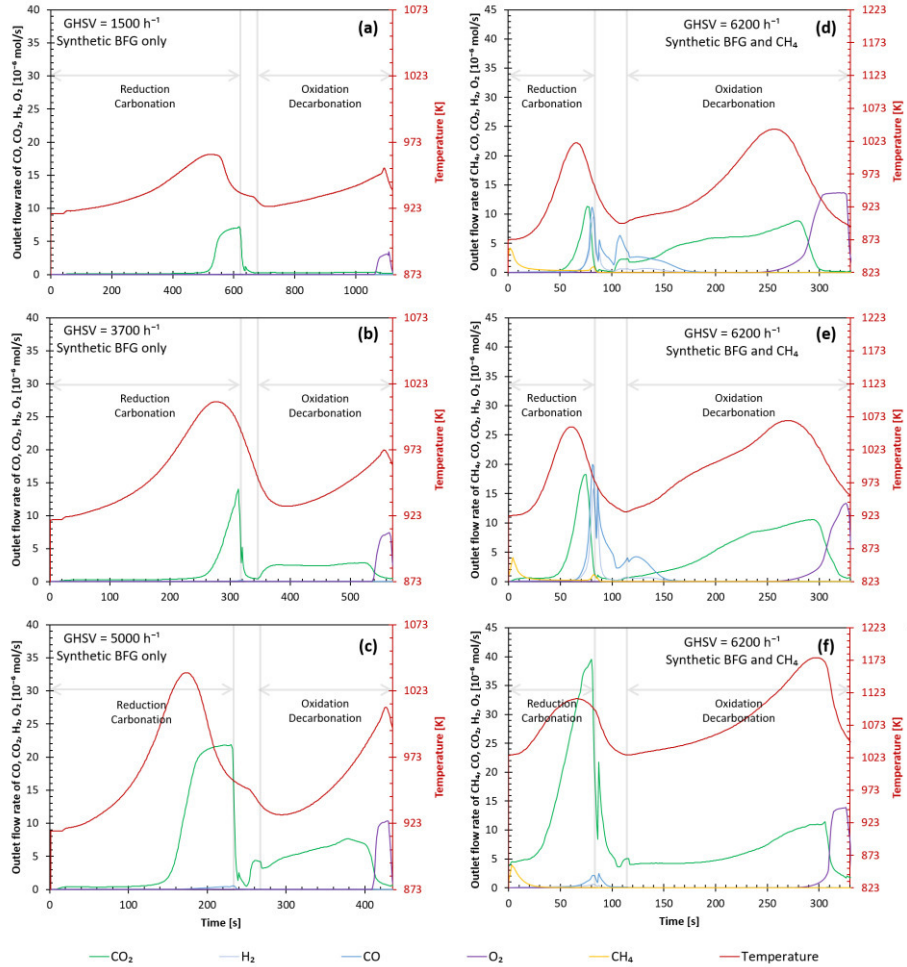
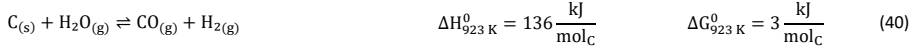


Figure 27: Measured outlet flow rates and temperature versus time over one cycle when synthetic BFG is used and the GHSV is kept constant for the inlet gas streams at (a) 1500 h<sup>-1</sup>, (b) 3700 h<sup>-1</sup>, and (c) 5000 h<sup>-1</sup> and when a mixture containing 20% CH<sub>4</sub> and

80% synthetic BFG is tested at a constant GHSV of  $6200\text{ h}^{-1}$  while the reactor furnace temperature is fixed at (d) 873 K, (e) 923 K, and (f) 1023 K.

An increase in reactor temperature by 50 K to 923 K did not considerably remedy the coking phenomenon described above (Figure 27 (e)). The higher temperature, which does not favour carbonation, caused less carbon capture. In the oxidation-decarbonation half-cycle, a higher  $\text{O}_2$  consumption suggested that, at this temperature, more  $\text{O}_2$  was consumed for the oxidation of the deposited coke. An increase in temperature to 1023 K had a considerable effect on the experimental results (Figure 27 (f)). Coking was almost completely avoided, possibly due to the high equilibrium partial pressure of  $\text{CO}_2$  at 1023 K.  $\text{CO}_2$  not captured could react with  $\text{CH}_4$  to form syngas via dry reforming along with steam methane reforming (equations (41) and (42), details of Gibbs free energy plots in Figure B5). Comparing the peak temperatures for each studied temperature, the desired effect from adding  $\text{CH}_4$  was most evident at higher temperatures. For experiments wherein the furnace temperature was varied at constant GHSV using synthetic BFG feed during reduction-carbonation, the reader is referred to Figure B9. These experimental results show that in the absence of  $\text{CH}_4$ , coking is not observed. Thus, when extending this process concept to other applications, it is important to consider the possibility of coking caused by  $\text{CH}_4$  or other hydrocarbons, for example, through thermodynamic analysis, and limit it by co-feeding adequate amounts of  $\text{H}_2\text{O}$  and/or  $\text{CO}_2$ .

Table 9 and Table 10 list a summary of the overall conversion of the reactive components and the maximum temperatures achieved during the half-cycles. The large difference in CaO conversion to CaCO<sub>3</sub> during the reduction-carbonation half-cycle and vice-versa during the oxidation-decarbonation half-cycle appear to be strongly related to the furnace temperature. As the furnace temperature increases, the decarbonation reaction is favoured both kinetically and thermodynamically. During the multiple cyclic tests carried out at 973 K and discussed in section 4.4.2.1, the difference between conversions of CaO and CaCO<sub>3</sub> was consistently less than 10%. This observation corroborates the values displayed in Table 9. The small difference in the conversions of NiO and Ni are also consistent with those observed in the multiple cycle test (Figure B6) and during the experiments conducted to study the influence of GHSVs (Table 8).

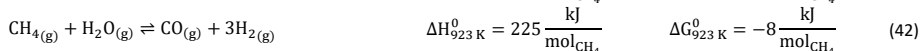
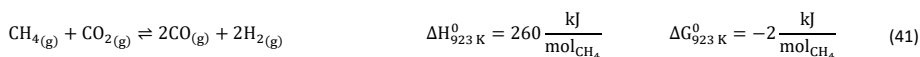


Table 9: Influence of the reactor furnace temperature on the conversions of the reactive components in the two half-cycles. Conversions of CH<sub>4</sub>, CO, H<sub>2</sub>, NiO, and CaO correspond to the reduction-carbonation half-cycle and the conversions of Ni and CaCO<sub>3</sub> correspond to the oxidation-decarbonation half-cycle.

Reactor furnace temperature [K]	Conversion [mol%]						
	CH <sub>4</sub>	CO	H <sub>2</sub>	NiO	Ni	CaO	CaCO <sub>3</sub>
873	83	83	56	91	83	48	17
923	95	72	34	89	90	43	20
1023	96	96	91	97	91	27	21

Table 10: Influence of the reactor furnace temperature on the maximum temperature achieved during the two half-cycles and the difference between them.

Reactor furnace temperature [K]	Maximum temperature during reduction-carbonation [K]	Maximum temperature during oxidation-decarbonation [K]	Difference in the maximum temperature of the 2 half-cycles [K]
873	1021	1041	20
923	1058	1067	9
1023	1114	1177	63

#### 4.4.3 Material characterisation

After the experimental run comprising 50 cycles (including 30 cycles with BFG and various experimental investigations testing GHSVs, temperatures, etc.), the material was characterised to explore its

stability and understand the causes of material deactivation. A confirmation of the material composition was obtained by EDX measurements in Table B1.

4.4.3.1 Dinitrogen sorption measurements

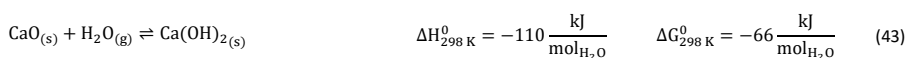
Numerous studies have shown that the textural properties worsen when the materials are used over multiple cycles in chemical [53] and calcium looping applications [104]. This is confirmed by comparing the major properties estimated by N<sub>2</sub> sorption of the as prepared material and the material after 50 cycles (post decarbonation-oxidation half-cycle) (Table 11). Further details of the isotherm and the loss of mesopores after 50 cycles are given in Figure B10 and Figure B11.

Table 11: Textural properties of the as prepared material and the material after 50 cycles (post decarbonation-oxidation) from liquid nitrogen sorption measurements.

	As prepared	After 50 cycles (post decarbonation-oxidation)
BET surface area [m <sup>2</sup> /g]	17	6
Pore volume [10 <sup>-9</sup> m <sup>3</sup> /g]	116	29
BJH average pore diameter [nm]	27	21
Particle size [nm]	61	170

#### 4.4.3.2 X-ray diffraction

Analysis of X-ray diffractograms of the as prepared and cycled material yields crystal phase-specific information (Figure 28 (a and b)). Interestingly, the as prepared material consisted mostly of  $\text{CaCO}_3$  and  $\text{Ca(OH)}_2$  instead of  $\text{CaO}$  (Figure B12 for quantitative phase analysis via Rietveld refinement), indicating high reactivity with  $\text{CO}_2$  and  $\text{H}_2\text{O}$  in the atmosphere to form calcium carbonate and calcium hydroxide (equation (43)).



The quantitative phase analysis by Rietveld refinement (Figure B12 and Figure B13 and Table B2) matched the phase composition found by EDX, indicating that the crystalline bulk phase has the same composition as the superficial composition measured by EDX. Comparing the as prepared material with the material after 50 cycles based on the peak broadening in XRD, the crystallite size of  $\text{NiO}$  decreased from 56 nm to 47 nm, whereas  $\text{CaO}$  increased from 10 nm to 63 nm. For  $\text{CaO}$ , the presence of  $\text{CaCO}_3$  and  $\text{Ca(OH)}_2$  makes the effect of sintering difficult to discern. In the cycled material,  $\text{NiO}$  crystallites with an average size of 47 nm co-existed with metallic  $\text{Ni}$  (not identified in the as prepared material) with an average crystallite size of 69 nm. A possible core-shell structure comprising a metallic  $\text{Ni}$  core and a  $\text{NiO}$  shell could make it difficult to estimate the intensity of sintering in the cycled material via XRD.  $\text{CeO}_2$  nano-particles may have sintered slightly under cyclic redox

conditions; an average CeO<sub>2</sub> crystallite size of 44 nm was estimated for the cycled materials, 9 nm larger than that of the as prepared material.

#### 4.4.3.3 Scanning transmission electron microscopy and elemental mapping

STEM-EDX imaging show finely dispersed NiO and CeO<sub>2</sub> on a Ca-based matrix for the as prepared material (Figure 28 (c) and (d)). As noted in the XRD results, Ca is present in the form of CaCO<sub>3</sub>, Ca(OH)<sub>2</sub>, and CaO in the as prepared material. The close contact between Ce and Ni in the as prepared material can also be noted in the individual elemental mapping (Figure B14). After 50 cycles, the STEM imaging and EDX-mapping (Figure 28 (e) and (f)) show that the imaged particles were decorated by CeO<sub>2</sub> nanoparticles at the edges. An onset of sintering is visible in the cycled materials, especially for Ni particles. Individual elemental maps of the cycled material show that Ni and CeO<sub>2</sub> remain closely associated with each other (Figure B15).

#### 4.4.3.4 Temperature-programmed reactions

CO<sub>2</sub>-TPCD results of the as prepared and cycled material show that there is a 12% decrease in the CO<sub>2</sub> capture capacity of the material upon being exposed to redox cycles (Figure 28 (g)). Carbonation of the as prepared material peaks at a temperature of 956 K, whereas that of the cycled material lies at 965 K, 9 K higher. The carbonation curve of the cycled material also appears flatter with a sharper transition to decarbonation (CO<sub>2</sub> release) indicating that in the given conditions, the material could not be fully carbonated due to less favourable kinetics.



The transition from carbonation to decarbonation for both materials occurs between 1086 to 1090 K, in close agreement with thermodynamics given that equilibrium  $\text{CO}_2$  partial pressure is 22 kPa at 1074 K.

The  $\text{H}_2$ -TPR of the as prepared material is similar to the  $\text{H}_2$ -TPR profile of bulk NiO reported in literature (Figure 28 (h)) [105]. Upon being cycled, the 2<sup>nd</sup> peak of the TPR shifts to a higher temperature, possibly, due to physical restructuring of the material and/or an effect of  $\text{CeO}_2$  or  $\text{CaO}$  on NiO (Figure 28 (e) and (f)). The  $\text{O}_2$ -TPO of the materials also indicates that, upon cycling, the  $\text{O}_2$  consumption peak shifts to 1025 K, 308 K higher than that of the as prepared material.

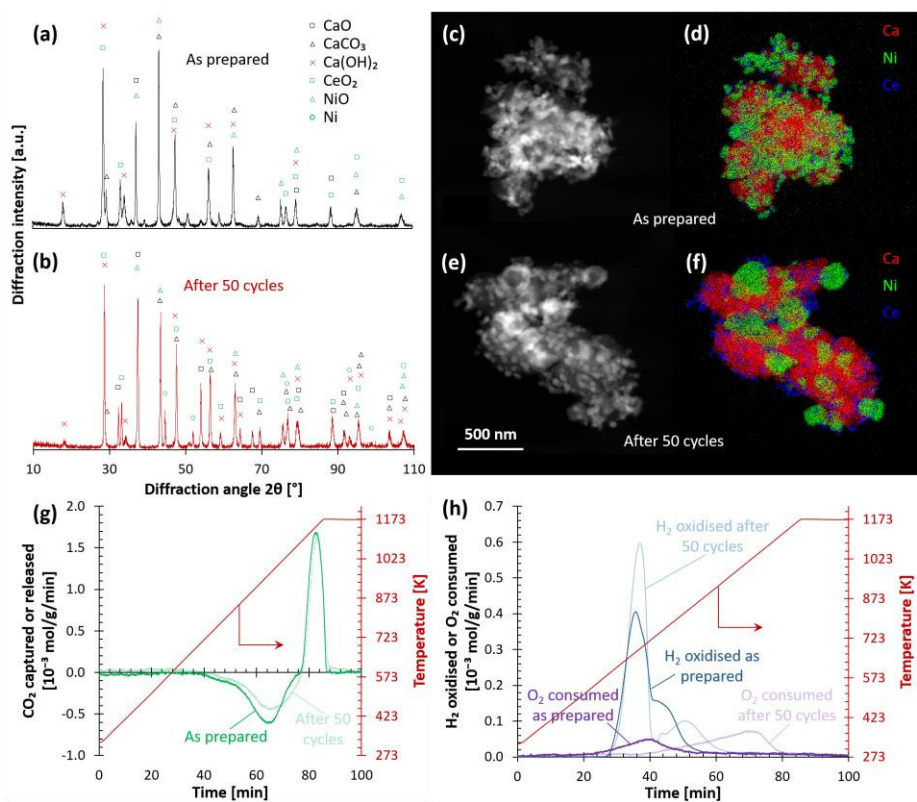


Figure 28: XRD of (a) as prepared and (b) the material after 50 cycles. Only peaks with intensities larger than 2% and 5% of the maximum intensity have been marked for (a) and (b). HAADF-STEM imaging for the (c) as prepared material and (e) the cycled material and their EDX mapping in (d) and (f). (g)  $\text{CO}_2$ -TPCD of the as prepared and the cycled materials using 20%  $\text{CO}_2$  in Ar (h)  $\text{H}_2$ -TPR and  $\text{O}_2$ -TPO of the as prepared and the cycled materials using 5%  $\text{H}_2$ /Ar and 5%  $\text{O}_2$ /Ar.

## 4.5 Conclusions and perspectives

A combination of chemical looping processes for CO<sub>2</sub> capture from steel mill gases is put forward based on process simulations and experiments in a laboratory fixed bed reactor. In light of heat management, the NiO/Ni pair is most suitable for the chemical looping combustion part of the process due to its capacity to liberate a substantial amount of heat upon oxidation of Ni by O<sub>2</sub>. The addition of a second loop for air separation (CLAS) minimises the required work input compared to a separate cryogenic air liquefaction unit. Herein, the manganese oxide pair Mn<sub>2</sub>O<sub>3</sub>/Mn<sub>3</sub>O<sub>4</sub> is the most optimal choice among commonly available oxygen carriers for the CLAS loop due to its favourable operating temperature (1100 to 1200 K) at ambient pressure.

A decrease in material utilisation of the proposed process has a considerable impact on its carbon capture capacity. When conversions of NiO and CaO decrease from 100% to 21% and 15%, carbon capture decreases from 86% to 60%. The inert CeO<sub>2</sub> content only slightly decreases the carbon capture. The temperature of the CLAS loop, which is operated isothermally, also influences the carbon capture of the process. A higher temperature in the CLAS loop, up to temperatures in the range of 1130 to 1140 K, favours higher carbon capture. Temperatures beyond this range require additional energy to be supplied to the CLAS loop for sustainable operation, which may come at the cost of additional CO<sub>2</sub> emissions. Addition of coke oven gas (COG)

to the proposed process can increase carbon capture from the blast furnace gas (BFG) by at least 20%.

An experimental investigation was carried out in a laboratory fixed bed reactor using synthetic BFG and  $\text{CH}_4$  over 50 cycles. The results indicated stable performance of materials and high material utilisation under different operating conditions. The characterisation of the materials before and after the cycles showed that the functionalities of the material, i.e. carbon capture and reduction-oxidation properties, were retained.

The intensified process concept presented in this work offers opportunities for  $\text{CO}_2$  capture with optimal use of the available chemical energy stored in the steel mill gases. The process avoids the use of an energy-intensive air separation unit, which is a major source of energy penalty for calcium looping and oxy-fuel combustion. Combining chemical looping combustion using an appropriate oxygen carrier with calcium looping further offsets the high energy requirement of the decarbonation step in the calcium looping process by transferring the heat of combustion to the endothermic decarbonation reaction. The combined chemical looping process can be operated flexibly, contributing to the heat and electricity demand of the steel mill while capturing the  $\text{CO}_2$  emissions it typically entails. The process concept can also be effectively applied for other sorption enhanced processes, such as sorption enhanced steam reforming or water-gas shift reaction to minimise the energy losses caused by the

use of an air separation unit. The promising features of this process make it interesting for further optimisation and investigation from an experimental and techno-economic perspective.

## Chapter 4

# CO<sub>2</sub> capture and conversion from the blast furnace gas

### Abstract

In this chapter, a combined chemical looping process to produce CO, a building block for the chemical industry, from the CO<sub>2</sub>-rich blast furnace gas of a steel mill is proposed. This cyclic process can make use of abundant Fe<sub>3</sub>O<sub>4</sub> and CaO as solid oxygen and CO<sub>2</sub> carriers at atmospheric pressure. A proof of concept was obtained in a laboratory-scale fixed bed reactor with synthetic blast furnace gas and Fe<sub>3</sub>O<sub>4</sub>/CaO = 0.6 kg/kg. CO production from the proposed process was investigated at both isothermal conditions (1023 K) and upon imposing a temperature program from 1023 to 1148 K. The experimental results were compared using performance indicators such as CO yield, CO space time yield, carbon recovery of the process, fuel utilisation, and solids' utilisation. The temperature-programmed CO production resulted in a CO yield of  $0.056 \pm 0.002$  mol per mol of synthetic blast furnace gas at an average CO space time yield of 7.6 mmol/kg<sub>Fe</sub>/s over 10 cycles, carbon recovery of  $48 \pm 1\%$ , fuel utilisation of  $23 \pm 2\%$ , and an average calcium oxide and iron oxide utilisation of  $22 \pm 1\%$  and  $11 \pm 1\%$ . These experimental performance indicators for the temperature-

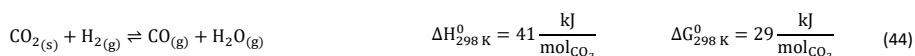
programmed CO production were consistently better than those of the isothermal implementation mode by 20 to 35%. Over 10 consecutive process cycles, no significant losses in CO yield were observed in either implementation mode. Process simulation was carried out for 1 million metric tonnes per year of equivalent CO<sub>2</sub> emissions from the blast furnace gas of a steel mill to analyse the exergy losses in both modes of operation. Comparison of the exergy efficiency of the temperature-programmed process to the isothermal process showed that the former is more efficient because of the higher CO concentration achievable, despite 20% higher exergy losses caused by heat transfer required to change temperature.

**This chapter was published as**

V. Singh, L.C. Buelens, H. Poelman, M. Saeys, G.B. Marin, V.V. Galvita, Carbon monoxide production using a steel mill gas in a combined chemical looping process, *Journal of Energy Chemistry*, 68 (2022) 811-825.

## 5.1 Introduction

In this chapter, the primary reaction that is broken down into two steps via chemical looping is the reverse water-gas shift reaction (rWGS) to produce CO (equation (44)) [106-111].



CO is an important platform molecule that is used for the production of synthetic fuels and for the synthesis of a plethora of precursors for the chemicals and plastics industry [1, 112, 113]. The CO/CO<sub>2</sub> stream from the proposed process could, for example, be converted into polyols by emerging and established technologies [114, 115]. This would not only reduce the CO<sub>2</sub> emissions from the iron and steel industry but also provide feedstock to the chemicals and plastics industry, thereby contributing to the goal of a circular carbon economy. The scope of this study in its broader context is schematised in Figure 29.



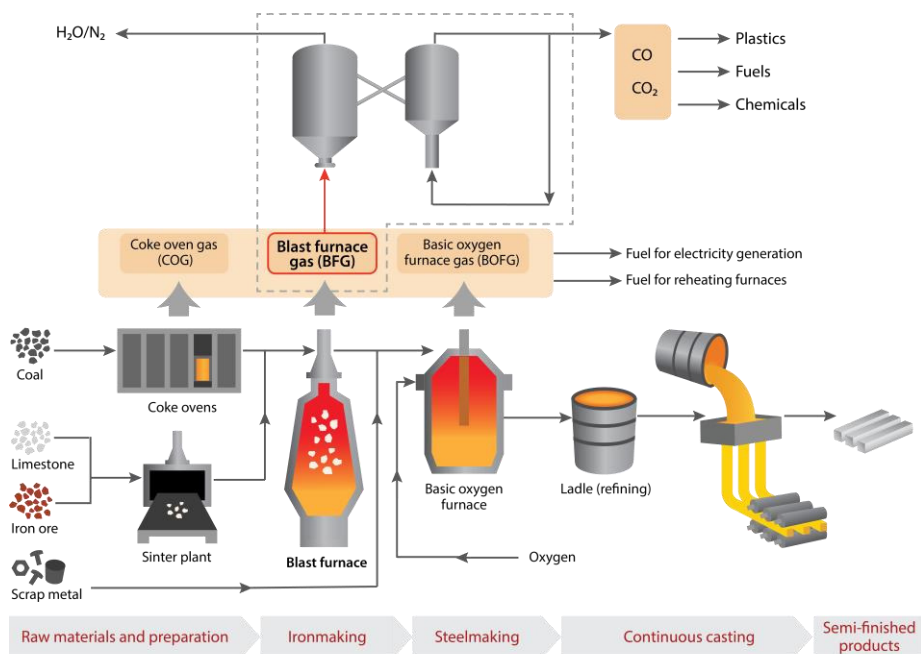


Figure 29: Blast furnace – basic oxygen furnace steelmaking process. The schematic inside the dashed lines in the top section of the figure illustrates the scope of this work within its broader context.

Production of CO from the BFG by breaking down the rWGS in the combined chemical looping process is achieved by using an oxygen carrier (OC) as a redox material for CO production together with a CO<sub>2</sub> carrier (CC) for shifting the equilibria towards desired products as displayed in Figure 30. Breaking down the rWGS via combined chemical looping offers the opportunity to circumvent the thermodynamic limitations of the steady state catalytic rWGS process and the associated energy penalties of separating different components from its product stream.

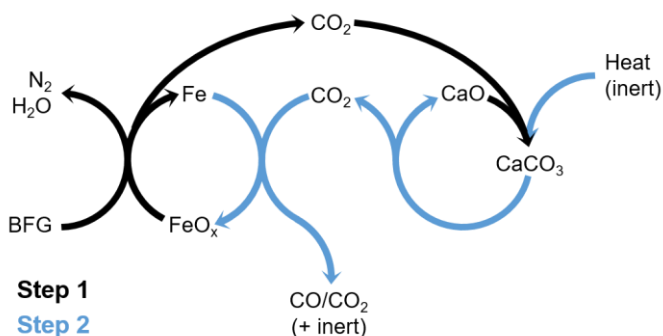


Figure 30: Process schematic for the combined chemical looping approach to produce CO from the BFG.

For the production of CO in the process concept,  $M_1O_x$ , the OC, and  $M_2O$ , the CC, in Figure 30 are selected based on the following criteria:

- $M_1O_x$  is reducible by  $H_2$  to form  $M_1$  and  $H_2O$ .
- $M_1O_x$  and  $M_1$  are reversibly reducible and oxidisable by CO and  $CO_2$ , respectively.
- $M_2O$  reversibly reacts with  $CO_2$  to form a metal carbonate,  $M_2CO_3$ .

During the reduction-carbonation step,  $H_2$  (1-5 mol%) and CO (20-28 mol%) in the BFG reduce the OC  $M_1O_x$  to  $M_1$  while forming  $H_2O$  and  $CO_2$ . The formed  $CO_2$  along with the  $CO_2$  already present in the BFG (17-25 mol%) is captured by  $M_2O$ . Thus,  $M_2O$  acts as a sink for the carbon in the BFG. In the next step (decarbonation-oxidation), heat and/or an inert gas is supplied to release the carbon captured in  $M_2CO_3$ .  $M_2CO_3$  decomposes to  $M_2O$  while releasing  $CO_2$ .  $M_1$  is oxidised by the released  $CO_2$  to  $M_1O_x$  while producing CO, thereby regenerating the materials for the next cycle.

Two candidate materials selected for this purpose are iron oxide ( $\text{Fe}_3\text{O}_4$ ) and calcium oxide ( $\text{CaO}$ ) as  $\text{M}_1\text{O}_x$  and  $\text{M}_2\text{O}$ , respectively. The chosen materials are both raw materials for the iron and steel industry. Thus, once the materials reach the end of their useful life-time due to insufficient productivity caused by deactivation phenomena such as sintering, poisoning, formation of inactive phase(s), attrition, etc. [116], they can be utilised for the production of steel in the steel mill. To elongate the useful life-time of the materials, support materials,  $\text{MgAl}_2\text{O}_4$  and  $\text{CeO}_2$  for iron oxide and calcium oxide were used. During the two steps or half-cycles, the reactions displayed in Table 12 occur. The scheme of reaction shows that  $\text{Fe}_3\text{O}_4/\text{FeO}/\text{Fe}$  and  $\text{CaO}/\text{CaCO}_3$  operate synergistically to maximise carbon capture in the reduction-carbonation step as well as maximise CO production in the decarbonation-oxidation step by shifting the equilibrium in favour of the desired products. The concept has been successfully utilised in super-dry reforming of methane [117] and sorption enhanced processes such as water gas-shift reaction [35]. In this chapter, by capturing the carbon content of the BFG using a combination of the OC and the CC in the first step,  $\text{H}_2$  in the BFG can be effectively used for further reducing the OC. The captured carbon can then be released by the CC in the second step and transformed from  $\text{CO}_2$  into CO by the OC in the absence of  $\text{H}_2$  and  $\text{H}_2\text{O}$ .

Table 12: Gas-solid reactions during the process with their standard reaction enthalpies and Gibbs free energies from NIST for CO, CO<sub>2</sub>, H<sub>2</sub>, H<sub>2</sub>O, Fe, Fe<sub>3</sub>O<sub>4</sub>, and CaO [118] and FactSage for CaCO<sub>3</sub> and FeO [119].

Reduction-carbonation			
Reaction	$\Delta H_{293\text{ K}}^0$ [kJ/mol <sub>(g)</sub> ]	$\Delta H_{1023\text{ K}}^0$ [kJ/mol <sub>(g)</sub> ]	$\Delta G_{1023\text{ K}}^0$ [kJ/mol <sub>(g)</sub> ]
Fe <sub>3</sub> O <sub>4(s)</sub> + H <sub>2(g)</sub> ⇌ 3 FeO <sub>(s)</sub> + H <sub>2O(g)</sub>	63	37	-22
FeO <sub>(s)</sub> + H <sub>2(g)</sub> ⇌ Fe <sub>(s)</sub> + H <sub>2O(g)</sub>	30	21	14
¼ Fe <sub>3</sub> O <sub>4(s)</sub> + H <sub>2(g)</sub> ⇌ ¾ Fe <sub>(s)</sub> + H <sub>2O(g)</sub>	38	25	1
Fe <sub>3</sub> O <sub>4(s)</sub> + CO <sub>(g)</sub> ⇌ 3 FeO <sub>(s)</sub> + CO <sub>2(g)</sub>	22	2	-24
FeO <sub>(s)</sub> + CO <sub>(g)</sub> ⇌ Fe <sub>(s)</sub> + CO <sub>2(g)</sub>	-11	-13	12
¼ Fe <sub>3</sub> O <sub>4(s)</sub> + CO <sub>(g)</sub> ⇌ ¾ Fe <sub>(s)</sub> + CO <sub>2(g)</sub>	-3	-10	1
CaO <sub>(s)</sub> + CO <sub>2(g)</sub> ⇌ CaCO <sub>3(s)</sub>	-179	-169	-20
Decarbonation-oxidation			
Reaction	$\Delta H_{293\text{ K}}^0$ [kJ/mol <sub>(g)</sub> ]	$\Delta H_{1023\text{ K}}^0$ [kJ/mol <sub>(g)</sub> ]	$\Delta G_{1023\text{ K}}^0$ [kJ/mol <sub>(g)</sub> ]
CaCO <sub>3(s)</sub> ⇌ CaO <sub>(s)</sub> + CO <sub>2(g)</sub>	179	169	20
¾ Fe <sub>(s)</sub> + CO <sub>2(g)</sub> ⇌ ¼ Fe <sub>3</sub> O <sub>4(s)</sub> + CO <sub>(g)</sub>	3	10	-1
Fe <sub>(s)</sub> + CO <sub>2(g)</sub> ⇌ FeO <sub>(s)</sub> + CO <sub>(g)</sub>	11	13	-12
3 FeO <sub>(s)</sub> + CO <sub>2(g)</sub> ⇌ Fe <sub>3</sub> O <sub>4(s)</sub> + CO <sub>(g)</sub>	-22	-2	24

## 5.2 Methods

### 5.2.1 Experimental proof of concept

The synthetic BFG had the following composition: 5.1 mol% H<sub>2</sub>, 23.8 mol% CO, 24.1 mol% CO<sub>2</sub>, 7 mol% He, and 40 mol% Ar. The gas flow rate was kept constant at  $4.1 \cdot 10^{-5}$  mol/s and the reactor pressure was controlled at 120 kPa by a back pressure regulator. For a typical experiment, 0.5 g of OC [355-500  $\mu$ m], 0.5 g of CC [355 - 500  $\mu$ m], and 1 g of  $\alpha$ -Al<sub>2</sub>O<sub>3</sub> (Final Advanced Materials Sàrl) acting as a solid diluent [230  $\mu$ m] were physically mixed and loaded in the reactor on a quartz wool plug (photos in Figure C21). A different size fraction of the diluent,  $\alpha$ -Al<sub>2</sub>O<sub>3</sub>, facilitated separation of the diluent from the reactive solids after the experiment. The flow of synthetic BFG for the reduction-carbonation lasted 180 s, immediately followed by a switch to Ar (acting as the diluent and the internal standard for quantification of outlet gases) for 300 s. By using 180 s as the time duration of the reduction-carbonation half-cycle, higher utilisation of materials can be achieved. Higher utilisation is important to detect potential sintering, minimise reactor size, and reduce pressure drop. For a reduction-carbonation half-cycle time of 180 s, the molar ratio of Fe<sub>3</sub>O<sub>4</sub> to BFG was 0.14 mol<sub>Fe<sub>3</sub>O<sub>4</sub></sub>/mol<sub>BFG</sub> and of CaO to BFG was 0.98 mol<sub>CaO</sub>/mol<sub>BFG</sub>.

Two modes of operation were tested: isothermal and temperature-programmed CO production. In the former, the temperature for both half-cycles was kept constant at 1023 K, whereas

in the temperature-programmed mode, the temperature during decarbonation-oxidation was increased from 1023 K to 1148 K at 25 K/min and brought back to 1023 K. A schematic with the details of the experimental design is depicted in Figure 31. 1023 K was selected as the minimal temperature for the experiments due to faster decarbonation kinetics of  $\text{CaCO}_3$  at these temperatures, thereby providing a good compromise to compare the isothermal and the temperature-programmed processes (the latter of which benefits from higher temperatures).

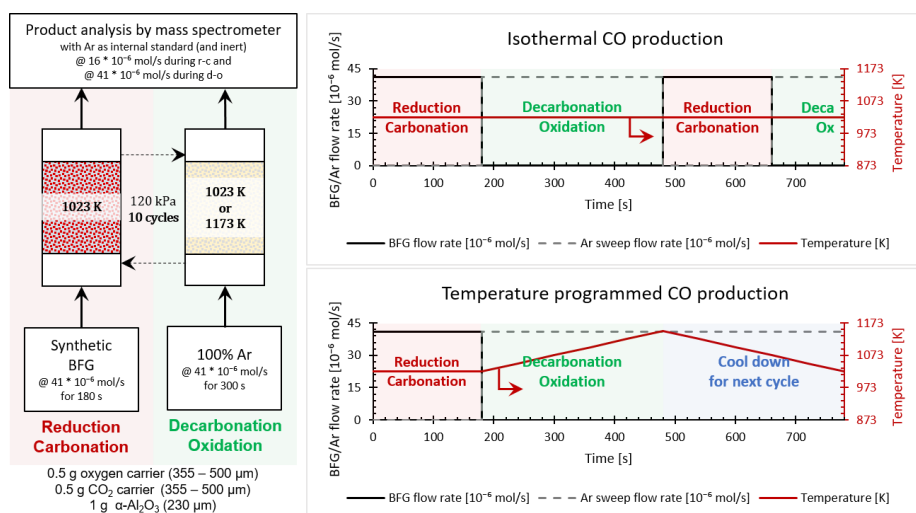


Figure 31: Specifications of the experimental design for the proof of concept.

Before starting each experiment, the solids were pre-treated by reduction using  $\text{H}_2$  and subsequent oxidation using  $\text{CO}_2$  at 973 K and 1173 K. This ensured the absence of the  $\text{Fe}_2\text{O}_3$  phase which can significantly affect the results of the first cycles as it is more readily

reducible by CO/H<sub>2</sub> compared to other FeO<sub>x</sub> ( $x \leq 1.33$ ) species. During this pre-treatment, reduction was carried out using a 70% H<sub>2</sub>/Ar mixture for approximately 30 minutes and oxidation was carried out using a 70% CO<sub>2</sub>/Ar mixture for approximately 15 minutes. After oxidation using CO<sub>2</sub>, the solids were exposed to Ar at elevated temperatures of 1173 K to decarbonate all CaCO<sub>3</sub> that was formed in the CC. Proof of complete regeneration of CaO in the CC was obtained from the negligible CO<sub>2</sub> concentration measured in the outlet stream.

### 5.3 Process calculations

Thermodynamic data for the process calculations were obtained from NIST and FactSage [118, 119]. Data for FeO and CaCO<sub>3</sub> were obtained from FactSage, whereas data for other species were obtained from NIST. For the process simulations, the data available from Aspen Plus® V10 was used for the gas phase species.

#### 5.3.1 Process simulation

Process simulations were performed in Aspen Plus® V10. Table 13 lists the setup of the flowsheet for the process simulation and

Table 14 displays the specifications of the process simulation. Unless mentioned otherwise, other specifications were the default values on Aspen Plus® V10. A schematic of the flowsheet created on Aspen Plus® is displayed in Figure 32.

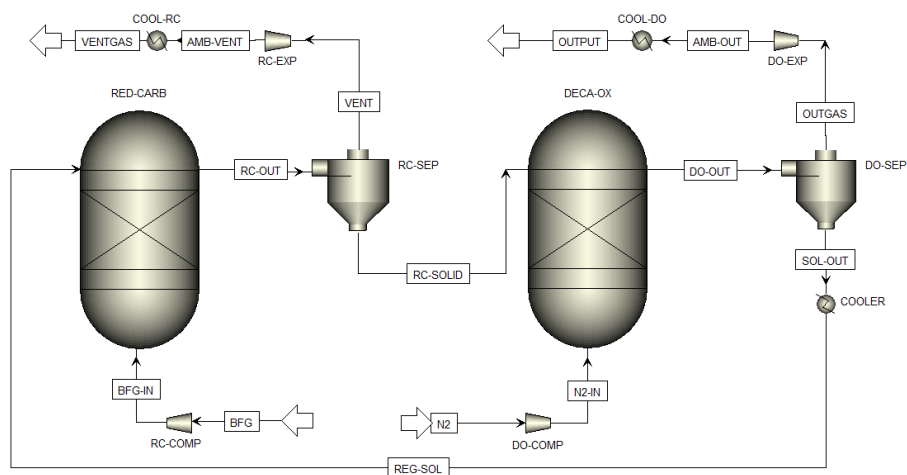


Figure 32: Aspen Plus V10 process flowsheet.

The heat capacity of all the solid components was modified with equations for estimating the heat capacity taken from NIST [118], FactSage [119], and Barin [120]. For all simulation results, the equilibrium constants for CO/CO<sub>2</sub> and H<sub>2</sub>/H<sub>2</sub>O redox reactions with Fe/Fe<sub>3</sub>O<sub>4</sub>, for the reverse water-gas shift reaction, and for carbonation/decarbonation of CaO/CaCO<sub>3</sub> were checked and found to be in good agreement with equilibrium constants determined by manual calculations.

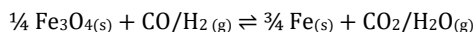


Table 13: Aspen Plus® setup of modules, property methods, material databanks, and models.

Flowsheet setup	
Property method	PR-BM and STEAM-TA for free water method
Databank	PURE36, INORGANIC, SOLIDS
Solid components	C (graphite), CaO, CaCO <sub>3</sub> , Ca(OH) <sub>2</sub> , CeO <sub>2</sub> , Fe <sub>3</sub> O <sub>4</sub> , Fe, Fe <sub>3</sub> C, MgAl <sub>2</sub> O <sub>4</sub>
Fluid components	CO, CO <sub>2</sub> , H <sub>2</sub> , H <sub>2</sub> O, N <sub>2</sub>
Stream class	MIXCISLD
Unit operation models	
Reactor(s)	RGibbs
Gas-solid separators	SSplit
Heat exchanger(s)	Heater
Mechanical operation models	
Compressor(s) and turbine(s)	Compr

FeO was not considered (see Table 14) based on the experimental results described in sections 5.4.2 and 5.4.3.3. The mass of solids circulating was determined as per the experimental method. In the experimental proof-of-concept, the amount of OC available for reduction-carbonation was two times higher than that required ( $\approx 1 \bullet$

$10^{-3}$  mol) for complete oxidation of the reductants fed ( $\approx 2.1 \cdot 10^{-3}$  mol) for the given reduction-carbonation half-cycle time (180 seconds) based on the stoichiometry displayed in equation (45).



In the process simulation, the molar flow rate of the OC was analogously set such that it was 2 times higher than the molar flow rate required to completely oxidise the reductants via equation (45). Similarly, the amount of CaO used in the experiment was two times higher than required ( $\approx 7.1 \cdot 10^{-3}$  mol) for capturing all the  $\text{CO}_2$  in the BFG and all the CO in the BFG that could have been oxidised ( $\approx 3.5 \cdot 10^{-3}$  mol) during the reduction-carbonation half-cycle that lasted 180 s. Analogously, in the process simulation, the molar flow rate of CaO was set such that it was two times higher than the sum of the molar flow rates of CO and  $\text{CO}_2$ .

The process simulations described in this work differ from other works involving chemical looping [45, 121] in that the product distribution from experimental yields is not input to the simulator, but instead the simulator yields the product distribution based on thermodynamics of the involved components [122]. This is done through Aspen Plus's RGibbs reactor, which uses Gibbs free energy minimisation with phase splitting to calculate equilibrium. The equilibrium is calculated for any number of components in the solid and fluid phases. The results of the simulation are compared with those from the experiments and discussed in the results section 5.4.4.1. Thus,

the experimental findings supply: 1) the information that redox transitions of  $\text{FeO}_x$  (where  $x = 0$  to  $1.33$ ) occur between Fe and  $\text{Fe}_3\text{O}_4$  and 2) the mass of solids contacting the mass of inlet BFG during the reduction-carbonation half-cycle. This calculated mass is subsequently transferred to the decarbonation-oxidation half-cycle.

Table 14: Specifications and assumptions of the process simulation.

Specifications of operating conditions	
Ambient conditions	298 K and 101 kPa
Pressure in the reactors	121 kPa
Inlet BFG	114.1 tonnes/hour (corresponding to 1 MMta of equivalent CO <sub>2</sub> emissions if the BFG would be combusted) H <sub>2</sub> : 79 mol/s, CO: 367 mol/s, CO <sub>2</sub> : 373 mol/s, N <sub>2</sub> : 728 mol/s
Composition of circulating solids	50% Fe <sub>2</sub> O <sub>3</sub> /MgAl <sub>2</sub> O <sub>4</sub> on gravimetric basis 83% CaO/CeO <sub>2</sub> on gravimetric basis
Flow rate of circulating solids	Fe <sub>3</sub> O <sub>4</sub> : 224 mol/s, CaO: 1484 mol/s, CeO <sub>2</sub> : 101 mol/s, MgAl <sub>2</sub> O <sub>4</sub> : 378 mol/s
Components permitted to form in the reducer-carbonator	C (graphite), CaO, CaCO <sub>3</sub> , Ca(OH) <sub>2</sub> , Fe <sub>3</sub> O <sub>4</sub> , Fe, Fe <sub>3</sub> C, CO, CO <sub>2</sub> , H <sub>2</sub> , H <sub>2</sub> O
Components permitted to form in the decarbonator-oxidiser	CaO, CaCO <sub>3</sub> , Fe <sub>3</sub> O <sub>4</sub> , CO, CO <sub>2</sub>
Components treated as inert	CeO <sub>2</sub> , MgAl <sub>2</sub> O <sub>4</sub> , N <sub>2</sub>
Outlet pressure of turbines	101 kPa
Design specifications (Design spec)	
Temperature of the decarbonator-oxidiser (for the temperature-programmed mode)	Varied such that outlet flow rate of CaCO <sub>3</sub> from decarbonator-oxidiser = $3 \cdot 10^{-9}$ mol/s (indicating full decarbonation of CaCO <sub>3</sub> )
N <sub>2</sub> fed to the decarbonator-oxidiser (for the isothermal mode)	Varied such that outlet flow rate of CaCO <sub>3</sub> from decarbonator-oxidiser = $3 \cdot 10^{-9}$ mol/s (indicating full decarbonation of CaCO <sub>3</sub> )
Specifications of auxiliary units	
Compressors and turbines	72% isentropic efficiency 100% mechanical efficiency

Four different cases were studied in the process simulations:

1. Isothermal: wherein the process was simulated at 1013 K with an external feed for N<sub>2</sub>.
2. Temperature-programmed (mild temperature change): the reduction-carbonation step was simulated at 1013 K and the temperature in the decarbonation-oxidation step was determined by Aspen Plus® to be 1097 K for achieving full decarbonation of CaCO<sub>3</sub> in the absence of N<sub>2</sub> feed.
3. Temperature-programmed (large temperature change): the reduction-carbonation step was simulated at 923 K to improve carbon recovery from the BFG and the temperature in the decarbonation-oxidation step was determined by Aspen Plus® to be 1090 K for achieving full decarbonation of CaCO<sub>3</sub> in the absence of N<sub>2</sub> feed. In this case, formation of FeO could be considered but the assumption that FeO is not formed would not affect the results.
4. Combustion: a stoichiometric quantity of air was fed for the near complete combustion of the BFG adiabatically.

### 5.3.2 Exergy analysis

An overall exergetic efficiency ( $\eta_{\text{exergy}}$ ) of the investigated processes was calculated using equation (46).

$$\eta_{\text{exergy}} = \frac{\dot{E}x_{\text{output}}}{\dot{E}x_{\text{input}}} * 100$$

The exergy of different streams/processes was calculated as follows [123]:

Exergy of work (compressors or turbines) =  $W$

Exergy of heat (heat exchangers and reactors) =  $\left(1 - \frac{T_0}{T}\right) * \dot{Q}$

Exergy for separation/mixing =  $R * T_0 \left[ \left( \sum_p \dot{n}_{ip} * \sum_i x_{ip} * \ln x_i \right) - \left( \sum_f \dot{n}_{if} * \sum_i x_{if} * \ln x_i \right) \right]$

Standard chemical exergy of stream =  $\sum_j \dot{n}_j \left( \Delta G_f^0 + \sum_{\text{elements}} n_{\text{element}} * ex_{\text{element}}^0 \right)$

The process flow sheet used for the calculations is displayed in Figure 33.

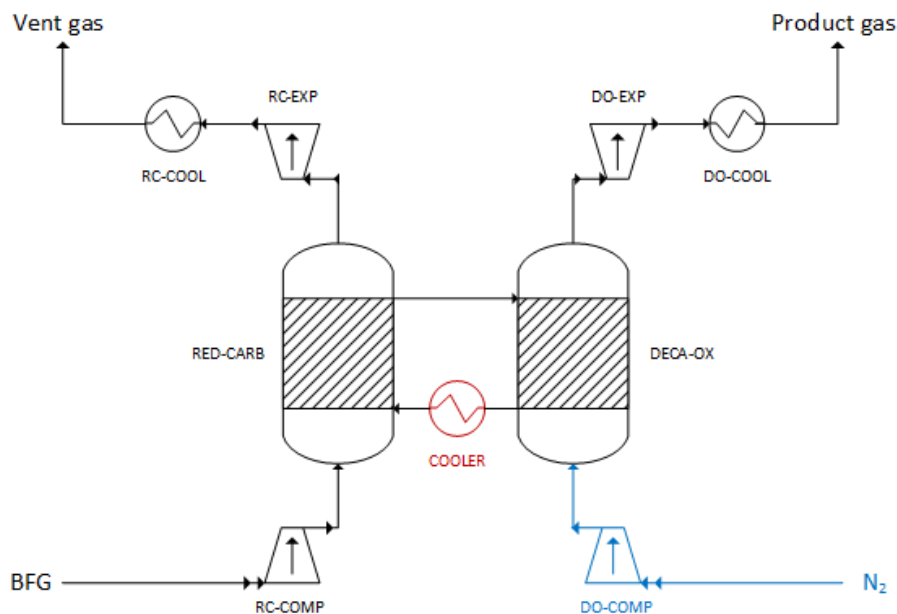


Figure 33: Process flowsheet used in the exergy analysis of isothermal and temperature-programmed CO production. Notations for the different sections were harmonised with those of the Aspen Plus simulation. The sections in red pertain to the temperature-programmed CO production process and the ones in blue are exclusively for the isothermal CO production process.

### 5.3.3 Process and experimental performance indicators

The maximum oxygen transfer capacity of the OC ( $N_{OC}$ ) is assumed to be 4/3 O atoms per Fe atom; representative of the redox transitions between Fe and  $Fe_3O_4$  (equation (45)). Equation (51) is used for determining the oxygen transfer capacity of the material used in the reactor for the experiments.

$$N_{OC} = \frac{m_{OC} * w_{Fe_2O_3,OC}}{MM_{Fe_2O_3}} * 2 * \frac{4}{3}$$

The total amount of exchangeable O atoms from non-stoichiometric  $CeO_{2-\delta}$  is neglected as only a small proportion of O atoms ( $\delta < 0.1$ ) from  $CeO_2$  are available in the given reaction conditions [95].

Analogously, as per the stoichiometry of the carbonation reaction of CaO, the maximum capacity of  $CO_2$  capture is calculated using equation (52).

$$N_{CC} = \frac{m_{CC} * w_{CaO,OC}}{MM_{CaO}}$$

The utilisation (U) of the OC and the CC are calculated as follows:

$$U_{OC,r-c} = \frac{\int_0^{t_{r-c}} ((\dot{n}_{H_2,in} - \dot{n}_{H_2,out}) + (\dot{n}_{CO,in} - \dot{n}_{CO,out})) dt}{N_{OC}} * 100$$

$$U_{OC,d-o} = \frac{\int_0^{t_{d-o}} \dot{n}_{CO,out} dt}{N_{OC}} * 100$$

$$U_{CC,r-c} = \frac{\int_0^{t_{r-c}} ((\dot{n}_{CO_2,in} - \dot{n}_{CO_2,out}) + (\dot{n}_{CO,in} - \dot{n}_{CO,out})) dt}{N_{CC}} * 100$$

$$U_{CC,d-o} = \frac{\int_0^{t_{d-o}} (\dot{n}_{CO_2,out} + \dot{n}_{CO,out}) dt}{N_{CC}} * 100$$

Fuel utilisation (FU) and carbon recovery (CR) during the reduction-carbonation half-cycle are defined as follows:

$$FU = \frac{\int_0^{t_{r-c}} ((\dot{n}_{H_2,in} - \dot{n}_{H_2,out}) + (\dot{n}_{CO,in} - \dot{n}_{CO,out})) dt}{\int_0^{t_{r-c}} (\dot{n}_{H_2,in} + \dot{n}_{CO,in}) dt} * 100 \quad (57)$$

$$CR = \frac{\int_0^{t_{r-c}} ((\dot{n}_{CO_2,in} - \dot{n}_{CO_2,out}) + (\dot{n}_{CO,in} - \dot{n}_{CO,out})) dt}{\int_0^{t_{r-c}} (\dot{n}_{CO_2,in} + \dot{n}_{CO,in}) dt} * 100 \quad (58)$$

The instantaneous and averaged CO space time yield (STY) during the decarbonation-oxidation half-cycle are calculated using equations (60) and (61), respectively. STY is calculated on the basis of mass of Fe. The mass of Fe is calculated using the relation in equation (59).

$$M_{Fe} = \frac{m_{OC} * w_{Fe_2O_3,OC}}{1000 * MM_{Fe_2O_3}} * 2 * MM_{Fe} \quad (59)$$

$$STY_{CO,inst} = \frac{\dot{n}_{CO,out}}{M_{Fe}} \quad (60)$$

$$STY_{CO,avg} = \frac{\int_0^{t_{d-o}} \dot{n}_{CO,out} dt}{M_{Fe} * t_{d-o}} \quad (61)$$

The carbon balance (CB) and oxygen balance (OB) of the experiments (overall experiment for isothermal operation and each cycle for temperature-programmed CO production) are calculated using equations (62) and (63).

$$CB = \frac{\int_0^{t_{total}} ((\dot{n}_{CO_2,in} - \dot{n}_{CO_2,out}) + (\dot{n}_{CO,in} - \dot{n}_{CO,out})) dt}{\int_0^{t_{total}} (\dot{n}_{CO_2,in} + \dot{n}_{CO,in}) dt} * 100 \quad (62)$$

$$OB = \frac{\int_0^{t_{r-c}} (2 * \dot{n}_{CO_2,in} + \dot{n}_{CO,in}) dt - \int_0^{t_{d-o}} (2 * \dot{n}_{CO_2,out} + \dot{n}_{CO,out}) dt}{\int_0^{t_{r-c}} (2 * \dot{n}_{CO_2,in} + \dot{n}_{CO,in}) dt} * 100 \quad (63)$$

All the proof-of-concept experimental results were reproduced in at least 3 independent runs with the oxygen and carbon balances deviating less than 7 mol% and 5 mol%.



## 5.4 Results and discussion

### 5.4.1 Characterisation of materials

The BET specific surface area and pore volume of the OC displayed in Table 15 were comparable to previously reported values for the material synthesised using the same technique [51, 53]. The proposed process relies on both the bulk phase and available surface of the employed materials. Previous studies established that cyclic processes at high temperatures cause a rapid decrease in specific surface area and pore volume with increasing number of cycles entailing decreased reactivity of the solids due to sintering [53, 116, 124, 125]. The application of sintering resistant supports such as  $\text{MgAl}_2\text{O}_4$  and  $\text{CeO}_2$  for the OC [53] and CC [126] hinders this phenomenon. The isotherms of the OC and the CC are displayed in Figure 34 and Figure 35.

Table 15: Textural properties of the as prepared materials from nitrogen sorption measurements at 77 K.

	Oxygen carrier	CO <sub>2</sub> carrier
BET surface area [ $\text{m}^2/\text{g}$ ]	$41.5 \pm 0.3$	$6.3 \pm 0.3$
Pore volume [ $10^{-9} \text{m}^3/\text{g}$ ]	$258 \pm 0.7$	$17.5 \pm 0.1$
BJH desorption pore diameter [nm]	$22.5 \pm 0.2$	$32.7 \pm 5.4$
Particle size [nm]	$33 \pm 0.3$	$237 \pm 12$

Based on the IUPAC classification [62], the oxygen carrier shows characteristics of a Type IV(a) isotherm with an H2(b) type hysteresis (Figure 34), indicating mesoporosity with a wide mesopore size distribution. The isotherm of the CO<sub>2</sub> carrier resembles a Type II isotherm (Figure 35) with evidence of macroporosity and negligible mesoporosity.

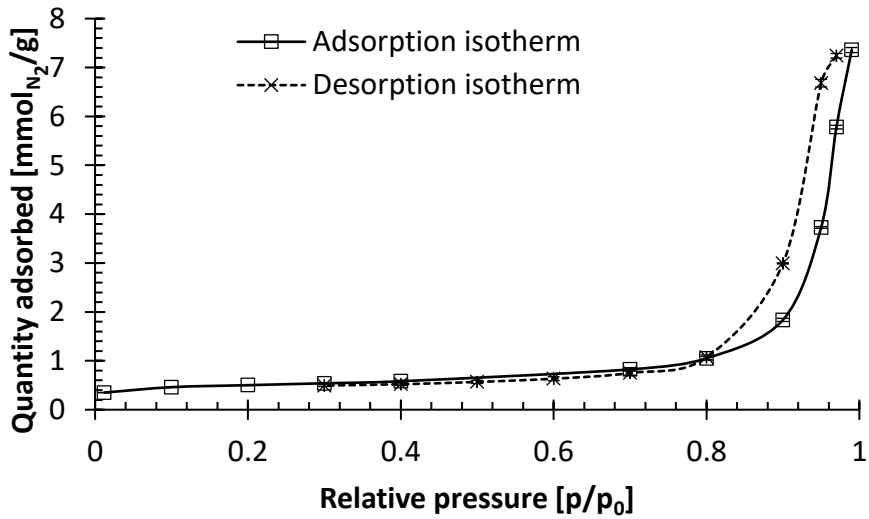


Figure 34: Nitrogen sorption isotherm of the oxygen carrier at 77 K.  $p_0$  on the x-axis represents atmospheric pressure and  $p$  the pressure during the measurement. All 69 measured points were interpolated to provide 22 common points at regular pressure intervals for the assessment of the standard deviation depicted by the error bars.

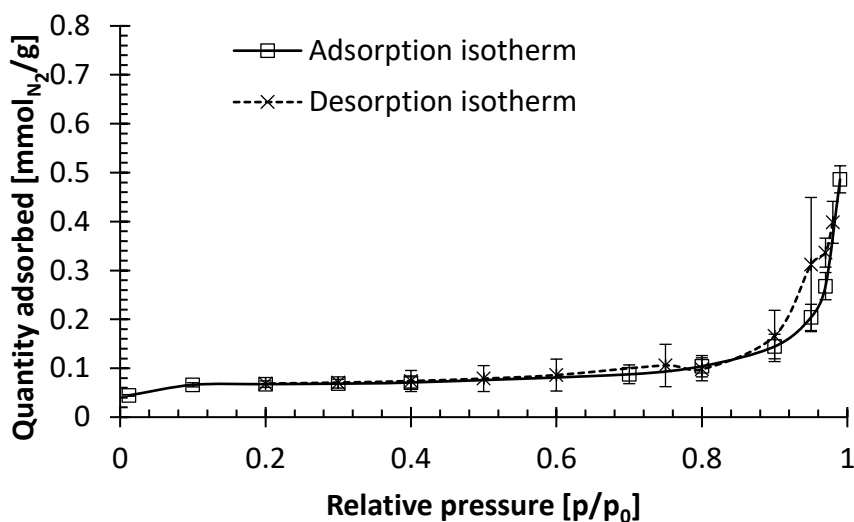


Figure 35: Nitrogen sorption isotherm of the CO<sub>2</sub> carrier at 77 K.  $p_0$  on the x-axis represents atmospheric pressure and  $p$  the pressure during the measurement. All 69 measured points were interpolated to provide 22 common points at regular pressure intervals for the assessment of the standard deviation depicted by the error bars.

The elemental composition of the OC and CC displayed in Table 16 match with the expected composition from the syntheses of the materials. It is important to note that the EDX measurements indicate the superficial composition of the materials up to a micrometre deep into the material surface. To estimate the bulk phase properties of the materials, XRD measurements were performed on the OC and CC. These measurements were further analysed by Rietveld refinement to quantify the phase compositions and estimate the crystallite size of the different phases present in the materials.

Table 16: Elemental composition obtained by energy dispersive x-ray spectroscopy (EDX) expressed in mass percentage. The error indicates the standard deviation based on four measurements.

Element	Oxygen carrier		CO <sub>2</sub> carrier	
	Measured	Expected	Measured	Expected
Fe	35.9 ± 2.2	35.0	-	-
Mg	6.5 ± 0.4	8.5	-	-
Al	17.5 ± 1.6	19.0	-	-
Ca	-	-	40.4 ± 8.7	59.1
Ce	-	-	14.4 ± 6.8	14.1
O	40.1 ± 3.4	37.5	45.2 ± 15.4	26.8

X-ray diffractograms of the calcined OC and the CC displayed in Figure 36 (a) and (b) confirmed the presence of mixed Fe-Mg-Al-O phases in the OC and of CaCO<sub>3</sub> and Ca(OH)<sub>2</sub> in the CC. The Rietveld refinement of the different phases is displayed in Figure C1 and Figure C2 for the OC and the CC with further details of the refinement displayed in Table C4. The material properties obtained from the Rietveld refinement of the XRD data (Figure 36 (b)) corroborate the estimated composition from Rietveld refinement and EDX analysis for the CC (Table 16). The average crystallite size from Rietveld refinement of XRD data of the OC and the CC (Figure 36) also corroborated the average particle size estimated by N<sub>2</sub> sorption measurements (Table 15). For the OC, the application of Rietveld refinement on the XRD data showed that the masses of all elements were underestimated

compared to those from EDX analysis. It is likely that a significant portion of the iron in the OC formed amorphous phase(s), defect rich phase(s), or mixed Fe-Mg-Al-O phase(s) with a very small crystallite size ( $< 2$  nm) that cannot be detected with X-ray diffraction. Small crystallite sizes are unlikely due to exposure of the material to high temperature (which typically accelerates sintering) but amorphousness was also proposed in other studies [127, 128]. By comparing the phase quantification estimated by XRD Rietveld refinement and the expected composition, the missing (possibly amorphous or defect-rich) phase would contain 85 mass% Fe, 6 mass% Mg, and 9 mass% Al on an oxygen free basis, constituting no less than 30 mass% of the OC. Comparing the background of the refinement with the diffraction peaks, the degree of crystallinity was estimated to be 63 vol%.

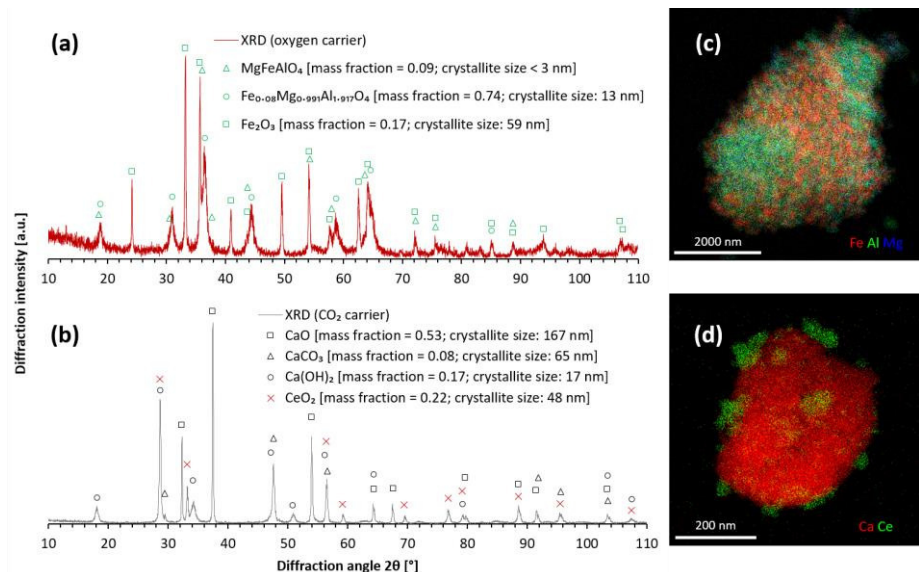


Figure 36: X-ray diffractogram (XRD) of the calcined (a) OC and (b) CC and their STEM-EDX maps in (c) and (d), respectively. Peaks which have an intensity higher than 5% and 1% of the maximum peak intensity are marked and identified on the plot for the calcined OC (a) and CC (b), respectively. The indexes in (a) and (b) display the crystallite sizes and phase fraction estimated by Rietveld refinement.

For the proposed chemical looping process, the amount of exchangeable lattice oxygen atoms in the OC and the CO<sub>2</sub> sorption capacity of the CC must be as large as possible with both solids possessing maximum resistance to material sintering. The importance of these two properties for both materials stems from practical reasons such as lower pressure drop, smaller reactor size, replenishment rate of solids, etc. at an industrial scale. To quantitatively estimate the realistic maximum amount of exchangeable oxygen atoms in the OC and the maximum capacity to capture CO<sub>2</sub> in the CC, temperature-programmed

reduction and oxidation were performed on the OC and temperature-programmed carbonation-decarbonation on the CC.

Figure 37 (a) displays the consumption of oxygen atoms in the OC by reaction with  $H_2$  in the gas phase to form  $H_2O$ . Due to calcination of the synthesised OC in air, the iron in the calcined OC exists in the form of  $Fe_2O_3$  (confirmed via XRD in Figure 36). The three peaks observed in the TPR are typical for the reduction of  $Fe_2O_3$  and represent the transitions of  $Fe_2O_3$  to  $Fe_3O_4$  ( $687 \pm 2$  K),  $Fe_3O_4$  to  $FeO$  ( $846 \pm 4$  K), and finally, from  $FeO$  to  $Fe$  ( $1075 \pm 10$  K) [129, 130]. After the  $H_2$ -TPR, the fully reduced OC was oxidised by  $CO_2$  to quantify the amount of oxygen atoms that could be replenished in the OC while producing CO (Figure 37 (b)). The single peak at  $752 \pm 7$  K is known to be representative of the oxidation of  $Fe$  to  $Fe_3O_4$  and is further corroborated by the cumulative oxygen consumed during the  $CO_2$ -TPO and the ex-situ XRD of the material after the  $CO_2$ -TPO (Figure C3) [129, 130]. It is also known that  $FeO$  is unstable below 850 K which causes direct oxidation of  $Fe$  to  $Fe_3O_4$  by  $CO_2$  below this temperature [125]. Figure 37 c displays the consumption of oxygen atoms in the OC, that were previously replenished by  $CO_2$ , via  $H_2$ -TPR. The first peak of the transition from  $Fe_2O_3$  to  $Fe_3O_4$  seen in Figure 37 a does not appear in Figure 37 c because of (thermodynamically) unfavourable oxidation of  $Fe_3O_4$  to  $Fe_2O_3$  by  $CO_2$  at 1173 K (or lower temperatures) and atmospheric pressure. The second peak for the transition from  $Fe_3O_4$  to  $FeO$  observed in Figure 37 c was possibly shifted to higher temperatures

because of sintering caused by prior exposure to temperatures of up to 1173 K. Based on the CO<sub>2</sub>-TPO and the subsequent H<sub>2</sub>-TPR for the Fe to Fe<sub>3</sub>O<sub>4</sub> transitions, the amount of exchangeable oxygen atoms (oxygen storage capacity) in the OC was estimated to be  $6.4 \pm 1.0$  mmol/g<sub>OC</sub>. Based on the EDX measurements, if all Fe atoms were available for providing lattice oxygen atoms representing redox transitions between Fe to Fe<sub>3</sub>O<sub>4</sub> transitions, the oxygen storage capacity of the OC would be  $8.6 \pm 0.5$  mmol/g<sub>OC</sub>. Thus, not all the Fe atoms added during the synthesis of the OC were found to be available for providing lattice oxygen atoms associated with FeO<sub>x</sub> (x = 0.914 to 1.5) for redox reactions. This could possibly be due to the formation of a phase with Al and/or Mg that is difficult to reduce in the tested conditions.

Figure 37 d displays the capture of CO<sub>2</sub> from the gas phase by the CC and the subsequent release of the captured CO<sub>2</sub> at increasing temperatures. The change from capture of CO<sub>2</sub> to its release from the carrier occurred at 1091 K. This is in agreement with thermodynamic data of CaO/CaCO<sub>3</sub> which estimate that the temperature to switch from carbonation to decarbonation in the given conditions (partial pressure of CO<sub>2</sub>  $\approx$  25 – 27 kPa) is between 1078 - 1082 K. Based on the carbonation and decarbonation observed during the TPCD, the amount of CO<sub>2</sub> captured was estimated to be 10.3 mmol<sub>CO2</sub>/g<sub>CC</sub>. The theoretical capacity based on the composition estimated by EDX was  $13.8 \pm 0.7$  mmol<sub>CO2</sub>/g<sub>CC</sub> and from Rietveld refinement 13.6 mmol<sub>CO2</sub>/g<sub>CC</sub>. The discrepancy might be caused by the increasing solid state diffusion



limitations during the ongoing formation of  $\text{CaCO}_3$ . The relatively large (average) crystallite size of CaO from Rietveld refinement of the CC's XRD (Table C4 and Figure 36) and low specific surface area (Table 15) support the plausibility of this hypothesis, according to which the bulk of large CaO crystallites becomes increasingly inaccessible for the carbonation reaction due to formation of  $\text{CaCO}_3$  at their surfaces leading to lower measured capacities.

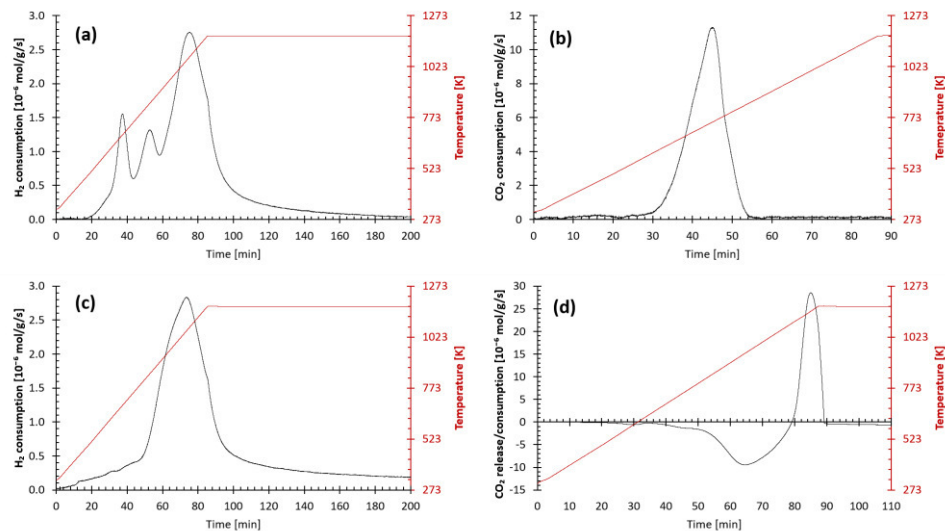


Figure 37: Temperature-programmed reactions (TPRe) with a temperature ramp of 10 K/min up to 1173 K and a total flow rate of  $45 \cdot 10^{-6} \text{ mol/s}$ . (a):  $\text{H}_2$ -TPR under a flow of 5 mol%  $\text{H}_2$  in Ar for the determination of exchangeable oxygen atoms in the calcined OC; (b)  $\text{CO}_2$ -TPO under a flow of 100%  $\text{CO}_2$  for the determination of replenish-able oxygen atoms in the fully reduced OC; (c)  $\text{H}_2$ -TPR under a flow of 5 mol%  $\text{H}_2$  in Ar for the determination of exchangeable oxygen atoms in the OC oxidised by  $\text{CO}_2$ ; (d)  $\text{CO}_2$ -TPCD under a flow of 25%  $\text{CO}_2$  in He for the determination of the total  $\text{CO}_2$  capture and release capacity.

## 5.4.2 Experimental proof of concept

### 5.4.2.1 Isothermal cycling

The isothermal production of CO in the first cycle of the process is depicted in Figure 38 a. In the first 20 to 30 seconds of the process during the reduction-carbonation half-cycle, the  $H_2$  and CO from the synthetic BFG were almost completely oxidised, whereas breakthrough of  $CO_2$ , also present in the synthetic BFG, was observed quasi instantaneously; its amount being determined by the equilibrium partial pressure of  $CO_2$  in the presence of excess CaO. After the first 20 – 30 seconds of this half-cycle, incoming  $H_2$  from the synthetic BFG was no longer fully oxidised. On the other hand, the outlet CO flow rate, representing CO that was not oxidised, gradually increased towards the end of the half-cycle to equal the inlet flow rate of CO from synthetic BFG. The reduction-carbonation half-cycle ended after 180 s and the inlet gas was switched to pure Ar.

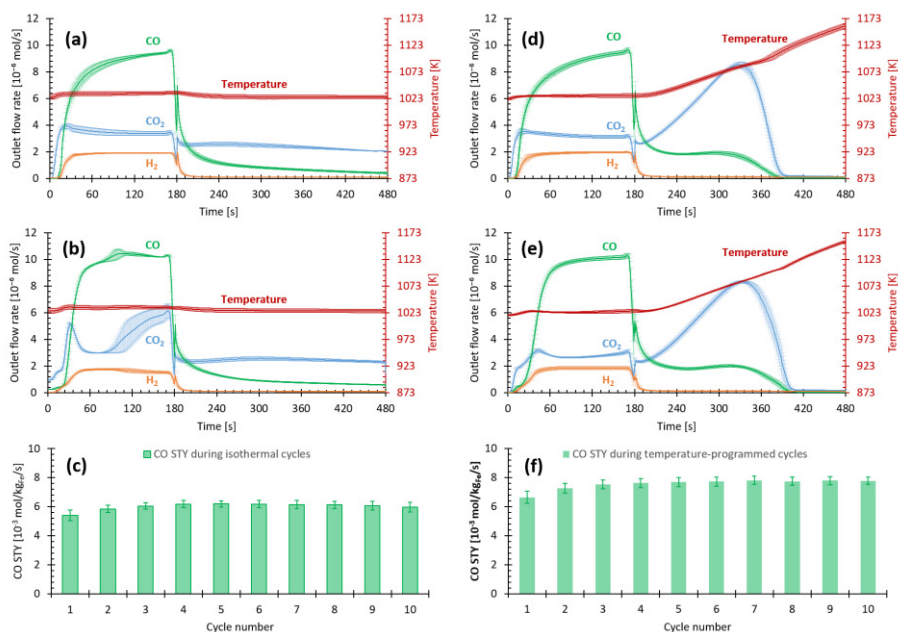


Figure 38: Outlet flow rates and temperature versus time during the 1<sup>st</sup> (top; (a) for isothermal cycles and (d) for temperature-programmed cycles) and the 10<sup>th</sup> (middle; (b) for isothermal and (e) for temperature-programmed cycles) cycles. Average CO STY over 10 cycles during the decarbonation-oxidation half-cycles (bottom; (c) for isothermal cycles and (f) for temperature-programmed cycles). Inlet gas flow rate during reduction-carbonation:  $41 \cdot 10^{-6}$  mol/s ( $10 \cdot 10^{-6}$  mol/s CO;  $10 \cdot 10^{-6}$  mol/s CO<sub>2</sub>;  $2 \cdot 10^{-6}$  mol/s H<sub>2</sub>; rest: Ar and He). Inlet gas flow rate during decarbonation-oxidation:  $41 \cdot 10^{-6}$  mol/s Ar. Error bars indicate the standard deviation from 3 independent experiments.

During the switch to Ar, a fluctuation was consistently observed in all experiments which could be indicative of sudden pressure and flow rate changes upon switching the gas flow despite the application of a back pressure regulator. A sharp drop in CO and H<sub>2</sub> was observed in the first few seconds of this half-cycle, representing the CO and H<sub>2</sub>

from the previous half-cycle being pushed out of the reactor. Unlike the  $\text{H}_2$  flow rate (which dropped to zero), the  $\text{CO}$  and  $\text{CO}_2$  flow rate reached a constant throughout the decarbonation-oxidation half-cycle corresponding to the intended reactions of decarbonation of  $\text{CaCO}_3$  and re-oxidation of reduced  $\text{FeO}_x$  ( $x \leq 1.33$ ). This steady level of  $\text{CO}_2$  and  $\text{CO}$  at 480 s indicated that longer feeding of Ar was needed to fully regenerate  $\text{CaO}$  and  $\text{FeO}_x$ .

In order to further assess the consequences of this incomplete regeneration, 10 consecutive cycles were executed. Figure 38 (b) shows the outlet flow rates during the 10<sup>th</sup> cycle. The accumulation of  $\text{CaCO}_3$  and thus, the corresponding depletion of  $\text{CaO}$  available for  $\text{CO}_2$  capture, resulted in an earlier breakthrough of  $\text{CO}_2$  and lower carbon capture in the reduction-carbonation half-cycle, as indicated by the higher flow rates compared to the 1<sup>st</sup> cycle. The slightly but significantly smaller flow rate of  $\text{H}_2$  when compared to the inlet flow rate as well as the slightly higher flow rate of  $\text{CO}$  compared to the inlet flow rates are likely due to the rWGS that is favoured at high temperatures and can be catalysed by  $\text{FeO}_x$  species that form in the reactor bed during the reduction-carbonation half-cycle [131]. An exhaustive explanation on why this rWGS is less important, if it occurs at all, during the first cycle is given based on an analysis of the thermodynamic driving forces at play and is presented in the Appendix C.

#### 5.4.2.2 Temperature-programmed cycling

In order to increase the driving force for decarbonation-oxidation, a linear temperature program was implemented during the decarbonation-oxidation step of the cycle. Figure 38 (d) shows that for the 1<sup>st</sup> cycle of the temperature-programmed implementation, the outlet flow rates during the reduction-carbonation half-cycle resemble those for the isothermal CO production in Figure 38 (a), as both were operated in similar conditions of pressure and temperature (120 kPa and 1023 K) using solids that were exposed to exactly the same conditions before the cycle began. During the decarbonation-oxidation, an increased thermodynamic driving force was exerted by increasing the temperature rapidly at 25 K/min. This resulted in complete decarbonation of the CC and maximal regeneration of the OC. The increase in CO<sub>2</sub> production rate with temperature proved that the increasing thermodynamic driving force was effective. Despite the increasing thermodynamic driving force and increasing temperature which favour faster kinetics, the plateau in the production rate of CO suggests that the oxidation process may be limited by processes that are less dependent on temperature than the chemical reaction of oxidation itself (for example, bulk diffusion).

Figure 38 (e) displays the outlet flow rates of different components in the 10<sup>th</sup> cycle of temperature-programmed cycling which resemble those in the 1<sup>st</sup> cycle displayed in Figure 38 (d). This can be attributed to the nearly complete regeneration of the CC and the OC. The reduction-carbonation half-cycle in Figure 38 (e) indicates a slightly

higher CO outlet flow rate and a slightly lower CO<sub>2</sub> flow rate suggesting the acting influence of the rWGS. Figure C17 displays that the reaction quotient for the rWGS was, on average, further away from its equilibrium value but the evidence is ambiguous due to the variations observed in independent experiments (represented by the error bars). Thus, it is not clear if the redox conditions of the proposed chemical looping process may cause the development of active sites that catalyse the rWGS in the temperature-programmed implementation. It should be noted that since reduction of FeO<sub>x</sub> species by CO has more favourable thermodynamics (see  $\Delta G^0$  values in Table 12) than by H<sub>2</sub>, catalysing the rWGS in-situ during the reduction-carbonation half-cycle may be potentially beneficial for the process.

CO space time yields displayed in Figure 39 indicate that, upon repeated cycling, the production of CO in temperature-programmed conditions increased and continued for a longer duration (see cycle 1 and cycle 10 results). This could be caused by better reduction of the OC upon repeated cycling due to increased surface area from the formation of pores/cracks and/or enrichment of the surface with Fe cations [132, 133]. It was found that the CO produced in the temperature-programmed process,  $0.056 \pm 0.002 \text{ mol}_{\text{CO}}/\text{mol}_{\text{BFG}}$ , was consistently 20 to 25% higher than in the isothermal process. From the above discussion, it is concluded that the temperature-programmed process is more effective than the isothermal operation mode due to nearly complete regeneration of the material and higher CO yields.

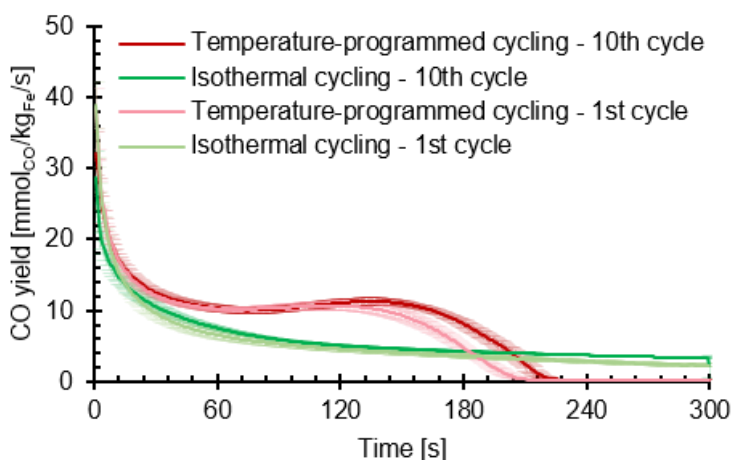


Figure 39: Instantaneous CO space time yield during the decarbonation-oxidation half-cycle for the isothermal and temperature-programmed CO production routes for the 1<sup>st</sup> and 10<sup>th</sup> cycles. Error bars represent standard deviation obtained from 3 independent experiments.

### 5.4.3 Assessment of process performance indicators and cycled materials

#### 5.4.3.1 Fuel utilisation

Fuel utilisation, representative of the utilisation of H<sub>2</sub> and CO in the synthetic BFG (see equation (57)), during temperature-programmed CO production and the isothermal implementation mode was relatively low at values between 20 – 25 mol% and similar for both processes in the 1<sup>st</sup> cycle (Figure 40). As can be seen in Figure 38, a reduction-carbonation half-cycle time of less than 25 seconds could increase the fuel utilisation to values > 65 mol% (Table 17). Based on the experimental results (Figure 41 and Figure 42), shorter cycle-times may, apart from higher fuel utilisation, also result in potentially richer



CO streams as in super-dry reforming of methane but this would come at the cost of lower utilisation of the OC and the CC [117]. On average, the fuel utilisation in the 10<sup>th</sup> cycle was around 13% lower for the isothermal CO production process than that in the temperature-programmed process. As the number of cycles increased, the fuel utilisation during the isothermal process decreased progressively, but marginally (Figure 40).

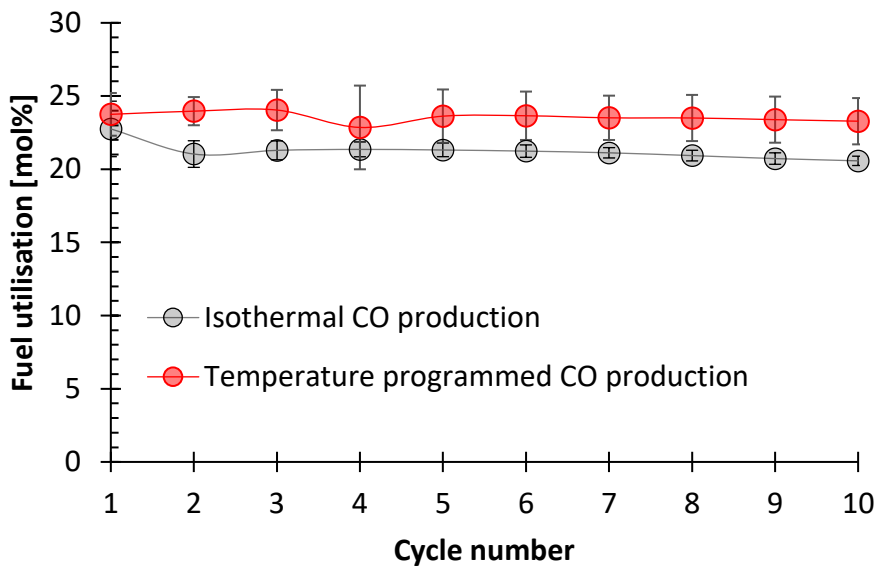


Figure 40: Utilisation of fuel (CO and H<sub>2</sub>) in the reduction and carbonation half-cycle for the isothermal (grey circles) and temperature-programmed (red circles) CO production.

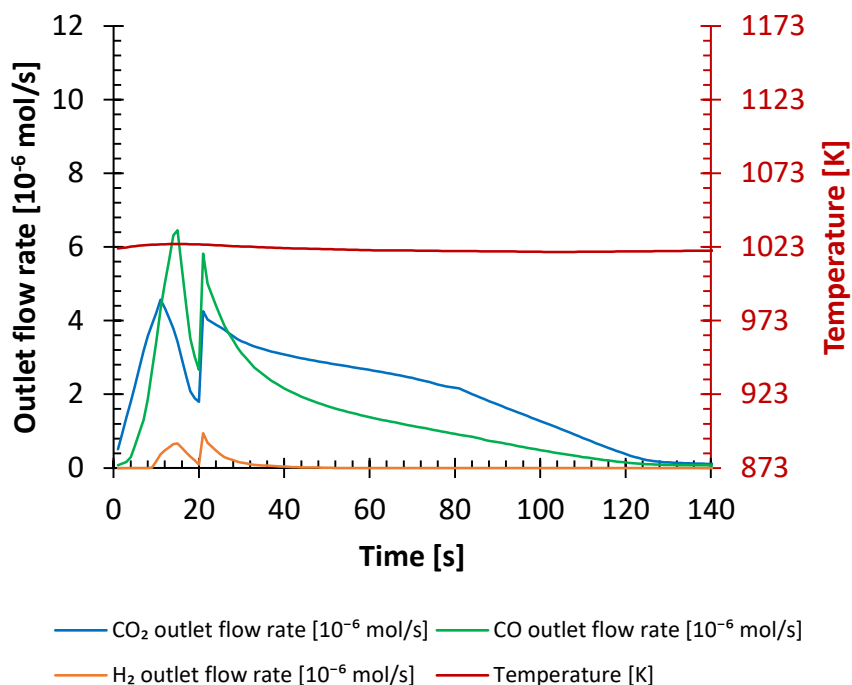


Figure 41: Experimental results of the 10<sup>th</sup> cycle of isothermal CO production with shortened reduction-carbonation half-cycle time (20 seconds). Inlet gas flow rate during reduction-carbonation:  $41 \cdot 10^{-6}$  mol/s ( $10 \cdot 10^{-6}$  mol/s CO;  $10 \cdot 10^{-6}$  mol/s  $\text{CO}_2$ ;  $2 \cdot 10^{-6}$  mol/s  $\text{H}_2$ ; rest: Ar and He). Inlet gas flow rate during decarbonation-oxidation:  $41 \cdot 10^{-6}$  mol/s Ar.

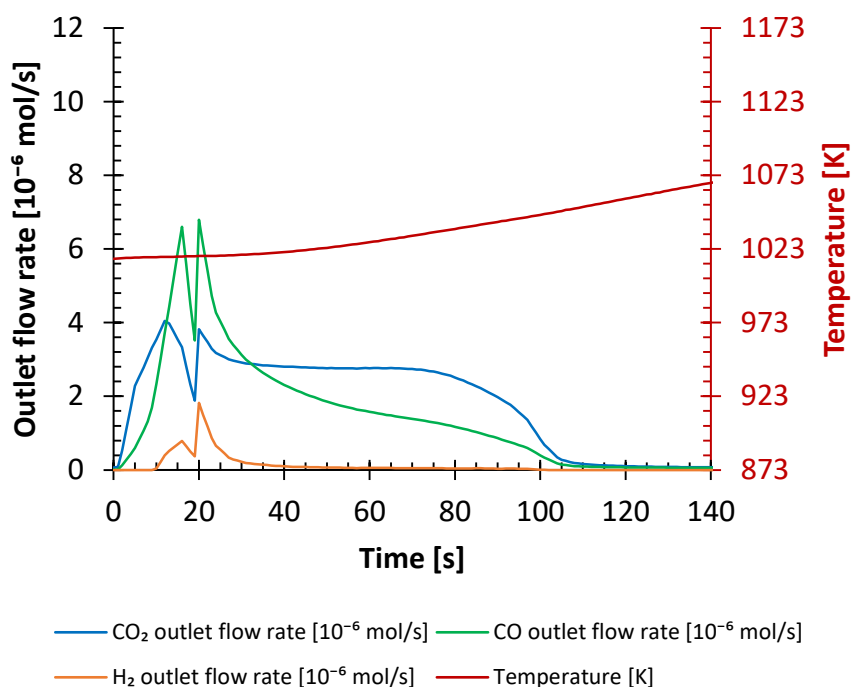


Figure 42: Experimental results of the 10<sup>th</sup> cycle of temperature-programmed CO production with shortened reduction-carbonation half-cycle time (20 seconds). Inlet gas flow rate during reduction-carbonation:  $41 \cdot 10^{-6}$  mol/s ( $10 \cdot 10^{-6}$  mol/s CO;  $10 \cdot 10^{-6}$  mol/s  $\text{CO}_2$ ;  $2 \cdot 10^{-6}$  mol/s  $\text{H}_2$ ; rest: Ar and He). Inlet gas flow rate during decarbonation-oxidation:  $41 \cdot 10^{-6}$  mol/s Ar.

#### 5.4.3.2 Carbon recovery

Carbon recovery (see equation (58)) is representative of the fraction of carbon content in the BFG (CO and  $\text{CO}_2$ ) that is transferred to the product stream of the process. For temperature-programmed production of CO, an almost constant carbon recovery of  $48 \pm 1$  mol% from the synthetic BFG was maintained over 10 cycles (Figure 43). Carbon recovery in the temperature-programmed implementation

mode was found to be 23 mol% higher than that of the isothermal CO production (Figure 43). The carbon recovery is dependent on the capture of CO<sub>2</sub> from the BFG by the CC as well as on the oxidation of CO in the BFG by the OC. Because of the incomplete decarbonation of the CC in the isothermal production of CO, the capture of CO<sub>2</sub> from the BFG was diminished. CO oxidation by the OC was low (20 – 30 mol%) for isothermal and temperature-programmed CO production because of the reduction-carbonation half-cycles being longer than 30 seconds.

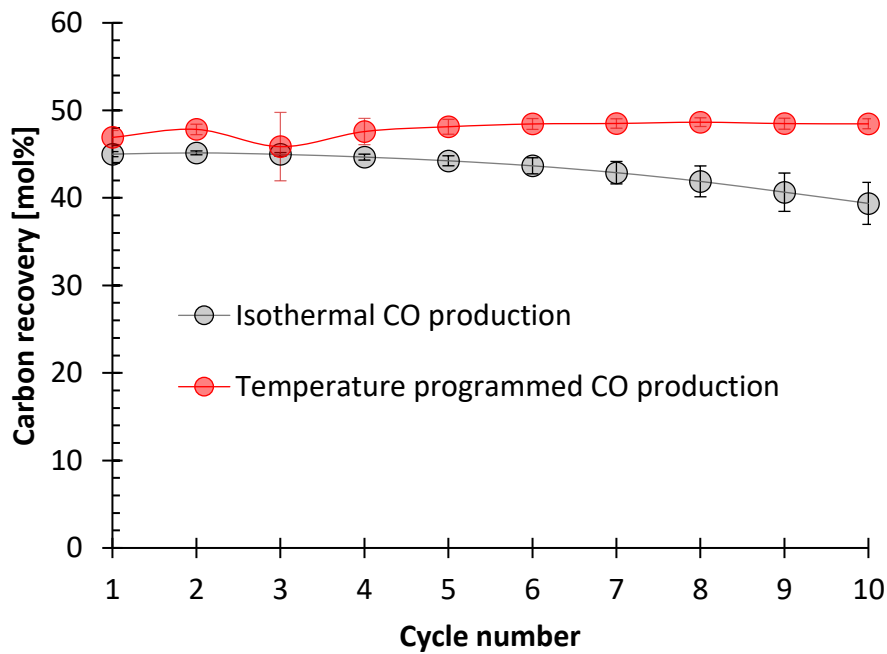


Figure 43: Carbon recovery over 10 cycles in isothermal (grey filled circles) and temperature-programmed (red filled circles) CO production.

#### 5.4.3.3 Utilisation of the oxygen carrier

During the temperature-programmed production of CO, the average material utilisation was almost constant at  $11 \pm 1$  mol% (Figure 44). The materials used for temperature-programmed production of CO were analysed to estimate the amount of OC left unutilised after 10 cycles by oxidation with 70% CO<sub>2</sub>/Ar. It was found that 4 mol% of the OC was still reduced (left un-oxidised) after the end of the 10<sup>th</sup> decarbonation-oxidation half-cycle. As discussed earlier, the oxidation rate in decarbonation-oxidation half-cycle appeared to be limited by processes less sensitive to temperature than chemical reaction. Thus, some of the OC was left unutilised despite full decarbonation of CaCO<sub>3</sub>. From the analysis and Rietveld refinement of ex-situ XRD of the materials over the temperature-programmed cycles (1<sup>st</sup>, 5<sup>th</sup>, and 10<sup>th</sup> in Figure C8, Figure C9, and Figure C4, respectively with quantified details in Table C4), it was confirmed that, from the 5<sup>th</sup> cycle onwards, the OC retains identical crystal structures after decarbonation-oxidation during the temperature-programmed cycles and Fe<sub>3</sub>O<sub>4</sub> is formed after each cycle is completed. This suggests stable redox transitions of the OC after, at most, 5 cycles, corresponding with the stable experimental performance to produce CO.

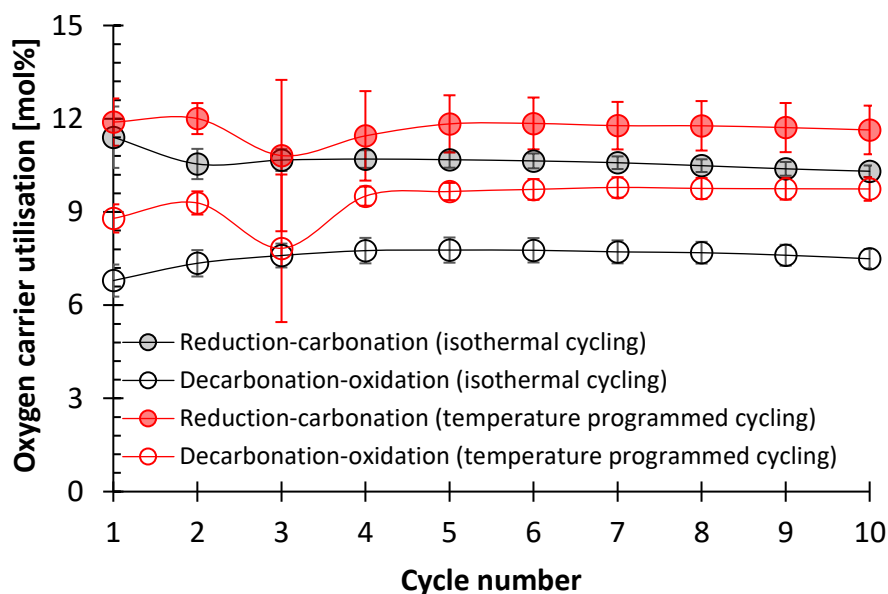


Figure 44: Utilisation of the oxygen carrier for isothermal (grey) and temperature-programmed (red) processes for CO production. Open and filled circles indicate decarbonation-oxidation and reduction-carbonation half-cycles.

The loss of capacity in the isothermal CO production route was not unexpected because not all of the OC was regenerated during each cycle as seen in Figure 38 (a). In an independent experiment, the materials, after 10 cycles of isothermal CO production, were heated to 1173 K and a 70% CO<sub>2</sub>/Ar mixture was sent (at  $4.1 \cdot 10^{-5}$  mol/s) over the materials to regenerate all the OC to its highest expected oxidation state i.e. Fe<sub>3</sub>O<sub>4</sub> till no more CO was produced. It was found that 7 mol% of the OC could still be regenerated after 10 isothermal cycles of CO production. In another independent experiment, the materials were analysed by Rietveld refinement of XRD (Figure C7) after 10 cycles of isothermal CO production and compared with XRD of the OC after CO<sub>2</sub>-

TPO of Figure 37 b (results of XRD Rietveld refinement displayed in Figure C3 and Table C4). A 33% decrease in exchangeable O atoms (as in  $\text{Fe}_3\text{O}_4$  and  $\text{Fe}_{0.932}\text{O}$ ) for the cycled materials was confirmed by phase quantification through Rietveld refinement. The reader is referred to Figure C10 to track the evolution of the crystalline phases of the materials during isothermal CO production obtained by ex-situ XRD. Further details of the Rietveld refinement applied on the materials after 1 cycle (Figure C5), 5 cycles (Figure C6), and 10 cycles (Figure C7) are also presented in Table C4. It must be noted that this calculation using XRD data cannot account for oxygen atoms that may be present in amorphous, defect-rich, or very small crystallites of iron oxides ( $< 3 \text{ nm}$ ).

#### 5.4.3.4 Utilisation of the $\text{CO}_2$ carrier

Based on the decarbonation-oxidation half-cycle, the utilisation of the CC in the 10<sup>th</sup> cycle for the temperature-programmed production of CO was 1.5 times higher than that of the isothermal process (Figure 45). For temperature-programmed CO production, utilisation of the CC remained stable for both the reduction-carbonation half-cycle and the decarbonation-oxidation half-cycle with a constant difference between them. In an independent experiment, the materials were analysed after the 10<sup>th</sup> reduction-carbonation half-cycle to confirm the formation of  $\text{CaCO}_3$  by ex-situ XRD (Figure C12). In another independent experiment, the materials after 10 cycles of temperature-programmed CO production were analysed (Figure C4) and compared to the calcined CC (Figure C3 and Table C4). No traces of  $\text{CaCO}_3$  were detected in the XRD

as expected from the temperature-programmed experimental results displayed in Figure 38d wherein  $\text{CaCO}_3$  decomposition was accelerated by the process conditions.

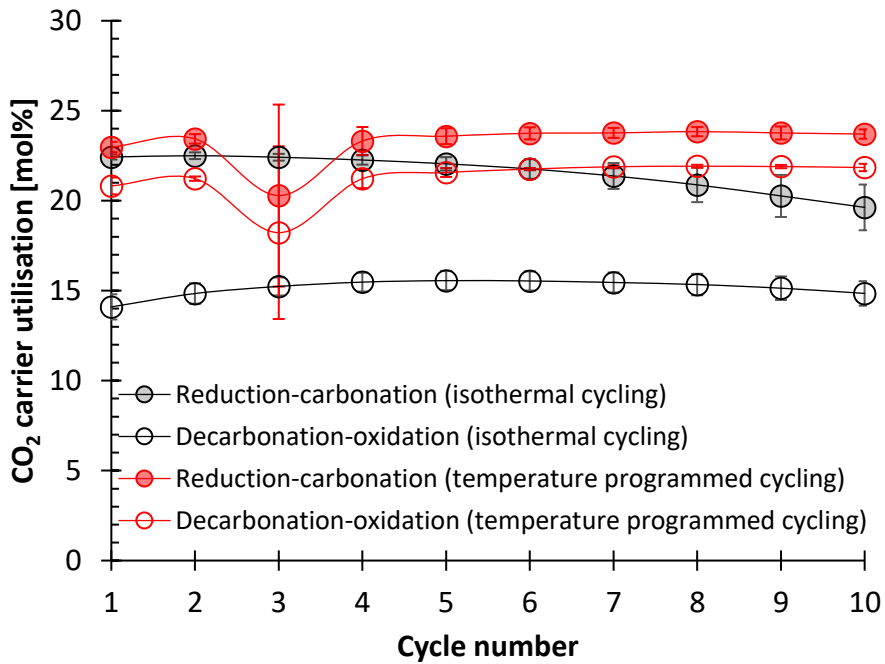


Figure 45: Utilisation of the  $\text{CO}_2$  carrier for isothermal (grey) and temperature-programmed (red) open circles)  $\text{CO}$  production. Open and filled circles indicate decarbonation-oxidation and reduction-carbonation half-cycles.

The stable performance of the CC during the temperature-programmed cycles could be partially attributed to the presence of  $\text{CO}$  during the decarbonation-oxidation half-cycle.  $\text{CaCO}_3$  has a low melting point and is, thus, prone to sintering at temperatures as low as 585 K [100]. Exposure of  $\text{CaCO}_3$  to higher temperature and for longer periods of time is known to strongly influence the deactivation of  $\text{CaO}$ -based



sorbents [134]. Higher CO<sub>2</sub> partial pressure can cause the kinetics of decarbonation to be slower [135] and thus, elongate the time during which CaCO<sub>3</sub> is exposed to temperatures well above the threshold temperature at which its sintering is hastened. The combined chemical looping approach described in this work avoids this effect by lowering the partial pressure of CO<sub>2</sub> due to conversion of the released CO<sub>2</sub> to CO, and thus it has the potential to improve the usable life-time of the CC in the process.

The isothermal CO production showed consistent decrease in the utilisation of the CC and appeared to be limited by the decarbonation-oxidation half-cycle. From the experimental results displayed in Figure 38 (a), not all the CC was decarbonated (based on the continued flow of CO<sub>2</sub> towards the termination of the cycle) leading to accumulation of CaCO<sub>3</sub> in consecutive cycles. In an independent experiment, this was estimated by increasing the temperature to 1173 K (in an Ar flow of  $4.1 \cdot 10^{-5}$  mol/s) at the end of 10 cycles to fully decarbonate the CC. The experimental results (Figure 46) indicate that 39 mol% of the CC's capacity was left unutilised due to the accumulation of CaCO<sub>3</sub>. During the decarbonation experiment, simultaneous flow of CO in the outlet was observed, indicating the presence of oxidisable FeO<sub>x</sub> species. The analysis of the ex-situ XRD of the materials after 10 cycles of isothermal CO production from another independent experiment (Figure C7) revealed that 71 mol% of CaO in the CC existed in its carbonated CaCO<sub>3</sub> form.

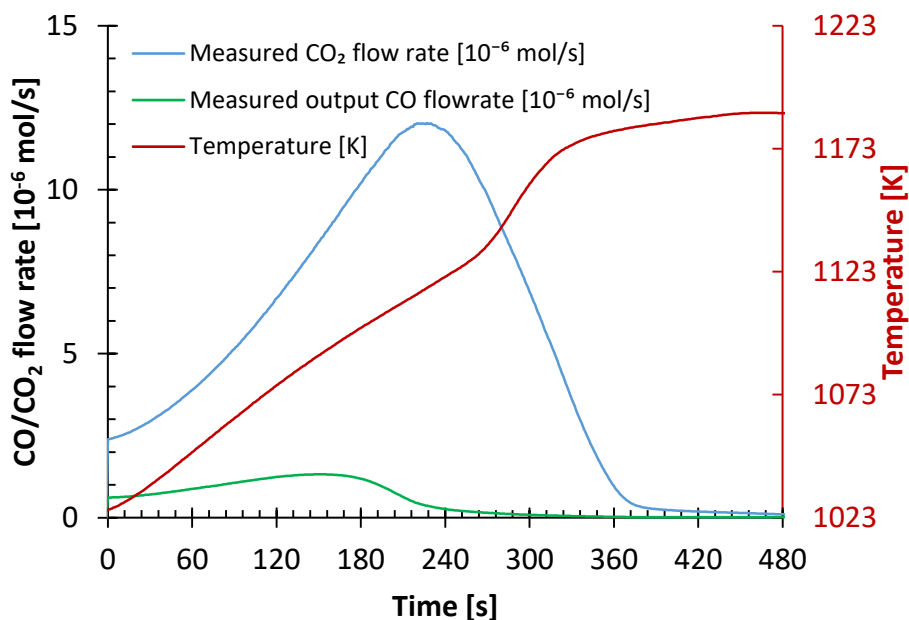


Figure 46: Experimental results of the post-treatment of the oxygen carrier and the CO<sub>2</sub> carrier after 10 cycles of isothermal CO production. Inlet gas flow rate during post-treatment:  $41 \cdot 10^{-6}$  mol/s Ar.

Table 17: Comparison of process parameters (during the 10th cycle) to estimate the influence of varying the reduction-carbonation half-cycle time for reduction-carbonation carried out at 1023 K (Figure 41 and Figure 42).

Operation mode	R-C half-cycle time [s]	Fuel utilisation [mol%]	Carbon recovery [mol%]	CO:CO <sub>2</sub> molar ratio in outlet	Average OC utilisation [mol%]	Average CC utilisation [mol%]	
Isothermal	20	62 – 74	71 – 97	0.64 – 0.87	–	3.7	4.7
Isothermal	180	23 ± 2	39 ± 2	0.43	8.9 ± 0.2	17.2 ± 1	

---

Temperatur e- programme d	20	68 – 77	74 – 97	0.74 1.02	–	4		4.7
Temperatur e- programme d	180	21 ± 3	48 ± 1	0.36 0.02	±	10.7 0.3	±	22.8 0.2

---

#### 5.4.4 Process calculations

As seen in the proof of concept experiments, the proposed concept breaks down the rWGS (equation (44)) into two steps and intensifies the process by the use of the OC and the CC to shift the equilibria. This strategy provides the opportunity to circumvent thermodynamic constraints imposed when the rWGS occurs at a single set of steady state conditions and also avoids energy and cost-intensive unit operations to separate CO, CO<sub>2</sub>, H<sub>2</sub>, N<sub>2</sub>, and H<sub>2</sub>O in the outlet stream of the rWGS.

When all H<sub>2</sub> in the BFG is oxidised in the reduction-carbonation step, a maximum theoretical concentration of approximately 60 mol% CO is achievable in the outlet of the decarbonation-oxidation step. The rest of the outlet gas can be CO<sub>2</sub> or a mixture of CO<sub>2</sub> and a diluent. A higher purity of CO can be achieved from the process by:

1. Adding more reductants (for example, H<sub>2</sub>, CO, CH<sub>4</sub>, etc.) with corresponding additions of OC and, if necessary, CC to the reduction-carbonation step which would, in turn, enable the

reduction of captured  $\text{CO}_2$  to CO in the decarbonation-oxidation step. This may be achieved in the steel mill by using a part of the reductant rich coke oven gas (61 mol%  $\text{H}_2$ , 22 mol%  $\text{CH}_4$ , 4 mol% CO) or basic oxygen furnace gas (54 mol% CO, 3 mol%  $\text{H}_2$ ) with the BFG [58].

2. Further purification of the CO-containing outlet stream from the decarbonation-oxidation step. This can be achieved through a subsequent calcium looping process to remove the remaining  $\text{CO}_2$  at the expense of additional energy.

Reduction-carbonation is favourable at lower temperatures since it is an overall exothermic reaction, mostly due to the strongly exothermic carbonation of CaO. Conversely, higher temperatures favour the endothermic decarbonation-oxidation half-cycle. Despite the contrary requirements for the two half-cycles, the decarbonation-oxidation half-cycle can still proceed at the same temperature as the reduction-carbonation half-cycle by the use of a diluent which drives the decarbonation reaction as per Le Chatelier's principle.

#### 5.4.4.1 Process simulation

Depending on the time scales on which each of the steps occur, chemical looping processes can be applied industrially either by a set of parallel fixed beds to which the programmed conditions are implemented or by circulating the carrier materials between as many reactors as numbers of steps into which the global process has been split. For the sake of illustration and mathematical convenience, the

latter scenario has been considered in what follows. In order to test the effect of varying conditions on the two investigated processes and to estimate the corresponding exergy losses, simulations were carried out using Aspen Plus® V10. An exemplary block diagram for the simulations using a feed of 125000 Nm<sup>3</sup>/h, equivalent to 1 MMta of related CO<sub>2</sub> emissions from the BFG and corresponding to steel production ranging between 0.7 – 1 MMta<sub>steel</sub> [42], is displayed in Figure 47. The order of magnitude of the carrier solids circulation flow rate at steady state conditions is comparable to corresponding solid flow rates in existing industrial processes, for example, that of the solid catalyst in Fluid Catalytic Cracking (FCC) of heavy crude oil fractions [96].

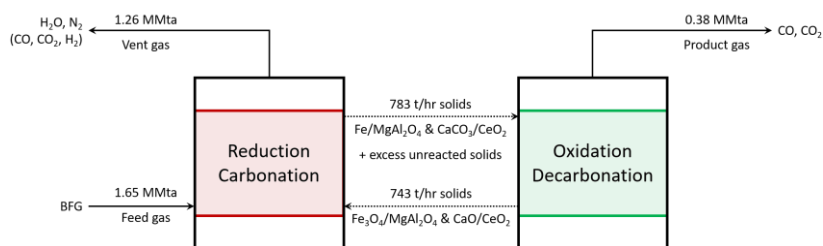


Figure 47: Block flow diagram with mass flows generated from simulation of the temperature-programmed CO production at 1013 K and 121 kPa.

Two “RGibbs” reactors were used to calculate the equilibrium of the 2 half-cycles, the reduction-carbonation and the decarbonation-oxidation half-cycles with solids circulating between them. The RGibbs reactors can be likened to perfectly mixed reactors such as fully fluidised bed reactors. However, they were used as a first

approximation for the fixed bed reactor by restricting the solid phase products to match those found during the experiments.

To simplify the comparative exergy analysis, all outlet streams were cooled and depressurised to 298 K and 101 kPa, i.e. the so called dead state for exergy analysis, by the application of coolers and turbines. Solid separators were used in the process simulation to separate the solids from the gases after being processed in the half-cycles. These solid-gas separators in the process scheme are used only for the sake of the simulation and do not carry an energy penalty.

The inlet gas was sent to the reduction-carbonation half-cycle at 1.6 MMta at 298 K and 101 kPa. The OC, magnetite ( $\text{Fe}_3\text{O}_4$ ) supported on spinel ( $\text{MgAl}_2\text{O}_4$ ), and the CC, quicklime ( $\text{CaO}$ ) supported on ceria ( $\text{CeO}_2$ ) were circulating in excess corresponding to the experimental proof of concept i.e. 2 times more than necessary for fully oxidising the reductants and capturing of  $\text{CO}_2$  in the BFG as well as the  $\text{CO}_2$  formed by oxidation of CO. For the isothermal CO production case, the  $\text{N}_2$  flow was increased such that the CC and OC were fully regenerated. In the temperature-programmed case, a temperature “swing” (instantaneous temperature change) was employed instead of a time-dependent increase in temperature for the sake of simplicity of the simulation. As  $\text{N}_2$  flow is not necessary for the temperature-programmed case because the reaction can occur from the heat supplied, the temperature in the reactor representing the decarbonation-oxidation half-cycle was varied such that full regeneration of CC and OC occurred.

The temperature during the reduction-carbonation half-cycle was varied to quantify the consequences on the exergy of the process, outlet gas composition, carbon recovery, and the fuel utilisation (Figure 48). A decrease in temperature leads to an increase in carbon recovery due to favourable thermodynamics of the carbonation reaction of CaO ( $\Delta G^0 = -35 \text{ kJ/mol}_{\text{CO}_2}$ ;  $p_{\text{CO}_2, \text{eq}} = 1 \text{ kPa}$  at 923 K vs  $\Delta G^0 = -22 \text{ kJ/mol}_{\text{CO}_2}$ ;  $p_{\text{CO}_2, \text{eq}} = 8 \text{ kPa}$  at 1013 K) and the corresponding effect on CO oxidation (removal of  $\text{CO}_2$  enhances CO oxidation as per Le Chatelier's principle). On the other hand, the  $\text{H}_2$  conversion decreases with decreasing reduction-carbonation temperature (Figure 49). As the amount of CO in BFG is much higher than that of  $\text{H}_2$ , the overall fuel efficiency benefits from a lower reduction-carbonation temperature. An increase in  $\text{H}_2$  conversion has the potential to improve the  $\text{CO}_2$  utilisation of the process but as can be seen in Figure 48, the  $\text{CO}:\text{CO}_2$  ratio remains more or less constant at 1.1 up to 953 K and decreases to lower values at higher reduction-carbonation temperatures. If all the  $\text{H}_2$  and CO could be oxidised in the reduction-carbonation half-cycle, the  $\text{CO}:\text{CO}_2$  ratio in the decarbonation-oxidation half-cycle would be 1.5. The BFG has a  $\text{CO}:\text{CO}_2$  ratio of approximately 0.99, thus, an increased  $\text{CO}:\text{CO}_2$  ratio in the outlet stream of the process represents better  $\text{CO}_2$  utilisation in the process through  $\text{H}_2$  oxidation.

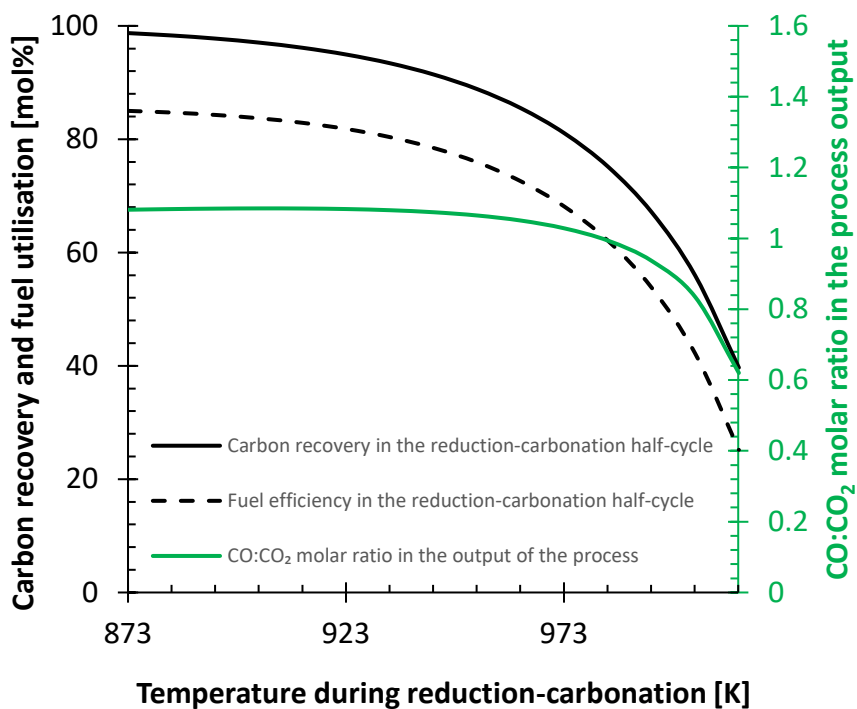


Figure 48: Effect of temperature in the reduction-carbonation half-cycle on the carbon recovery and fuel efficiency of the process with the corresponding influence on the CO:CO<sub>2</sub> ratio of the process (secondary axis).



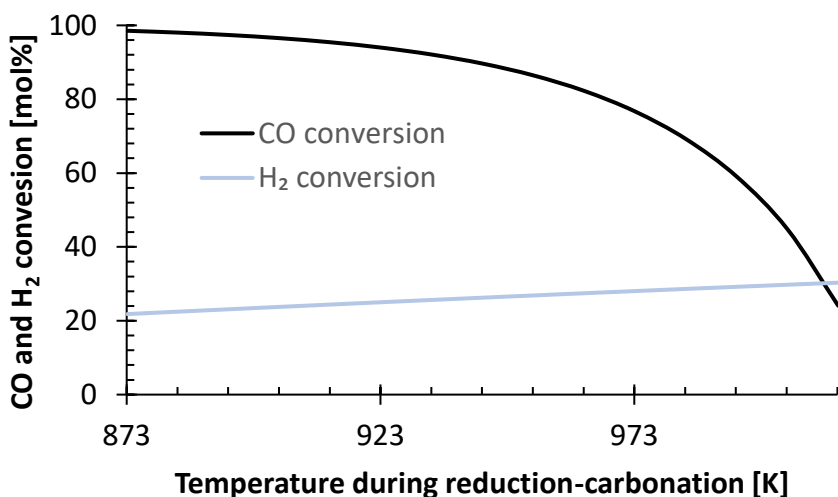


Figure 49: Effect of temperature during the reduction-carbonation half-cycle on the conversion of CO into CO<sub>2</sub> and H<sub>2</sub> into H<sub>2</sub>O.

For the temperature-programmed production of CO, the reduction-carbonation temperature also has an effect on the decarbonation-oxidation temperature, which is ideally the temperature at which no external supply of inert gas is required to drive the decarbonation-oxidation reaction and achieve full regeneration of the materials i.e. complete closure of the two loops. A lower reduction-carbonation temperature leads to higher CO production. The higher CO production helps to decarbonate the CC at lower temperatures because the produced CO acts as a diluent for shifting the equilibrium to further release CO<sub>2</sub>. When both half-cycles are carried out in the same reactor bed, a lower temperature difference between the 2 half-cycles is desirable to avoid thermal stresses in the equipment arising from rapid thermal cycling of the system [89]. A lower temperature difference, on

the other hand, comes at the cost of lower fuel utilisation and lower CO<sub>2</sub> utilisation due to lower H<sub>2</sub> oxidation in the reduction-carbonation half-cycle (Figure 49 and Figure 50).

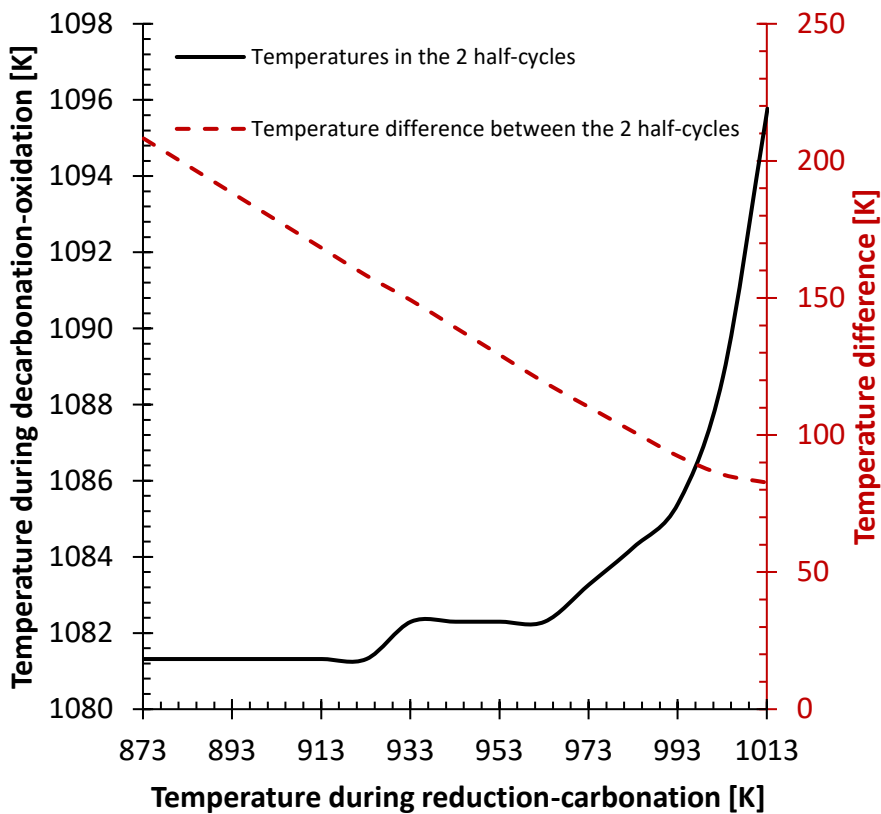


Figure 50: Effect of temperature in the reduction-carbonation half-cycle on the minimum required temperature in the decarbonation-oxidation half-cycle for fully regenerating the materials. The secondary axis depicts the corresponding temperature difference between the two half-cycles.

The results of the process simulation corroborated the experimental data as displayed in Table 18. The positive carbon and

oxygen balance (+4.3 mol% and +5.7 mol%) could have led to the lower CO:CO<sub>2</sub> ratio and higher carbon recovery. The temperature-programmed CO production was used for comparison to the simulation because both the simulation and the temperature-programmed mode of operation ensure complete regeneration of solids. The total heat input in the temperature-programmed CO production was 2.2 MW. This heat requirement of 2.2 MW to drive the temperature-programmed chemical looping process corresponds to 91 kJ/mol of CO<sub>2</sub> converted to CO, which is roughly two times higher than that heat required to convert CO<sub>2</sub> to CO via rWGS. To put this into perspective, the heat of combustion of the inlet BFG in the process simulation was 127 MW.

Table 18: Comparison of simulation results with experimental results for the temperature-programmed CO production over 10 cycles. All values are expressed in mol%. The standard deviation was obtained from 3 independent experiments.

	Fuel utilisation	Carbon recovery	OC utilisation	CC utilisation	CO:CO <sub>2</sub> ratio
Experiment	23.6 ± 1.5	47.9 ± 1	10.5 ± 0.5	22.2 ± 0.7	0.36 ± 0.02
Simulation*	25.2	39.7	12.6	19.8	0.62

\* simulation at 1013 K.

#### 5.4.4.2 Exergy analysis

The Aspen Plus® simulation also allows an exergy analysis of the process to be carried out. The process flow diagram used for this

analysis is displayed in Figure 33 with similar notations as in the Aspen Plus® simulation.

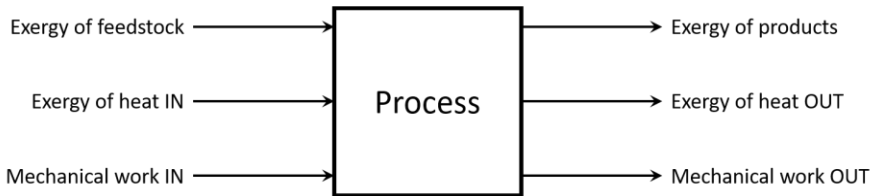


Figure 51: Block flow diagram for the exergy analysis of the process. Exergy of feedstock or products comprises of chemical exergy and the exergy of mixing of different components in the feedstock or products.

As the inlet and outlet streams had a mixed composition, their exergy content consists of two contributions: exergy of mixing (equation (49), a negative contribution for mixtures) and chemical exergy (equation (50)). In order to take into account the degree of dilution of the CO-containing outlet stream by N<sub>2</sub> and CO<sub>2</sub> when comparing different cases, a theoretical separation step to separate all the components in the product gas was also considered (Figure 52).

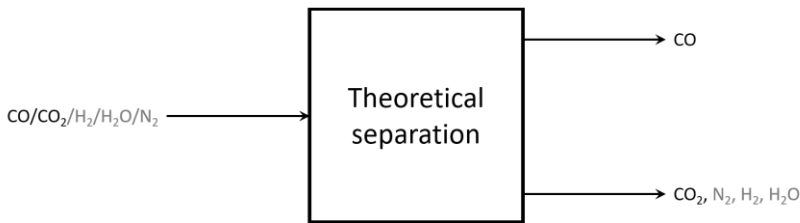


Figure 52: Additional theoretical separation step considered for the exergy analysis to compare the chemical looping processes (isothermal and temperature-programmed). The greyed words represent components not present in the product stream of the temperature-programmed chemical looping process.

A benchmark scenario was considered wherein the BFG is combusted to assess the current best practice. In this benchmark scenario, to minimise exergy losses, a stoichiometric quantity of air was used for nearly complete oxidation of the BFG in an RGibbs reactor operated adiabatically. Thus, the benchmark scenario represents the most exergetically efficient approach to combust the BFG. An additional case for temperature-programmed CO production, called temperature-programmed (large temperature change), was also considered following the simulation results of Figure 48 wherein the reduction-carbonation half-cycle was simulated at 923 K. The experimental results for this case are also displayed in Figure C19 and Figure C20 with more details specified in Table C5.

The results of the exergy analysis displayed in Table 19 show that all the chemical looping processes considered are exergetically more efficient than combustion, the best available technology for using BFG. For the chemical looping processes, major exergy losses occur due to the endothermicity of the decarbonation-oxidation half-cycle. A comparison between isothermal CO production and temperature-programmed CO production shows that the exergy losses due to separation are significant for the isothermal process, thereby resulting in its lower exergy efficiency. The isothermal process requires additional use of N<sub>2</sub> causing increased losses due to heating the N<sub>2</sub> feed and also increased exergy losses of separating the CO from the product mixture, resulting in an overall exergy destruction of 13.3 kJ/mol<sub>CO</sub>

compared with 8.5 kJ/mol<sub>CO</sub> for the temperature-programmed case. These results suggest that the exergy destruction rate for CO production is more than 56% higher than in the temperature-programmed process configuration. For the isothermal case, the exergy losses from heat transfer are lower than that of the temperature-programmed case, but on the other hand, the losses due to separating the CO from the product gas mixture are higher. The theoretical separation step for the isothermal case also yields a pure CO stream and a mixed CO<sub>2</sub>/N<sub>2</sub> stream, whereas in the temperature-programmed case, the theoretical separation step yields a pure CO and a pure CO<sub>2</sub> stream. The theoretical separation considers only the minimum energy required to separate a certain component from a mixture. In reality, the energy required to carry out the separation would be far higher [136]. Thus, the exergy analysis within the scope of this work can provide a fair assessment for comparing chemical looping and combustion but would require significant broadening of its scope for comparing chemical processes involving one or more separation steps. Detailed versions of the exergy analysis are presented in Table C1, Table C2, and Table C3. During the process, some of the CO formed is lost in the vent gas stream (see Figure 47). The CO recovered from this stream by a theoretical separation step is also considered for exergy analysis and the results are displayed as values in brackets in Table 19.

Experimental results and process simulations (Figure 48 and Figure 49) indicate that the process can be further optimised by changing the temperatures of each half-cycle and tuning the duration of the half-cycles. Improved carbon recovery (by 50 – 100%), fuel utilisation (by 190 – 230%), and CO yield (by 250 – 300%) can be achieved by varying the aforementioned parameters but this would come at the cost of under-utilisation of the solids (decrease by 50 – 80%). A trade-off between fuel utilisation and solids utilisation may be estimated by a techno-economic analysis of the process and reactor productivity (Table C6). The materials remained fairly stable over the 10 cycles tested in this study, but more experimentation with increased number of cycles is necessary to estimate the useful life-time of the materials in the process. The outlet gas during the reduction-carbonation half-cycle contains calorific fuels such as H<sub>2</sub> and CO which may be further utilised within the process. In addition, the real BFG contains moisture, trace quantities of sulphur, cyanides, and other impurities [58]. Experimental determination of how these trace impurities can affect the materials used in the proposed process and the process itself is of interest.

Table 19: Comparison of exergy losses and during isothermal, temperature-programmed CO production, and complete combustion.

Case	$T_{r-c}$ [K]	$T_{d-o}$ [K]	Exergy loss of chemical energy [MW]	Exergy loss of heat transfer [MW]	Exergy loss of work [MW]	Exergy loss of mixing and separation [MW]	Total exergy loss [MW]	Exergy loss to produce CO [kJ/molCO]	Exergy loss to convert CO <sub>2</sub> [kJ/molCO <sub>2</sub> ]	Exergetic efficiency [%]
Isothermal	101 3	101 3	-0.69	2.44	-1.64	1.38	1.50 (3.15)	13.3 (8.02)	62.5 (131)	99.2 (98.2)
Mild temperature change	101 3	109 7	-0.69	2.93	-1.21	-0.08	0.96 (2.61)	8.50 (6.64)	40.0 (109)	99.4 (98.5)
Large temperature change	923	109 0	-0.57	7.93	-0.96	-0.96	5.45 (5.70)	14.9 (14.7)	276 (288)	97.8 (97.7)
Combustion*	-	-	111	-98	-2.55	-0.12	10.6	-	-	91.5

\*Adiabatic temperature during combustion: 1622 K.

Values in brackets indicate the performance indicators when the CO in the vent gas stream (see Figure 47) is also recovered by a theoretical separation step.



## 5.5 Conclusions

A proof of concept for producing a CO-enriched stream almost free of H<sub>2</sub> from synthetic blast furnace gas (BFG) by combined chemical looping paves the way for an industrial application of cheap and abundant metal oxides, Fe<sub>3</sub>O<sub>4</sub> and CaO. The applied materials were stable and active for at least 10 cycles despite being exposed to very high temperatures up to 1148 K and alternating redox conditions for the production of CO. The more intensive temperature-programmed CO production yielded  $0.056 \pm 0.002 \text{ mol}_{\text{CO}}/\text{mol}_{\text{BFG}}$ , 23 mol% more CO than at isothermal conditions for identical cycle times. The utilisation of the CO<sub>2</sub> carrier at the end of 10 cycles during the isothermal and temperature-programmed CO production was  $14.8 \pm 0.7$  and  $21.8 \pm 0.2$  mol% and that of the OC was  $7.5 \pm 0.3$  and  $9.7 \pm 0.4$  mol%. Carbon recovery from the synthetic BFG of the steel mill during temperature-programmed CO production was  $48.0 \pm 0.6$  mol%, 23 mol% higher than in isothermal CO production. At the expense of lower solids utilisation, the CO yield in the temperature-programmed mode was increased by 250 – 300% and the carbon recovery by 50 – 100% with the possibility for further optimisation.

Ex-situ XRD analysis of the oxygen carrier, Fe<sub>2</sub>O<sub>3</sub> supported on MgAl<sub>2</sub>O<sub>4</sub>, suggested the existence of complex, defect-rich and/or amorphous Fe-Mg-Al-O phases by comparing the quantified phases with the estimations made by energy dispersive X-ray measurements. Tracking the material's crystal structure over the 10 cycles of

temperature-programmed CO production via ex-situ XRD confirmed stable redox transitions of the oxygen carrier after the 5<sup>th</sup> cycle, corroborating the stable experimental performance of the oxygen carrier for producing CO. The analysis showed that the CO<sub>2</sub> carrier, CaO supported on CeO<sub>2</sub>, is fully decarbonated during the temperature-programmed cycles, whereas, during the isothermal cycles, an increasing accumulation of CaCO<sub>3</sub> was observed, indicating loss of the CO<sub>2</sub> carrier's capacity. No significant changes in the crystallite sizes of the active components in the oxygen carrier and CO<sub>2</sub> carrier were observed for the temperature-programmed mode. Deactivation of the CO<sub>2</sub> carrier was likely inhibited due to the inherent characteristics of the process which ensures lower partial pressure of CO<sub>2</sub> at high temperatures during the decarbonation-oxidation half-cycle due to the concomitant production of CO. Temperature-programmed reactions (reduction, oxidation, carbonation, and decarbonation) on the oxygen carrier and the CO<sub>2</sub> carrier showed that 10 mass% of the oxygen carrier consisted of exchangeable lattice oxygen atoms whereas 45 mass% of the CO<sub>2</sub> carrier was available for capturing CO<sub>2</sub>. The characteristics of the temperature-programmed reactions corroborate results previously reported in literature and theoretical thermodynamic estimations.

Process simulations in Aspen Plus® were corroborated by the experimental data and these simulation results were used for exergy analyses. The temperature-programmed process is exergetically more efficient than the isothermal implementation because, despite larger

exergy losses due to heat transfer, it avoids large  $N_2$  streams that have to be heated, fed, and subsequently separated. Exergy analysis also shows that investigated chemical looping processes are exergetically more efficient than combustion of the BFG, the current best available technique to use the BFG. The proposed technology has the potential to be a viable alternative for BFG utilisation in the steel industry. Rather than combusting the BFG, it provides the possibility of converting up to 20 mol%  $CO_2$  in the BFG to more valuable CO by utilising the  $H_2$  present in the BFG. Further research related to the techno-economics of the process, oxygen and  $CO_2$  carriers with favourable thermodynamic properties, kinetics of the chemical reactions occurring, and modelling of the reactors would benefit the proposed process in bringing it closer to practical implementation.

## Chapter 5

# Auto-thermal CO production from the blast furnace gas

### Abstract:

The iron and steel industry is a carbon-intensive industry and one of the largest industrial sources of CO<sub>2</sub> emissions. In this work, we show how the steel mill gases can be conditioned using three metal oxides to produce a CO/CO<sub>2</sub> stream that can be used for the production of chemicals, thereby preventing the emission of carbon to the atmosphere as CO<sub>2</sub>. Abundant oxides of iron and manganese, characterised by their readiness to capture and release gaseous O<sub>2</sub>, and calcium oxide, characterised by its capacity to capture and release gaseous CO<sub>2</sub> can be deployed in this process. Process analysis indicates that by fully utilising the chemical energy of the carbon-rich blast furnace gas (BFG) of the steel mill, 37% of the associated CO<sub>2</sub> emissions can be eliminated. A techno-economic evaluation shows that further reduction of CO<sub>2</sub> emissions is viable. Preliminary estimations indicate that the costs for processing BFG through the proposed process are 46 EUR<sub>2020</sub>/tonne<sub>BFG</sub>. The sources of revenue are the product CO/CO<sub>2</sub> stream (0.2 tonne<sub>product</sub>/tonne<sub>BFG</sub>) and electricity constituting 85% and 14% of the total revenue with the remaining 1% obtained by the sale of

spent metal oxides used in the process. The technical feasibility of the process was experimentally proven in a fixed bed reactor to produce a CO/CO<sub>2</sub> stream and an H<sub>2</sub>O-rich stream while the metal oxides were periodically regenerated in alternating redox conditions. Thirty executed cycles indicated stable performance of the process. The proposed process concept can be applied to any gas stream containing CO<sub>2</sub> and fuel.

**This chapter was published as**

V. Singh, L.C. Buelens, H. Poelman, M. Saeys, G.B. Marin, V.V. Galvita, Upcycling the carbon emissions from the steel industry into chemicals using three metal oxide loops, *Energy Advances*, (2022).

## 6.1 Introduction

The combined use of CaO and Fe<sub>3</sub>O<sub>4</sub> has already been successfully demonstrated for CO<sub>2</sub> capture and conversion in the previous chapter. The additional use of another metal oxide, Mn<sub>3</sub>O<sub>4</sub>, ensures that the heat necessary for the reverse water-gas shift reaction is optimally provided and there are negligible emissions of unreacted CO and H<sub>2</sub> from the process [137]. Fe<sub>3</sub>O<sub>4</sub> and Mn<sub>3</sub>O<sub>4</sub> can both act as oxygen carriers (OCs), but the thermodynamic equilibrium oxygen partial pressure ( $p_{O_2,eq}$ ) [138] of Mn<sub>3</sub>O<sub>4</sub> while transitioning to MnO is roughly 10 orders of magnitude higher than that of Fe<sub>3</sub>O<sub>4</sub> to FeO and FeO to Fe. A higher  $p_{O_2,eq}$  indicates that near complete oxidation of fuel or reductants is thermodynamically favoured. CaCO<sub>3</sub>, acting as the CO<sub>2</sub> carrier (CC), can be characterised by its thermodynamic equilibrium CO<sub>2</sub> partial pressure ( $p_{CO_2,eq}$ ) while transitioning to CaO. A low  $p_{CO_2,eq}$  indicates favourability towards carbonation i.e. capture of CO<sub>2</sub>. Depending on the selected operating conditions, the OCs and CC can be replaced by other oxides [139-141]. The low costs, natural abundance, and environmentally benign nature of iron, manganese, and calcium oxides make them a preferable choice for industrial application. In Figure 53 and Figure 54, the temperature dependence of  $p_{CO_2,eq}$  and  $p_{O_2,eq}$  of the oxides used for the experimental work is displayed. Depending on the kinetics, time-scales, and optimum conditions of the desired chemical reactions, the process could either be carried out in a series of packed bed reactors, in moving beds, or in interconnected fluidised bed reactors.

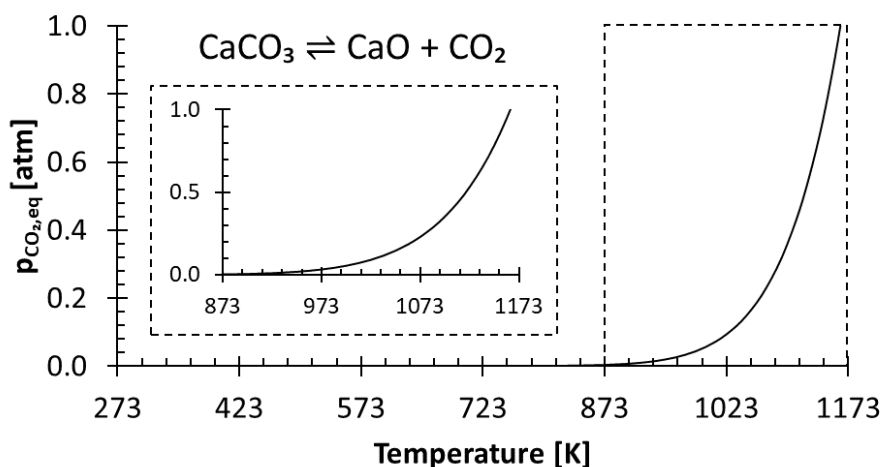


Figure 53: The variation of the thermodynamic equilibrium partial pressure of  $\text{CO}_2$  against temperature at a pressure of 101.3 kPa. Data for  $\text{CaO}$  and  $\text{CO}_2$  from NIST[118] and of  $\text{CaCO}_3$  from FactSage (FactPS database) [119].

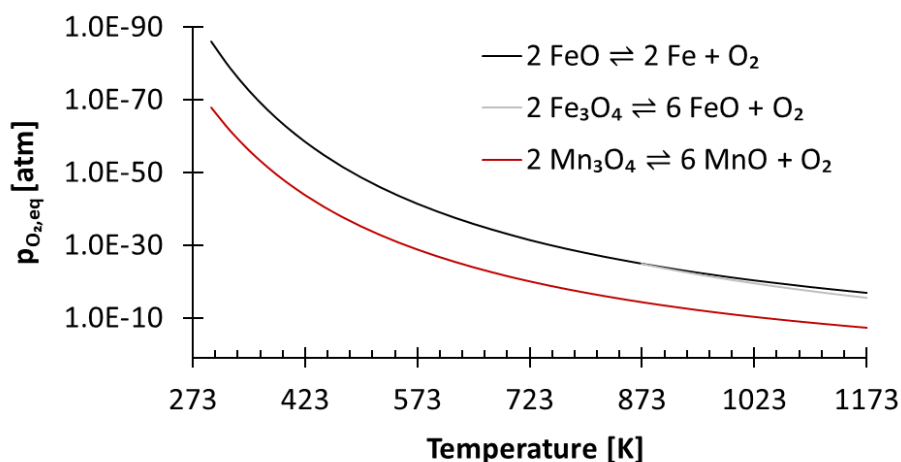


Figure 54: The variation of the thermodynamic equilibrium partial pressure of  $\text{O}_2$  against temperature at a pressure of 101.3 kPa. Note that  $\text{FeO}$  is unstable below 843 K. Data for  $\text{Fe}_3\text{O}_4$ ,  $\text{Fe}$ , and  $\text{O}_2$  from NIST[118] and of  $\text{FeO}$ ,  $\text{Mn}_3\text{O}_4$ , and  $\text{MnO}$  from FactSage (FactPS database) [119].

One of the challenges of deploying chemical looping on a commercial scale is its relative complexity and high capital expenses [50, 67]. Thus, in this chapter, the proposed technology is first assessed from a techno-economic and exergetic perspective based on process simulations for an industrial production unit. The techno-economics and exergy efficiencies are compared to catalytic rWGS with conventional downstream separation processes. We chose catalytic rWGS as a benchmark for fair comparison because our process concept, in essence, breaks down the rWGS reaction into two steps. Although catalytic rWGS is currently not practiced on an industrial scale, it is gaining increased attention because of its sound ability to promote carbon circularity via CO<sub>2</sub> utilisation and its technological maturity [142, 143]. The proposed process concept, in its entirety, is experimentally demonstrated in a fixed bed reactor set-up. In the forthcoming sections, the methods used for the simulation, analyses, and experimental work are outlined and the results of the applied methods are presented and discussed.



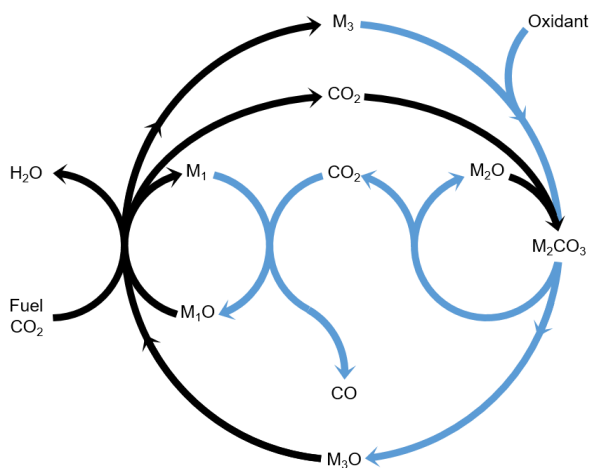


Figure 55: General concept [137] of a two-step process wherein a feed gas containing fuel(s) and  $CO_2$  (see black arrows) come into contact with metal oxide pairs that can oxidise fuel(s) partially ( $M_1O/M_1$ ) and almost completely ( $M_3O/M_3$ ) and a metal oxide ( $M_2O$ ) that is capable of capturing the produced  $CO_2$  in the form of a carbonate ( $M_2CO_3$ ) under the process conditions of the first step. When the feed gas is switched to an oxidising gas (see blue arrows), at least one of the 2 redox pairs is capable of being oxidised by  $CO_2$  while the other is readily oxidised by  $O_2$ , releasing heat and decreasing the partial pressure of  $CO_2$  such that the release of the captured  $CO_2$  and its conversion to  $CO$  are favoured.

6.2 Methods

6.2.1 Process simulation

Process simulation was performed in Aspen Plus® V10, assuming fluidised bed reactors for the sake of simplicity. A block flow diagram of the process with mass flows is displayed in Figure 56. The BFG utilised in the process corresponds to the production of approximately 2.6 megatonnes (MT) of steel per year [42], which is typical for an integrated steel mill. Figure 56 also presents the main specifications of the process simulation. Further details of the flowsheet (Figure D13) are listed in Table D4. Unless mentioned otherwise, other specifications were the default values of the simulator.

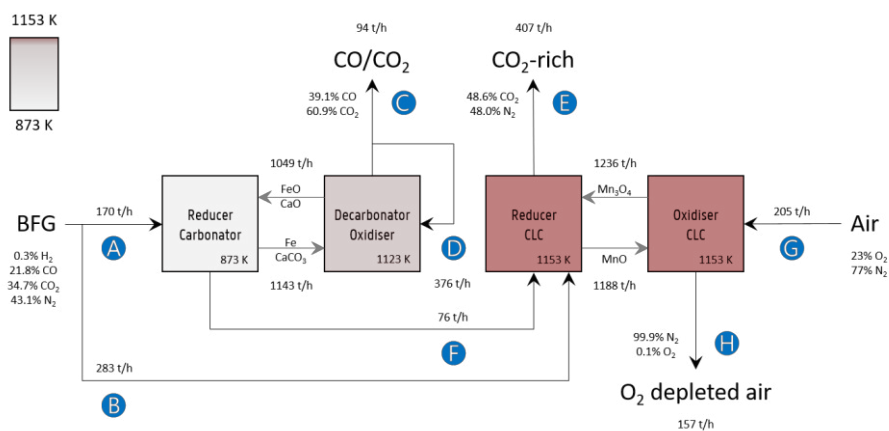


Figure 56: Block flow diagram of the process concept with mass flow rates. Labels: A: BFG feed for producing a CO/CO<sub>2</sub> product stream (C), B: additional BFG feed for generating the heat via chemical looping combustion to fulfil the heat demand in the decarbonator-oxidiser, D: recycled portion of product stream as a sweep or fluidising gas, E: CO<sub>2</sub> released by combusting additional BFG and partly oxidised BFG (F) via

chemical looping combustion (CLC), G: air fed to replenish the lattice oxygen consumed during CLC, and H: O<sub>2</sub> depleted air. The compositions of the gas streams are given on a mass basis. Note that, for brevity and simplicity sake, the flows of inert solids MgAl<sub>2</sub>O<sub>4</sub>, and CeO<sub>2</sub> that are used for imparting stability to the oxygen carriers (FeO<sub>x</sub> and Mn<sub>3</sub>O<sub>4</sub>) and CO<sub>2</sub> carrier (CaCO<sub>3</sub>) and of the make-up flows are not displayed. Details are mentioned in Table 20 and in Figure D13.

Table 20: Specifications of the process simulation. Capital letters in brackets refer to the labels in Figure 56.

	Reducer-carbonator	Decarbonator-oxidiser	Reducer CLC	Oxidiser CLC
Temperature [K]	873	1123	1153	1153
Pressure [kPa]	101	101	101	101
Inlet gas flow [kg/s]	(A) = 47	4 • (C) = 104	(B) + (F) = 100	(G) = 57
Inlet gas composition [mass basis]	0.3% H <sub>2</sub>		0.4% H <sub>2</sub>	
	21.8% CO	39.1% CO	17.5% CO	
	34.7% CO <sub>2</sub>	60.9% CO <sub>2</sub>	27.5% CO <sub>2</sub>	
	43.1% N <sub>2</sub>		54.4% N <sub>2</sub>	77% N <sub>2</sub>
			0.2% H <sub>2</sub> O	23% O <sub>2</sub>
Inlet solid flow [kg/s]	222	248	432	420
Inlet solids composition [mass basis]	31% FeO	20% FeO	79% Mn <sub>3</sub> O <sub>4</sub>	25% Mn <sub>3</sub> O <sub>4</sub>
	34% MgAl <sub>2</sub> O <sub>4</sub>	32% MgAl <sub>2</sub> O <sub>4</sub>	21% MgAl <sub>2</sub> O <sub>4</sub>	22% MgAl <sub>2</sub> O <sub>4</sub>
	29% CaO	13% CaO		53% MnO
	6% CeO <sub>2</sub>	5% CeO <sub>2</sub>		
		6% Fe		
		23% CaCO <sub>3</sub>		
Design specifications	Corresponds to approximately 1 MT/year of CO <sub>2</sub> emissions if the inlet gas had been combusted	80% of the outlet gas is recycled	Inlet gas flow (B) adjusted such that the sum of heat produced in CLC equals heat requirement of decarbonator-oxidiser	Inlet gas flow (G) adjusted to oxidise all MnO.

The experimental results of this work show that 80%  $\text{Mn}_2\text{O}_3/\text{MgAl}_2\text{O}_4$  is very stable for chemical looping combustion of the blast furnace gas (BFG). Based on the experimental results, the circulation rate of  $\text{Mn}_3\text{O}_4$  displayed in Figure 56 were determined assuming a conservative solids conversion of 70%. Similarly, 50%  $\text{Fe}_2\text{O}_3/\text{MgAl}_2\text{O}_4$  is known to have very high chemical stability and an average residual oxygen transfer capacity between 24 to 31% after 1000 redox cycles (assuming redox transitions between Fe and FeO) [53]. The solids circulation rate of  $\text{FeO}_x$  was determined using these values. Finally, the data from Fu et al. [144] reporting CaO conversion of around 50% was used to determine the circulation rate of CaO in the process simulation. It should be noted that higher conversions of synthetic  $\text{CO}_2$  carriers over multiple cycles have been reported [145]. Given the high chemical stability of the oxygen carriers, the make-up ratio of fresh oxygen carrier to the process was determined by the attrition rate of the materials. Based on the attrition resistance of a manganese-based oxygen carrier estimated by Costa et al. [146], it was assumed that the lifetime of the 80%  $\text{Mn}_2\text{O}_3/\text{MgAl}_2\text{O}_4$  is 11000 hours. Similarly, the lifetime of 50%  $\text{Fe}_2\text{O}_3/\text{MgAl}_2\text{O}_4$  is assumed to be 1250 hours, corresponding to the attrition resistance of an Fe-based oxygen carrier based on the work by Gayan et al. [147]. It is noteworthy that Fe-based oxygen carriers prepared via more sophisticated synthesis techniques with estimated lifetime of up to 33000 hours have also been reported [148]. The ratio of the molar flow rate of CaO to that of the

sum of CO and CO<sub>2</sub> (CO is expected to be oxidised by FeO to form CO<sub>2</sub>) is approximately 2 and it is assumed that the ratio of fresh make-up sorbent to the sum of the molar flowrates of CO and CO<sub>2</sub> is 0.05 (5%), corresponding with the results reported by Fu et al. [144]. Based on the analysis and assumptions discussed above, it is estimated that the amounts of fresh 80% Mn<sub>2</sub>O<sub>3</sub>/MgAl<sub>2</sub>O<sub>4</sub>, 50% Fe<sub>2</sub>O<sub>3</sub>/MgAl<sub>2</sub>O<sub>4</sub>, and 83% CaO/CeO<sub>2</sub> would approximately be 1 kt/year, 5 kt/year, and 77 kt/year respectively. To put this into perspective, for the simulated production of 2.6 MT/year of steel, the requirement of iron ore and limestone in the blast furnace alone is approximately 468 and 67 kt/year [58].

In order to compare the proposed process in Figure 56 with conventional technology, a process combining rWGS followed by a downstream separation train was also simulated (block diagram with mass flows depicted in Figure D11 and flowsheet in Figure D12). By setting the temperature of the rWGS reactor to 866 K, an outlet flow of CO equivalent to that of the proposed chemical looping process was achieved. Pressure swing adsorption (PSA) was chosen for H<sub>2</sub> separation from the mixed product stream because it is the most mature and widely used technology to separate H<sub>2</sub> from a syngas mixture [149]. It should be noted that separating H<sub>2</sub> from mixtures containing less than 15 mol% H<sub>2</sub> (H<sub>2</sub> content of the gas after rWGS is 3 mol%) is not straightforward for conventional technologies such as PSA, membrane separation, and cryogenic distillation [150, 151]. Due to the large quantity of N<sub>2</sub> to be separated, cryogenic distillation was selected for

the separation of N<sub>2</sub> from the product mixture of the rWGS reactor because of its competitiveness at larger scales [152]. Freezing of CO<sub>2</sub> in the distillation column could possibly be avoided by using advanced technologies such as CFZ<sup>TM</sup> (controlled freezing zone) that would help save the capital expenses of a separate CO<sub>2</sub> removal unit [153]. The small amount of methane produced in the rWGS process is neglected and its separation was not modelled.

The carbon footprint (CF) of the process is defined using equation (64) [154], where  $\dot{m}_{\text{CO}_2, \text{E}}$  is the mass flow rate of CO<sub>2</sub> in stream E and  $\dot{m}_{\text{product}, \text{C}}$  is the mass flow rate of the product stream C, inclusive of CO and CO<sub>2</sub> (see Figure 56 for the alphabetic labels).

$$\text{CF} = \frac{\dot{m}_{\text{CO}_2, \text{E}}}{\dot{m}_{\text{product}, \text{C}}} \quad (64)$$

The carbon footprint of the catalytic rWGS, defined as the mass ratio of the CO<sub>2</sub> released to the environment and the 50% CO/CO<sub>2</sub> product stream, is highly dependent on the greenhouse gas emissions intensity of electricity production because electricity constitutes the majority of its external energy demand owing to its downstream separation processes. Based on the values of 2019 in the EU, it is assumed that the greenhouse gas emissions intensity of electricity from the grid is 255 kg/MWh [155].

Apart from the carbon footprint, another metric useful for indicating the performance of the proposed chemical looping process is the carbon recovery (CR) defined by equation (65), where  $\dot{n}_{\text{CO}, \text{C}}$  and

$\dot{n}_{\text{CO}_2,\text{C}}$  are the molar flow rates of CO and CO<sub>2</sub> in the product stream C and  $\dot{n}_{\text{CO},\text{A}}$  and  $\dot{n}_{\text{CO}_2,\text{A}}$  are their molar flow rates in feed stream A. The carbon recovery is the fraction of the amount of carbon fed (see stream A in Figure 56), in the form of CO and CO<sub>2</sub>, to the reducer-carbonator which is transferred to the product stream (see stream C in Figure 56).

$$\text{CR} = \frac{\dot{n}_{\text{CO},\text{C}} + \dot{n}_{\text{CO}_2,\text{C}}}{\dot{n}_{\text{CO},\text{A}} + \dot{n}_{\text{CO}_2,\text{A}}} \quad (65)$$

For rWGS, the heat necessary for the chemical reaction is obtained from combusting excess unreacted H<sub>2</sub> separated in the PSA (Figure D11) instead of combusting a carbonaceous fuel. Thus, the carbon recovery of the rWGS is effectively 1.

The reduction of CO<sub>2</sub> emissions (RCE) when using BFG is calculated using equation (66), where  $\dot{m}_{\text{CO}_2,\text{C}}$  and  $\dot{m}_{\text{CO},\text{C}}$  are the mass flow rates of CO<sub>2</sub> and CO in outlet stream C,  $\dot{m}_{\text{BFG},\text{A+B}}$  is the mass flow rate of the inlet BFG (A and B),  $\text{MM}_{\text{BFG}}$  is the average molar mass of BFG, and  $x_{\text{CO}}$  and  $x_{\text{CO}_2}$  are the mole fractions of CO and CO<sub>2</sub> in the BFG.

$$\text{RCE} = \frac{\dot{m}_{\text{CO}_2,\text{C}} + \dot{m}_{\text{CO},\text{C}} * \frac{\text{MM}_{\text{CO}_2}}{\text{MM}_{\text{CO}}}}{\frac{\dot{m}_{\text{BFG},\text{A+B}}}{\text{MM}_{\text{BFG}}} * (x_{\text{CO}} + x_{\text{CO}_2}) * \text{MM}_{\text{CO}_2}} * 100 \quad (66)$$

The denominator on the right hand side of equation (66) shows the amount of CO<sub>2</sub> that would have been emitted when BFG would have been combusted in a power plant (instead of being separated and used in the chemical industry) and the numerator shows the CO/CO<sub>2</sub> stream



(C in Figure 56) that could be used in the chemicals industry or for the production of synthetic fuels.

To assess the energy efficiency of the proposed process, the energy return on energy invested (EROEI) [156] displayed in equation (67) was calculated. This metric is the ratio of the energy output and the energy input of the process. For the chemical looping process, the energy output comprises the CO/CO<sub>2</sub> product stream and heat that can be used for generating electricity, whereas the energy input comprises only the BFG. On the other hand, for the catalytic steady-state rWGS process, the output comprises the CO/CO<sub>2</sub> product stream and a separate H<sub>2</sub> stream, while the energy input comprises the BFG and the electricity demand for the downstream separation processes. It is noteworthy that the analyses are limited to the investigated processes and the surroundings [157] and do not take into account, for example, the energy efficiency with which electricity is supplied to the catalytic steady-state rWGS process.

$$\text{EROEI} = \frac{\dot{E}_{n_{\text{out}}}}{\dot{E}_{n_{\text{in}}}} \quad (67)$$

### 6.2.2 Exergy analysis

An exergy analysis was carried out using the results of the process simulation. Exergy of a system is defined as the maximum shaft work that can be done by the composite of the system and a specified reference environment [93]. The total exergy ( $E_{\text{total}}$ ) of a stream is

defined as the sum of its physical and thermochemical exergy (equation (68)).

$$E_{\text{total}} = E_{\text{physical}} + E_{\text{thermochemical}} \quad (68)$$

The physical exergy ( $E_{\text{physical}}$ ) was estimated using Aspen Plus with a reference state of 298 K and 101 kPa (the so-called “dead state”). The thermochemical exergy of the streams was calculated using equation (69), where  $\dot{n}$  is the total molar flow rate of the stream,  $x_i$  is the molar fraction of the  $i^{\text{th}}$  component,  $e_{\text{chem},i}$  is the standard chemical exergy of the  $i^{\text{th}}$  component from Szargut [94],  $R$  is the universal gas constant, and  $T_0$  is the reference temperature, i.e. 298 K. The latter part of equation (69) associated with mixing exergy is not applicable to solids. The scope of the exergy analysis is limited to the streams and blocks depicted in Figure 56 for the chemical looping process and in Figure D11 for the catalytic rWGS.

$$E_{\text{thermochemical}} = \dot{n} \sum x_i e_{\text{chem},i} + \dot{n} \sum x_i T_0 R \ln(x_i) \quad (69)$$

The exergy from a heat source  $E_{\text{physical},Q}$  at a temperature  $T$  is given by equation (70), where  $Q$  is the amount of heat released and  $T_0$  is the reference temperature, i.e. 298 K.

$$E_{\text{physical},Q} = Q * \left(1 - \frac{T_0}{T}\right) \quad (70)$$

The exergy efficiency of the process,  $\eta_{\text{exergy,process}}$ , is then given by equation (71).

$$\eta_{\text{exergy,process}} = \frac{\dot{Ex}_{\text{out}}}{\dot{Ex}_{\text{in}}} * 100 \quad (71)$$

The exergy efficiency of the H<sub>2</sub> PSA column ( $\eta_{\text{exergy,PSA}}$ ) is calculated using the relation derived by Dunikov and Blinov [158] and presented by equation (72). A number of simplifying assumptions were made such as no exergy losses due to transient heat losses caused by the heat of adsorption/desorption and 100% product, i.e. H<sub>2</sub> recovery.  $p_{\text{in}}$  and  $p_{\text{out}}$  were assumed to be 6300 kPa and 580 kPa based on typical industrial values [149]. The partial pressure of desorbed H<sub>2</sub> ( $p_{\text{H}_2}$  in equation (72)), was assumed to be 101 kPa. Recovery of work from expanding the tail gas from 580 kPa to 101 kPa was neglected. The H<sub>2</sub> from the PSA was assumed to have a purity of 100%.

$$\eta_{\text{exergy,PSA}} = \frac{\ln\left(\frac{p_{\text{H}_2}}{p_{\text{in}} * x_{\text{H}_2}}\right) - \ln(x_{\text{H}_2})}{\frac{1 - x_{\text{H}_2}}{x_{\text{H}_2}} * \ln\left(\frac{p_{\text{in}}}{p_{\text{out}}(1 - x_{\text{H}_2})}\right)} * 100$$

For cryogenic distillation, the energy input, in the form of electricity is estimated using empirical relations derived by Lange [159] using the so-called “distillation resistance”  $\Omega$  in °C<sup>-1</sup> given in equation (73), where  $w_{\text{N}_2}$  is the mass fraction of N<sub>2</sub> in the inlet stream and  $\text{BP}_{\text{N}_2}$  and  $\text{BP}_{\text{CO}}$  are the boiling points of N<sub>2</sub> and CO in °C. The boiling points of N<sub>2</sub> and CO are present in the denominator because N<sub>2</sub> is the product to be separated and CO is the component with the next highest boiling point in the feed stream.

$$\Omega_{\text{N}_2} = 100 * \frac{w_{\text{N}_2}}{\text{BP}_{\text{N}_2} - \text{BP}_{\text{CO}}}$$

The energy transfer (ET) and heat transfer duty (HD) in GJ/tonne<sub>feed</sub> for carrying out the distillation are given by equations (74)

and (75). These equations are based on industrial distillation columns for distilling components whose boiling point ranges from -250°C to 136°C for the top stream (lighter component) and from -210°C to 350°C for the bottom stream (heavier component). Thus, they are expected to be applicable for the separation of N<sub>2</sub> (boiling point = -196°C) from a mixture containing CO, CH<sub>4</sub>, and CO<sub>2</sub> with boiling points equal to -191, -161, and -78°C respectively [159]. The deviation for the energy transfer duty (equation (74)) and heat duty (equation (75)) are  $\pm 1$  and  $\pm 0.7$  GJ/tonne<sub>feed</sub>.

$$ET = 1.1 * \Omega_{N_2}$$

$$HD = 0.57 * \Omega_{N_2}$$

Since the majority of the energy input for cryogenic distillation is required by pumps and compressors, the difference between the energy transfer duty (which includes the energy consumption from pumps and compressors) and heat duty is assumed to be the electrical energy (electrical energy  $\approx$  exergy) input to drive the separation. The exergy efficiency ( $\eta_{\text{exergy, distillation}}$ ) of the cryogenic distillation column is given by equation (76), where the denominator indicates the minimum reversible work required to bring about the separation and the subscripts "feed" and "products" refer to the mole fraction of the  $i^{\text{th}}$  component in the feed and product[136].

$$\eta_{\text{exergy, distillation}} = \frac{T_0 R * (\dot{n}_{\text{product}} \sum x_{i, \text{product}} \ln(x_{i, \text{product}}) - \dot{n}_{\text{feed}} \sum x_{i, \text{feed}} \ln(x_{i, \text{feed}}))}{ET - HD} * 100$$

The minimum reversible work displayed in the denominator of equation (76) is used for determining the energy required for separating

H<sub>2</sub>O from the product mixture of rWGS, i.e., it is assumed that separation of H<sub>2</sub>O from the mixture has an exergy efficiency of 100%.

### 6.2.3 Techno-economic assessment

The price of the feedstock BFG was calculated using its lower heating value (2.6 GJ/tonne) and the average EU natural gas cost for non-household consumers based on its gross calorific value in 2020 (3.4 EUR/GJ for consumption higher than 130 MW – band I6 [160]). Assuming that natural gas is 100% methane (with a higher calorific value of 55.5 GJ/tonne), the price of BFG was estimated at 9 EUR/tonne, in agreement with estimations made by others [161].

The cost of product stream ( $c_{\text{product}}$ ) was calculated using equation (77) as a first approximation, where  $c_i$  and  $w_i$  are the cost and mass fraction of the  $i^{\text{th}}$  component. The production of polyols can sequentially utilise the CO<sub>2</sub> and CO content of the product gas stream, thereby making the simple cost estimation employed here reasonable.

$$c_{\text{product}} = c_{\text{CO}_2} w_{\text{CO}_2} + c_{\text{CO}} w_{\text{CO}}$$

The cost of producing commercial CO via the widely used steam methane reforming process followed by rWGS is highly dependent on the cost of natural gas and amounts to roughly double the price of methane on a mass basis [162]. Using the price of natural gas mentioned above, the cost of CO was estimated to be 390 EUR/tonne, corresponding well with costs of CO reported in literature [121, 163]. The cost of CO<sub>2</sub> was assumed to be 50 EUR/tonne [164]. As the product streams from both processes have approximately 50 mol% CO/CO<sub>2</sub>

content, the price of the product stream is between 180 and 190 EUR/tonne.

Capital investment (CI) inside battery limits (ISBL) calculations were made using empirical relations derived by Lange [165] given in equation (78). The values were converted to 2020 equivalent USD using the US Bureau of Labor Statistics' [166] inflation calculator and then converted to EUR at 0.9 EUR/USD.

$$CI (ISBL) = 2 * (ET)^{0.65}$$

It is noteworthy that the estimations made by this approach have an accuracy of -50 to +100%, but serve very well for comparing the novel process with more conventional processes. A Lang factor of 4 was used to estimate the capital expenses outside battery limits (OSBL) (see equation (79)), thereby adding a conservative buffer to the capital expenses estimated using equation (78).

$$CI (OSBL) = 4 * CI (ISBL)$$

A capital charge (CaCh) of 12% per year was used for the proposed chemical looping process as well as the steady-state catalytic rWGS[167]. Assuming that the plant is operational throughout the year with 5% downtime, the annualised capital expenses (CAPEX) per tonne of product produced are calculated using equation (80). Note that CI (OSBL) in the equation (80) is converted to EUR<sub>2020</sub>.

$$CAPEX = \frac{CI (OSBL) * \frac{CaCh}{100}}{24 * 365 * \dot{m}_{product,C} * 95\%}$$

Operating expenses are composed of the cost of feedstock (BFG), cost of the materials for the proposed chemical looping process

and the catalytic rWGS process, operation and maintenance (O&M) costs (4% of the capital costs inside battery limits per year [77]), and the net amount of electricity (if required). The net amount of electricity necessary for running the H<sub>2</sub>-PSA column is calculated by taking into account the exergy efficiency (see equation (72)) and the minimum reversible work necessary to bring about the separation (see denominator of equation (76)), while assuming that all energy would be supplied by electricity. For the sake of simplicity, the electricity requirement for operating the distillation column to cryogenically separate N<sub>2</sub> from the CO, CO<sub>2</sub>, and N<sub>2</sub> mixture is assumed to be the difference between the energy transfer duty (equation (74)) and the heat duty (equation (75)). The heat duty, which typically requires natural gas, is assumed to be negligible. The viability of this simplified calculation scheme was tested for O<sub>2</sub> production in a conventional cryogenic air separation unit (ASU) and was able to predict its energy consumption with an accuracy of  $\pm 10\%$  (further details are in Appendix D).

For the proposed chemical looping process, the cost of materials included the cost of oxygen carriers 50% Fe<sub>2</sub>O<sub>3</sub>/MgAl<sub>2</sub>O<sub>4</sub> and 80% Mn<sub>2</sub>O<sub>3</sub>/MgAl<sub>2</sub>O<sub>4</sub> and the CO<sub>2</sub> sorbent 83% CaO/CeO<sub>2</sub>, all of which had been used for the experimental demonstration. These costs were estimated using the step-based method described by Baddour et al. and are expected to have an accuracy of  $\pm 20\%$  [168, 169]. The oxygen carriers studied in this work, 50% Fe<sub>2</sub>O<sub>3</sub>/MgAl<sub>2</sub>O<sub>4</sub> and

80%  $\text{Mn}_2\text{O}_3/\text{MgAl}_2\text{O}_4$ , were estimated to have a cost of 1100 EUR/tonne and 1330 EUR/tonne (see Table D6 and Table D6 of Appendix D), close to the values reported in literature [167]. The  $\text{CO}_2$  carrier, 83%  $\text{CaO}/\text{CeO}_2$ , was estimated to cost 390 EUR/tonne, approximately 10 times higher than the cost of natural limestone [170]. Detailed calculations are presented in Appendix D with due considerations to the lifetime of the materials. A  $\text{Ni}/\text{Al}_2\text{O}_3$  catalyst, known to be effective for rWGS [171], was selected as the catalyst of choice for rWGS because of its lower cost compared to platinum group metal (PGM) catalysts. The annualised cost of the catalyst was conservatively estimated by assuming that the catalyst consumption is 0.01 kg/tonne<sub>product</sub>, one order of magnitude lower than the ideal catalyst consumption [154]. Total operating expenses (OPEX) are, thus, given by equation (81) as the sum of the costs of feedstock and materials (F&M), O&M, and electricity (if purchased).

$$\text{OPEX} = c_{\text{F\&M}} + c_{\text{O\&M}} + c_{\text{electricity}}$$

The proposed chemical looping process is a source of excess heat that can be effectively used for electricity generation using steam turbines. Assuming that the steam turbines have a conservative exergy efficiency of 48% [172] (corresponding to an electrical efficiency of 33% for the chemical looping process, a conservative value for gas-fed chemical looping combustion at atmospheric pressure [173]), electricity can be effectively sold to the grid or its purchase for the steel mill avoided at a cost of 0.04 EUR/kWh [174], corresponding to the 2020



electricity price in the EU for a consumption higher than 150 GWh (band I6). Other sources of revenue include the sale of excess  $H_2$  (at the price of 2000 EUR/tonne [175]) and revenue from recovering Ni from spent catalysts for the catalytic steady state rWGS. For the proposed chemical looping process, sale of scrap metal (oxides) also generates some revenue. The sale of  $N_2$  (purity>99%) from the CLC oxidiser (see stream H in Figure 56) or from the cryogenic distillation of the steady state rWGS process (stream D in Figure D11) is not considered in this analysis. Further details of the costs to generate the revenue are given in the Appendix D.

$$PC = CAPEX + OPEX$$

The net income (NI) is calculated using equation (83), wherein revenue is generated from the sale of products i.e. chemicals ( $CO$ ,  $CO_2$ ,  $H_2$ ), electricity, and solid materials (spent oxygen carriers,  $CO_2$  carriers and catalyst).

$$NI = \text{Revenue} - PC$$

#### 6.2.4 Experimental proof of concept

For the experiments related to the proof of the process concept, the materials in the reactor were arranged as shown in Figure 57.

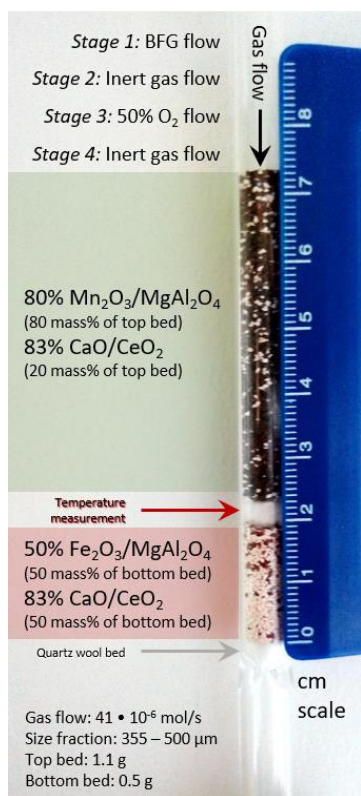


Figure 57: Laboratory reactor bed to carry out the proof of concept experiments and experimental specifications. The scale bar on the right indicates the length in cm. Gas flow:  $41 \cdot 10^{-6}$  mol/s. Size fraction of solids: 355 – 500  $\mu\text{m}$ . Top bed (manganese oxide and calcium oxide): 1.1 g. Bottom bed (iron oxide and calcium oxide): 0.5 g.

For the experiment, the top bed consisted of a 1.1 g physical mixture containing pellets of 80%  $\text{Mn}_2\text{O}_3/\text{MgAl}_2\text{O}_4$  and 83%  $\text{CaO}/\text{CeO}_2$  in a 9:2 mass ratio and the bottom bed consisted of a 0.5 g mixture containing pellets of 50%  $\text{Fe}_2\text{O}_3/\text{MgAl}_2\text{O}_4$  and 83%  $\text{CaO}/\text{CeO}_2$  in a 1:1 (by mass) ratio loaded in the reactor on a quartz wool plug. The sieve fraction of the pellets was in the range of 355 to 500  $\mu\text{m}$  to limit the

pressure drop in the bed. The two beds were arranged to exploit the functionalities of all the materials used: in the top bed, during reduction, complete oxidation of feed gas was achieved with CO<sub>2</sub> capture and during oxidation, fed O<sub>2</sub> was completely consumed while liberating heat to be used for CaCO<sub>3</sub> decomposition. In the bottom bed, during reduction, H<sub>2</sub> and CO in the BFG reduced FeO<sub>x</sub>, complemented by CO<sub>2</sub> capture via CaO. During oxidation, CO<sub>2</sub> released upstream and in-situ was converted to CO while regenerating FeO<sub>x</sub> and CaO. Each cycle consisted of 4 stages: (1) reduction with BFG for 240 seconds, (2) reactor purge with inert Ar for 60 seconds to sweep out unconverted reactants and products, (3) oxidation with 50% O<sub>2</sub> in Ar for 60 seconds to ensure that heat is generated quickly and used for the reaction instead of being dissipated to the surroundings, and (4) purge with inert Ar for 1500 seconds to sweep out unconverted reactants and products. 30 redox cycles were executed, of which the first 5 had a reduction (stage 1) time of 180 s instead of 240 s to gauge the operating limits of the system.

The total moles of Ca, Fe, and Mn (only when used) in the reactor are calculated using equations (84) to (86).

$$N_{\text{Ca}} = \frac{m_{\text{CC}} * w_{\text{CaO}}}{MM_{\text{CaO}}}$$

$$N_{\text{Fe}} = \frac{m_{\text{Fe-OC}} * w_{\text{Fe}_2\text{O}_3} * 2}{MM_{\text{Fe}_2\text{O}_3}}$$

$$N_{\text{Mn}} = \frac{m_{\text{Mn-OC}} * w_{\text{Mn}_2\text{O}_3} * 2}{MM_{\text{Mn}_2\text{O}_3}}$$

The utilisation of the oxygen transfer capacity and the CO<sub>2</sub> carrying capacity in both half-cycles were calculated using equations (87) to (89).

$$U_{Mn} = \frac{\int_{\text{start of stage-2}}^{\text{end of stage-4}} (2 * (\dot{n}_{O_2, \text{in}} - \dot{n}_{O_2, \text{out}})) dt}{N_{Mn}}$$

$$U_{Ca} = \frac{\int_{\text{start of stage-2}}^{\text{end of stage-4}} (\dot{n}_{CO_2, \text{out}} + \dot{n}_{CO, \text{out}}) dt}{N_{Ca}}$$

$$U_{Fe} = \frac{\int_{\text{start of stage-2}}^{\text{end of stage-4}} (\dot{n}_{CO, \text{out}}) dt}{N_{Fe}}$$

For the calculations of material utilisation, it is assumed that the fresh materials placed in the reactor consist exclusively of Fe<sub>2</sub>O<sub>3</sub> and MgAl<sub>2</sub>O<sub>4</sub> in the Fe-based oxygen carrier, CaO and CeO<sub>2</sub> for the CO<sub>2</sub> carrier, and, Mn<sub>2</sub>O<sub>3</sub> and MgAl<sub>2</sub>O<sub>4</sub> in the Mn-based oxygen carrier. The presence of CeO<sub>2</sub> for oxidation of reductants is neglected since in the given reaction conditions it can only contribute a small portion of its lattice oxygen atoms while being reduced to non-stoichiometric CeO<sub>2-δ</sub> (δ < 0.1) [95].

The fuel efficiency (FE) of the process is calculated using equation (90).

$$FE = \frac{\int_{\text{start of stage-1}}^{\text{end of stage-2}} ((\dot{n}_{H_2, \text{in}} - \dot{n}_{H_2, \text{out}}) + (\dot{n}_{CO, \text{in}} - \dot{n}_{CO, \text{out}})) dt}{\int_0^{t_{r-c}} (\dot{n}_{H_2, \text{in}} + \dot{n}_{CO, \text{in}}) dt} * 100$$

The reactor productivity (RP) for the proof of concept experiments is given by equation (92), where r = bed radius = 3.75 • 10<sup>-3</sup> m, h = height of the bed ≈ 7.3 • 10<sup>-2</sup> m, and CT = total cycle time = 0.52 hours.

$$RP = \frac{\int_{\text{start of stage-2}}^{\text{end of stage-4}} (\dot{n}_{\text{CO}_2, \text{out}} * MM_{\text{CO}_2} + \dot{n}_{\text{CO}, \text{out}} * MM_{\text{CO}}) dt}{\pi * r^2 * h * CT} * 100$$

The carbon balance (CB) and oxygen balance (OB) are computed using equations (92) and (93).

$$\frac{CB}{100} = \frac{\int_0^{t_{\text{total}}} (\dot{n}_{\text{CO}_2, \text{in}} + \dot{n}_{\text{CO}, \text{in}}) dt - \int_0^{t_{\text{total}}} (\dot{n}_{\text{CO}_2, \text{out}} + \dot{n}_{\text{CO}, \text{out}}) dt}{\int_0^{t_{\text{total}}} (\dot{n}_{\text{CO}_2, \text{in}} + \dot{n}_{\text{CO}, \text{in}}) dt}$$

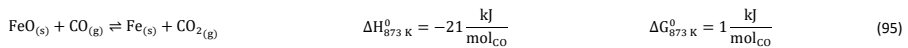
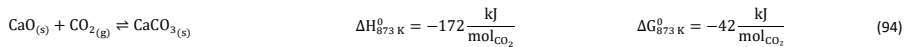
$$\frac{OB}{100} = \frac{\int_0^{t_{\text{total}}} (2 * \dot{n}_{\text{CO}_2, \text{in}} + \dot{n}_{\text{CO}, \text{in}} + 2 * \dot{n}_{\text{O}_2, \text{in}}) dt - \int_0^{t_{\text{total}}} (2 * \dot{n}_{\text{CO}_2, \text{out}} + \dot{n}_{\text{CO}, \text{out}} + 2 * \dot{n}_{\text{O}_2, \text{out}}) dt}{\int_0^{t_{\text{total}}} (2 * \dot{n}_{\text{CO}_2, \text{in}} + \dot{n}_{\text{CO}, \text{in}} + 2 * \dot{n}_{\text{O}_2, \text{in}}) dt}$$

Carbon and oxygen balances were closed within 10% and 15% for all experiments.

## 6.3 Results and discussion

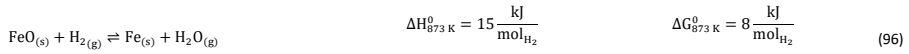
### 6.3.1 Process simulation

The base case of the proposed process was simulated by setting the reducer-carbonator to a temperature of 873 K to maximise carbon capture because the  $p_{\text{CO}_2, \text{eq}}$  of  $\text{CaCO}_3$  at this temperature is approximately 0.3 kPa (equation (94)). The capture of  $\text{CO}_2$  favours oxidation of CO in the BFG (equation (95)) via Le Chatelier's principle, leading to an overall carbon recovery of around 98% (equation (65)). A higher temperature would result in lower carbon recovery.



The higher carbon recovery comes at the cost of lower utilisation or oxidation of  $\text{H}_2$  (equation (96)) in the BFG (around 11% of inlet  $\text{H}_2$  is oxidised when the reducer-carbonator is at 873 K). Higher  $\text{H}_2$  utilisation is favoured at higher temperature (see Figure D2 for an equilibrium

diagram) because of reduction of FeO and also due to increased favourability of the rWGS (equation (44)).



The reduction-carbonation reaction is highly exothermic and its heat can be utilised within the steel mill or be used for the generation of electricity.

Conversely, the decarbonation-oxidation step is highly endothermic (equations (94) and (95) from right to left) and is operated at a temperature of 1123 K to avoid the use of N<sub>2</sub> or another inert to decarbonate the CaCO<sub>3</sub>. The production of CO during decarbonation decreases the partial pressure of CO<sub>2</sub>, thereby extending the lifetime of the CO<sub>2</sub> carrier [134] and improving the kinetics of decarbonation [135]. The heat for the chemical reactions during the decarbonation-oxidation step and the heat to increase the temperature of the solids is provided by the near complete oxidation of the gas stream exiting the reducer-carbonator (see F in Figure 56) and additional BFG (see B in Figure 56) via chemical looping combustion (CLC), operated isothermally at 1153 K, a temperature higher than that at which the decarbonator-oxidiser (1123 K) is operated to enable heat transfer. The gas exiting the oxidiser of CLC (stream H in Figure 56) consists of 99%+ N<sub>2</sub>. Although this stream, in this study, is not considered to be of any economic value apart from the heat it carries, it could be useful to feed the loop seals (non-mechanical pneumatic valves [176]) in case the proposed process

is carried out in a moving bed or a fluidised bed reactor or be used as a purge gas in case a series of fixed bed reactors are deployed.

The gas exiting the reducer of CLC (see E in Figure 56) comprising 39 mol% (50 mass%)  $\text{CO}_2$  on a dry basis is the source of process  $\text{CO}_2$  emissions. These emissions are accounted for in the carbon footprint of the process (see equation (64)), which amounts to 2.1 tonnes of  $\text{CO}_2$  per tonne of product. This value is lower than the maximum value of 6 tonnes of  $\text{CO}_2$  per tonne of product suggested for sustainable development of commodities and fuels [154]. It is noteworthy that the high fraction of  $\text{CO}_2$  in this stream (roughly 10 times larger than from conventional gas fired combustion [177]) also makes it more favourable for economical  $\text{CO}_2$  capture and storage or further utilisation [178]. A summary of the outlet gas streams from the chemical looping process is displayed in Table 21.

Table 21: Specifications of the outlet gases of the process simulation (see C, E, and H in Figure 56). Capital letters in brackets refer to the labels in Figure 56.

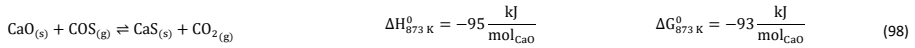
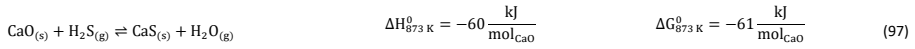
Stream label	C	E	H
Temperature [K]	1123	1153	1153
Pressure [kPa]	101	101	101
Outlet flow [kg/s]	26	44	113
Composition [mass basis]	39.1% CO 60.9% CO <sub>2</sub>	48.6% CO <sub>2</sub> 48.0% N <sub>2</sub> 3.3% H <sub>2</sub> O CO < 16 ppm H <sub>2</sub> < 0.2 ppm	99.9% N <sub>2</sub> 0.1% O <sub>2</sub>

For the rWGS simulation, a fraction of the H<sub>2</sub> separated from PSA is combusted using air (air to fuel ratio ≈ 1.3) to form a product stream containing only H<sub>2</sub>O and depleted air. The fraction of H<sub>2</sub> combusted was determined by the heat necessary for the endothermic rWGS. The carbon recovery of rWGS is, thus, 100% and its carbon footprint is largely determined by the greenhouse gas emissions intensity of the electricity the process uses for carrying out the separation, which is further discussed in the next sections. The outlet of the rWGS contains a small fraction of CH<sub>4</sub> formed due to methanation (≈ 0.3 mol%), which is not considered for separation.

The BFG of a steel mill is known to contain trace quantities of sulphur (approximately 10 ppm) in the form of H<sub>2</sub>S or COS [58]. These sulphurous compounds are expected to be captured by CaO via reactions displayed in equations (97) and (98). The formed CaS cannot be used for CO<sub>2</sub> capture and may be considered to be a part of spent CO<sub>2</sub> sorbent. In the base case, the molar flow of CaO in the fresh CO<sub>2</sub>



sorbent added (make-up flow of the CO<sub>2</sub> sorbent) is 3 orders of magnitude higher than that of H<sub>2</sub>S in the inlet stream. Thus, the sulphur in the BFG can be effectively removed from the outlet CO/CO<sub>2</sub> stream (see C in Figure 56).



The low amounts of inlet sulphur in the form of H<sub>2</sub>S are not expected to affect the iron oxide or the manganese oxide because of unfavourable thermodynamics [179]. Thus, when additional BFG is fed to the chemical combustion loop, the sulphurous compounds are expected to be oxidised to SO<sub>x</sub> and exit in the outlet CO<sub>2</sub>-rich stream (see E in Figure 56). For the rWGS simulation, it is assumed that the trace quantities of sulphur are removed from the BFG before being fed to the rWGS reactor.

By separating and using the CO/CO<sub>2</sub> stream by the proposed process for the production of chemicals, a 37% reduction in CO<sub>2</sub> emissions (equation (66)) can be achieved, when compared to the best available technology of combusting the BFG with air for combined heat and power. Apart from the production of polyols [114, 115] and the production of synthetic fuels [180-182], other pathways to use the CO/CO<sub>2</sub> product stream from the proposed process could be production of basic chemicals such as acetic acid, formic acid, etc. [131, 183] using renewable H<sub>2</sub>. By using bio-coal instead of fossil coal in the blast furnace of the steel mill [184], the products formed by the CO/CO<sub>2</sub> gas stream

of the proposed chemical looping process can be made free of fossil fuels.

The chemical looping process has an EROEI (equation (67)) of 0.95, which is three times higher than that of the catalytic steady-state rWGS. This metric indicates the energy efficiency or the so-called first law efficiency of the two processes. The quality of the energy is taken into account by considering exergy, as described below, to arrive at the exergy efficiency or the second law efficiency.

### 6.3.2 Exergy analysis

The energy requirements for the chemical looping process comes solely from the BFG. Since a part of this BFG is combusted, it is important to estimate the “useful work” (exergy) while taking such an approach. If only the thermochemical fraction of the total exergy is considered (see equation (69)), the exergy efficiency of the chemical looping process is around 32% (equation (71)). Using high temperatures in chemical looping allows a large fraction of the heat (contributing to physical exergy in equation (68)) required for the transformation of feed to products to be recovered as useful work. The major sources of heat for recovery in the chemical looping process are 1) the reduction-carbonation step, 2) the hot product gases (streams C and E in Figure 56), and 3) the hot solids exiting the reduction-carbonation step. When accounting for the recoverable heat at high temperature, the exergy efficiency of the proposed chemical looping process can be as high as 82%. Typically, high temperature heat can be converted to electricity

using a steam turbine. Taking into account the exergy losses for steam turbines (exergy efficiency is assumed to be 48%), the anticipated exergy efficiency of the chemical looping process is 59.8%. The breakdown of the exergy discussed above is illustrated in Figure 58, wherein the anticipated exergy efficiency is the sum of physical exergy recoverable as electricity and thermochemical exergy of products.

For the rWGS process, the exergy input comprises mainly imported electricity to drive the separation processes. The thermochemical exergy of products is slightly higher (about 1%) than that of the feed because CO is more exergetic than  $H_2$  and heat is consumed to convert  $H_2$  to CO (see equation (44)). Figure 58 shows that a large fraction of the total exergy is required for the cryogenic separation of  $N_2$  and this requirement dwarves the exergy required for the  $H_2$  separation by PSA. An important conclusion from this analysis is that increasing the conversion of  $H_2$  in rWGS by increasing the temperature or not separating  $H_2$  at all can only slightly improve the exergy efficiency of rWGS. The exergy efficiency of the cryogenic distillation to separate  $N_2$  was estimated via equation (76) to be around 1%, which is not surprising considering the large amounts of  $N_2$  to be removed from the outlet stream of rWGS and the small difference of about 4 K in the boiling points of  $N_2$  and CO. The atypical task of removing  $H_2$  in a highly diluted stream via PSA also caused a lower exergy efficiency of about 4% based on equation (72). Thus, the anticipated exergy efficiency, as displayed in Figure 58, is simply the

difference between the total exergy input and the exergy requirement for H<sub>2</sub>-PSA and cryogenic separation of N<sub>2</sub>, which is equal to 32.0%. The above analysis shows that the proposed chemical looping process is energetically far more efficient than chemical conversion via steady state rWGS followed by conventional separation techniques.

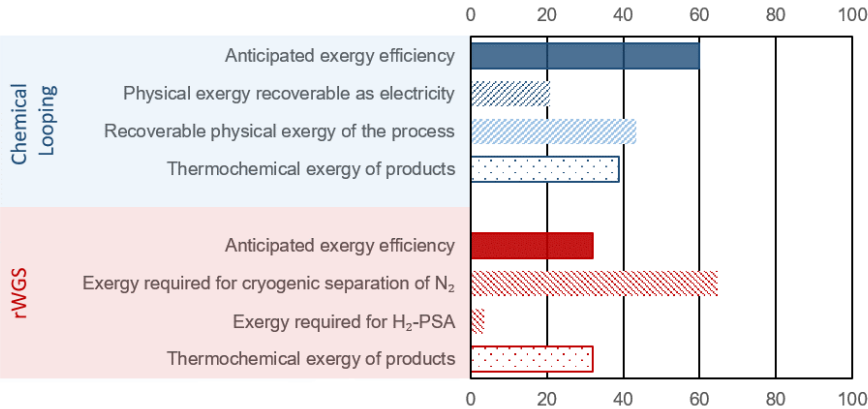


Figure 58: Exergy analysis of the proposed chemical looping process (in blue) and conventional rWGS with downstream purification (in red). For the sake of brevity, the negligible exergy required for separation of H<sub>2</sub>O is not displayed. The displayed values represent the exergy content in different streams/processes normalised to the total exergy input.

### 6.3.3 Techno-economic assessment

Chemical looping makes use of a solid intermediate that undergoes several redox cycles (in the case of oxygen carriers) or carbonation-decarbonation cycles (for CO<sub>2</sub> carriers) over the course of its useful lifetime. Thus, the cost of these solids and their lifetime are important parameters that can influence the economic feasibility of the process. Synthetic CO<sub>2</sub> carriers such as the one used in this work are

known to be resistant against sintering compared to most forms of natural limestone and thus, are expected to have a longer lifetime [9, 145, 185]. Upon reaching the end of their useful lifetime, large quantities of these solid materials become available for other purposes. The advantage of proximity to the steel mill is that the Fe-based oxygen carrier and a portion of the CaO based CO<sub>2</sub> carrier can be used for the production of steel. The rest of the spent CO<sub>2</sub> carrier could find use in the cement industry [186, 187]. The manganese based oxygen carrier with a very high loading (80 mass%) could replace manganese ore used in the metallurgical industry. Similarly, it is assumed that Ni from the spent Ni-based catalyst can be recovered, thereby allowing to minimise the cost of fresh catalysts. The prices of the spent materials are displayed in Table D8 and are based on 5 to 10 year average prices from public market data unless mentioned otherwise.

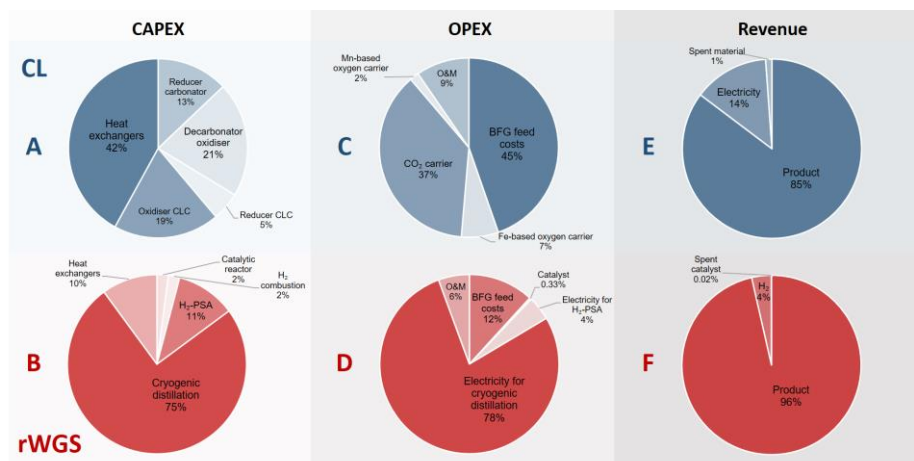


Figure 59: Breakdown of the contribution to the costs constituting the CAPEX, OPEX, and revenue for the proposed chemical looping (CL) process and rWGS process with downstream separation. A, C, and E (in blue) show the breakdown of the CAPEX, OPEX, and revenue generated for the proposed chemical looping process (total CAPEX: 122 EUR<sub>2020</sub>/tonne<sub>product</sub> and OPEX: 100 EUR<sub>2020</sub>/tonne<sub>product</sub>), whereas B, D, and F (in red) show the corresponding breakdown for the rWGS (total CAPEX: 99 EUR<sub>2020</sub>/tonne<sub>product</sub> and OPEX: 136 EUR<sub>2020</sub>/tonne<sub>product</sub>). O&M stands for operation and maintenance.

Figure 59 shows the breakdown of the CAPEX, OPEX, and revenue of the proposed chemical looping process and the catalytic rWGS with downstream separation processes. The capital expenses for chemical looping (Figure 59 A) are dominated by the heat exchangers to recover the physical exergy of the process in the form of heat followed by the decarbonator-oxidiser, which requires the highest heat input in the process. For the corresponding rWGS case, the separation processes, H<sub>2</sub>-PSA and cryogenic distillation, are most prominent, emphasising the complexity of separation processes to produce a

CO/CO<sub>2</sub> stream [113, 188]. As the chemical energy of the BFG is solely responsible for driving the proposed chemical looping process, the cost of feedstock BFG forms nearly 50% of the OPEX (see Figure 59 C). For energy-intensive production of chemicals, it is very typical that the cost of feedstock is the principal contributor to the overall production costs [189]. Because of the high make-up of fresh CO<sub>2</sub> carrier, the operating expenses of the proposed chemical looping process is significantly influenced by the cost of the CO<sub>2</sub> carrier. The relatively longer lifetime of the oxygen carriers minimises their contribution to the overall OPEX despite being roughly 3 times more expensive than the CO<sub>2</sub> carrier on a mass basis. On the other hand, more than 75% of the OPEX of the rWGS derives from the electricity demand for cryogenic distillation. As the CAPEX and OPEX are strongly dependent on the energy transfer duty, the separation processes of the rWGS having the highest energy requirements determine the overall production costs. The OPEX breakdown of the rWGS also shows that the low consumption of the catalyst makes the cost of replacing the catalysts negligible. Finally, for the proposed chemical looping process, apart from the CO/CO<sub>2</sub> product stream, electricity can also be a co-product along with the sale of spent oxygen carriers and CO<sub>2</sub> carriers. It is noteworthy that if the CO<sub>2</sub> leaving the process (see stream E in Figure 56) is taken into account, the greenhouse gas emissions intensity of the produced electricity is 1 order of magnitude higher than that of the electricity available in the grid [155]. This is because the electricity in the proposed chemical

looping process is generated at the expense of carbon-rich BFG originating from fossil coal. For the rWGS process, the excess  $H_2$  is a co-product. Interestingly, although the production of  $H_2$  is approximately 300 times lower (per unit of mass) than that of the main product, it does contribute significantly to the revenue because of its high value [175]. Due to the strong dependence of the rWGS process on electricity, it has an indirect carbon footprint (equation (64)) of 0.8 tonnes of  $CO_2$  per tonne of  $CO/CO_2$  product [155].

The CAPEX estimations used in this study have a fairly large degree of uncertainty between -50 to 100%. Thus, a sensitivity analysis was performed to study the influence of the under- or overestimation of CAPEX and other variables such as the cost of natural gas, electricity, and the costs and lifetime of the solids or catalyst used. Figure 60 shows the results of the sensitivity analysis. The origin on the x-axis represents the base case. Each variable in the analysis was varied independently by keeping the other variables constant at their base values. The y-axis displays the “net income” calculated using equation (83), wherein all the terms are normalised against the product  $CO/CO_2$  stream.



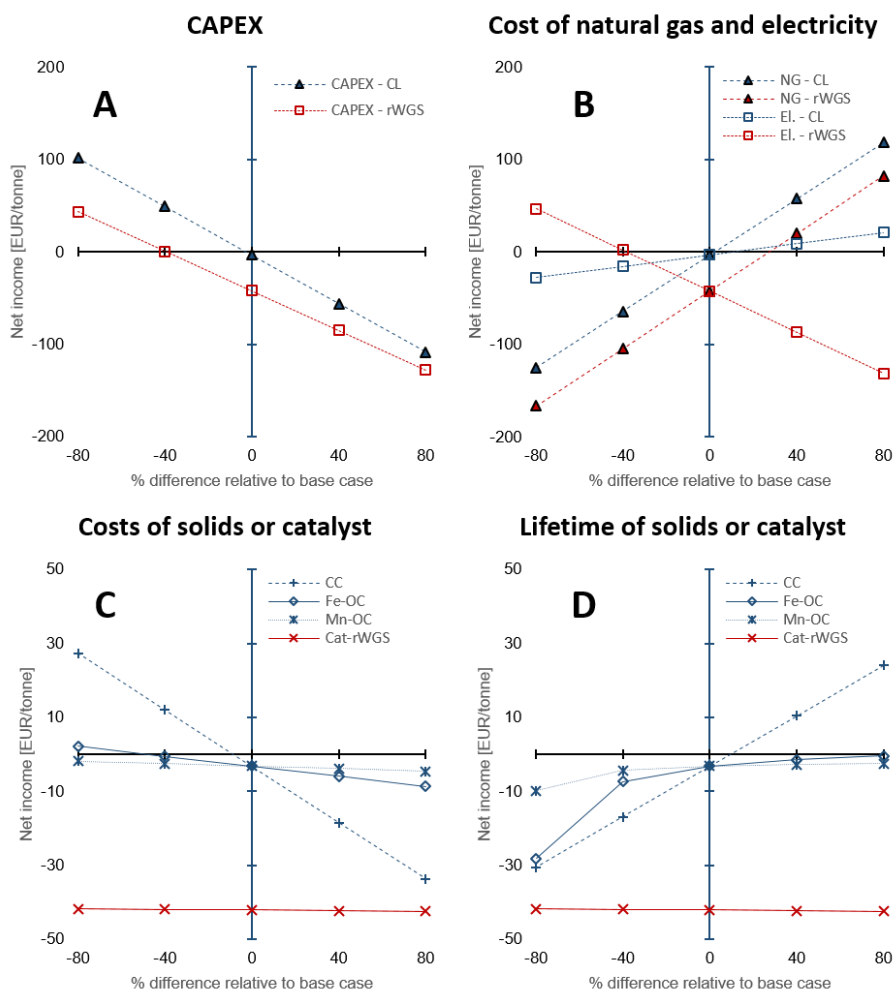


Figure 60: Sensitivity analysis to examine the effect of A: CAPEX estimation, B: Cost of natural gas and electricity, C: Costs of solids: oxygen carriers and CO<sub>2</sub> carrier, or catalyst, and D: their lifetime on the net income defined as the difference between the revenue and the production costs, i.e., CAPEX and OPEX. Abbreviations used in the figure legends: CL – chemical looping, NG – natural gas, El. – electricity, CC – Ca-based CO<sub>2</sub> carrier, Fe-OC – iron based oxygen carrier, Mn-OC – manganese based oxygen carrier, and Cat-rWGS – Ni/Al<sub>2</sub>O<sub>3</sub> catalyst for the reverse water-gas shift reaction.

The sensitivity analysis on the CAPEX displayed in Figure 60 A, shows that for higher than expected capital expenses, significant incentives (for example, an increase in CO<sub>2</sub> prices to approximately 220 EUR<sub>2020</sub>/tonne from 50 EUR<sub>2020</sub>/tonne) would be required to make the processing of the BFG competitive with conventional technologies to produce CO (steam methane reforming followed by reverse water-gas shift [112, 188]). The CAPEX of the chemical looping process is around 18% higher than that of the rWGS process and hence, the sensitivity analysis shows a steeper slope for the change in net income with change in the CAPEX. Figure 60 B shows the influence of the cost of electricity and natural gas on the processes. Depending on the energy mix of the electricity grid, the cost of electricity and natural gas may be highly linked, but in this case, they are treated as independent from each other to highlight the peculiarities of the chemical looping process compared to rWGS followed by downstream separation processes. The price of commercial carbon monoxide is strongly dependent on the price of natural gas[162], thus, an increase in the price of natural gas increases (by a factor of 2 assuming a linear correlation) the market price of CO, thereby increasing the revenue of both processes, which results in an increased net income. The rWGS process is heavily dependent on electricity and thus, lower electricity prices result in increased net income, whereas for the chemical looping process lower electricity prices cause a loss of revenue since the proposed process is a net generator of electricity. An increase in the price of natural gas is

expected to increase the cost of electricity when the electricity in the grid comes from natural gas combustion. An increased price of natural gas would result in a more pronounced increase in the market price of CO. In such a scenario, the chemical looping process would be heavily favoured because of increased revenue from sale of CO and surplus electricity.

The low catalyst consumption in the rWGS makes the net income of the process almost invariant to the cost of the catalyst and its lifetime as seen in Figure 60 C and Figure 60 D. On the other hand, analysis shows that the net income is very sensitive to the CO<sub>2</sub> carrier's cost and also its lifetime because of the large quantities of the material consumed by the process. A decrease in the cost of the CO<sub>2</sub> carrier by 40% or an increase of its lifetime by 40% causes the net income to increase to a value between 15 to 20 EUR/tonne<sub>product</sub>, which is significant for a bulk chemical when compared to the production costs (sum of CAPEX and OPEX) of about 210 EUR/tonne<sub>product</sub> (note that there exist other sources of revenue apart from the sale of product – see Figure 59 E). Compared to the CO<sub>2</sub> carrier, the lifetime and costs of the oxygen carriers have a milder influence on the net income because the quantities involved are 1 order of magnitude smaller.

In the above discussion, changes in the price of CO<sub>2</sub> or carbon tax/carbon credit were not considered. The carbon footprint (equation (64)) of the CO/CO<sub>2</sub> product stream is significantly larger than that of the rWGS process (2.1 tonnes/tonne of product vs 0.8 tonnes/tonne of

product). However, it must be noted that the source of CO<sub>2</sub> emissions in the proposed chemical looping process (stream E in Figure 56) is highly concentrated in CO<sub>2</sub> (mass fraction of CO<sub>2</sub> on dry basis: 0.5), thereby making it much more compliant for CO<sub>2</sub> capture. Using the equation derived by House et al. [178] based on the Sherwood plot, it can be shown that the cost of capturing CO<sub>2</sub> from the proposed chemical looping would be more than 3 times lower than it would be for the flue gas of a natural gas fired power plant, which is estimated to be approximately 70-80 \$<sub>2020</sub>/tonne [190, 191] (calculations are presented in the Appendix D). Thus, it would be more economical to completely eliminate CO<sub>2</sub> emissions from the proposed chemical looping process than in the conventional rWGS followed by downstream separation via mature technologies under atypical circumstances.

#### 6.3.4 Experimental proof of concept

The experimental proof of concept involving the use of 3 metal oxides, namely, CaO, FeO<sub>x</sub> ( $x = 1$  to 1.3), and Mn<sub>3</sub>O<sub>4</sub> was carried out at a temperature of approximately 1023 K. This temperature was chosen because it provided a good compromise between carbon recovery (equation (65)) and the kinetics of decarbonation. All the materials used, FeO<sub>x</sub> ( $x < 1.3$ ) for converting CO<sub>2</sub> to CO, CaO for CO<sub>2</sub> capture and carbon recovery, and MnO for O<sub>2</sub> capture and heat generation were functional over multiple cycles as displayed in Figure 61 B, C, and D. The fuel efficiency (equation (90)) for all cycles was higher than 90% and the

reactor productivity (equation (91)) was above 50 kg<sub>product</sub>/m<sup>3</sup>/h for all the tested cycles [154, 165, 192].

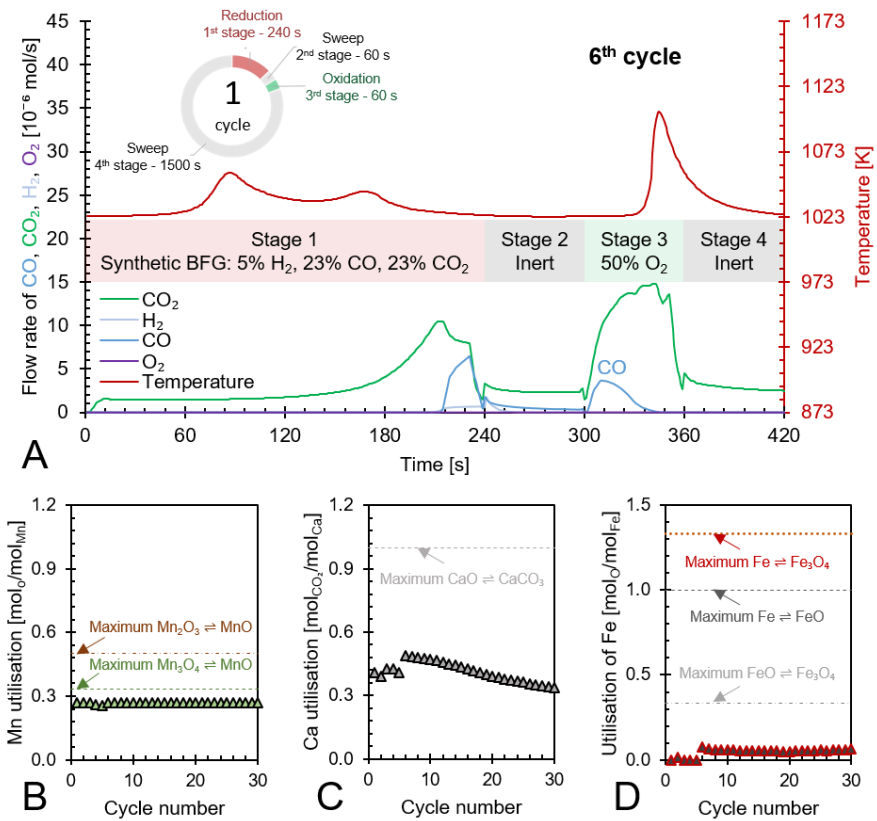


Figure 61: Anti-clockwise from top to bottom – A: the 6<sup>th</sup> cycle of the proposed chemical looping process showcasing its capabilities to use/store the chemical energy from synthetic BFG in stage 1 to produce CO (in stages 2 to 4) while completely using the fed O<sub>2</sub> in stage 3 to create heat for the decarbonation of CaCO<sub>3</sub>, B – utilisation of Mn in the top portion of the bed and its maximum possible utilisation based on reaction stoichiometry, C – utilisation of Ca as CaO in the top and bottom beds of the reactor and its maximum possible utilisation based on reaction stoichiometry, and D – utilisation of Fe in the bottom bed and its maximum possible utilisation based on the transitions of its redox pairs Fe/FeO, Fe/Fe<sub>3</sub>O<sub>4</sub>, or FeO/Fe<sub>3</sub>O<sub>4</sub>.

Figure 61 A displays the experimental results of the 6<sup>th</sup> cycle as an example of a single cycle (corresponding experimental results in an empty reactor are shown in Figure D10). During the reduction stage (stage 1), the reduction of the oxygen carriers,  $\text{Mn}_3\text{O}_4$  and  $\text{FeO}_x$ , occurs with carbonation of  $\text{CaO}$  in an overall exothermic reaction. The exothermicity of the reaction causes the temperature to steadily increase. During this stage, only small amounts of  $\text{H}_2$  or  $\text{CO}$  break through the bed and the amount of  $\text{CO}_2$  in the outlet depends on the equilibrium  $\text{CO}_2$  partial pressure of  $\text{CaCO}_3$ , which is favourably lower at lower temperatures, and the reactivity of  $\text{CaO}$ . Figure 61 A shows that  $\text{CO}_2$  breakthrough occurs at about 200 s, indicating the lack of  $\text{CaO}$ 's reactivity despite excess quantities being available in the reactor (Figure 61 C). A higher reactivity of  $\text{CaO}$  would have resulted in further  $\text{CO}_2$  capture and consistently lower outlet  $\text{CO}_2$  flow. As large quantities of gases are captured in the reduction stage (roughly 50 vol% of the synthetic BFG contains  $\text{CO}$  and  $\text{CO}_2$ , the majority of which is captured by  $\text{CaO}$ ), the outlet molar flow rate of the gas decreases. In the second stage, a purge gas is introduced to the reactor with the same inlet molar flow as that in the reduction stage. This purge gas,  $\text{Ar}$ , favours the decarbonation reaction of  $\text{CaCO}_3$  because it decreases the partial pressure of  $\text{CO}_2$ . The  $\text{CO}_2$  from the decarbonation reaction reacts with the reduced  $\text{FeO}_x$  species to form  $\text{CO}$  ( $< 2 \cdot 10^{-6}$  mol/s), which further accelerates the decarbonation reaction via Le Chatelier's principle [117]. Because the decarbonation reaction is highly endothermic,

visible from the decline in temperature during the second stage, an oxidant stream containing  $O_2$  is fed to the reactor in the oxidation stage (stage 3) to provide the heat necessary for decarbonation by oxidising the reduced MnO in the top bed. As the oxidant stream is fed to the reactor at the same inlet flow rate as the gases in the previous stages, the near complete consumption of  $O_2$  by oxidation of MnO (no  $O_2$  breakthrough observed) causes an overall decrease in the total flow rate. This is visible from the sudden decrease in the measured outlet flow rates of the different gases. As the third stage proceeds, the heat generated not only causes a notable increase in temperature but also favours the decarbonation reaction, which is proved by the increased flow rates of CO and  $CO_2$ . Finally, in the fourth stage, a purge gas feed completes the cycle and prepares the reactor for the next cycle.

The manganese oxide oxygen carriers exhibit highly stable chemical reactivity over multiple cycles (Figure 61 B), thereby justifying the assumption for the process simulation and techno-economic study that other deactivation phenomena may necessitate fresh manganese oxide to be used in the process. Figure 61 C shows that the Ca utilisation is lower in the first 5 cycles. This was caused by the lower reduction time in the first 5 test cycles compared to the remaining 30 cycles. For the sake of completeness, the experimental results of the first 5 cycles are displayed in Figure D5 to Figure D9. Loss of the chemical reactivity of CaO seen in Figure 61 C was likely caused by material sintering. However, this loss is taken into account for the techno-economic study

by considering the addition of fresh CaO to the process (77 kt/year). Figure 61 D shows that Fe utilisation begins after a few cycles because of excess  $\text{Mn}_3\text{O}_4$ , which combusts all the inlet BFG preventing the  $\text{FeO}_x$  in the bottom bed to be reduced during the first stage. Once the  $\text{FeO}_x$  in the bottom bed is reduced, stable chemical reactivity is maintained throughout the tested cycles, which corroborates recent experimental findings [193] and the assumptions made for the process simulation and techno-economic study. Figure 61 D also shows that there is sub-optimal utilisation of Fe. In a fixed bed reactor, higher fuel efficiency typically results in lower material utilisation. One way to circumvent this issue is to use a reverse flow reactor [194, 195], wherein, if the oxidising flow inlet is from top to bottom (see Figure 57), then the reducing gas inlet flow is from bottom to top or vice-versa. For fluidised bed or moving bed reactors, the complete oxidation of reductants to provide energy can simply be carried out in another set of reactor(s) as displayed in Figure 56.

For the process simulations, a low temperature for the reduction-carbonation was used and a higher temperature for the decarbonator-oxidiser. In order to mimic these conditions, the reader is referred to an independent experiment was performed with the Fe-based oxygen carrier, 50%  $\text{Fe}_2\text{O}_3/\text{MgAl}_2\text{O}_4$  and the  $\text{CO}_2$  carrier, 83%  $\text{CaO}/\text{CeO}_2$  by imposing a temperature program (displayed in Figure C20). In this experiment, it is demonstrated that a molar  $\text{CO}:\text{CO}_2$  ratio of



approximately 1 is achievable in the process with a reactor productivity in the range of 98 to 115 kg/m<sup>3</sup>/h.

Requirements of a) large temperature changes in different steps of the process and b) influx of new solids because of deactivation make fluidised beds or moving bed reactors the preferable choice for industrial operation because they avoid thermal stresses to the reactor's material of construction and facilitate uninterrupted operation [196]. In moving bed reactors, highly exothermic and endothermic reactions can lead to significant heat management issues such as hot and/or cold spots. These issues can be managed more readily in fluidised bed reactors [197]. Thus, for the given selection of metal oxides and inlet feed of BFG, fluidised bed reactors may be the preferred choice of reactor type. The operating conditions such as the requirement of temperatures in the different steps or half-cycles of chemical looping and the exothermicity or endothermicity of reactions are determined by the choice of metal oxides. Thus, by choosing metal oxides which facilitate isothermal operation and improve heat management (for example, by splitting the heat of combustion approximately equally over the reduction and oxidation half-cycles), the reactor choice can be further simplified. The use of computational screening of materials could facilitate the search for the ideal combination of metal oxides for the proposed technology [88, 140, 141, 198]. A demonstration of this process on a pilot scale at optimum conditions would help bring it closer to practical implementation and

provide data for further determining its technical and economic viability for large scale efficient utilisation of CO<sub>2</sub>.

## 6.4 Conclusions

A process concept is developed based on chemical looping that exploits equilibrium oxygen partial pressure of metal oxides and equilibrium CO<sub>2</sub> partial pressure of metal carbonates for the production of a CO-rich stream from any gas stream containing fuel and CO<sub>2</sub> under optimal operating conditions. This process concept was adapted to completely utilise the chemical energy of a process gas from the steel industry, the blast furnace gas, and demonstrated in a laboratory fixed bed reactor. The proposed process produces an enriched CO/CO<sub>2</sub> stream free of N<sub>2</sub> from the blast furnace gas, thereby avoiding the CO<sub>2</sub> emissions that combustion of the blast furnace gas typically entails and providing the chemicals industry with valuable feedstock that can be used for creating carbon-based chemicals such as plastics or synthetic fuels.

The process that we have developed makes use of materials composed of cheap and abundant metal oxides which are non-toxic, easy to prepare, use, and dispose. These materials can be, for example, oxides of iron, manganese, and calcium. The analysis carried out in this work shows that the chemical looping process with its advantage of inherent product separation makes it very competitive with a combination of commercially applied technologies to achieve the same performance. Moreover, the fact that the developed process operates

at high temperatures between 873 K and 1153 K enables it to have a very high exergy efficiency. By implementing this technology, a 37% reduction in CO<sub>2</sub> emissions can be achieved, when compared to the current best available technology of combusting the blast furnace gas with air. The rest of the CO<sub>2</sub> emissions from the proposed process can be far more easily captured and stored or utilised to achieve net zero CO<sub>2</sub> emissions than those from a conventional power plant.

Preliminary techno-economic assessment suggests that the developed process would be economically viable when the 50 mol% CO/CO<sub>2</sub> is sold at a price of approximately 190 EUR/tonne for the base case scenario. At this product price, the profits from the proposed chemical looping process are higher than those from conventional steady-state catalytic reverse water-gas shift with downstream separation by 40 EUR/tonne. The economic viability of the process is strongly dependent on the cost and lifetime of the Ca-based CO<sub>2</sub> carrier and the market price of natural gas and electricity.

## Chapter 6

# Intensified blue H<sub>2</sub> production with in situ CO<sub>2</sub> utilisation

### Abstract:

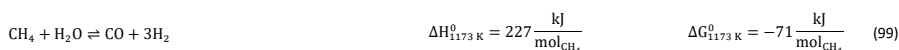
Hydrogen is anticipated to play an increasingly important role as a clean energy carrier but its current production, predominantly through steam methane reforming, causes up to 3% of annual global CO<sub>2</sub> emissions. Herein a carbon-efficient two-step chemical looping process to address the limitations of conventional grey H<sub>2</sub> production is developed. This process for blue hydrogen production operates between 923 to 998 K and involves three solid intermediates: oxides of iron, nickel, and calcium. In the first step, an H<sub>2</sub>-rich stream is produced by co-feeding steam and methane to these materials in a fixed bed, while in the second step, a CO-rich stream is produced by regenerating the materials with an air-like mixture. Proof-of-concept experiments achieved an H<sub>2</sub> concentration of more than 65 mol% and a CO<sub>2</sub> conversion of more than 80%.

### **This chapter was published as**

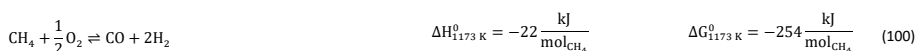
V. Singh, L.C. Buelens, H. Poelman, M. Saeys, G.B. Marin, V.V. Galvita. Intensifying blue hydrogen production by in situ CO<sub>2</sub> utilisation. Journal of CO<sub>2</sub> Utilization. 61 (2022) 102014.

## 7.1 Introduction

Hydrogen production is highly energy-intensive and was responsible for emitting almost one gigatonne of CO<sub>2</sub> to the environment in 2018 [32]. Steam methane reforming (equation (99)) is the most mature and widely applied technology [31], but it suffers from significant drawbacks such as 1) the necessity to supply heat at very high temperatures because of the endothermicity of the reaction, 2) generation of heat for producing excess steam (2 to 3 times more than the stoichiometric requirement [31, 199]) to limit deactivation phenomena such as coking [200] and shift the reaction equilibrium towards H<sub>2</sub> production, and 3) purification and separation of H<sub>2</sub> from a product mixture containing CO, CO<sub>2</sub>, CH<sub>4</sub>, and H<sub>2</sub>O using water-gas shift reactors and pressure swing adsorption (PSA).

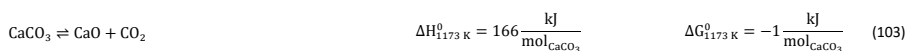
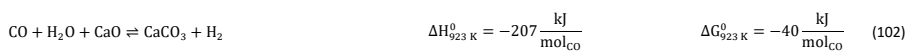
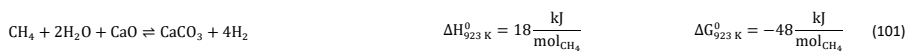


Points 1) and 2) can be addressed by either catalytic partial oxidation (CPO) of methane to syngas (equation (100)) or a combination of partial oxidation with steam methane reforming [201]. However, improved heat management from CPO comes at the cost of safety concerns related to mixing gaseous fuel and O<sub>2</sub> at a high temperature, deactivation due to coking, and sub-stoichiometric yields of H<sub>2</sub> [202-204].



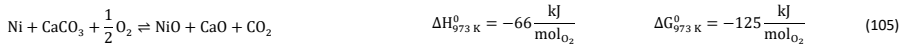
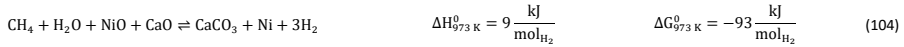
Points 1) and 3) are addressed by sorption-enhanced steam methane reforming (SESR) to produce so-called blue hydrogen, i.e. hydrogen

based on fossil fuel with CO<sub>2</sub> capture. SESR (presented by equation (101) in its simplified form) and the closely related sorption-enhanced water-gas shift (SEWGS) (equation (102)) are highly promising technologies that use a CO<sub>2</sub> sorbent such as CaO to shift the thermodynamic equilibrium towards high purity H<sub>2</sub> at temperatures around 923 K [205]. The captured CO<sub>2</sub> is then, in a second step, released through decomposition of CaCO<sub>3</sub> (equation (103)) by supplying heat at temperatures of around 1173 K [79] or by decreasing the partial pressure of CO<sub>2</sub> [206] so that the decarbonated CO<sub>2</sub> carrier, CaO, can be re-used for SESR and SEWGS. The substantial energy required for the decarbonation is a major drawback of these two process concepts [207].

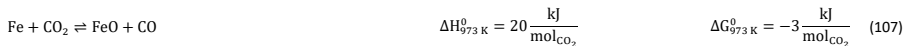
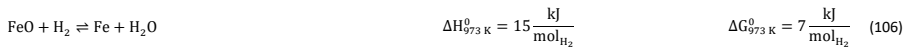


To overcome the limitations of the state of the art, this work developed a solution to shift the equilibria in the desired direction and improve the heat management by using three solid intermediates. An oxygen carrier such as NiO replaces O<sub>2</sub> used for the partial oxidation of methane (equation (100)) while a CO<sub>2</sub> carrier is used to favour the production of H<sub>2</sub>. In a first step (equation (104)), the endothermic reduction of NiO to Ni by CH<sub>4</sub> is coupled with the exothermic carbonation of CaO by CO<sub>2</sub> (reverse reaction of equation (103)). Once NiO is reduced, Ni catalyses the endothermic steam methane reforming

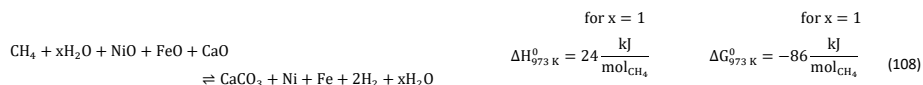
reaction (equation (99)) while any CO<sub>2</sub> formed continues to be captured by CaO (equation (102)) [208]. In a second step (equation (105)), O<sub>2</sub> from air or another source is used for the exothermic oxidation of Ni to NiO, which provides heat for the endothermic decarbonation of CaCO<sub>3</sub> (equation (103)) to release the captured CO<sub>2</sub> [209].



An oxygen carrier such as FeO<sub>x</sub> (where x = 0.9 to 1.3) is placed downstream of the first two solids for achieving in situ utilisation of the released CO<sub>2</sub> [210]. In the first step, a fraction of the H<sub>2</sub> produced reduces FeO<sub>x</sub> to Fe (equation (106), where FeO is shown as an example). In the second step, the CO<sub>2</sub> released from the decarbonation of CaCO<sub>3</sub> oxidises the Fe back to FeO<sub>x</sub> (equation (107)). Such application of the Fe/FeO<sub>x</sub> cycle is also known as chemical looping – reverse water-gas shift (CL-rWGS) [106, 108, 211, 212]. The combination of CL-rWGS with a CO<sub>2</sub> carrier has been successfully demonstrated in super-dry reforming [117] and other combined chemical looping processes [1, 213]. This combination allows decarbonation to occur at a far lower temperature than the typical range of 1173 K to 1223 K and ensures the CO<sub>2</sub> partial pressure remains low, thereby extending the life-time of the CO<sub>2</sub> carrier [9, 100, 134].



The net overall reaction equations of the first and second step of the proposed process are given in equations (108) and (109) and a process schematic is presented in Figure 62. Thus, optimal heat management is achieved by splitting the heat of the partial methane oxidation to syngas (equation (100)) into two steps for an intensified process that can produce separate high purity streams of H<sub>2</sub>, a clean energy carrier, and CO, a platform molecule for a plethora of carbon based products [214]. Such a concept differs from chemical looping partial oxidation which produces syngas, a mixture of CO and H<sub>2</sub>, in one step and an O<sub>2</sub>-depleted stream in another [215, 216]. It also differs from chemical looping reforming, either with CO<sub>2</sub> and/or H<sub>2</sub>O, which requires supply of heat in at least one of the two steps of the process and creates a mixed syngas stream in at least one step of the process [217, 218].





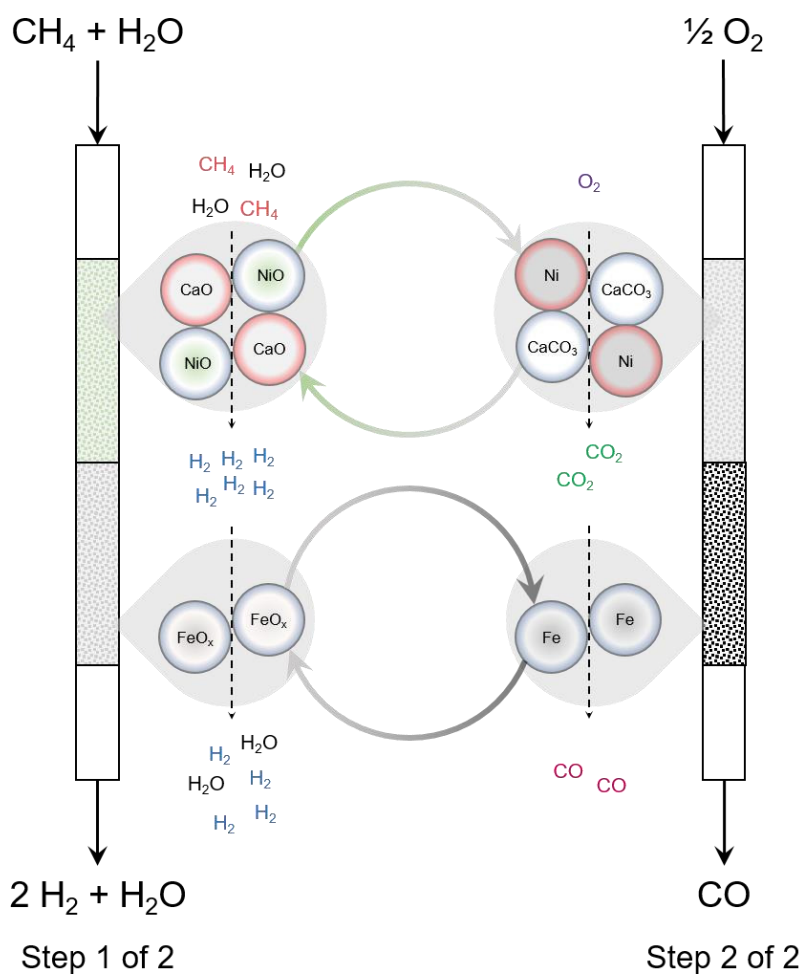


Figure 62: Schematic representations of the process with the left half depicting a first step for  $\text{H}_2$  production and the right half depicting  $\text{CO}$  production in a second step. The blue and red shading at the peripheries of the solid intermediates (represented by circles) indicate heat uptake or release in that step. Steam is added to the feed gas in step 1 to shift reaction equilibrium towards  $\text{H}_2$  production in the top half of the bed and create conditions less favourable for coke formation. For the sake of simplicity, an equimolar ratio of  $\text{H}_2\text{O}$  and  $\text{CH}_4$  in step 1 of 2 is shown.

## 7.2 Methods

### 7.2.1 Thermodynamic calculations

To quantify the thermodynamic boundaries of the process, equilibrium calculations were carried out using the 'Equilib' module and FactPS database in FactSage 8.1 [119]. All calculations were performed assuming 1 mol of NiO, CaO, Fe<sub>3</sub>O<sub>4</sub>, CH<sub>4</sub> and H<sub>2</sub>O unless mentioned otherwise. The formation of mixed calcium iron oxides was restricted because 1) their formation is experimentally not observed and 2) FeO<sub>x</sub> and CaO are spatially separated in the reactor on a micrometer scale. For calculating the equilibrium conversion of CH<sub>4</sub> in CPO, negligible coke formation was assumed.

### 7.2.2 Concept demonstration

For the experimental proof of concept, the multifunctional material comprising NiO, CaO, and CeO<sub>2</sub> was situated in the top bed and a physical mixture of the oxygen and CO<sub>2</sub> carriers was situated in the bottom bed (Figure 63). The CO<sub>2</sub> carrier was placed in close proximity to the Fe-based oxygen carrier in the lower bed to further capture any carbon containing compounds via reactions (102) and (103). All three materials, the multifunctional material, oxygen carrier, and CO<sub>2</sub> carrier were pelletised, crushed, and sieved to obtain aggregates in the size range of 355 to 500 µm before being used in the reactor. For feeding steam, a Coriolis MFC (Brooks-Coriolis) was used to feed deionised water to an evaporator operating at 453 K. The inlet lines and valves

were heated by heat tracing elements with a temperature set point of 403 K.

The process concept was tested in different conditions (temperature and time duration) over multiple cycles. The first ten cycles were performed at 973 K with a cycle time of 334 seconds. After the first 10 cycles, O<sub>2</sub> was introduced in the reactor bed for an extended period to check if coke was deposited after the previous oxidation half-cycle (10<sup>th</sup> cycle). The next ten cycles (11 to 20) were again executed at 973 K with a shortened cycle time (89 seconds). In the 21<sup>st</sup> cycle, the hypothesis of carbon capture via calcium oxide was tested by ramping the temperature instead of introducing 21% O<sub>2</sub>/Ar in the second step of the process. Thereafter, 3 cycles (22 to 24) were executed at 923 K with a cycle time of 334 seconds used previously. The process temperature was increased for the next cycle (25<sup>th</sup> cycle) to 998 K and finally, in the 26<sup>th</sup> cycle, process conditions identical to the first 10 cycles were applied.

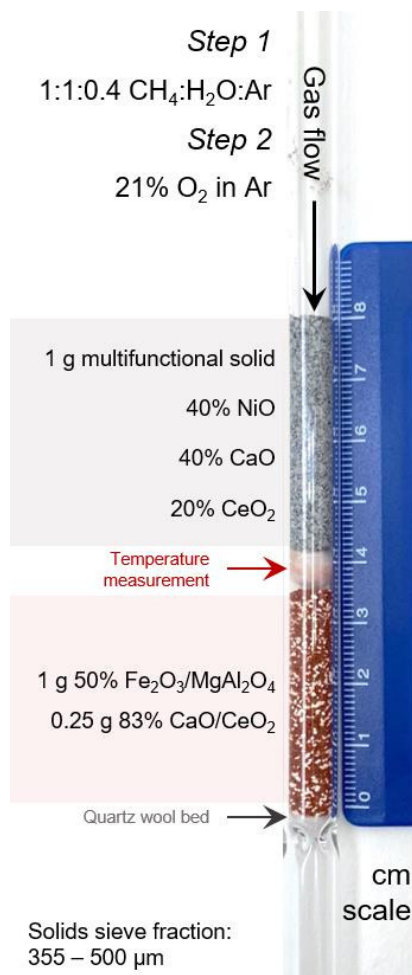


Figure 63. Fixed bed reactor configuration for the production of an H<sub>2</sub> and CO-rich stream in a 2-step looping process. Percentages for solids and gases are displayed in mass% and mol%.

### 7.2.3 Process and experimental performance metrics

To assess the performance of the experiment, materials, and process concept, the following performance metrics are defined and quantified.

The carbon balance (CB) calculated using equation (110) was closed within 7% for all experiments.  $t_{\text{total}}$  (s) indicates the time at which the cycle ends, i.e. when there is no further outlet flow of CO or CO<sub>2</sub>.  $\dot{n}_A$  (mol/s) represents the molar flow rate of component “A” and the subscripts in and out indicate inlet and outlet flows.

$$\text{CB} = \frac{\int_0^{t_{\text{total}}} \dot{n}_{\text{CH}_4, \text{in}} dt - \int_0^{t_{\text{total}}} \dot{n}_{\text{CO}_2, \text{out}} dt - \int_0^{t_{\text{total}}} \dot{n}_{\text{CO}, \text{out}} dt}{\int_0^{t_{\text{total}}} \dot{n}_{\text{CH}_4, \text{in}} dt}$$

CH<sub>4</sub> and CO<sub>2</sub> conversions ( $X_{\text{CH}_4}$  and  $X_{\text{CO}_2}$ ) are calculated over the first and second step of the process.  $t_{\text{step 1}}$  and  $t_{\text{step 2}}$  indicates the total time duration of step 1 and step 2.

$$X_{\text{CH}_4} = \frac{\int_0^{t_{\text{step 1}}} \dot{n}_{\text{CH}_4, \text{in}} dt - \int_0^{t_{\text{step 1}}} \dot{n}_{\text{CH}_4, \text{out}} dt}{\int_0^{t_{\text{step 1}}} \dot{n}_{\text{CH}_4, \text{in}} dt} * 100$$

$$X_{\text{CO}_2} = \frac{\int_0^{t_{\text{step 2}}} \dot{n}_{\text{CO}, \text{out}} dt}{\int_0^{t_{\text{step 2}}} (\dot{n}_{\text{CO}, \text{out}} + \dot{n}_{\text{CO}_2, \text{out}}) dt} * 100$$

Utilisation of Ni and Fe ( $U_{\text{Ni}}$  and  $U_{\text{Fe}}$ ) are based on the outlet gas flows of the second step, whereas the utilisation of Ca ( $U_{\text{Ca}}$ ) is based on the outlet gas flows of the first step.  $n_{\text{Ni}}$ ,  $n_{\text{Fe}}$ , and  $n_{\text{Ca}}$  are the moles of Ni, Fe, and Ca in the reactor bed.

$$U_{\text{Ni}} = \frac{\int_0^{t_{\text{step 2}}} (2 * (\dot{n}_{\text{O}_2, \text{in}} - \dot{n}_{\text{O}_2, \text{out}})) dt}{N_{\text{Ni}}}$$

$$U_{\text{Fe}} = \frac{\int_0^{t_{\text{step 2}}} (\dot{n}_{\text{CO}, \text{out}}) dt}{N_{\text{Fe}}}$$

$$U_{\text{Ca}} = \frac{\int_0^{t_{\text{total}}} \dot{n}_{\text{CH}_4, \text{in}} dt - \int_0^{t_{\text{step 1}}} \dot{n}_{\text{CO}_2, \text{out}} dt - \int_0^{t_{\text{step 1}}} \dot{n}_{\text{CO}, \text{out}} dt}{N_{\text{Ca}}}$$

The maximum experimental utilisation ( $\overline{U}_x$ ) is calculated based on the stoichiometry of reactions (equation (109) for Ni and Fe and

equation (108) for Ca). For every mol of CH<sub>4</sub> fed, a maximum of 1 mol of CO could be produced by Fe and a maximum of 1 mol of CO<sub>2</sub> could be captured by Ca. Similarly, for every mol of O<sub>2</sub> fed, a maximum of 2 mol of Ni could be utilised.

$$\overline{U}_{Ni} = \frac{\int_0^{t_{\text{step } 2}} (2 * (\dot{n}_{O_2, \text{in}} - \dot{n}_{O_2, \text{out}})) dt}{N_{Ni}}$$

$$\overline{U}_{Fe} = \frac{\int_0^{t_{\text{step } 1}} (\dot{n}_{CH_4, \text{in}}) dt}{N_{Fe}}$$

$$\overline{U}_{Ca} = \frac{\int_0^{t_{\text{step } 1}} (\dot{n}_{CH_4, \text{in}}) dt}{N_{Ca}}$$

The H<sub>2</sub> and CO concentrations ( $y_{H_2}$  and  $y_{CO}$ ) expressed in mol% are calculated using equations (119) and (120) on an H<sub>2</sub>O and Ar free basis.

$$y_{H_2} = \frac{\int_0^{t_{\text{step } 1}} (\dot{n}_{H_2, \text{out}}) dt}{\int_0^{t_{\text{step } 1}} (\dot{n}_{CO, \text{out}} + \dot{n}_{CO_2, \text{out}} + \dot{n}_{CH_4, \text{out}} + \dot{n}_{H_2, \text{out}}) dt} * 100$$

$$y_{CO} = \frac{\int_0^{t_{\text{step } 2}} (\dot{n}_{CO, \text{out}}) dt}{\int_0^{t_{\text{step } 2}} (\dot{n}_{CO, \text{out}} + \dot{n}_{CO_2, \text{out}} + \dot{n}_{CH_4, \text{out}} + \dot{n}_{H_2, \text{out}}) dt} * 100$$

The reactor productivity (RP) defined in equation (121) has the units of  $\left(\frac{\text{kg}_{\text{product}}}{\text{m}^3_{\text{reactor}} \cdot \text{h}}\right)$  and  $MM_{H_2}$  and  $MM_{CO}$  are molar masses of H<sub>2</sub> and CO in kg/mol,.  $V_{\text{reactor}}$  is calculated by measuring the length of the packed bed (Figure 63) and assuming that the reactor has a cylindrical shape.

$$RP = \frac{\int_0^{t_{\text{step } 1}} (\dot{n}_{H_2, \text{out}}) dt * MM_{H_2}}{V_{\text{reactor}} * t_{\text{step } 1}} + \frac{\int_0^{t_{\text{step } 2}} (\dot{n}_{CO, \text{out}}) dt * MM_{CO}}{V_{\text{reactor}} * t_{\text{step } 2}}$$

## 7.3 Results and Discussion

### 7.3.1 Material characterisation

SEM-EDX results displayed in Table 22 confirmed that the composition of the synthesised material was close to the targeted composition. A summary of the textural properties of the synthesised materials displayed in Table 23 indicates modest surface areas, particle sizes, and pore volumes. The X-ray diffractograms of the synthesised materials containing calcium (Figure 64 A and B) show the existence of  $\text{Ca(OH)}_2$  and  $\text{CaCO}_3$ . These phases are formed because of the high reactivity of  $\text{CaO}$  in the synthesised material with  $\text{H}_2\text{O}$  and  $\text{CO}_2$  in ambient air. The diffraction peaks of the synthesised oxygen carrier, 50%  $\text{Fe}_2\text{O}_3/\text{MgAl}_2\text{O}_4$ , show the existence of complex spinel phases and  $\text{Fe}_2\text{O}_3$  (Figure 64 C). Temperature programmed reduction and carbonation-decarbonation of the multifunctional material (Figure 65 A and B) indicate the material has a total oxygen storage capacity of  $4.3 \text{ mmolO/g}_{\text{material}}$  and  $\text{CO}_2$  capture/release capacity of  $5.1 \text{ mmolCO}_2/\text{g}_{\text{material}}$ . Detailed characterisation of 50%  $\text{Fe}_2\text{O}_3/\text{MgAl}_2\text{O}_4$  and 83%  $\text{CaO/CeO}_2$  has been reported in previous publications [53, 193].

Table 22: Elemental composition using energy dispersive x-ray spectroscopy (EDX) expressed in mass percentage (on an oxygen-free basis) of the materials used for the experimental demonstration of the process concept. The error indicates the standard deviation based on at least four measurements. Values in brackets indicate expected values based on the nominal composition.

Element	50% Fe <sub>2</sub> O <sub>3</sub> /MgAl <sub>2</sub> O <sub>4</sub>	83% CaO/CeO <sub>2</sub>	40% CaO - 40% NiO - 20% CeO <sub>2</sub>
Fe	59.9 ± 1.5 (56.0)	-	-
Ni	-	-	42.5 ± 1.2 (41.2)
Mg	10.8 ± 0.4 (13.7)	-	-
Al	29.3 ± 1.8 (30.3)	-	-
Ca	-	74 ± 4 (81)	34.8 ± 0.9 (37.5)
Ce	-	26 ± 4 (19)	22.7 ± 0.8 (21.3)

Table 23: Textural properties of the as prepared materials from nitrogen sorption measurements at 77 K.

	50% Fe <sub>2</sub> O <sub>3</sub> /MgAl <sub>2</sub> O <sub>4</sub>	83% CaO/CeO <sub>2</sub>	40% NiO – 40% CaO – 20% CeO <sub>2</sub>
BET surface area [m <sup>2</sup> /g]	41.5	6.3	8.5
Pore volume [10 <sup>-9</sup> m <sup>3</sup> /g]	258	18	23
BJH desorption pore diameter [nm]	22.5	32.7	16.6
Particle size [nm]	33	237	130



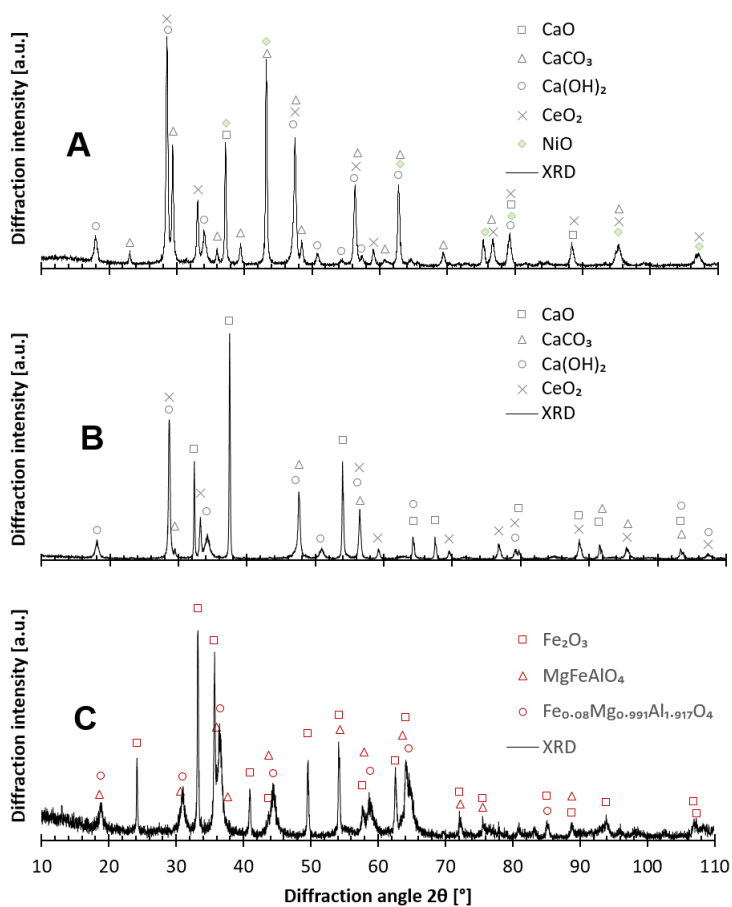


Figure 64: X-ray diffractograms of A: 40% NiO – 40% CaO – 20% CeO<sub>2</sub>, B: 50% Fe<sub>2</sub>O<sub>3</sub>/MgAl<sub>2</sub>O<sub>4</sub>, and C: 83% CaO/CeO<sub>2</sub>.

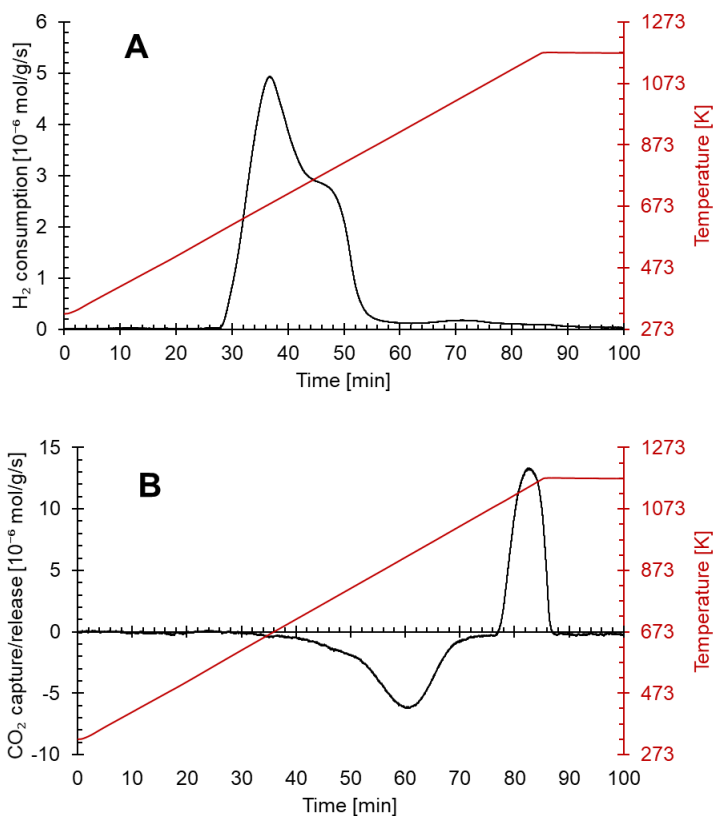


Figure 65: TPre with a temperature ramp of 10 K/min up to 1173 K and a total flow rate of  $45 \cdot 10^{-6}$  mol/s for the multifunctional material, 40% NiO – 40% CaO – 20% CeO<sub>2</sub>. A: H<sub>2</sub>-TPR under a flow of 5 mol% H<sub>2</sub> in Ar for the determination of exchangeable oxygen atoms; B: CO<sub>2</sub>-TPCD under a flow of 20% CO<sub>2</sub> in Ar for the determination of the CO<sub>2</sub> capture and release capacity.

### 7.3.2 Thermodynamic assessment

Thermodynamic analysis shows that the conversion of  $\text{CH}_4$  ( $X_{\text{CH}_4}$ ) and the concentration of  $\text{H}_2$  ( $y_{\text{H}_2}$ ) are impacted differently by an increase in temperature.  $y_{\text{H}_2}$  is negatively impacted by an increase in temperature because the sorption effect of  $\text{CaO}$  diminishes with increasing temperature (Figure E4). As shown in Figure 66 A, an increase in temperature by approximately 80 K causes a marginal increase of  $X_{\text{CH}_4}$  by 1%. These results show that using a  $\text{CO}_2$  carrier such as  $\text{CaO}$  plays an influential role in shifting the equilibrium towards  $\text{H}_2$ , thereby allowing production of  $\text{H}_2$  streams with high purity (>70%).

Unlike temperature, an increase in pressure at different temperatures causes a drop in  $X_{\text{CH}_4}$ . This is caused because steam methane reforming (equation (99)) forms 4 product moles from 2 reactant moles and is, thus, favoured by lower product partial pressure according to Le Chatelier's principle. Increasing the total pressure increases the partial pressure of  $\text{CO}_2$  formed from oxidation and water-gas shift reactions. The increased partial pressure of  $\text{CO}_2$  favours its capture by  $\text{CaO}$ , thereby resulting in a product stream with a higher  $y_{\text{H}_2}$ . As shown in Figure 66 B, the improvement in  $y_{\text{H}_2}$  is limited only to a certain pressure range beyond which increasing total partial pressure causes decreased  $y_{\text{H}_2}$ . This suggests that beyond a certain range of pressure, upon increasing the total pressure, the negative influence of

decreased  $\text{CH}_4$  conversion becomes greater than the positive influence of sorption enhancement on  $y_{\text{H}_2}$ .

As iron oxide is used as a redox active oxygen carrier for CL-rWGS, its reduction during  $\text{H}_2$  production is critical to ensure that the captured  $\text{CO}_2$  is converted to  $\text{CO}$  in the second step of the process. An increase in steam partial pressure impedes the reduction of iron oxide because of thermodynamic constraints (Figure E6). Figure 66 C shows that as long as the molar ratio of  $\text{H}_2\text{O}$  to  $\text{CH}_4$  is less than 1.5, reduction of iron oxide remains feasible. The influence of  $\text{H}_2\text{O}$  to  $\text{CH}_4$  molar ratio is not significant on either  $X_{\text{CH}_4}$  or  $y_{\text{H}_2}$ . The small decreasing trend in  $X_{\text{CH}_4}$  up till  $\text{H}_2\text{O}$  to  $\text{CH}_4$  molar ratio of 1.65 corresponds with a weakening sorption enhancement effect noted by decreasing conversions of  $\text{CaO}$  (not shown). This can be attributed to the decreasing partial pressure of  $\text{CO}_2$  caused by increasing the fraction of steam. Beyond a  $\text{H}_2\text{O}$  to  $\text{CH}_4$  molar ratio of 1.65,  $\text{CaO}$  conversion increases and appears to be favoured by improved thermodynamic conditions for steam methane reforming and water-gas shift reaction.

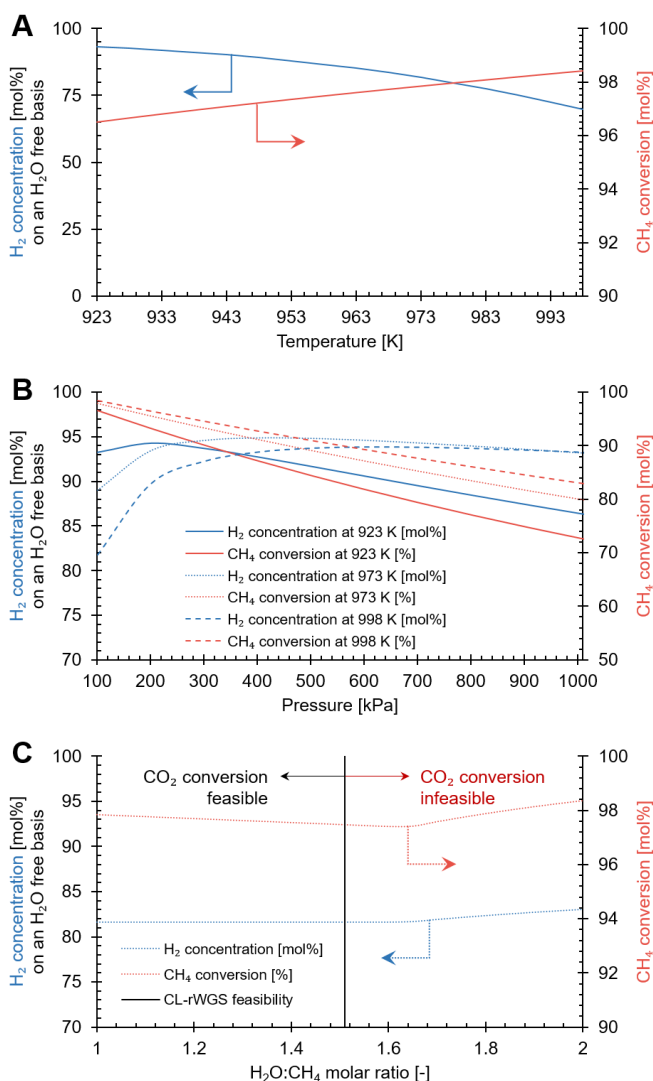


Figure 66: Thermodynamic analyses to examine the influence of temperature (A) and total pressure (B) on  $\text{H}_2$  purity and  $\text{CH}_4$  conversion. In sub-figure A, the pressure was kept constant at 101 kPa and the  $\text{H}_2\text{O}:\text{CH}_4$  molar ratio was kept constant at 1. In sub-figure B, only the  $\text{H}_2\text{O}:\text{CH}_4$  molar ratio was kept constant at 1. In sub-figure C, the temperature was kept constant at 973 K and the pressure was kept constant at 101 kPa.

### 7.3.3 Concept demonstration

Figure 67 shows the experimental results of the process at temperatures between 923 and 998 K. The selected temperature range ensures that the reaction kinetics are sufficiently fast and that carbonation of CaO is thermodynamically favoured (a detailed treatment of thermodynamics over a wider temperature range is provided in Appendix E– Figure E1 to Figure E8). Figure 67 A shows that at 923 K, CO<sub>2</sub> capture is highly efficient and very little CO (1.6 mol%) and CO<sub>2</sub> (1.6 mol%) were observed in the outlet flow during the first step. However, a lower temperature of 923 K results in a fairly low conversion of CH<sub>4</sub> of around 53% (equation (111)) and a time-averaged H<sub>2</sub> concentration of 47% (equation (119)). Increasing the process temperature to 973 K (Figure 67 B), an H<sub>2</sub> concentration of 64 mol% was observed in the first step, corresponding to 71% CH<sub>4</sub> conversion. When the temperature was further increased to 998 K, the concentration of H<sub>2</sub> increased to 65 mol% and that of CH<sub>4</sub> decreased to 15 mol%, indicating a higher conversion of CH<sub>4</sub> (from 71% at 973 K to 81% at 998 K). The dilution of the feed stream with Ar, an inert used for analytical purposes, in the first step decreases the effectiveness of the CO<sub>2</sub> carrier (i.e. less CO<sub>2</sub> captured) by lowering the partial pressure of any CO<sub>2</sub> that is formed, contributing to lower CH<sub>4</sub> conversion due to weaker influence of sorption enhancement on the process (equation (104)). Sub-equilibrium CH<sub>4</sub> conversion could also be explained by the limited availability of metallic Ni for catalysing the reforming and water-gas

shift reactions. More metallic Ni can be made available by using shorter cycle times, which implies that the amount of O<sub>2</sub> fed in step 2 becomes insufficient to oxidise the excess Ni available in the reactor bed to NiO. This causes an increase of CH<sub>4</sub> conversion to 80% at 973 K (up from 71%) corresponding to an increase in Ni not participating in Ni/NiO redox transitions (experimental results are displayed in Figure E9). Based on these results and the thermodynamic calculations described in the previous section 7.2.1 (Figure 66 A), there is a clear scope for further optimisation of the temperature, pressure, and H<sub>2</sub>O:CH<sub>4</sub> molar ratio used in the first step.

In the second step, starting from the 170<sup>th</sup> second, the inlet gas was switched from the CH<sub>4</sub>, H<sub>2</sub>O, and Ar feed to an air-like mixture comprising 21 mol% O<sub>2</sub> in Ar. These conditions were maintained during 165 seconds to ensure that for every mole of CH<sub>4</sub> fed in the first step, 0.5 mole of O<sub>2</sub> was used (corresponding to the stoichiometric amount of O<sub>2</sub> required by partial oxidation of CH<sub>4</sub> shown in equation (100)). At 923 K (Figure 67 A), the slower kinetics and unfavourable thermodynamics of decarbonation probably caused the lower CO production. In the experimental runs at 973 K and 998 K (Figure 67 B and C), almost immediately after the gas stream was switched, a sharp increase in the CO outlet flow was followed by a stable period of CO production and finally, a slow decline. No breakthrough of the fed O<sub>2</sub> was observed in any of the experiments at temperatures between 923 and 998 K, thereby confirming the near complete consumption of O<sub>2</sub> by

Ni. By increasing the operating temperature to 998 K, 79% of the  $\text{CO}_2$  released in the second step was converted to CO (equation (112)), resulting in a CO concentration of 58 mol% on an  $\text{H}_2\text{O}$  and Ar free basis. A large fraction of the outlet gas from the second step was composed of  $\text{H}_2$ , likely caused by remnant  $\text{H}_2\text{O}$  in the tubes carrying the inlet gases causing the production of  $\text{H}_2$  on reduced Fe (reverse of reaction (106)). Eliminating the remnant  $\text{H}_2\text{O}$ , possibly by an intermediate purge step and more efficient tube heating, should drastically improve the CO concentration of the outlet gas in the second step by avoiding 1) the water-gas shift reaction and 2) the oxidation of reduced  $\text{FeO}_x$  by  $\text{H}_2\text{O}$  instead of  $\text{CO}_2$ . A small fraction of  $\text{CaCO}_3$  that remained after the second step was decarbonated by a temperature ramp to 1073 K in Ar flow (Figure E10). Incomplete decarbonation of  $\text{CaCO}_3$  is caused by heat loss from the reactor and can be avoided by improved insulation of the reactor chamber to allow near adiabatic operation. For example, at 998 K, after the second step, only 14% of the  $\text{CaCO}_3$  had not been decarbonated.



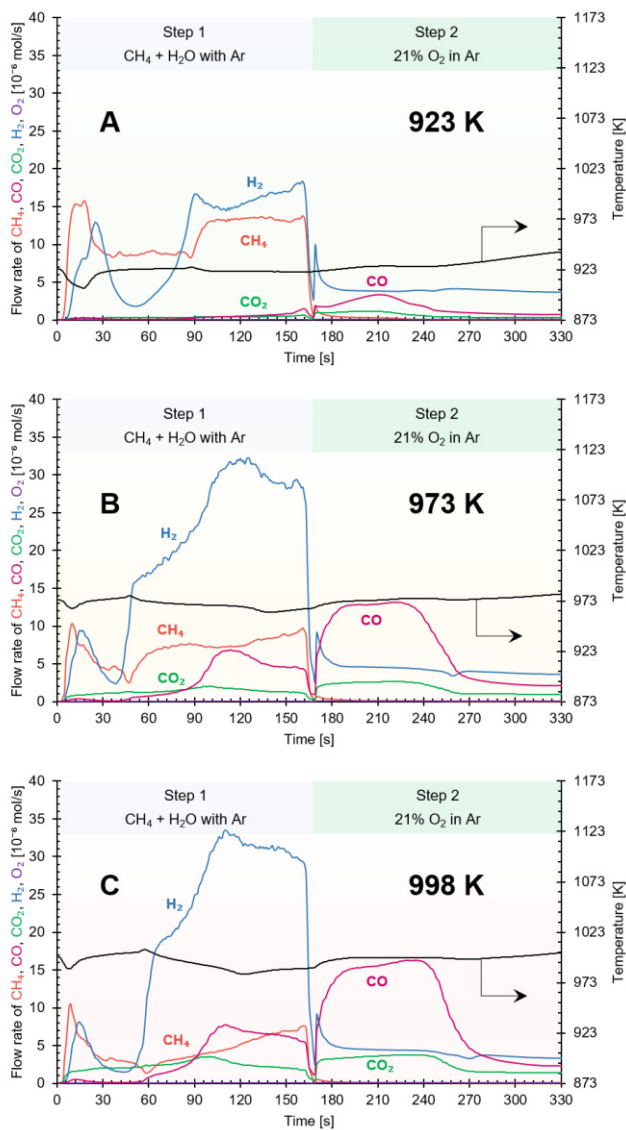


Figure 67. Proof-of-concept experiment for the 2-step chemical looping process to produce an H<sub>2</sub>-rich stream in step 1 and a CO-rich stream in step 2, performed at different temperatures and 120 kPa. The experimental results shown here were A) at 923 K (cycle#24 in Figure 69), B) at 973 K (cycle#26 in Figure 69), and C) at 998 K (cycle#25 in Figure 69).

To prove that the process strategy is driven by carbon storage in the CO<sub>2</sub> carrier and not as carbon from methane cracking and reverse Boudouard reaction [219] (Figure E1 and Figure E2), an experiment was performed in which Ar was fed instead of an O<sub>2</sub>/Ar mixture and a temperature ramp was imposed in the second step. The results (Figure 68) show that, in the absence of fed O<sub>2</sub>, a CO-rich stream is still produced by decarbonation of CaCO<sub>3</sub> via increased temperature and reduced partial pressure of CO<sub>2</sub>. To confirm that coke accumulation is avoided in the cyclic operation of the described process concept, an O<sub>2</sub> post-treatment was executed after the first 10 cycles of the experimental campaign (Figure E11). The accumulation of coke over 10 cycles was negligible as expected from the addition of steam in the first step and oxidising conditions in the second step [220, 221]. After more than 20 cycles, the ratio of H<sub>2</sub> produced in the first step to that of CO produced in the second step was approximately 2 for the experimental runs between 973 K and 998 K, corresponding to the H<sub>2</sub>/CO ratio expected from partial oxidation of CH<sub>4</sub> (equation (100)). Since the process concept produces an H<sub>2</sub>-rich and CO-rich stream alternatingly, a set of parallel packed bed reactors operating simultaneously [40] and/or the use of a buffer vessel [222] could provide a consistent flow of both product streams.

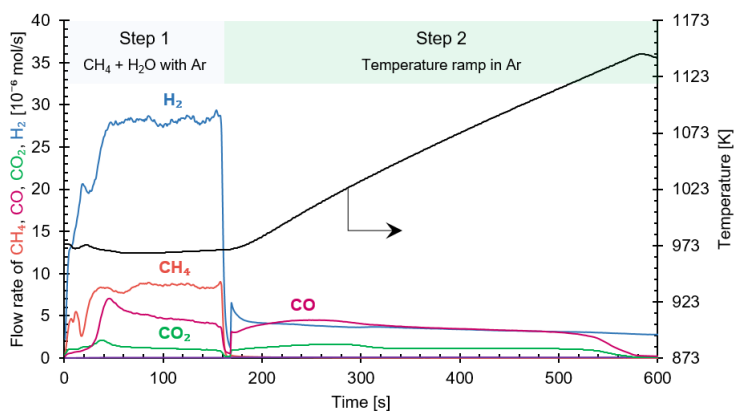


Figure 68: Experiment to prove that the carbon content of CH<sub>4</sub> is captured by CaO (cycle#21 in Figure 69). Total gas flow rate:  $55 \cdot 10^{-6}$  mol/s. Duration of the first step: 169 seconds.

### 7.3.4 Process and experimental performance indicators

Figure 69 shows that the process performance remains consistent over multiple cycles. Textural properties and temperature programmed reactions of materials after the experiments (Table E1 and Figure E12) also prove that the materials retain their functional properties and do not show significant degradation of their textural properties. Figure 69 A shows that only a small fraction (32%) of catalytically active Ni is present from cycles 1 to 10. Thus, if the catalytic conversion of  $\text{CH}_4$  is lower than desired, the fraction of catalytically active Ni available could be increased by utilising a smaller fraction of Ni for redox cycling between Ni/NiO. Indeed, by reducing the cycle time in cycles 11 to 20, a consistently higher conversion of  $\text{CH}_4$  is observed (Figure 69 F). Figure 69 B and C show underutilisation of the oxygen carrier  $\text{FeO}_x$  and  $\text{CO}_2$  carrier  $\text{CaCO}_3$ , which causes an excessively large bed and thus, lower reactor productivity (Figure 69 E). The reactor productivity is, except for the short cycles 11 to 20, higher than  $100 \text{ kg}_{\text{product}}/\text{m}^3_{\text{reactor}}/\text{h}$ , the minimum value for industrial application recommended by Lange [154, 165]. An even higher productivity can be achieved by further optimisation of the material utilisation. In Figure 69 D, concentrations of  $\text{H}_2$  observed in the first step (more than 60% on an  $\text{H}_2\text{O}$  and Ar free basis) over multiple cycles are consistently higher than the equilibrium  $\text{H}_2$  concentrations (52 to 58%, depending on the temperature) for steady-state catalytic partial oxidation of methane. The concentration of  $\text{H}_2$  measured during the experiments exceeds that obtained in an

industrial auto-thermal reforming plant (64% H<sub>2</sub>) which is operated at a far higher temperature of 1323 K [223]. Thermodynamic calculations suggest that further increasing the H<sub>2</sub> concentration in the first step to reach 70% or more is feasible (Figure 66). In the second step, CO concentrations typically higher than 50% are achieved with a very high fraction of CO<sub>2</sub> from decarbonation being converted to CO (>80%) (Figure 69 F). If air is used as an oxidant, a minimum N<sub>2</sub> dilution of 66 mol% based on stoichiometry (equation (109)) could be expected. Although such a CO-rich stream could be directly used in the steel industry as a partial substitute for coke, using pure O<sub>2</sub> or a mixture of O<sub>2</sub> and CO<sub>2</sub> as the oxidant could limit the dilution of the CO-rich steam. Note that O<sub>2</sub> is typically produced in an air separation unit (ASU) consuming about 200 kWh of electricity for every tonne of O<sub>2</sub> produced [224] and may, therefore, cause additional CO<sub>2</sub> emissions of around 0.2 kg<sub>CO<sub>2</sub></sub>/kg<sub>H<sub>2</sub></sub> (assuming carbon intensity of 255 kg<sub>CO<sub>2</sub></sub>/MWh<sub>e</sub> [155]). Since CO<sub>2</sub> emissions of a state-of-the-art H<sub>2</sub> production plant are 9 - 11 kg<sub>CO<sub>2</sub></sub>/kg<sub>H<sub>2</sub></sub> [149], the impact of using pure O<sub>2</sub> on the CO<sub>2</sub> emissions of the process is expected to be negligible.

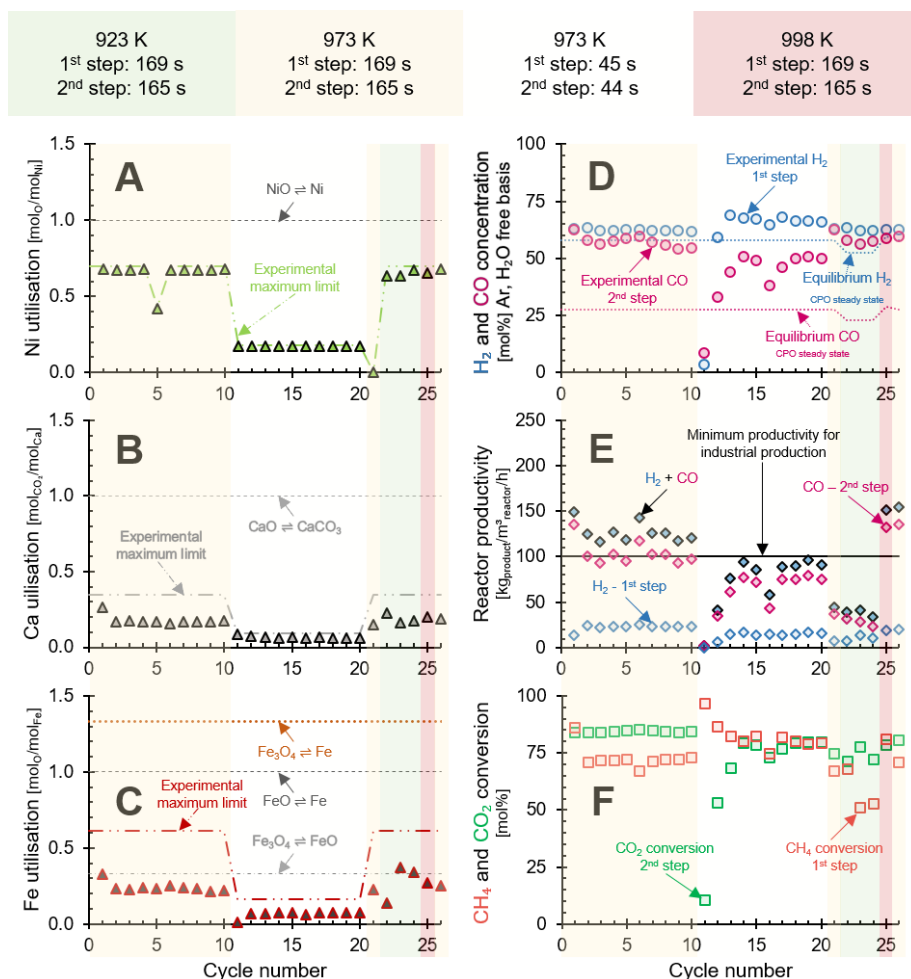


Figure 69. Process and materials performance over multiple cycles wherein the symbols represent experimental values. Colour codes on top indicate the conditions used during the cycles. A: utilisation of Ni based on the O<sub>2</sub> uptake in the second step, B: utilisation of Ca based on the outlet flow of carbon containing gases – CO, CO<sub>2</sub>, and CH<sub>4</sub>, C: utilisation of Fe based on CO produced (equation (107)). D: concentrations of H<sub>2</sub> and CO in the first and second step of the process compared to the equilibrium concentrations calculated by FactSage for catalytic partial oxidation of methane (CPO), assuming no coke is formed. E: productivity of the process and the minimum

productivity for sustainable industrial production recommended by Lange [154, 165]. F: conversion of  $\text{CH}_4$  in the first step and of  $\text{CO}_2$  in the second step of the process. In A, B, and C, the dotted or dashed lines indicate the maximum utilisation of the materials in the bed, whereas the dot-dashed line indicates the maximum experimental utilisation possible based on reaction stoichiometry and gas feed (see equations (113) to (118)).

## 7.4 Conclusions

To summarise, this process concept for blue hydrogen production avoids safety issues associated with the direct mixing of  $\text{O}_2$  and  $\text{CH}_4$ , while applying  $\text{O}_2$  for facilitating heat management by distributing process heat in two steps, each of which couples endo- and exothermic reactions, thereby, allowing for a far lower operating temperature compared with conventional  $\text{CH}_4$  reforming. The concept also circumvents thermodynamic equilibrium constraints imposed on the state-of-the-art technology and avoids coke formation, responsible for significant performance loss in industrial operation. In conclusion, the effectiveness of a two-step catalyst assisted chemical looping strategy to achieve enriched  $\text{H}_2$  production with inherent separation of  $\text{CO}_2$  and its conversion to  $\text{CO}$  is demonstrated. This concept can be applied to any hydrocarbon stream by optimising the process conditions and selecting the appropriate oxygen and  $\text{CO}_2$  carriers.

## Chapter 7

### Conclusions and perspectives

#### Conclusions

In this thesis, four new combined chemical looping process concepts for reducing CO<sub>2</sub> emissions of energy-intensive industries were developed, experimentally tested, and analysed. These process concepts combine processes which have been known for decades (chemical looping combustion and calcium looping) and centuries (chemical looping air separation). This work shows how these historical processes can be combined together to tackle today's pressing challenges. For the iron and steelmaking industry, a concept focused solely on CO<sub>2</sub> capture from steel mill gases was developed. This process concept combines endothermic and exothermic reactions and improves the exergy efficiency by increasing the reversibility of the process. The process concept can eliminate up to 85% of CO<sub>2</sub> emissions caused by the combustion of typical steel mill gases without compromising the heat provided by the steel mill gases for the heat demand of the steel plant. In another developed process concept, earth-abundant metals iron oxide and calcium oxide were used together to convert part of CO<sub>2</sub> to CO using the H<sub>2</sub> already present in the steel mill gas. Iron and calcium oxide are also raw materials for steel production and thus, this process concept can accelerate carbon circularity while also providing a pathway for spent iron and calcium oxide to be used in the steel



industry. Experimental results to demonstrate this process concept show that a change in temperature for running the process is more favourable than using a single temperature for capturing  $\text{CO}_2$  and oxidising  $\text{H}_2$  in one step and converting the captured  $\text{CO}_2$  to  $\text{CO}$  in another step. An exergy analysis of this process concept supports the favourability of applying a change in temperature. A further development of this process concept involved the use of manganese oxide to enable auto-thermal operation. This process concept was demonstrated experimentally and it was proven that, despite its complexity, it is economically competitive with a combination of conventional technologies for achieving equivalent product streams. The techno-economic and exergy analysis of this process concept highlighted the advantage of inherent product separation intrinsic to chemical looping processes. Finally, the process concept was extended to produce  $\text{H}_2$  and  $\text{CO}$  as two separate streams from a hydrocarbon such as methane. The experimental results proved that the product concentrations achieved by the chemical looping approach were higher than the equilibrium concentrations achieved in steady-state processes. Analysis of the results also showed that a high reactor productivity that is necessary for commercial operation was achieved.

### Perspectives

Carbon capture and storage may be most relevant in the short term future (over the next decade) while the use of  $\text{CO}$  produced from  $\text{CO}_2$  gains traction. Over the long term, the two concepts breaking down the

reverse water-gas shift reaction to produce a CO/CO<sub>2</sub> stream from steel mill gases could play a role in creating a circular carbon economy. Iron and steelmaking cause up to 9% of global CO<sub>2</sub> emissions, whereas long distance mobility (aviation, ships, transport trucks, etc.) is responsible for around 6% of global CO<sub>2</sub> emissions. If the CO/CO<sub>2</sub> stream produced from the developed process concepts using steel mill gases can be combined with renewable H<sub>2</sub> for the production of synthetic fuels, a large proportion of fossil-derived CO<sub>2</sub> emissions can be eliminated. H<sub>2</sub> is expected to play a key role in several sectors as a clean energy vector. The high demand of green H<sub>2</sub>, i.e. H<sub>2</sub> made from renewable energy, is unlikely to be met in the short term future. Blue H<sub>2</sub> is, thus, foreseen to bridge the gap to a fossil-free future. The process concept developed in this work to produce blue H<sub>2</sub> possesses several key advantages that can be exploited in the short term future such as providing a pathway for circular carbon and its ability to use a wide variety of feed streams, for example, hydrocarbon mixtures, glycerol, biomethane, etc. For up-scaling of the developed process concepts, the choice of reactor technology is critical. For all three process concepts developed to process steel mill gases, a change in temperature appears favourable and thus, testing in fluidised bed reactors is necessary. Another critical factor for the success of these process concepts is the lifetime of the materials in challenging conditions. Several laboratory tests have confirmed that the tested materials remain stable over several cycles. However, intensive testing lasting for months under realistic conditions

will be vital for bringing these process concepts to practical implementation.

# Appendix A

Note that the calorific values are the lower calorific values. The price of any gaseous stream is calculated by multiplying the ratio of its lower calorific value and methane with the price of natural gas, assuming that natural gas is 100% methane.

Table A1: List of calorific resources from the agricultural industry.

Resource	Phase	Production (MT/year)	Price (EUR <sub>2020</sub> /year)	Calorific value (GJ/tonne)
Biogas	Gas	30 [225]	76	20 [226]
Rice husk	Solid	120 [227]	0.2 [228]	15 [229]
Rice straw	Solid	445 [230]	37 [231]	15 [229]
Sugarcane Bagasse	Solid	540 [232]	31 [233-236]	16 [229]
Wheat straw	Solid	584 [237]	42 [237]	18 [237]
Corn stalk	Solid	1000 [238]	22 [239]	18 [240]
PMR	Solid	51 [241]	72 [242]	15 [242]
PMR: EFBs	Solid	35 [19]	5 [243]	15 [244]
PMR: EFB oil	Liquid	6 [242]	666 [245]	12 [246]
Pine oil	Liquid	2 [247]	608 [248]	15 [246]

Table A2: List of calorific resources from the biorefining industry.

Resource	Phase	Production (MT/year)	Price (EUR <sub>2020</sub> /year)	Calorific value (GJ/tonne)
Bioethanol	Liquid	89 [249]	861 [250]	25 [251]
Glycerol	Liquid	4 [252]	480 [253]	16*

\* assuming 100% glycerol: C<sub>3</sub>H<sub>8</sub>O<sub>3</sub>

Table A3: List of calorific resources from the chemicals industry.

Resource	Phase	Production (MT/year)	Price (EUR <sub>2020</sub> /year)	Calorific value (GJ/tonne)
PSA tail gas from SMR	Gas	472 [31, 254]	17	4 [31]

Table A4: List of calorific resources from food waste.

Resource	Phase	Production (MT/year)	Price (EUR <sub>2020</sub> /year)	Calorific value (GJ/tonne)
Eggshells	Solid	9 [14]	96 [13]	3 [255]
Coffee grounds	Solid	6 [256]	55 [257]	21 [258]

Table A5: List of calorific resources from the iron and steel industry

Resource	Phase	Production (MT/year)	Price (EUR <sub>2020</sub> /year)	Calorific value (GJ/tonne)
Basic oxygen furnace gas	Gas	97 [42, 72]	21	6 [58]
Blast furnace gas	Gas	2045 [42, 72]	9	2 [58]
Coke oven gas	Gas	70 [42, 58, 72]	58	15 [58]

Table A6: List of calorific resources from municipal waste.

Resource	Phase	Production (MT/year)	Price (EUR <sub>2020</sub> /year)	Calorific value (GJ/tonne)
Cooking oil	Liquid	15 [259]	211 [260]	37 [261]
MSW	Solid	2010 [262]	74 [263]	20 [264]

Table A7: List of calorific resources from the petrochemical industry.

Resource	Phase	Production (MT/year)	Price (EUR <sub>2020</sub> /year)	Calorific value (GJ/tonne)
Coal	Solid	8103 [265]	54 [265]	27 [266]
Crude oil	Liquid	4485 [265]	421 [265]	42 [265]
Natural gas	Gas	2932 [265]	189 [265]	50*
Fischer- Tropsch tail gas	Gas	6 [191]	47	12 [267]
Carbon black tail gas	Gas	141 [268]	8	2 [268]

\* assuming 100% CH<sub>4</sub>.

Table A8: List of calorific resources from end-of-life plastics.

Resource	Phase	Production (MT/year)	Price (EUR <sub>2020</sub> /year)	Calorific value (GJ/tonne)
HDPE	Solid	40 [269]	226 [270]	34 [271]
LDPE	Solid	57 [269]	116 [270]	39 [271]
PET	Solid	33 [269]	573 [272]	21 [271]
PP	Solid	55 [269]	116 [270]	42 [271]

Table A 9: Gas composition of *low grade* gases.

Molar %	Carbon black tail gas [268]	PSA tail gas from SMR [31]	BFG [42]	BOFG [42]
CO <sub>2</sub>	3.6	51.0	21.6	20.0
CO	10.6	14.5	23.5	54.0
CH <sub>4</sub>	0.2	9.4	0.0	0.0
H <sub>2</sub>	8.0	23.7	3.7	3.2
C <sub>x</sub> H <sub>y</sub>	0.0	0.0	0.0	0.0
N <sub>2</sub>	36.2	0.6	46.6	18.1
H <sub>2</sub> O	41.4	0.0	4.0	4.0
Ar and/or O <sub>2</sub>	0.0	0.0	0.6	0.7

## Appendix B

### Theoretical calculations

#### Aspen Plus® simulation with a $\text{CO}_2/\text{N}_2$ mixture

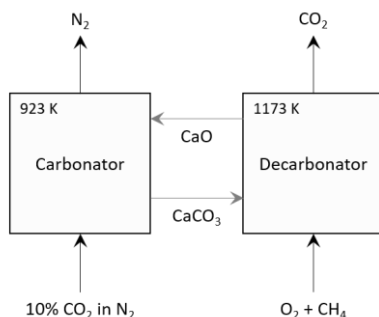


Figure B1: Block diagram of the Aspen Plus simulation used for estimating the minimum concentration of  $\text{CO}_2$  required to achieve adiabatic operation of the carbonator.

Process simulations carried out using Aspen Plus show that if the  $\text{CO}_2$  containing gas stream is fed to the carbonator at room temperature, there is always excess heat at the carbonator reactor temperature of 923 K when the  $\text{CO}_2$  concentration is higher than 12 mol% for a simplified  $\text{CO}_2/\text{N}_2$  mixture with 90% conversion of CaO. However, low conversions of CaO to  $\text{CaCO}_3$  are common due to deactivation of the  $\text{CO}_2$  carrier. For a low CaO conversion of 10%, the minimum  $\text{CO}_2$  concentration necessary to reach the carbonation temperature of 923 K adiabatically is 8 mol% for a simplified  $\text{CO}_2/\text{N}_2$  mixture. Under conditions with low CaO conversions, excess solid material (CaO) is heated to 1173 K and transported back to the carbonator. Thus, the excess unconverted CaO acts as a heat carrier leading to lower concentrations of  $\text{CO}_2$  necessary to adiabatically reach



923 K in the carbonator. These simulations show that depending on the CO<sub>2</sub> concentration in the flue gas and CaO conversion, removal of heat from the carbonator to control temperature is desirable so that equilibrium for carbonation remains favoured.

The specifications of the Aspen Plus® simulation are detailed in the methods sections (section 3.1) of the main text. The simulation was performed with 1 kmol/s inlet CO<sub>2</sub>. The reactor model used for the carbonator and decarbonator was RGIBBS. The temperature of the carbonator and decarbonator was kept constant at 923 K and 1173 K, respectively. The simulation was carried out at ambient pressure viz. 101.3 kPa, The amount of N<sub>2</sub> fed to the carbonator ( $x$  kmol/s) was varied from 2 to 20 kmol/s in the simulator to ensure that adiabatic operation of the carbonator (net heat removed or added =  $0.1 \pm 0.01$  W, equivalent to negligible heat). To estimate the effect of solids conversion on the minimum concentration of CO<sub>2</sub> required to ensure adiabatic operation, the CaO flow rate entering the carbonator was varied from 1 – 10 kmol/s roughly corresponding to 90% and 10% CaO conversion. The amount of CO<sub>2</sub> not captured from the inlet CO<sub>2</sub> stream ( $z$  kmol/s) is dependent on the thermodynamic equilibrium partial pressure of CO<sub>2</sub> for the carbonation reaction and is linked to the amount of N<sub>2</sub> inlet ( $x$  kmol/s). The higher the N<sub>2</sub> inlet, the higher the amount of CO<sub>2</sub> that is not captured.

## Integrating chemical looping air separation

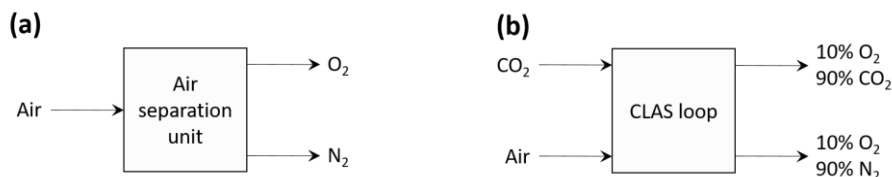


Figure B2: Block flow diagram to assess the minimum reversible work to produce  $O_2$  via (a) cryogenic distillation of air and (b) CLAS loop.

A simple case of  $O_2$  production is considered where dry air is assumed to be composed of  $O_2$  and  $N_2$ , constituting 21 mol% and 79 mol% respectively. Depending on the type of oxygen carrier employed and the process temperature, the partial pressure of  $O_2$  in the product  $CO_2/O_2$  stream can be tuned. For the sake of simplicity, it is assumed that at a given arbitrary temperature below the decarbonation temperature of 1173 K, the equilibrium partial pressure of  $O_2$  using an arbitrary oxygen carrier is 10 kPa, thereby, yielding a  $CO_2/O_2$  stream with 10 mol%  $O_2$  at given conditions. The CLAS loop is assumed to operate isothermally, implying that both half-cycles are at the same temperature. Thus, the two outlet streams from the CLAS loop have the same outlet equilibrium partial pressure of  $O_2$ . It is assumed that the  $CO_2$  entering the CLAS loop is pure and has a purity of 100%. The minimum work required (A), which takes into account the increase in the internal energy of the system, to carry out the processes displayed is given by equation (122).

$$A = RT_0 \left[ \left( \sum_{p=1}^P N_p \sum_i x_{pi} * \ln x_{pi} \right) - \left( \sum_{f=1}^F N_f \sum_i x_{fi} * \ln x_{fi} \right) \right]$$

The minimum reversible work required to separate O<sub>2</sub> and co-produce pure N<sub>2</sub> via the ASU is 6.1 kJ/mol<sub>O<sub>2</sub></sub>, whereas for CLAS, net reversible work amounting to -3.4 kJ/mol<sub>O<sub>2</sub></sub> is delivered. The latter occurs due to mixing of CO<sub>2</sub> with O<sub>2</sub> i.e. dilution of the pure CO<sub>2</sub> with O<sub>2</sub> produced by the CLAS loop. Dilution of the CO<sub>2</sub> with O<sub>2</sub> or vice-versa is not undesirable for the proposed process concept. For the given set of conditions in the CLAS loop when the equilibrium partial pressure of O<sub>2</sub> is 10 kPa at the assumed arbitrary reaction temperature, net reversible work to separate O<sub>2</sub> from air in the CLAS loop becomes necessary (i.e. A > 0) only when the inlet CO<sub>2</sub> stream has a purity of less than 96%. It should also be noted that the CO<sub>2</sub>/O<sub>2</sub> stream from the CLAS loop would already be preheated to a very high temperature before being fed to the oxidiser-decarbonator, unlike the O<sub>2</sub> from an ASU. Thus, the addition of a CLAS loop provides multiple benefits to the proposed process.

Additional process simulations

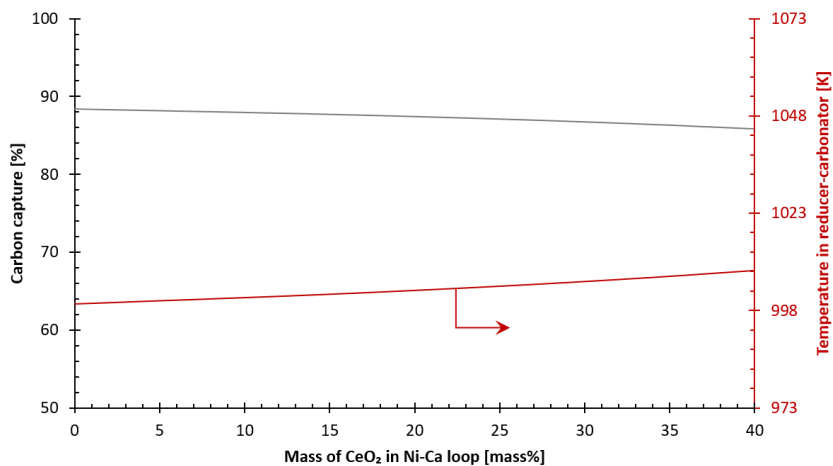


Figure B3: Influence of CeO<sub>2</sub> in the Ni-Ca loop on the CO<sub>2</sub> capture of the process.

Gibbs free energy plots

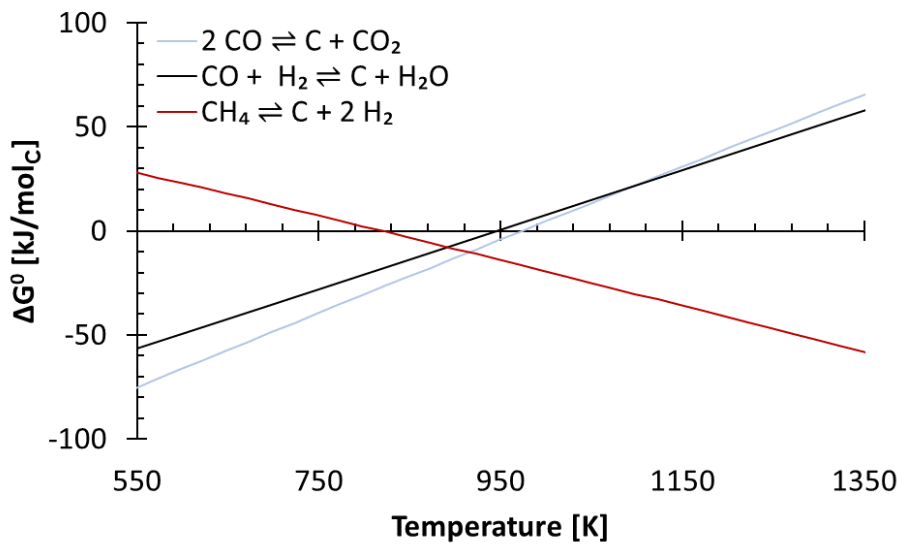


Figure B4: Standard Gibbs free energy against temperature for typical reactions involving C1 molecules that cause coking.

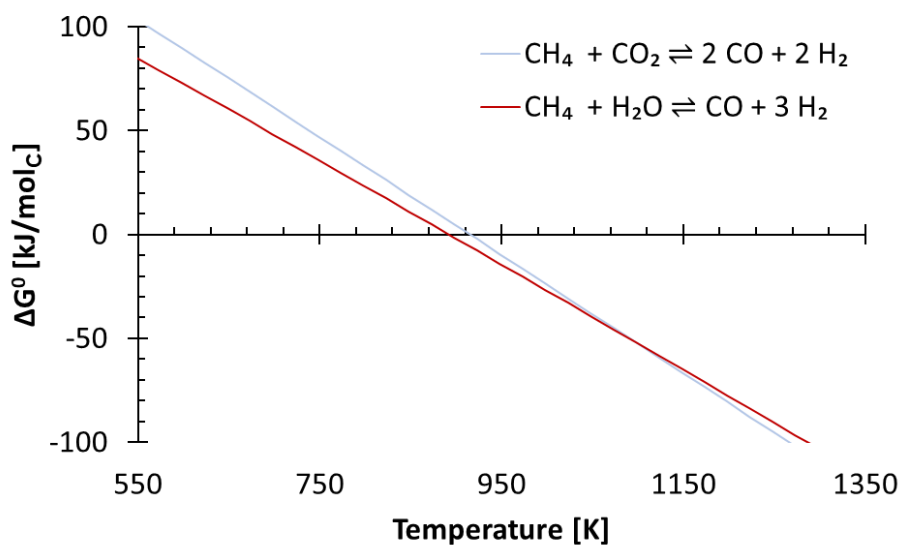


Figure B5: Standard Gibbs free energy against temperature for typical reforming reactions of  $\text{CH}_4$ .

Experimental results and data

Materials testing on a fixed bed reactor

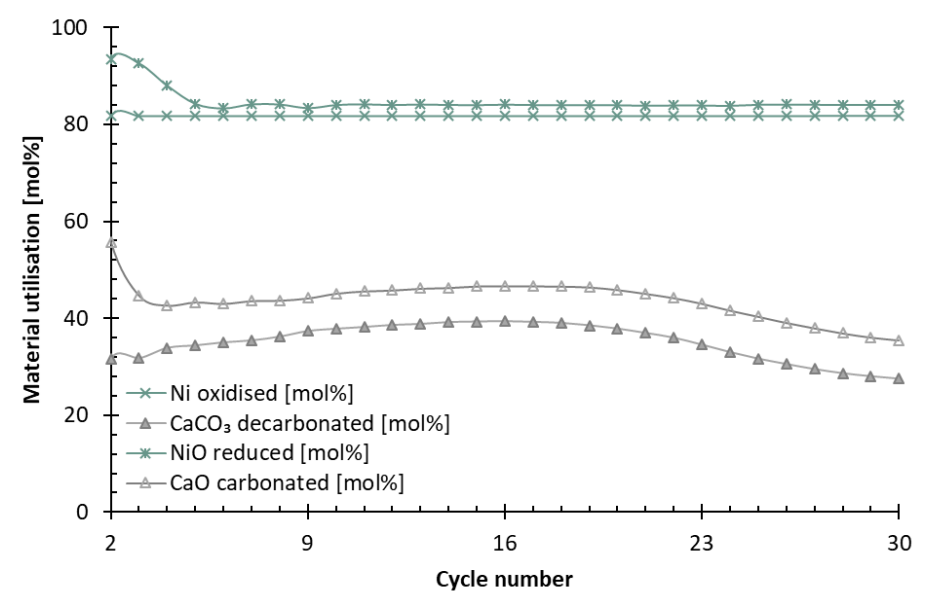


Figure B6: Evolution of the utilisation of the materials over multiple cycles, Ni oxidised and CaCO<sub>3</sub> decarbonated during the oxidation-decarbonation half-cycle and NiO reduced and CaO carbonated during the reduction-carbonation half-cycle.

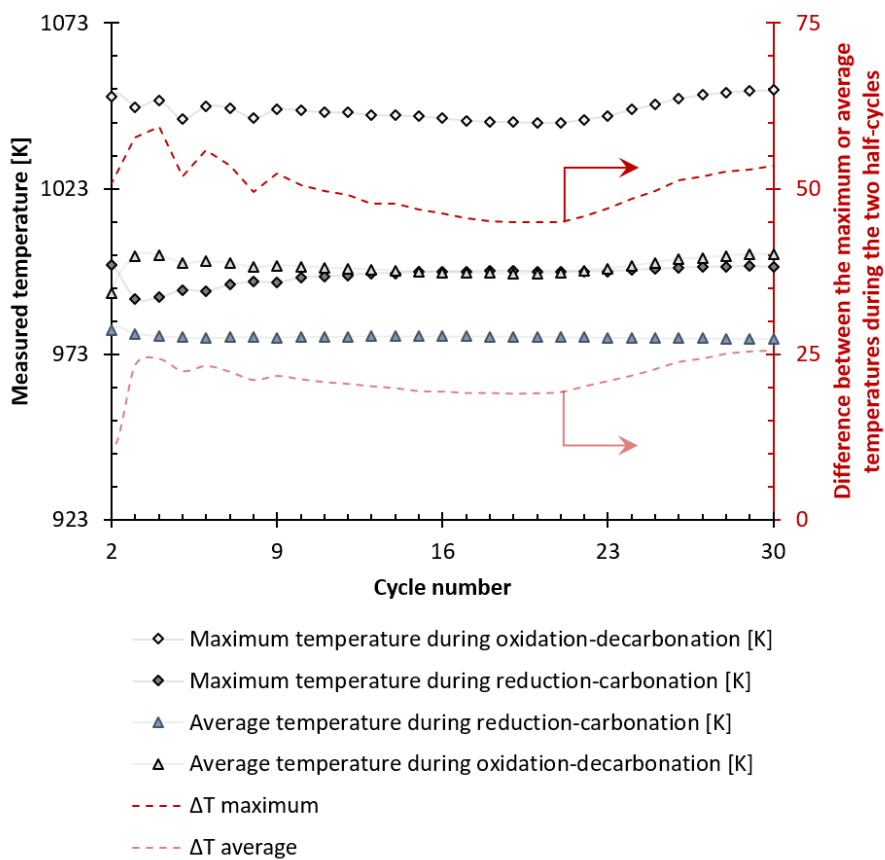


Figure B7: Maximum and average temperatures recorded during the two half-cycles of the multiple cycle test (on the primary y-axis on the left). Difference between the maximum temperatures of the half-cycles and between the average temperatures of the half-cycles (on the secondary y-axis on the right).

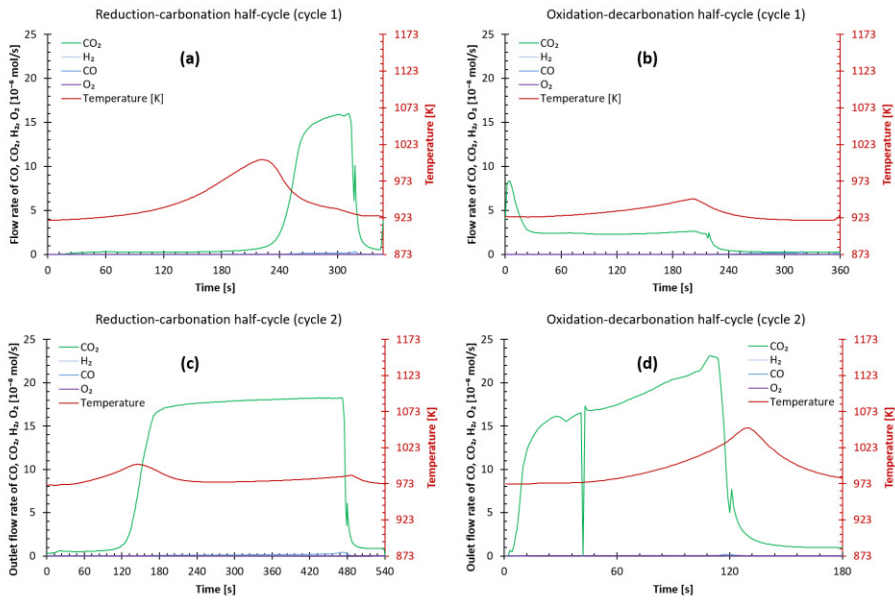


Figure B8: Outlet flow rates and temperature vs time during: (a) the reduction-carbonation half-cycle of the 1<sup>st</sup> cycle, (b) the oxidation-decarbonation half-cycle of the 1<sup>st</sup> cycle, (c) the reduction-carbonation half-cycle of the 2<sup>nd</sup> cycle, and (d) the oxidation-decarbonation half-cycle of the 2<sup>nd</sup> cycle. In the oxidation-decarbonation half-cycle of the 1<sup>st</sup> cycle, 21% O<sub>2</sub>/Ar was used instead of 50% O<sub>2</sub>/Ar. Synthetic BFG (molar composition: 5.1% H<sub>2</sub>, 23.8% CO, 24.1% CO<sub>2</sub>, 40% Ar, and 7% He) was used during the reduction-carbonation half-cycles. The inlet gases had a constant flow rate of  $41 \cdot 10^{-6}$  mol/s.



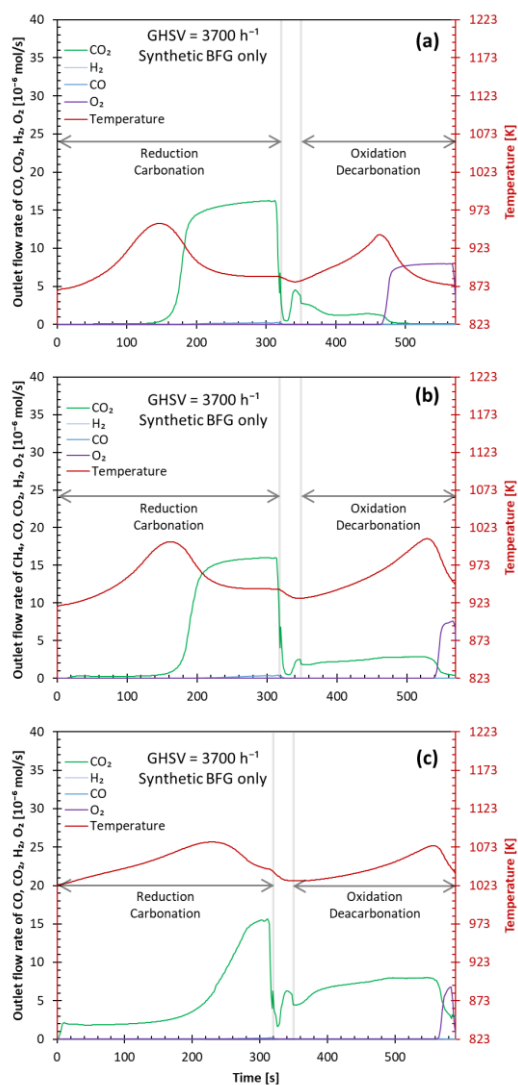


Figure B9: Measured outlet flow rates and temperature versus time over one cycle when synthetic BFG is used and the GHSV is kept constant at  $3700 \text{ h}^{-1}$  while the reactor furnace temperature is fixed at (a) 873 K, (b) 923 K, and (c) 1023 K. During reduction-carbonation, synthetic BFG (molar composition: 5.1%  $\text{H}_2$ , 23.8%  $\text{CO}$ , 24.1%  $\text{CO}_2$ , 40% Ar, and 7% He) was fed and during oxidation-decarbonation, 21%  $\text{O}_2/\text{Ar}$  was fed. The total inlet gas feed was kept constant at  $41 \cdot 10^{-6} \text{ mol/s}$ .

Material characterisation

Energy dispersive X-ray measurements

The measured mass content of the sample’s constituents (Ni, Ca, and Ce) and the expected mass content based on the amounts of precursor materials added during the synthesis are displayed in Table B1. The measurements did not take into account carbon or oxygen because some portion of Ca in the material tends to form Ca(OH)<sub>2</sub> and CaCO<sub>3</sub> upon exposure to ambient air. The standard deviation observed during the measurements are indicative of the inhomogeneity of the as prepared material. The EDX measurements indicated that there was no loss of precursor materials during the synthesis and inhomogeneity was limited.

Table B1: The mass content of the different components of the synthesised materials measured using EDX. The ± sign indicates the value of one standard deviation obtained from 5 different measurements.

	Ni [mass%]	Ca [mass%]	Ce [mass%]
Measured	43 ± 6	34 ± 3	23 ± 3
Expected	46	33	21

N<sub>2</sub> sorption measurements

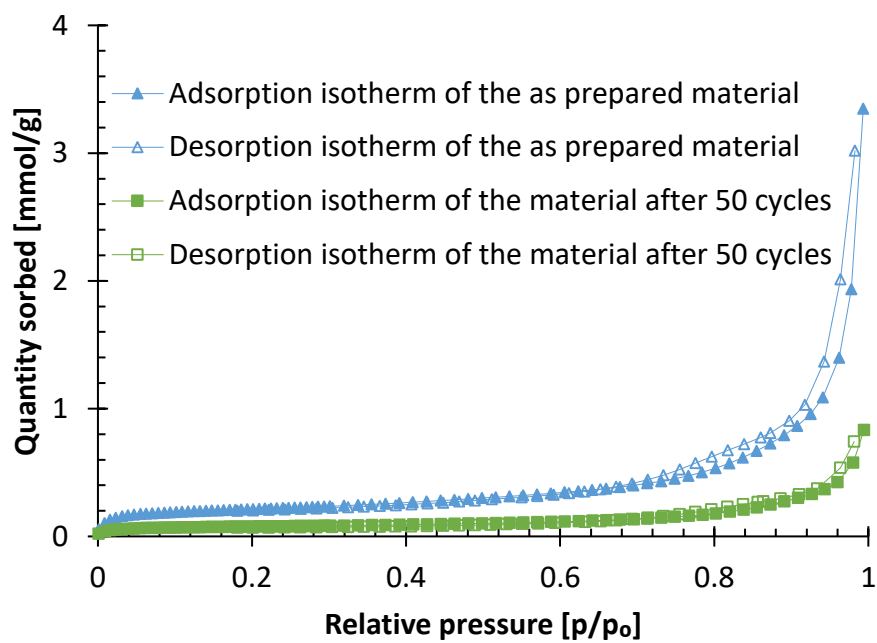


Figure B10: Measured isotherms of the as prepared (fresh) material and of the material after being cycled more than 50 times.

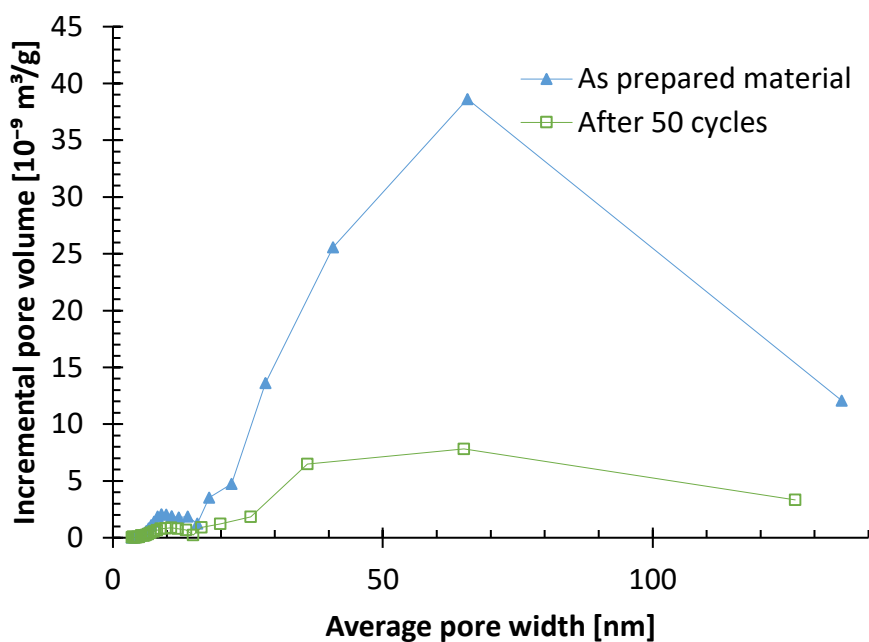


Figure B11: Pore size distribution based on incremental volume calculated using BJH theory applied on the desorption branch of the isotherm of the as prepared material and the material after being subjected to more than 50 cycles.

X-ray diffraction

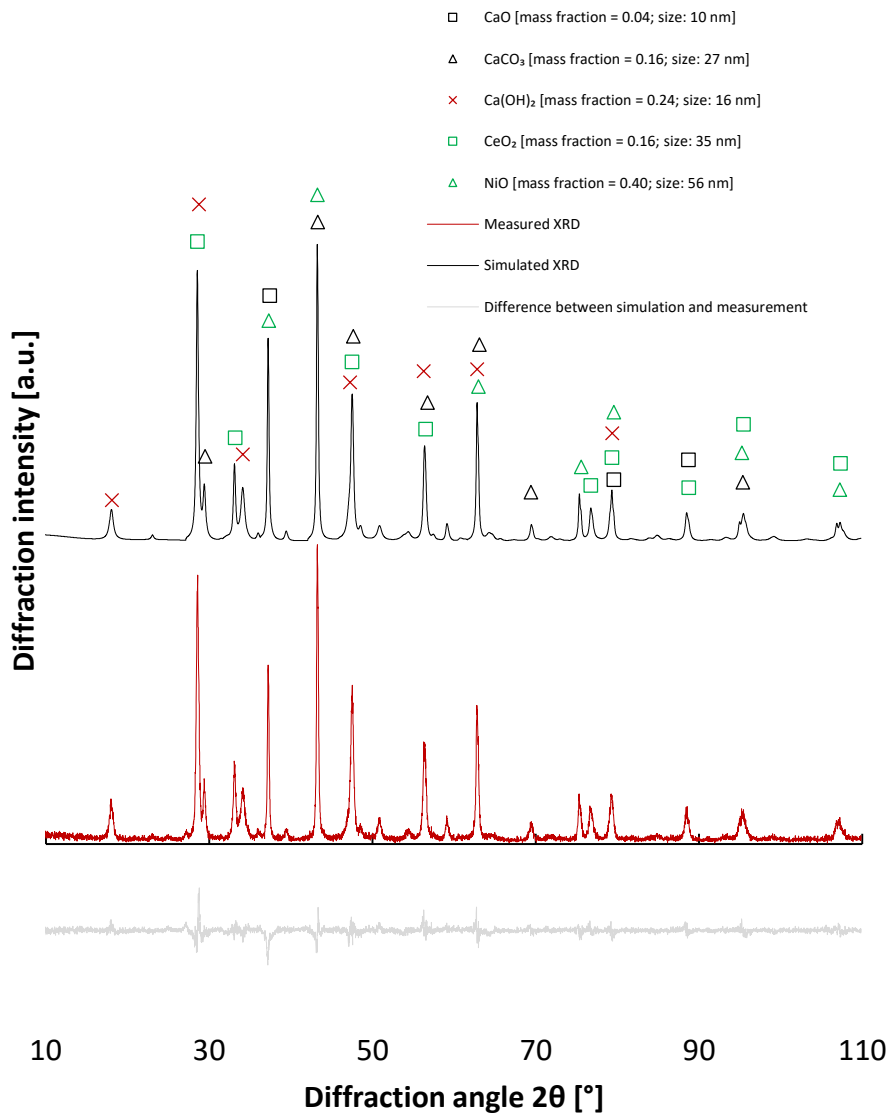


Figure B12: XRD of the as prepared material (in red, centre) with the XRD generated by Rietveld refinement (in black, top) and the difference between the observed and fitted diffractogram (in grey, bottom). Only peak intensities greater than 5% of the maximum intensity have been marked.

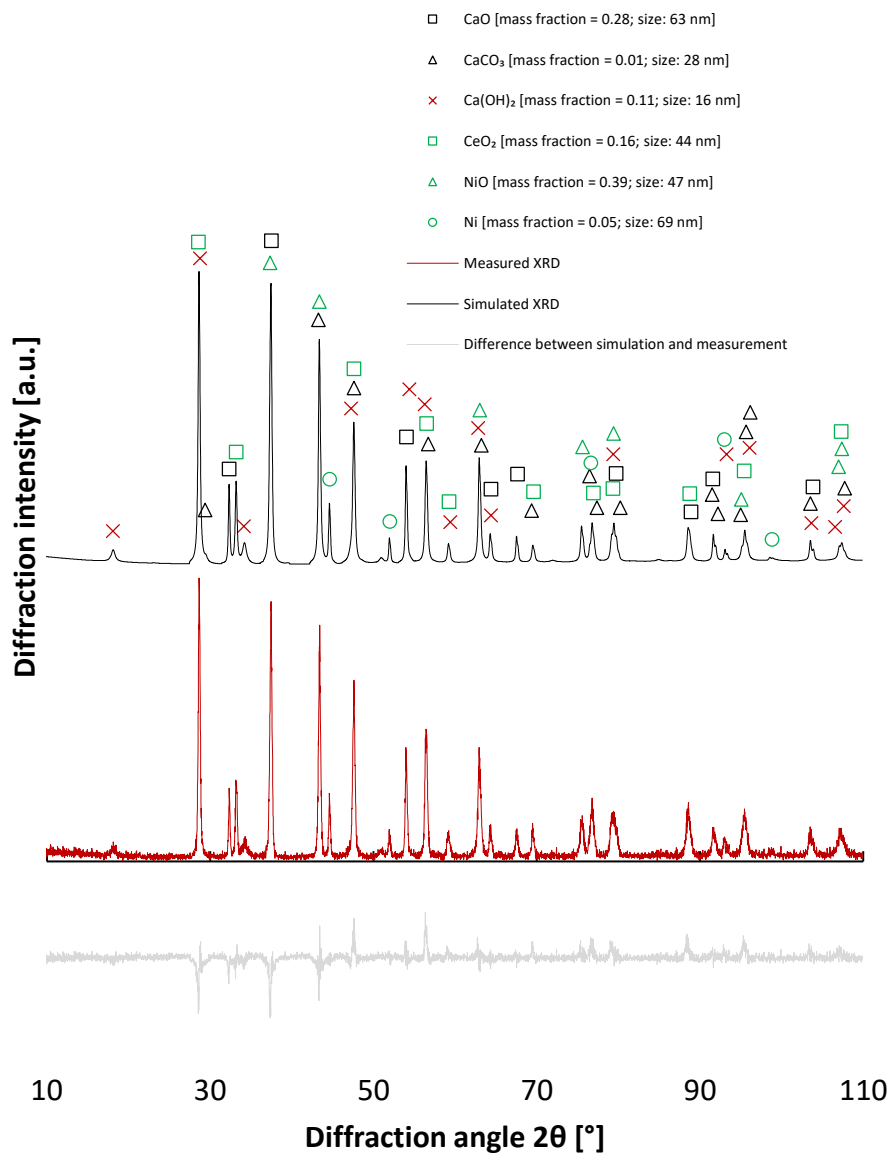


Figure B13: XRD of the material cycled 50 times (in red, centre) with the XRD generated by Rietveld refinement (in black, top) and the difference between the observed and

fitted diffractogram (in grey, bottom). Only peak intensities greater than 2% of the maximum intensity have been marked.

Table B2: Summary of the results for the Rietveld refinement of the cycled and as prepared materials.

Material	Phase	Lattice parameters [ $10^{-1}$ nm for a, b, and c or $^\circ$ for $\alpha$ , $\beta$ , and $\gamma$ ]						Crystal structure	Space group	Mass fraction	Crystallite size [nm]	$R_{wp}$	$\chi^2$
		a	b	c	$\alpha$	$\beta$	$\gamma$						
As prepared material (Figure B12)	CaO	4.815000	4.815000	4.815000	90	90	90	Cubic	F m 3 m	0.038	11	0.0894	1.614
	CaCO <sub>3</sub>	4.986516	4.986516	17.055128	90	90	120	Hexagonal	R -3 c	0.166	27		
	Ca(OH) <sub>2</sub>	3.589000	3.589000	4.911000	90	90	120	Hexagonal	P -3 m 1	0.237	17		
	CeO <sub>2</sub>	5.409259	5.409259	5.409259	90	90	90	Cubic	F m -3 m	0.156	35		
	NiO	4.180702	4.180702	4.180702	90	90	90	Cubic	F m 3 m	0.402	56		
Cycled material (Figure B13)	CaO	4.806520	4.806520	4.806520	90	90	90	Cubic	F m 3 m	0.277	63	0.2165	1.868
	CaCO <sub>3</sub>	4.990000	4.990000	17.061501	90	90	120	Hexagonal	R -3 c	0.013	28		
	Ca(OH) <sub>2</sub>	3.589000	3.589000	4.911000	90	90	120	Hexagonal	P -3 m 1	0.104	16		
	CeO <sub>2</sub>	5.410349	5.410349	5.410349	90	90	90	Cubic	F m -3 m	0.161	44		
	NiO	4.177453	4.177453	4.177453	90	90	90	Cubic	F m 3 m	0.393	47		
	Ni	3.522463	3.522463	3.522463	90	90	90	Cubic	F m 3 m	0.052	69		



## STEM-EDX mapping

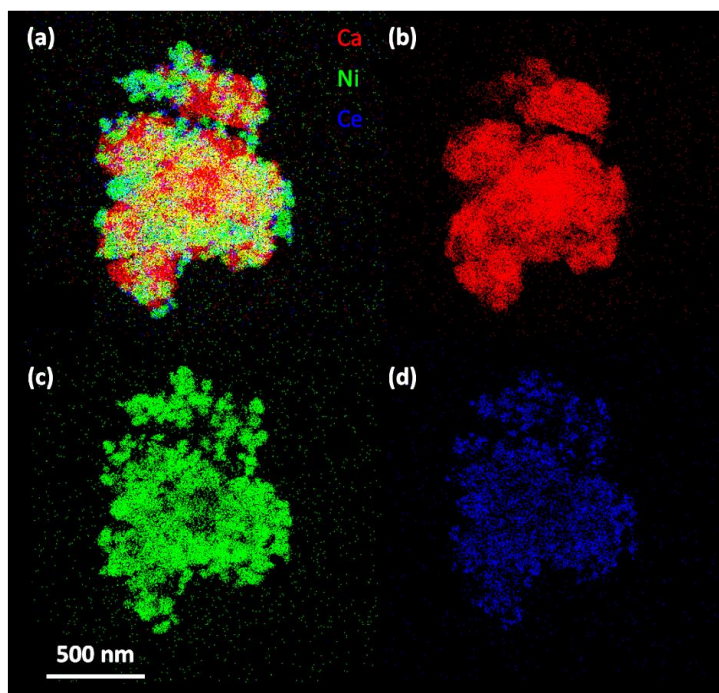


Figure B14: STEM-EDX mapping of the as prepared material: (a) overlay of Ca, Ni, and Ce mapping, (b) Ca mapping, (c) Ni mapping, and (d) Ce mapping.

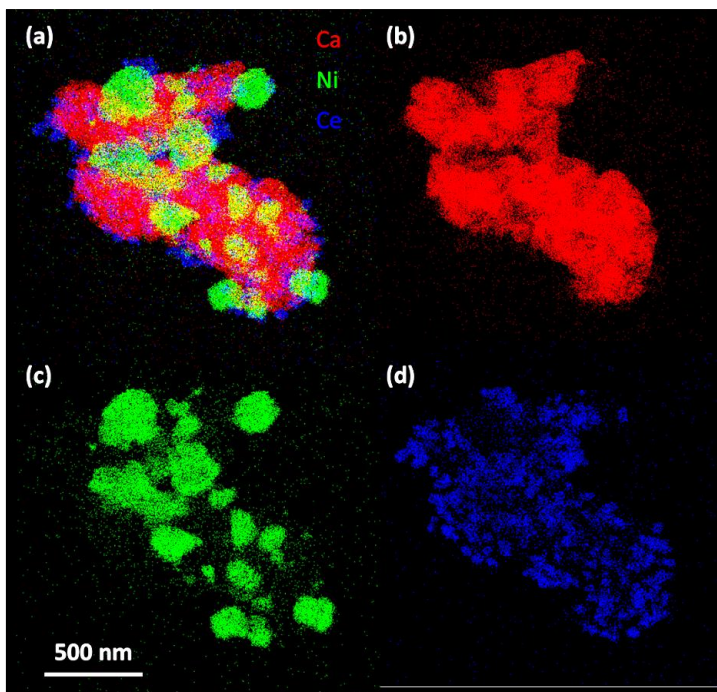


Figure B15: STEM-EDX mapping of the material after 50 cycles: (a) overlay of Ca, Ni, and Ce mapping, (b) Ca mapping, (c) Ni mapping, and (d) Ce mapping.

## Appendix C

### Results of exergy analysis

Table C1: Details of the exergy analysis of the isothermal CO production process for 1 MMta equivalent CO<sub>2</sub> emissions from BFG.

Aspen Plus flowsheet notation	Process or stream description	Temperature IN [K]	Temperature OUT [K]	Chemical exergy [MW]	Exergy work [MW]	Exergy of heat [MW]	Exergy of separation or mixing [MW]
BFG	Inlet BFG	298	-	128	0	0	-4.57
RC-COMP	Compressor for BFG	298	318	0	0.97	0	0
RED-CARB	Reduction-carbonation half-cycle	318	1013	0	0	-9.62	0
RC-EXP	Turbine for the vent gas	1013	972	0	-1.84	0	0
COOL-RC	Cooler for the vent gas	972	298	0	0	-19.3	0
VENTGAS	Process off-gas	-	298	93.9	0	0	-3.52
N2	Inert gas	298	-	0.78	0	0	0
DO-COMP	Compressor for inert (N <sub>2</sub> )	298	320	0	0.68	0	0
DECA-OX	Decarbonation-oxidation half-cycle	320	1013	0	0	52.9	0
DO-EXP	Turbine for expanding the outlet gas	1013	984	0	-1.45	0	0
COOL-DO	Cooler for the outlet gas	984	298	0	0	-21.5	0

OUTLET	Product gas of the process	-	298	35.3	0	0	-1.61
-	Minimum work to separate components from the product gas	298	298	0	0	0	7.31

---

Table C2: Details of the exergy analysis of the temperature-programmed CO production (mild temperature change) process for 1 MMta equivalent CO<sub>2</sub> emissions from BFG.

Aspen Plus flowsheet notation	Process or stream description	Temperature IN [K]	Temperature OUT [K]	Chemical exergy [MW]	Exergy work [MW]	Exergy of heat [MW]	Exergy of separation or mixing [MW]
BFG	Inlet BFG	298	-	128	0	0	-4.57
RC-COMP	Compressor for BFG	298	318	0	0.97	0	0
RED-CARB	Reduction-carbonation half-cycle	318	1013	0	0	-9.62	0
RC-EXP	Turbine for the vent gas	1013	972	0	-1.84	0	0
COOL-RC	Cooler for the vent gas	972	298	0	0	-19.3	0
VENTGAS	Process off-gas	-	298	93.9	0	0	-3.52
DECA-OX	Decarbonation-oxidation half-cycle	-	1097	0	0	51.5	0
DO-EXP	Turbine for expanding the outlet gas	1097	972	0	-0.34	0	0
COOL-DO	Cooler for the outlet gas	972	298	0	0	-6.87	0
OUTLET	Product gas of the process	-	298	34.5	0	0	-0.49

COOLER	To cool solids from decarbonation-oxidation half- cycle	1097	1013	0	0	-12.8	0
-	Minimum work to separate CO from product gas	298	298	0	0	0	0.49

---

Table C3: Details of the exergy analysis of the temperature-programmed CO production (large temperature change) process for 1 MMta equivalent CO<sub>2</sub> emissions from BFG.

Aspen Plus flowsheet notation	Process or stream description	Temperature IN [K]	Temperature OUT [K]	Chemical exergy [MW]	Exergy work [MW]	Exergy of heat [MW]	Exergy of separation or mixing [MW]
BFG	Inlet BFG	298	-	128	0	0	-4.57
RC-COMP	Compressor for BFG	298	318	0	0.97	0	0
RED-CARB	Reduction-carbonation half-cycle	318	923	0	0	-75.6	0
RC-EXP	Turbine for the vent gas	923	882	0	-1.12	0	0
COOL-RC	Cooler for the vent gas	882	298	0	0	-10	0
VENTGAS	Process off-gas	-	298	21.1	0	0	-1.19
DECA-OX	Decarbonation-oxidation half-cycle	-	1064	0	0	51.5	0
DO-EXP	Turbine for expanding the outlet gas	1097	972	0	-0.34	0	0



COOL-DO	Cooler for the outlet gas	972	298	0	0	-6.87	0
OUTLET	Product gas of the process	-	298	34.5	0	0	-1.21
COOLER	To cool solids from decarbonation-oxidation half- cycle	1064	923	0	0	-11.5	0
-	Minimum work to separate CO from product gas	298	298	0	0	0	1.21

---

### Rietveld refinement of X-ray diffraction measurements

The residual function  $R_{wp}$  (zero for a perfect fit) and goodness-of-fit  $\chi^2$  (unity is ideal) values of the Rietveld refinement of the XRD of the oxygen carrier (Figure C1) were 0.11 and 1.6, respectively. The  $R_{wp}$  and  $\chi^2$  values of the Rietveld refinement of the XRD of the CO<sub>2</sub> carrier (Figure C2) were 0.09 and 1.9, respectively.

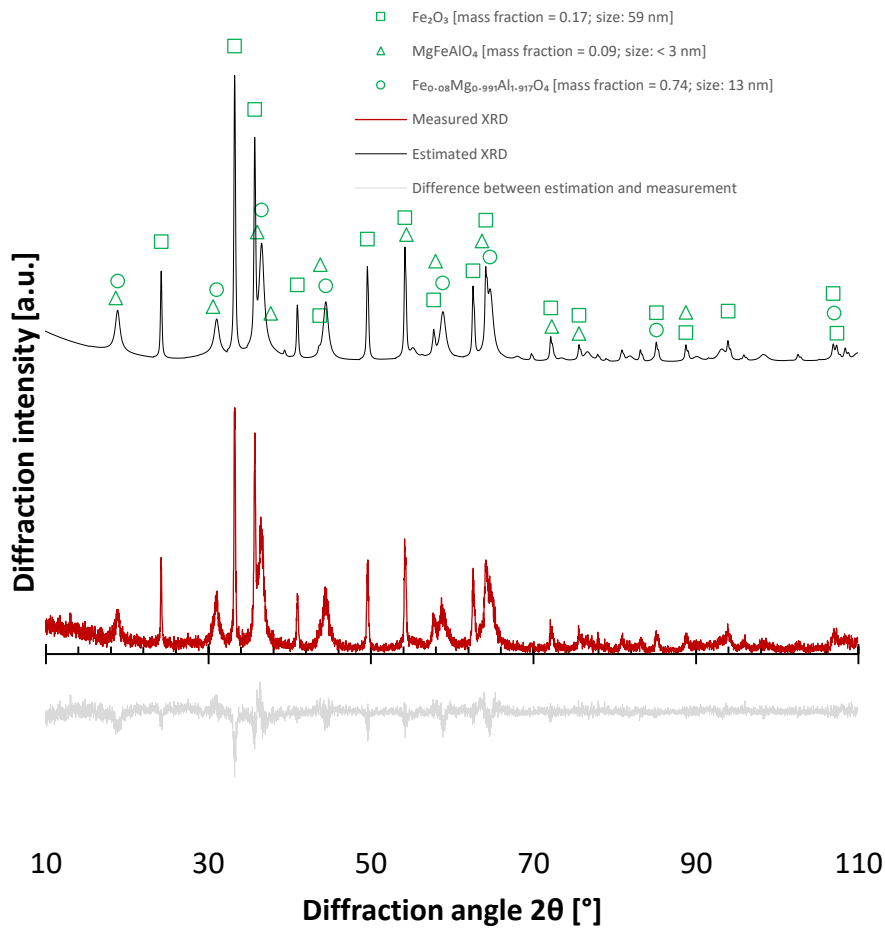


Figure C1: X-ray diffractogram of the calcined oxygen carrier (in red, center) with the X-ray diffractogram generated by Rietveld refinement (in black, top) and the difference between the observed and fitted diffractogram (in grey, bottom). Peaks which have an intensity greater than 5% of the maximum peak intensity are marked and identified on the plot.

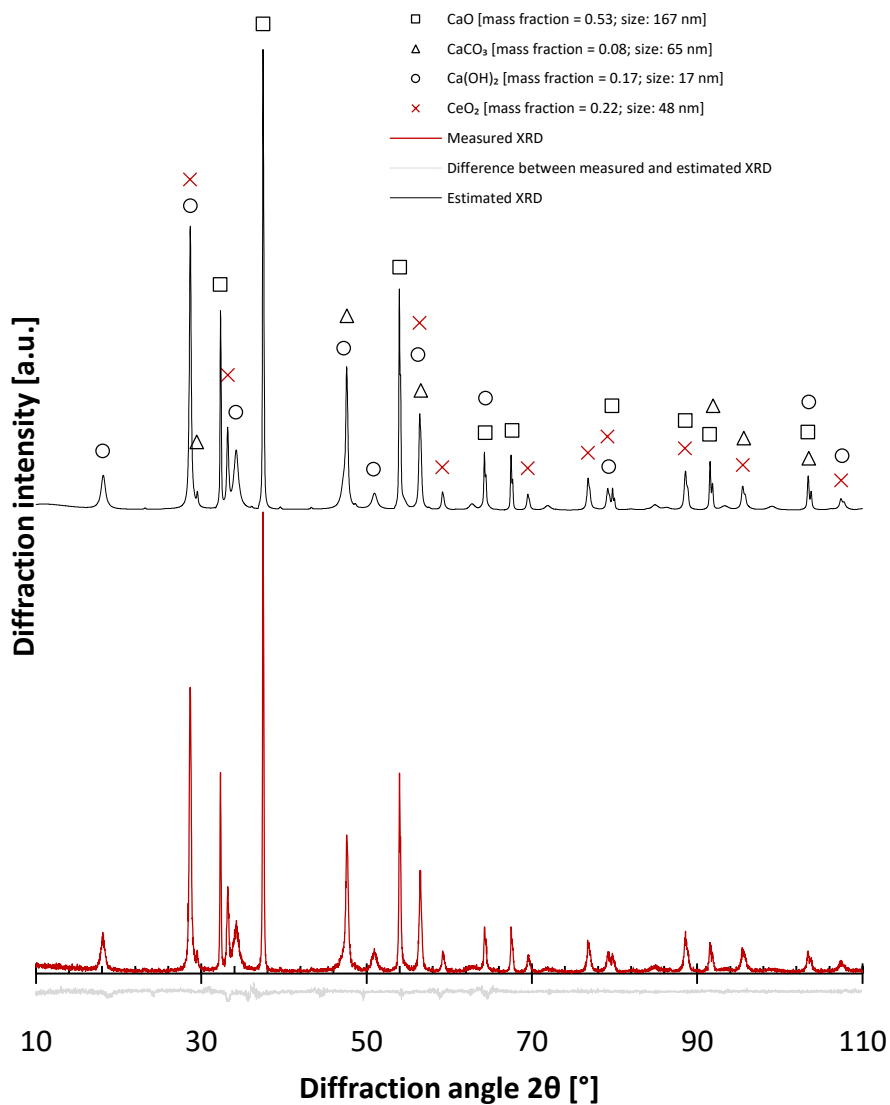


Figure C2: X-ray diffractogram of the calcined CO<sub>2</sub> carrier (in red, center) with the X-ray diffractogram generated by Rietveld refinement (in black, top) and the difference between the observed and fitted diffractogram (in grey, bottom). Peaks which have an intensity greater than 1% of the maximum peak intensity are marked and identified on the plot.

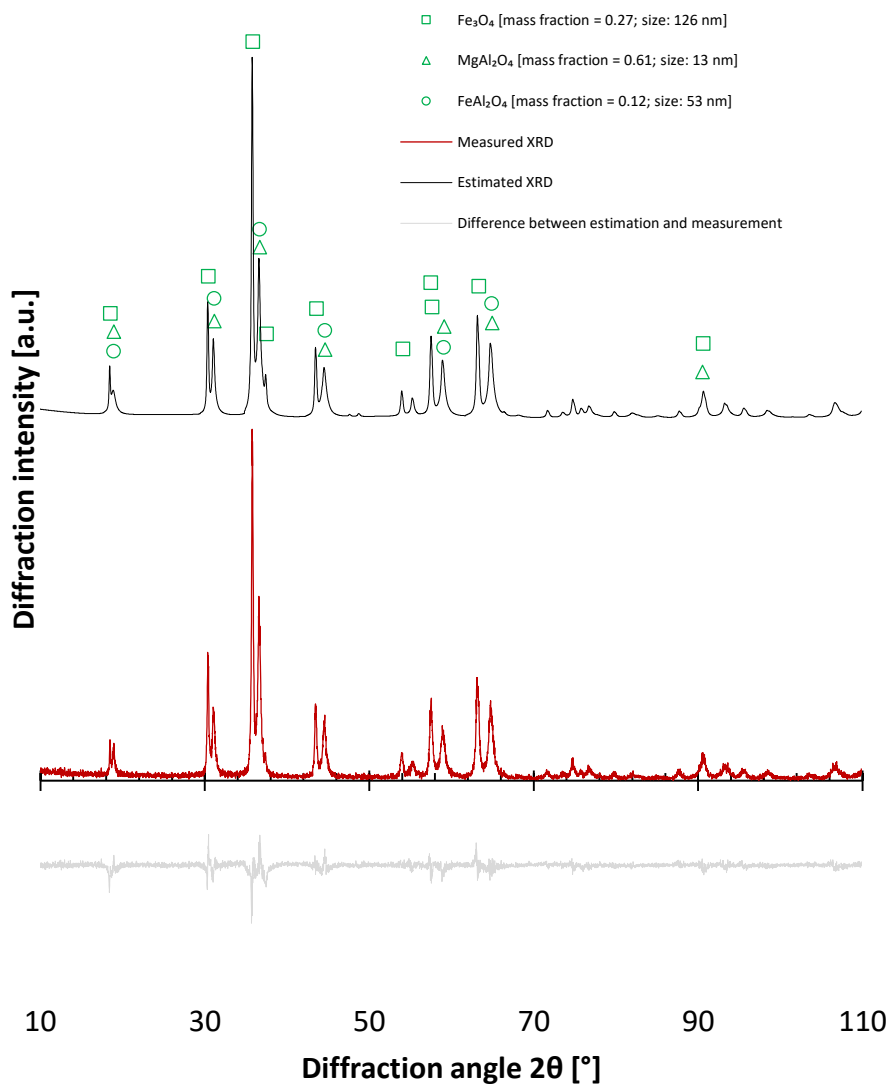


Figure C3: X-ray diffractogram of the oxygen carrier after being fully oxidised by  $\text{CO}_2$  (in red, center) with the X-ray diffractogram generated by Rietveld refinement (in black, top) and the difference between the observed and fitted diffractogram (in grey, bottom). Peaks which have an intensity greater than 5% of the maximum peak intensity are marked and identified on the plot.

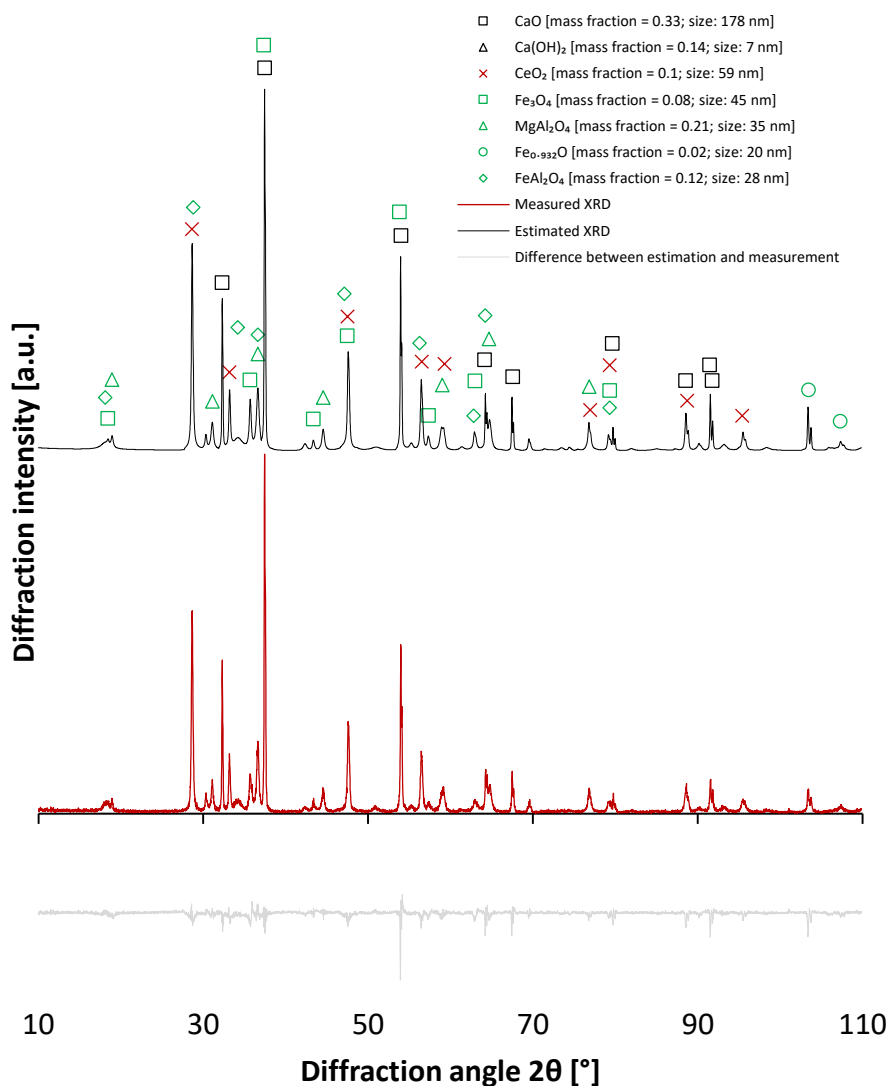


Figure C4: X-ray diffractogram of the oxygen carrier and the CO<sub>2</sub> carrier cycled 10 times for temperature-programmed production of CO (in red, center) with the X-ray diffractogram generated by Rietveld refinement (in black, top) and the difference between the observed and fitted diffractogram (in grey, bottom). Peaks which have an intensity higher than 2% of the maximum peak intensity are marked and identified on the plot.

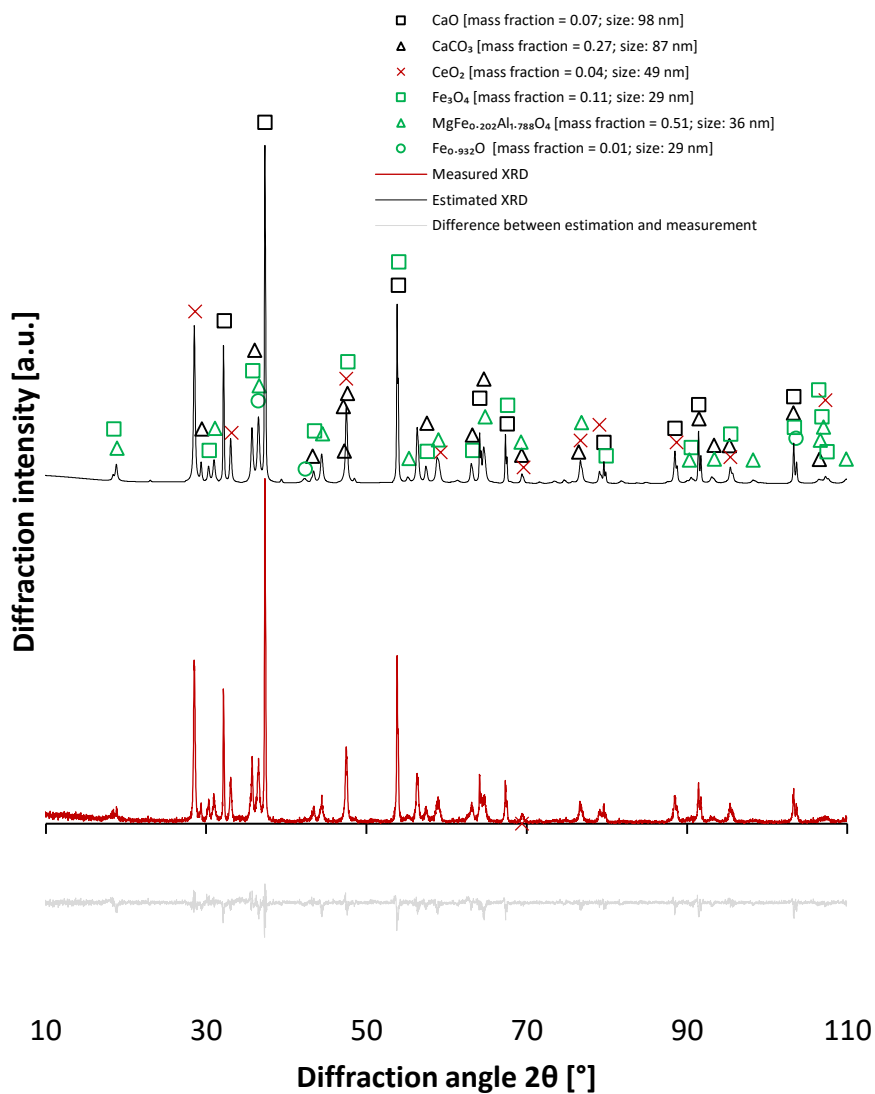


Figure C5: X-ray diffractogram of the oxygen carrier and the CO<sub>2</sub> carrier cycled once for isothermal production of CO (in red, center) with the X-ray diffractogram generated by Rietveld refinement (in black, top) and the difference between the observed and fitted diffractogram (in grey, bottom). Peaks which have an intensity higher than 1% of the maximum peak intensity are marked and identified on the plot.

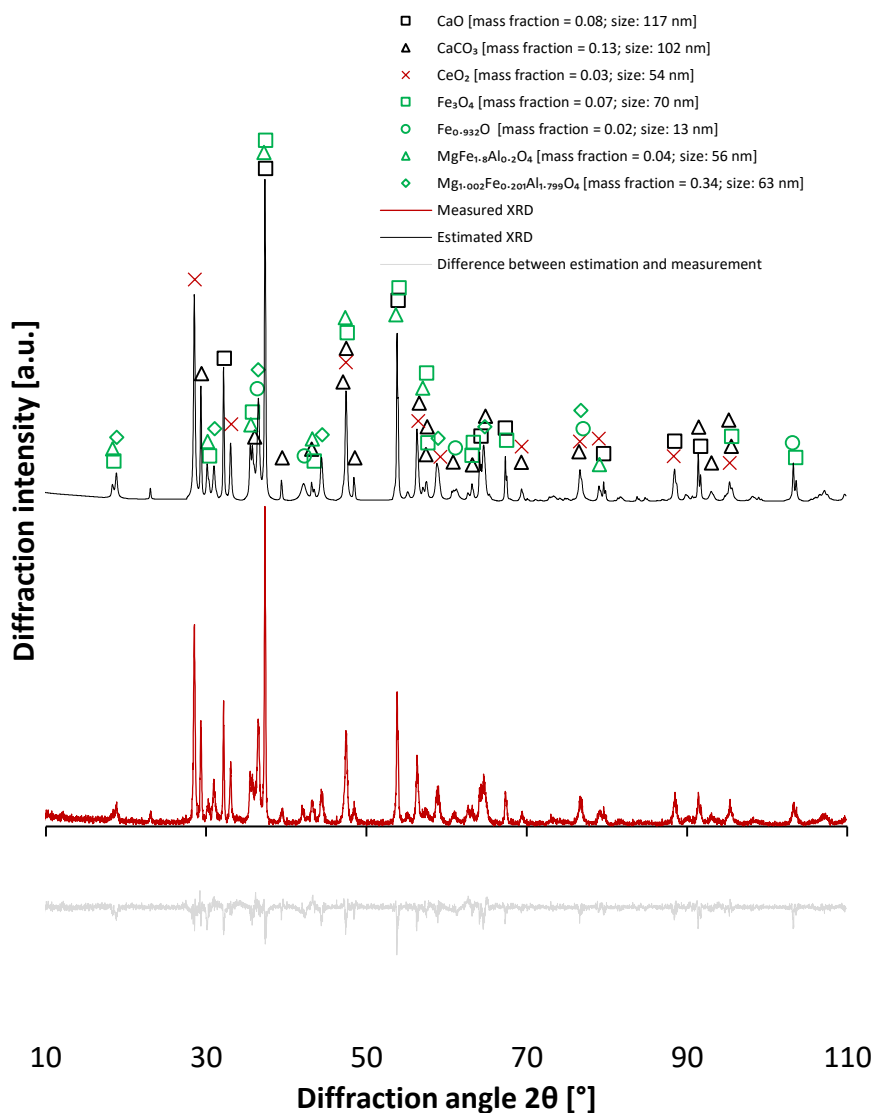


Figure C6: X-ray diffractogram of the oxygen carrier and the CO<sub>2</sub> carrier cycled 5 times for isothermal production of CO (in red, center) with the X-ray diffractogram generated by Rietveld refinement (in black, top) and the difference between the observed and fitted diffractogram (in grey, bottom). Peaks which have an intensity higher than 1% of the maximum peak intensity are marked and identified on the plot.



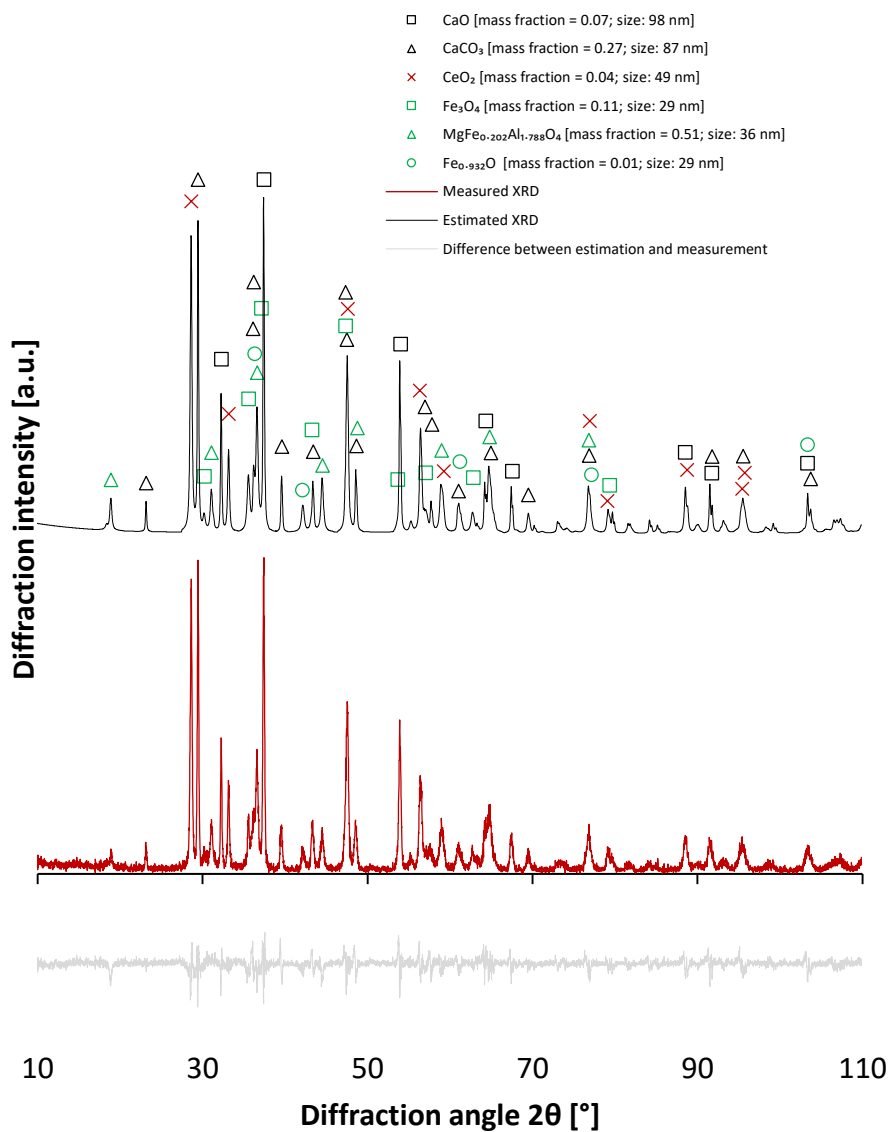


Figure C7: X-ray diffractogram of the oxygen carrier and the CO<sub>2</sub> carrier cycled 10 times for isothermal production of CO (in red, center) with the X-ray diffractogram generated by Rietveld refinement (in black, top) and the difference between the observed and fitted diffractogram (in grey, bottom). Peaks which have an intensity higher than 5% of the maximum peak intensity are marked and identified on the plot.

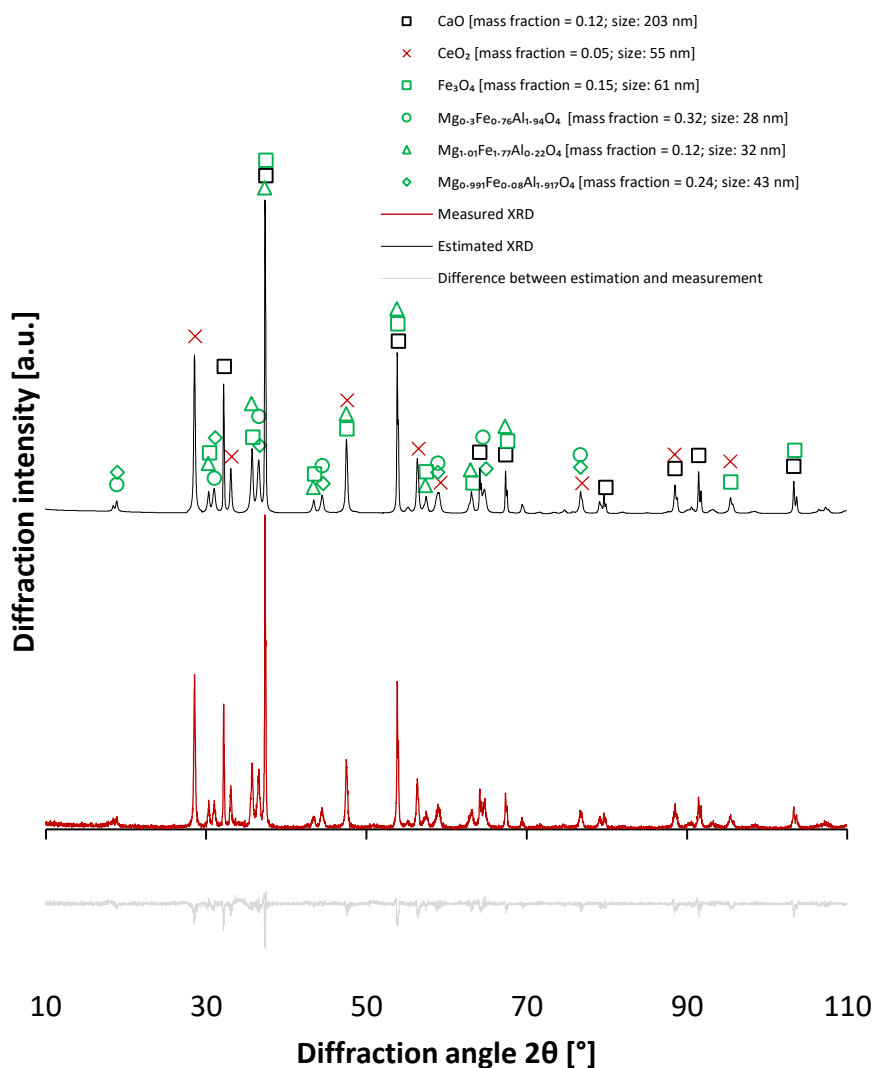


Figure C8: X-ray diffractogram of the oxygen carrier and the CO<sub>2</sub> carrier cycled once for temperature-programmed production of CO (in red, center) with the X-ray diffractogram generated by Rietveld refinement (in black, top) and the difference between the observed and fitted diffractogram (in grey, bottom). Peaks which have an intensity higher than 3% of the maximum peak intensity are marked and identified on the plot.

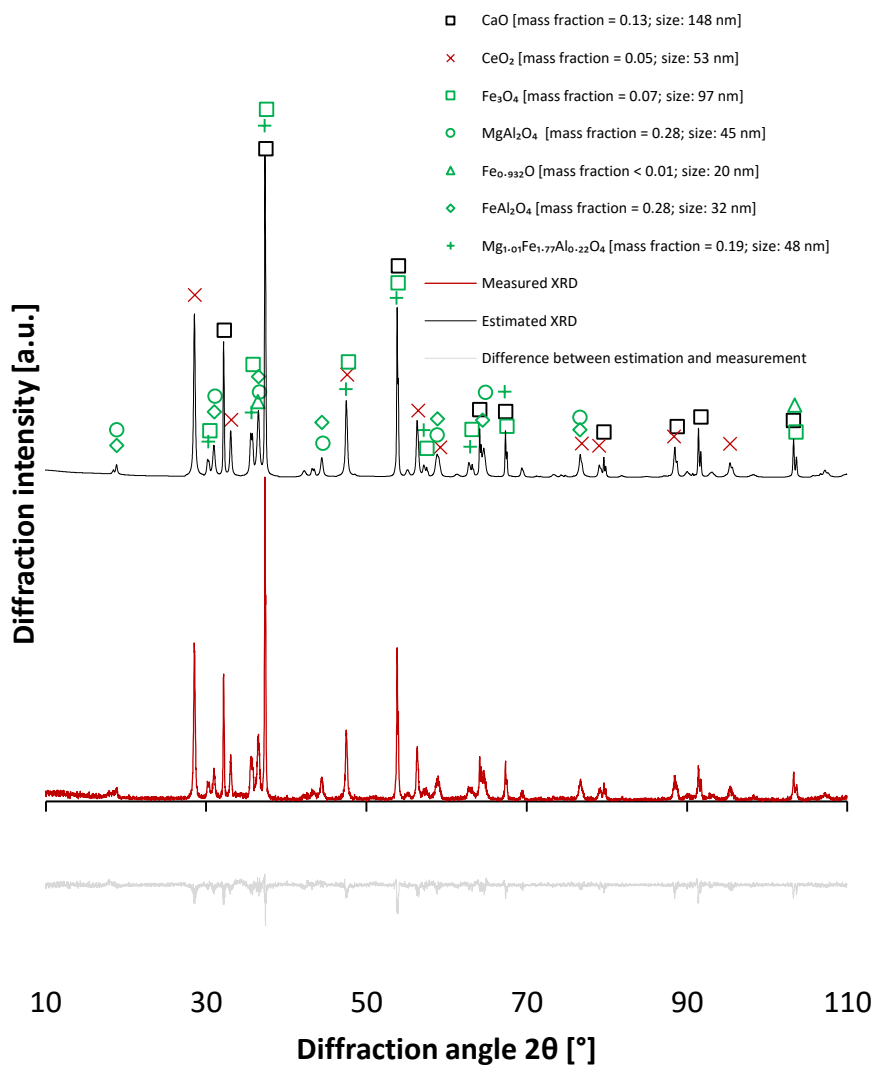


Figure C9: X-ray diffractogram of the oxygen carrier and the CO<sub>2</sub> carrier cycled 5 times for temperature-programmed production of CO (in red, center) with the X-ray diffractogram generated by Rietveld refinement (in black, top) and the difference between the observed and fitted diffractogram (in grey, bottom). Peaks which have an intensity higher than 3% of the maximum peak intensity are marked and identified on the plot.

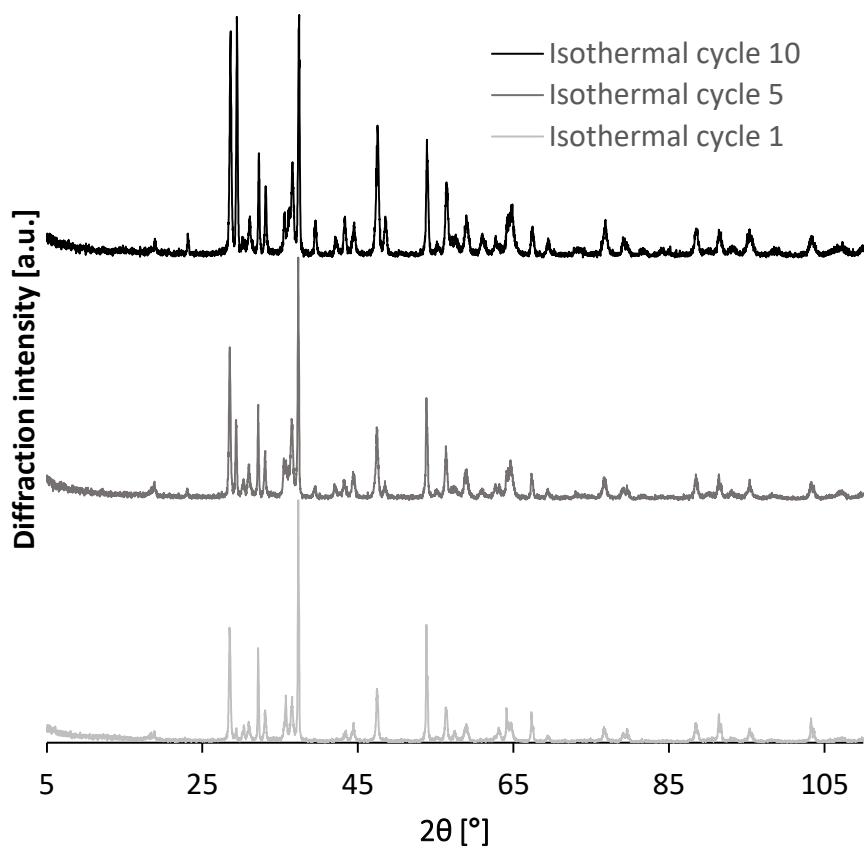


Figure C10: X-ray diffractograms displaying the evolution of the crystal structures of the materials upon being cycled in isothermal conditions to produce CO.

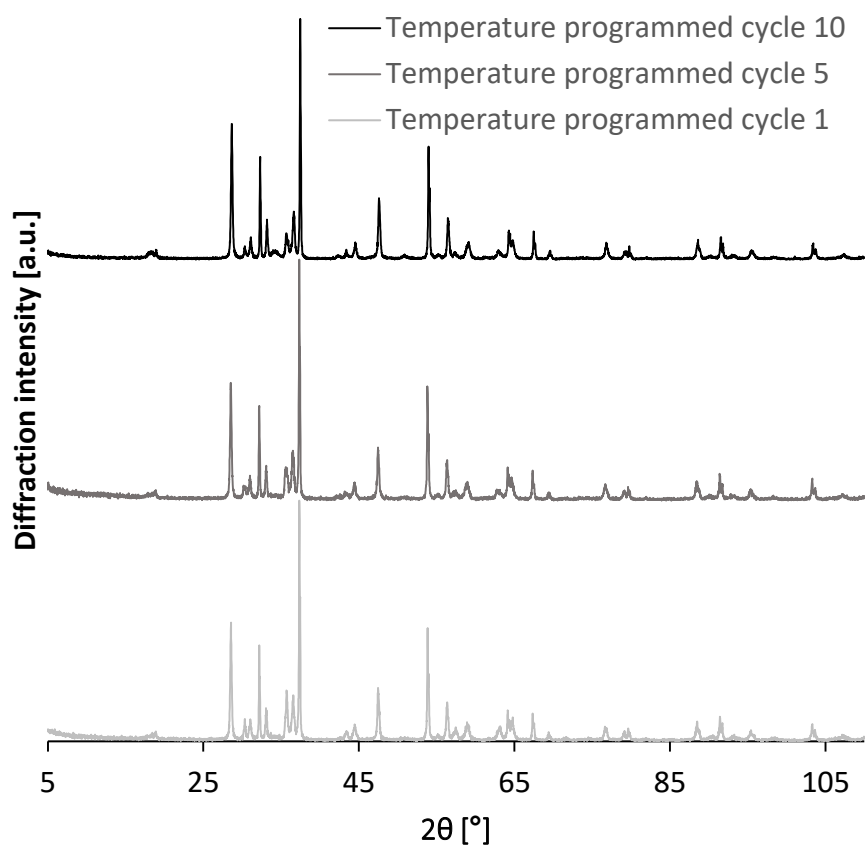


Figure C11: X-ray diffractograms displaying the evolution of the crystal structures of the materials upon being cycled in temperature-programmed conditions to produce CO.

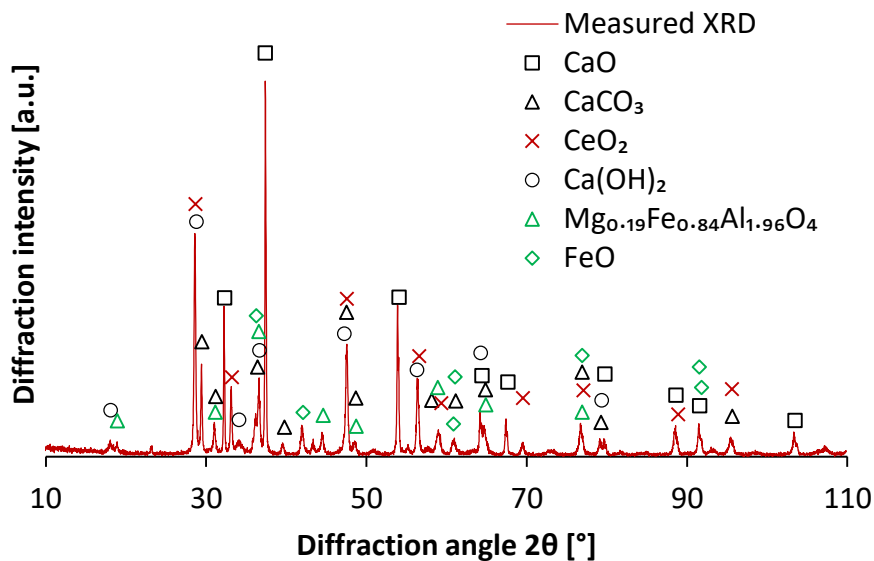


Figure C12: X-ray diffractogram of the oxygen carrier and the CO<sub>2</sub> carrier cycled 9 times for temperature-programmed production of CO and after the reduction-carbonation half-cycle of the 10<sup>th</sup> cycle. Peaks which have an intensity higher than 3% of the maximum peak intensity are marked and identified on the plot.

Table C4: Summary of the results for the Rietveld refinement of different materials and their phases.

Material	Phase	Lattice parameters [ $10^{-1}$ nm for a, b, and c or $^\circ$ for $\alpha$ , $\beta$ , and $\gamma$ ]						Crystal structure	Space group	Mass fraction	Crystallite size [nm]	Degree of crystallinity [%]	$R_{wp}$	$\chi^2$	Reference
		a	b	c	$\alpha$	$\beta$	$\gamma$								
As prepared oxygen carrier (Figure C1)	Fe <sub>2</sub> O <sub>3</sub>	5.027028	5.027028	13.72106	90	90	120	Hexagonal	R -3 c	0.17	59				[273]
	FeMgAlO <sub>4</sub>	8.269739	8.269739	8.269739	90	90	90	Cubic	F d -3m :1	0.09	< 3	63.3	0.2774	1.60 8	[274]
	Mg <sub>0.991</sub> Al <sub>1.917</sub> Fe <sub>0.08</sub> O <sub>4</sub>	8.151412	8.151412	8.151412	90	90	90	Cubic	F d -3m :2	0.74	13				[275]
As prepared CO <sub>2</sub> carrier (Figure C2)	CaO	4.809558	4.809558	4.809558	90	90	90	Cubic	F m 3 m	0.53	167				[276]
	CaCO <sub>3</sub>	4.989572	4.989572	17.07212	90	90	120	Hexagonal	R -3 c	0.08	65				[277]
	Ca(OH) <sub>2</sub>	3.590446	3.590446	4.916609	90	90	120	Hexagonal	P -3 m 1	0.17	15	80.1	0.2254	1.90 5	[278]
	CeO <sub>2</sub>	5.406900	5.406900	5.406900	90	90	90	Cubic	F m -3 m	0.22	48				[279]
After CO <sub>2</sub> -TPO of oxygen carrier (Figure C3)	Fe <sub>3</sub> O <sub>4</sub>	8.322095	8.322095	8.322095	90	90	90	Cubic	F d -3m :2	0.27	126				[280]
	MgAl <sub>2</sub> O <sub>4</sub>	8.134712	8.134712	8.134712	90	90	90	Cubic	F d 3 m	0.61	13	73.6	0.2631	1.86 6	[281]
	FeAl <sub>2</sub> O <sub>4</sub>	8.143417	8.143417	8.143417	90	90	90	Cubic	F d 3 m	0.12	53				[282]

After 10 isothermal cycles (Figure C7)	CaO	4.811486	4.811486	4.811486	90	90	90	Cubic	F m -3 m	0.07	98					[276]
	CaCO <sub>3</sub>	4.969181	4.969181	17.13672	90	90	120	Hexagonal	R -3 c	0.27	84					[277]
	CeO <sub>2</sub>	5.410340	5.410340	5.410340	90	90	90	Cubic	F m -3 m	0.04	49					[279]
	Fe <sub>3</sub> O <sub>4</sub>	8.380844	8.380844	8.380844	90	90	90	Cubic	F d -3 m :2	0.11	29	71.6	0.2855	2.028		[280]
	MgFe <sub>0.202</sub> Al <sub>1.788</sub> O <sub>4</sub>	8.150382	8.150382	8.150382	90	90	90	Cubic	F d -3 m :2	0.51	36					[283]
	Fe <sub>0.932</sub> O	4.290450	4.290450	4.290450	90	90	90	Cubic	F m -3 m	0.01	29					[284]
After 10 temperature programmed cycles (Figure C4)	CaO	4.811351	4.811351	4.811351	90	90	90	Cubic	F m -3 m	0.33	178					[276]
	Ca(OH) <sub>2</sub>	3.588777	3.588777	4.914087	90	90	120	Hexagonal	P -3 m 1	0.14	7					[278]
	CeO <sub>2</sub>	5.411065	5.411065	5.411065	90	90	90	Cubic	F m -3 m	0.1	59					[279]
	Fe <sub>3</sub> O <sub>4</sub>	8.362493	8.362493	8.362493	90	90	90	Cubic	F d -3 m :2	0.08	45	65.6	0.2749	2.579		[280]
	MgAl <sub>2</sub> O <sub>4</sub>	8.148464	8.148464	8.148464	90	90	90	Cubic	F d 3 m	0.21	35					[281]
	FeAl <sub>2</sub> O <sub>4</sub>	8.166385	8.166385	8.166385	90	90	90	Cubic	F d 3 m	0.02	28					[282]
	Fe <sub>0.932</sub> O	4.277724	4.277724	4.277724	90	90	90	Cubic	F m -3 m	0.12	20					[284]



After 1 isothermal cycle (Figure C5)	CaO	4.811273	4.811273	4.811273	90	90	90	Cubic	F m -3 m	0.12	143					[276]
	CaCO <sub>3</sub>	4.99	4.99	17.06150	90	90	120	Hexagonal	R -3 c	0.04	68					[277]
	CeO <sub>2</sub>	5.411	5.411	5.411	90	90	90	Cubic	F m -3 m	0.04	53					[279]
	Fe <sub>3</sub> O <sub>4</sub>	8.329378	8.329378	8.329378	90	90	90	Cubic	F d -3 m :2	0.17	47	68.1	0.2743	1.766		[280]
	MgFe <sub>0.202</sub> Al <sub>1.788</sub> O <sub>4</sub>	8.150382	8.150382	8.150382	90	90	90	Cubic	F d -3 m :2	0.62	36					[283]
	Fe <sub>0.932</sub> O	4.272313	4.272313	4.272313	90	90	90	Cubic	F m -3 m	< 0.01	17					[284]
After 5 isothermal cycles (Figure C6)	CaO	4.813507	4.813507	4.813507	90	90	90	Cubic	F m -3 m	0.08	117					[276]
	CaCO <sub>3</sub>	4.987987	4.987987	17.12259	90	90	120	Hexagonal	R -3 c	0.13	102					[277]
	CeO <sub>2</sub>	5.415439	5.415439	5.415439	90	90	90	Cubic	F m -3 m	0.03	54					[279]
	Fe <sub>3</sub> O <sub>4</sub>	8.320377	8.320377	8.320377	90	90	90	Cubic	F d -3 m :2	0.07	70	70.6	0.2912	1.744		[280]
	Mg <sub>1.002</sub> Fe <sub>0.201</sub> Al <sub>1.799</sub> O <sub>4</sub>	8.157459	8.157459	8.157459	90	90	90	Cubic	F d -3 m :1	0.63	34					[285]
	Fe <sub>0.932</sub> O	4.285614	4.285614	4.285614	90	90	90	Cubic	F m -3 m	0.02	13					[284]
	Al <sub>0.2</sub> Fe <sub>1.8</sub> MgO <sub>4</sub>	8.382446	8.382446	8.382446	90	90	90	Cubic	F d -3 m :2	0.04	56					[286]

After 1 temperature programmed cycle (Figure C8)	CaO	4.811368	4.811368	4.811368	90	90	90	Cubic	F m 3 m	0.12	203					[276]
	CeO <sub>2</sub>	5.411	5.411	5.411	90	90	90	Cubic	F m -3 m	0.05	55					[279]
	Fe <sub>3</sub> O <sub>4</sub>	8.327634	8.327634	8.327634	90	90	90	Cubic	F d -3 m :2	0.15	61					[280]
	Mg <sub>0.3</sub> Fe <sub>0.76</sub> Al <sub>1.94</sub> O <sub>4</sub>	8.162556	8.162556	8.162556	90	90	90	Cubic	F d -3 m :2	0.32	28	70.5	0.2647	1.74 3		[287]
	Mg <sub>1.01</sub> Fe <sub>1.77</sub> Al <sub>0.22</sub> O <sub>4</sub>	8.362035	8.362035	8.362035	90	90	90	Cubic	F d -3 m :2	0.12	32					[288]
	Mg <sub>0.991</sub> Fe <sub>0.08</sub> Al <sub>1.917</sub> O <sub>4</sub>	8.138499	8.138499	8.138499	90	90	90	Cubic	F d -3 m :2	0.24	42					[275]
After 5 temperature programmed cycles (Figure C9)	CaO	4.812316	4.812316	4.812316	90	90	90	Cubic	F m 3 m	0.13	148					[276]
	CeO <sub>2</sub>	5.413359	5.413359	5.413359	90	90	90	Cubic	F m -3 m	0.05	53					[279]
	Fe <sub>3</sub> O <sub>4</sub>	8.316873	8.316873	8.316873	90	90	90	Cubic	F d -3 m :2	0.07	97					[280]
	MgAl <sub>2</sub> O <sub>4</sub>	8.148464	8.148464	8.148464	90	90	90	Cubic	F d 3 m	0.28	45	68.3	0.2689	1.70 2		[281]
	FeAl <sub>2</sub> O <sub>4</sub>	8.166385	8.166385	8.166385	90	90	90	Cubic	F d 3 m	0.28	32					[282]
	Fe <sub>0.932</sub> O	4.277724	4.277724	4.277724	90	90	90	Cubic	F m -3 m	< 0.006	20					[284]
	Mg <sub>1.01</sub> Fe <sub>1.77</sub> Al <sub>0.22</sub> O <sub>4</sub>	8.367885	8.367885	8.367885	90	90	90	Cubic	F d -3 m :2	0.19	48					[288]

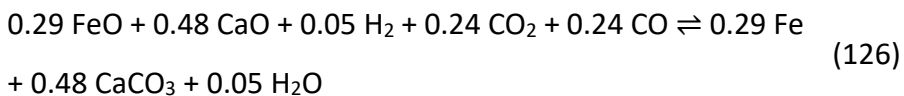
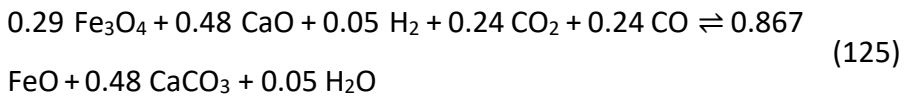
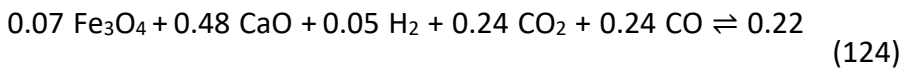
## Thermodynamic analysis

By computing the reaction quotient from the effluent gas concentration and comparing it with the equilibrium constants of the rWGS, reduction-carbonation, and decarbonation-oxidation reactions, it is possible to analyse the thermodynamic driving forces acting to direct the reactions taking place and also to identify the different phases involved in the reactions occurring in the reactor. A rearrangement of the De Donder equation displayed in (123) shows that the reaction rate ( $\dot{r}$ ) increases when the inverse of the reaction quotient deviates from the equilibrium constant ( $K_e$ ) [289]. When the value of the reaction quotient (or its inverse) approaches that of the equilibrium constant, the net reaction rate approaches a value of zero.

$$\dot{r} = \vec{r} \left( 1 - \frac{1}{K_e \prod_j a_j^{-\nu_j}} \right)$$

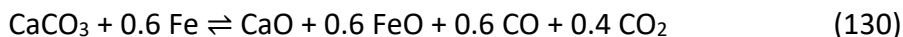
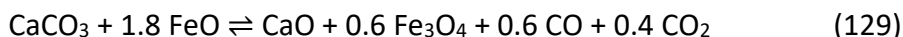
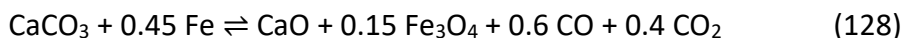
The reactions and their respective reaction quotients that can be considered in the given system are as follows:

Reduction-carbonation:



$$\text{Reaction quotient (expressed in kPa}^{0.28}\text{)} = [\text{H}_2\text{O}]^{0.05}[\text{CO}]^{-0.24}[\text{CO}_2]^{-0.24}[\text{H}_2]^{-0.05} \quad (127)$$

Decarbonation-oxidation:



$$\text{Reaction quotient (expressed in kPa)} = [\text{CO}_2]^{0.4}[\text{CO}]^{0.6} \quad (131)$$

rWGS:



$$\text{Reaction quotient} = [\text{H}_2\text{O}]^1[\text{CO}]^1[\text{CO}_2]^{-1}[\text{H}_2]^{-1} \quad (133)$$

wherein  $[x]$  denotes the activity of component 'x' and solids are assumed to have an activity of 1. For an ideal gas, the activity is equal to the partial pressure of the gas.

The equilibrium constant is calculated as follows:  $K_e = e^{-\Delta G^0/(RT)}$  where  $\Delta G^0$  = standard Gibbs free energy in kJ/mol, R is the universal gas constant in kJ/mol/K, and T is the temperature in K.

Figure C13 displays such an analytical calculation applied on the 10<sup>th</sup> reduction-carbonation half-cycle of isothermal CO production. After the first 30 seconds of the half-cycle, the rWGS effectively occurs to take the reaction quotient to its equilibrium value. This indicates that the gas-phase species, H<sub>2</sub>, CO, CO<sub>2</sub>, and H<sub>2</sub>O, in the reactor were effectively transformed to match the equilibrium value determined by the rWGS during the reduction-carbonation half-cycle. Based on the fact that the CO STY (see Figure 38 (c) in the manuscript) remained

almost constant over the 10 cycles, it can be speculated that the production of CO via rWGS during the reduction-carbonation half-cycle is favourable for the reduction of the OC, despite accumulation of  $\text{CaCO}_3$  in the CC preventing further capture of  $\text{CO}_2$ . The consistent reduction of OC during the reduction-carbonation half-cycle is discernible through the CO produced in the decarbonation-oxidation half-cycle over 10 cycles. This suggests that the rate at which the accumulation of reduced species  $\text{FeO}_x$  (where  $x < 1.33$ ) in the OC occurs is slower than that of  $\text{CaCO}_3$  in the CC. Over increasing number of cycles, a decrease in the CO STY could be expected due to near saturation of the CC with  $\text{CaCO}_3$  and of the OC with  $\text{FeO}_x$  (where  $x < 1.33$ ), which was not achieved over 10 cycles. Hence, in the isothermal implementation mode, periodic regeneration of the CC and OC could be necessary to maintain consistent CO STY.

In the first 30 seconds of the 1<sup>st</sup> reduction-carbonation half-cycle (Figure C14), atypical values of the reaction quotient were observed due to almost complete oxidation of CO and  $\text{H}_2$  by  $\text{Fe}_3\text{O}_4$  and a high capture rate of  $\text{CO}_2$  by CaO (displayed in Figure 38 (a)). In the first cycle, the role of the oxide surfaces that do not conform to known bulk phase thermodynamics may be prominently affecting the reaction quotient because the surface is still not as severely sintered as in the 10<sup>th</sup> cycle [290]. For example, for a few initial seconds in the first cycle (Figure 38 (a)), no outlet CO was observed indicating that thermodynamic constraints of bulk phase oxides were circumvented. The last few

seconds of the half-cycles were affected by the switch to Ar which led to atypical values of the reaction quotients that did not account for the pressure and flow rate changes that may have occurred in the reactor.

The trajectories of the reaction quotients in Figure C13 and Figure C14 indicate that the OC transitions between Fe and Fe<sub>3</sub>O<sub>4</sub> are achievable, as desired. This was further confirmed by tracing the trajectory of the reaction quotient during the decarbonation-oxidation half-cycle and is displayed in Figure C16.

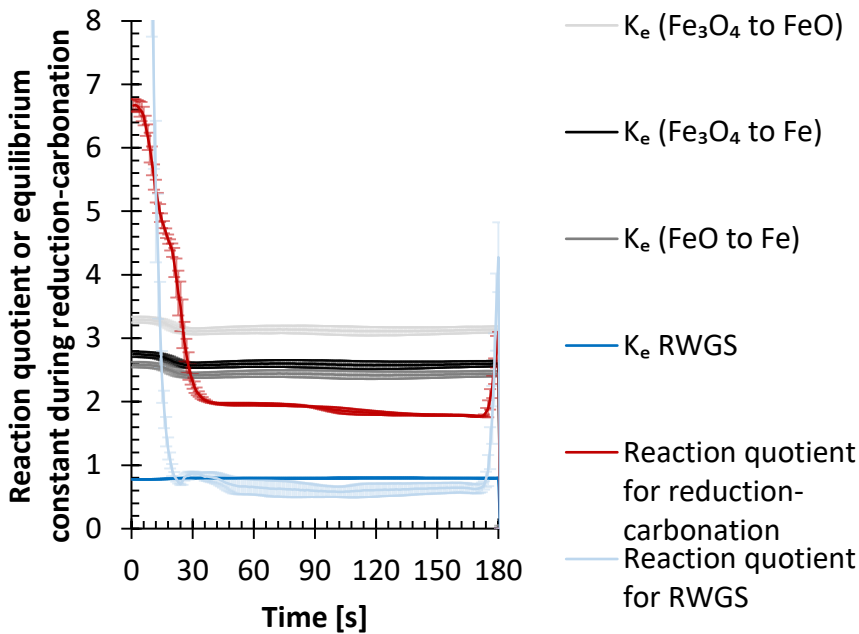


Figure C13: Reaction quotient and equilibrium constants in the 10<sup>th</sup> reduction-carbonation half-cycle of isothermal CO production. Error bars indicate the standard deviation obtained from three independent experiments.

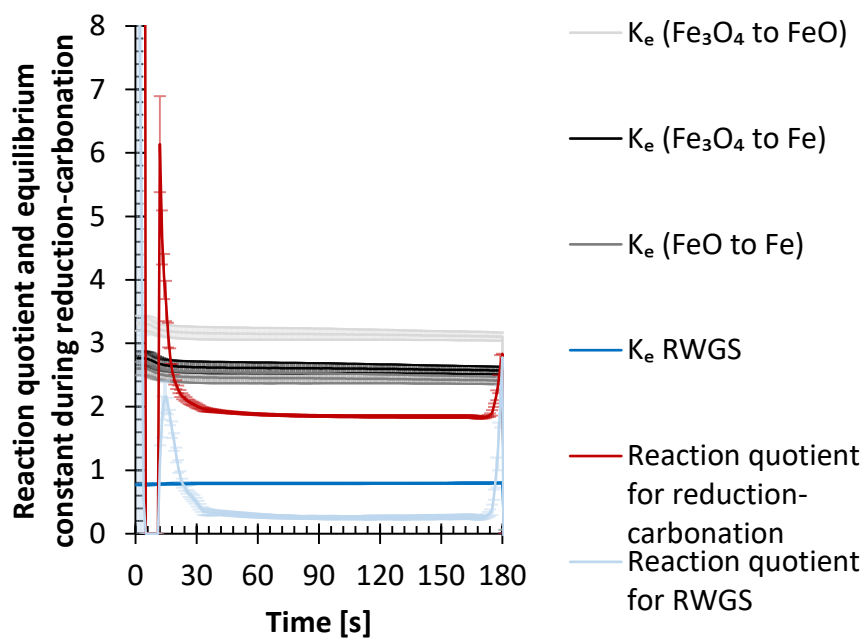


Figure C14: Reaction quotient and equilibrium constants in the 1<sup>st</sup> reduction-carbonation half-cycle of isothermal CO production. Error bars indicate the standard deviation obtained from three independent experiments.

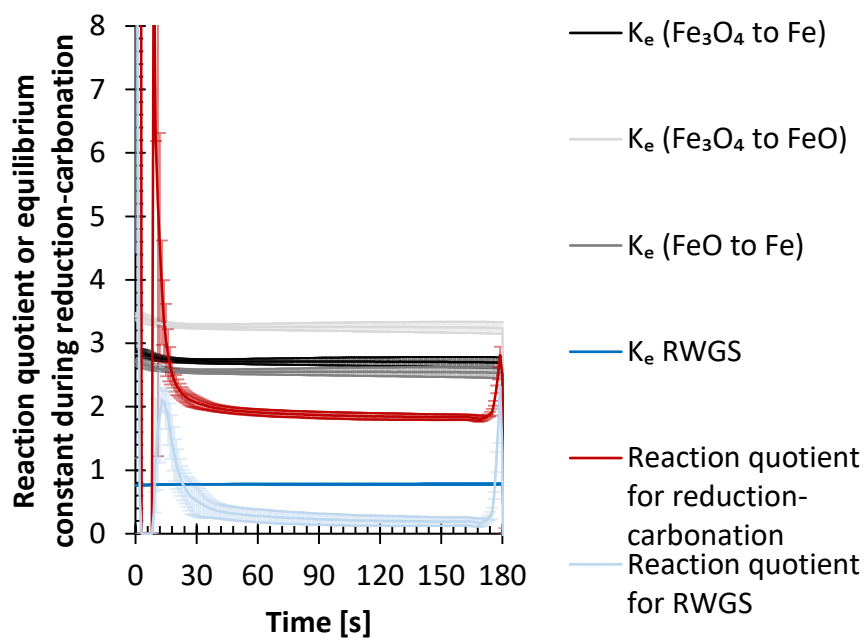


Figure C15: Reaction quotient and equilibrium constants in the 1<sup>st</sup> reduction-carbonation half-cycle of temperature-programmed CO production. Error bars indicate the standard deviation obtained from three independent experiments.



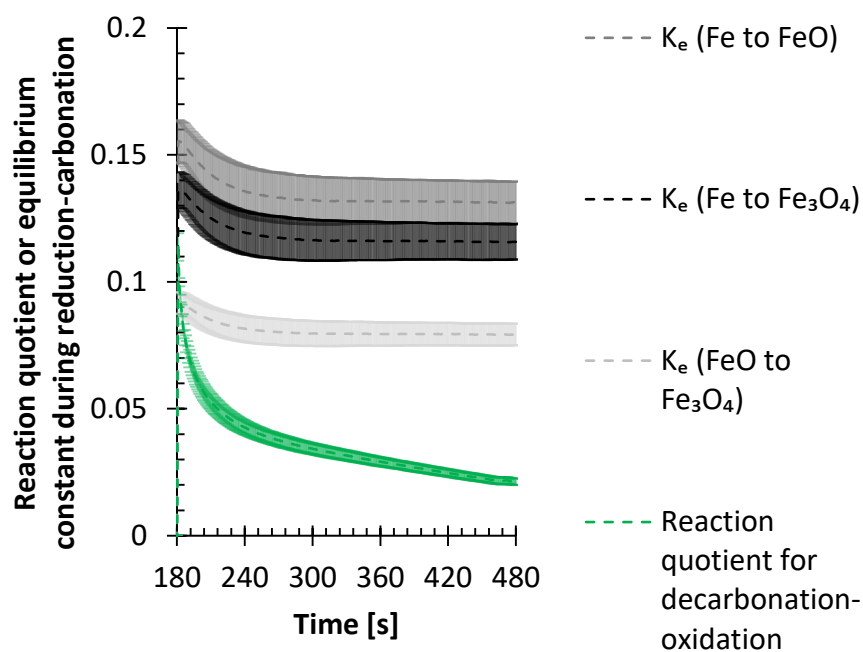


Figure C16: Reaction quotient and equilibrium constants in the 1<sup>st</sup> decarbonation-oxidation half-cycle of isothermal CO production. Error bars indicate the standard deviation obtained from three independent experiments.

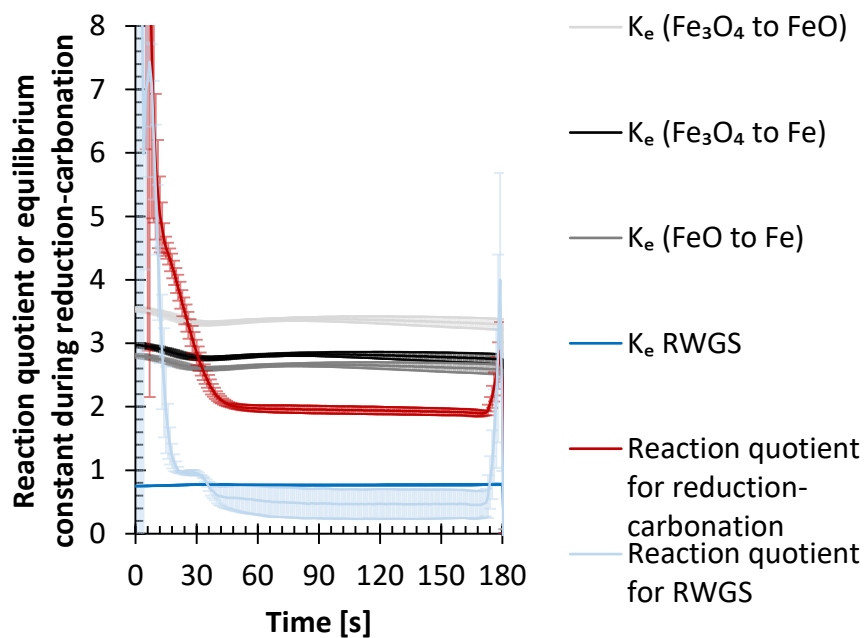


Figure C17: Reaction quotient and equilibrium constants in the 10<sup>th</sup> reduction-carbonation half-cycle of temperature-programmed CO production. Error bars indicate the standard deviation observed in three different experiments.

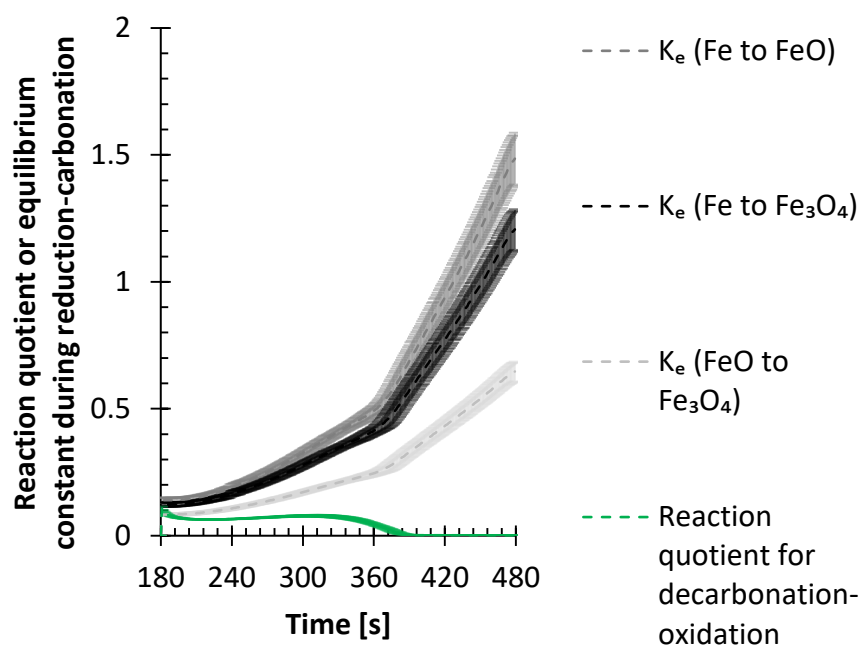


Figure C18: Reaction quotient and equilibrium constants in the 1<sup>st</sup> decarbonation-oxidation half-cycle of temperature-programmed CO production. Error bars indicate the standard deviation obtained from three independent experiments.

The increase in the thermodynamic driving force can also be visualised by the use of reaction quotients and the equilibrium constants, which are strongly affected by the temperature as displayed in Figure C18. The trajectory of the reaction quotient was not appreciably affected by the large increase in the thermodynamic driving force, which drives the reaction quotient towards the equilibrium constant. From the figure, it can also be noted that the reaction quotient does not tend towards the equilibrium constant determined by FeO to Fe<sub>3</sub>O<sub>4</sub> transitions, despite faster kinetics favoured by increased temperatures, thereby further validating that transitions from Fe to Fe<sub>3</sub>O<sub>4</sub> occur while forming intermediate FeO<sub>x</sub> species. The reaction quotient reached a value of zero towards the end of the cycle as the CaCO<sub>3</sub> was exhausted and no more CO<sub>2</sub> (and concomitant CO) could be released.

An analysis of the thermodynamic driving forces corresponding to the experimental reactor effluent composition highlighted the importance of rWGS during the reduction-carbonation half-cycle. Despite experimentally confirmed loss of the CC's capacity to capture CO<sub>2</sub>, the almost constant CO production during the decarbonation-oxidation half-cycles of the isothermal process for 10 cycles was likely caused due to the consistent reduction of the OC by the CO formed during rWGS in the reduction-carbonation half-cycle. The thermodynamic equilibria analyses also indicated that the necessary conditions for the redox transitions between Fe to Fe<sub>3</sub>O<sub>4</sub> were enabled

during both half-cycles of the cyclic tests. The formation of  $\text{Fe}_3\text{O}_4$  after the decarbonation-oxidation half-cycles was confirmed by ex-situ XRD analyses after multiple cycles (see Figure C4).

### Additional experimental results

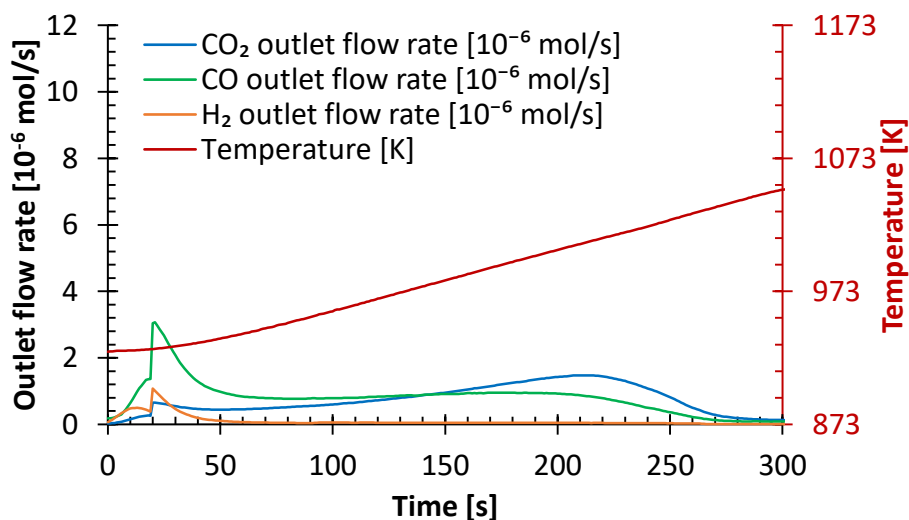


Figure C19: Experimental results of temperature-programmed CO production with shortened reduction-carbonation half-cycle time (20 seconds) and reduction-carbonation carried out at 923 K. Inlet gas flow rate during reduction-carbonation:  $41 \cdot 10^{-6}$  mol/s ( $10 \cdot 10^{-6}$  mol/s CO;  $10 \cdot 10^{-6}$  mol/s  $\text{CO}_2$ ;  $2 \cdot 10^{-6}$  mol/s  $\text{H}_2$ ; rest: Ar and He). Inlet gas flow rate during decarbonation-oxidation:  $41 \cdot 10^{-6}$  mol/s Ar. Materials were cycled 48 times (isothermally and in temperature-programmed conditions) before the experiment.

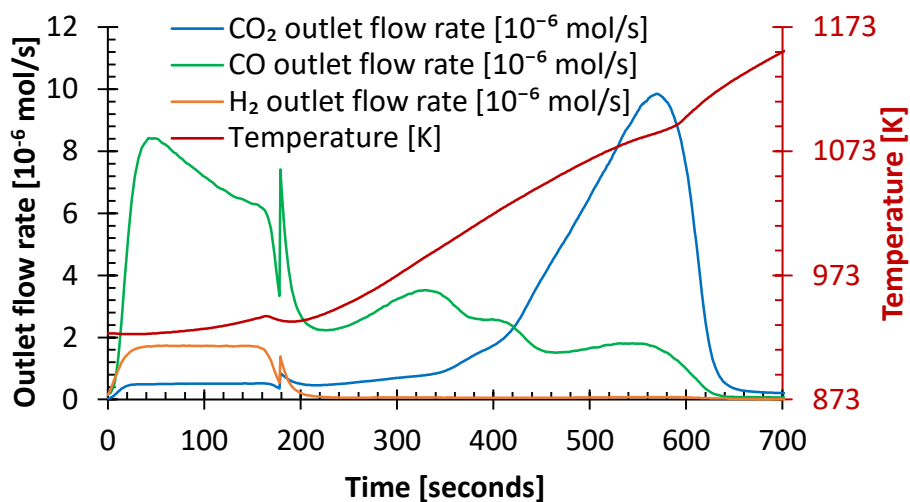


Figure C20: Experimental results of temperature-programmed CO production with shortened reduction-carbonation half-cycle time (180 seconds) and reduction-carbonation carried out at 923 K. Inlet gas flow rate during reduction-carbonation:  $41 \cdot 10^{-6}$  mol/s ( $10 \cdot 10^{-6}$  mol/s CO;  $10 \cdot 10^{-6}$  mol/s CO<sub>2</sub>;  $2 \cdot 10^{-6}$  mol/s H<sub>2</sub>; rest: Ar and He). Inlet gas flow rate during decarbonation-oxidation:  $41 \cdot 10^{-6}$  mol/s Ar. Materials were cycled 49 times (isothermally and in temperature-programmed conditions) before the experiment.

Table C5: Comparison of process parameters to estimate the influence of varying the reduction-carbonation half-cycle time for reduction-carbonation carried out at 923 K (Figure C19 and Figure C20).

Operation mode	r-c half-cycle time [s]	Fuel utilisation [mol%]	Carbon recovery [mol%]	CO:CO <sub>2</sub> molar ratio in outlet	Average OC utilisation [mol%]	Average CO <sub>2</sub> carrier utilisation [mol%]
Temperature - programmed	20	85 – 100	96 – 100	0.72 – 0.96	5.6	6.5
Temperature - programmed	180	32 – 50	76 – 91	0.43 – 0.66	20.4	34.8

The range of values for the process parameters of experiments with short reduction-carbonation half cycle times displayed in Table 17 and Table C5 were calculated based on the following equations (r-c: reduction-carbonation; d-o: decarbonation-oxidation):

$$FU_{r-c} = \frac{\int_0^{t_{r-c}} ((\dot{n}_{H_2,in} - \dot{n}_{H_2,out}) + (\dot{n}_{CO,in} - \dot{n}_{CO,out}))}{\int_0^{t_{r-c}} (\dot{n}_{H_2,in} + \dot{n}_{CO,in})} * 100$$

$$FU_{d-o} = \frac{\int_0^{t_{d-o}} \dot{n}_{CO,out}}{\int_0^{t_{r-c}} (\dot{n}_{H_2,in} + \dot{n}_{CO,in})} * 100$$

$$CR_{r-c} = \frac{\int_0^{t_{r-c}} ((\dot{n}_{CO_2,in} - \dot{n}_{CO_2,out}) + (\dot{n}_{CO,in} - \dot{n}_{CO,out}))}{\int_0^{t_{r-c}} (\dot{n}_{CO_2,in} + \dot{n}_{CO,in})} * 100$$

$$CR_{d-o} = \frac{\int_0^{t_{d-o}} (\dot{n}_{CO_2,out} + \dot{n}_{CO,out})}{\int_0^{t_{r-c}} (\dot{n}_{CO_2,in} + \dot{n}_{CO,in})} * 100$$

$$OCU_{average} = \frac{(OCU)_{r-c} + (OCU)_{d-o}}{2}$$

$$CCU_{average} = \frac{(CCU)_{r-c} + (CCU)_{d-o}}{2}$$

$$CCR = \frac{\int_0^{t_{d-o}} \dot{n}_{CO,out}}{\int_0^{t_{d-o}} \dot{n}_{CO_2,out}}$$

$$CCR \text{ (corrected)} = \frac{1}{\frac{\int_0^{t_{d-o}} \dot{n}_{CO,out}}{\int_0^{t_{d-o}} \dot{n}_{CO_2,out}}} - \frac{OB}{100} * \frac{1}{\frac{\int_0^{t_{d-o}} \dot{n}_{CO,out}}{\int_0^{t_{d-o}} \dot{n}_{CO_2,out}}}$$

$$OB = \frac{\int_0^{t_{r-c}} (2 * \dot{n}_{CO_2,in} + \dot{n}_{CO,in}) - \int_0^{t_{d-o}} (2 * \dot{n}_{CO_2,out} + \dot{n}_{CO,out})}{\int_0^{t_{r-c}} (2 * \dot{n}_{CO_2,in} + \dot{n}_{CO,in})} * 100$$



Figure C21: Photos of the reactor containing the solids used for the experiments. The red particles are those of the OC and the white particles are either the CC or the solid diluent,  $\alpha\text{-Al}_2\text{O}_3$ . The ruler has a cm based scale.



Table C6: Summary of reactor productivities at different conditions.

Operation mode	Reduction-carbonation half-cycle time [s]	Total cycle time [s]	Reduction-carbonation temperature [K]	CO productivity [kg/m <sup>3</sup> /h]
Isothermal	180	480	1023	34
Temperature-programmed	180	400	1023	52
Isothermal	20	130	1023	58
Temperature-programmed	20	110	1023	75
Temperature-programmed	20	300	923	46
Temperature-programmed	180	700	923	77

# Appendix D

## Calculations

### Thermodynamic calculations

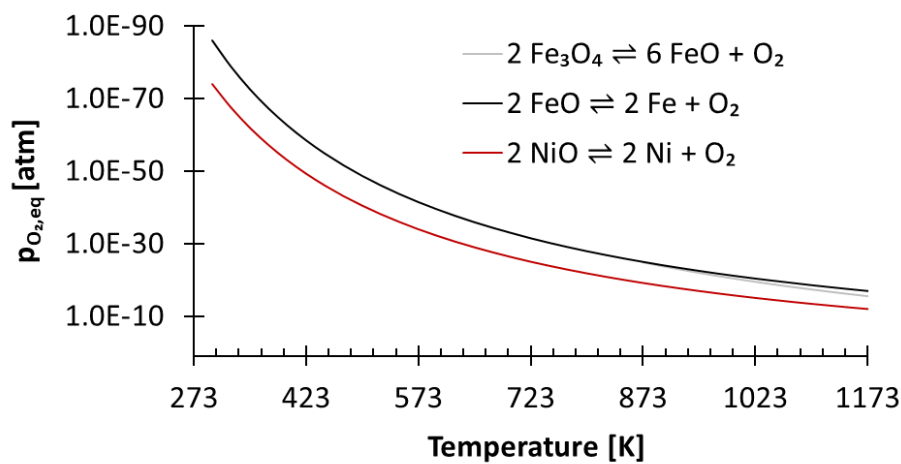


Figure D1: The variation of the thermodynamic equilibrium partial pressure of O<sub>2</sub> against temperature at a pressure of 101.3 kPa. Note that FeO is unstable below 843 K. Data for Fe<sub>3</sub>O<sub>4</sub>, Ni, Fe, and O<sub>2</sub> from NIST [118] and of FeO and NiO from FactSage (FactPS database) [119].

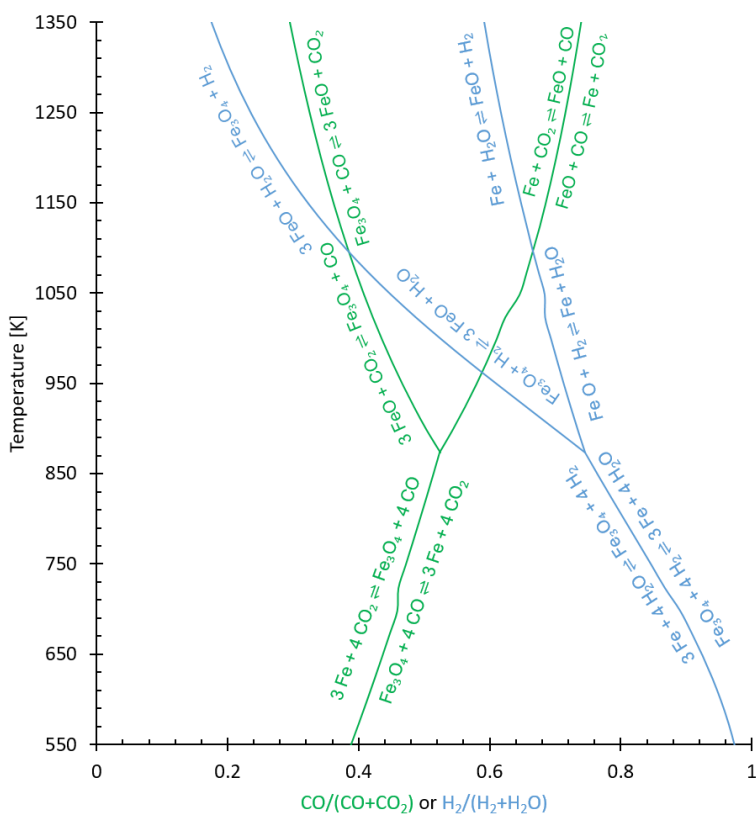


Figure D2: Bauer-Glaessner diagram generated using data from NIST [118] and FactSage (for FeO only).

Experimental results and data

Table D1: Textural properties of the as prepared materials from nitrogen sorption measurements at 77 K.

			50% Fe <sub>2</sub> O <sub>3</sub> /MgAl <sub>2</sub> O <sub>4</sub>	83% CaO/CeO <sub>2</sub>	80% Mn <sub>2</sub> O <sub>3</sub> /MgAl <sub>2</sub> O <sub>4</sub>
BET	surface	area	41.5 ± 0.3	6.3 ± 0.3	6.7 ± 0.2
	[m <sup>2</sup> /g]				
Pore	volume	[10 <sup>-9</sup>	258 ± 1	18 ± 1	20 ± 1
	m <sup>3</sup> /g]				
BJH	desorption	pore	22.5 ± 0.2	32.7 ± 5.4	36.4 ± 4.3
	diameter	[nm]			
Particle size [nm]			33 ± 0.3	237 ± 11.9	177 ± 4.3

Energy dispersive x-ray spectroscopy

SEM-EDX was performed on the as prepared OC and the CC to obtain their composition using a SEM JEOL JSM 5400 setup equipped with an INCA x-act extension (Oxford instruments) for Energy Dispersive X-ray spectrometry (EDX) measurements.

Table D2: Elemental composition using energy dispersive x-ray spectroscopy (EDX) or inductively coupled plasma coupled with optical emission spectroscopy (ICP-OES) expressed in mass percentage of the materials used for the experimental demonstration of the process concept. The error indicates the standard deviation based on at least four measurements. Values in brackets indicate expected values.

Element	50% Fe <sub>2</sub> O <sub>3</sub> /MgAl <sub>2</sub> O <sub>4</sub>	80% Mn <sub>2</sub> O <sub>3</sub> /MgAl <sub>2</sub> O <sub>4</sub>	83% CaO/CeO <sub>2</sub> **
Fe	36 ± 2 (35)	-	-
Mn	-	54 ± 1 (56)	-
Ni	-	-	-
Mg	6 ± 1 (8)	3 ± 0 (3)	-
Al	17 ± 2 (19)	8 ± 1 (8)	-
Ca	-	-	74 ± 4 (81)
Ce	-	-	26 ± 4 (19)
O	40 ± 3 (37)	34 ± 1 (33)	-

\*\* measurement on an oxygen free basis.

## X-ray diffraction

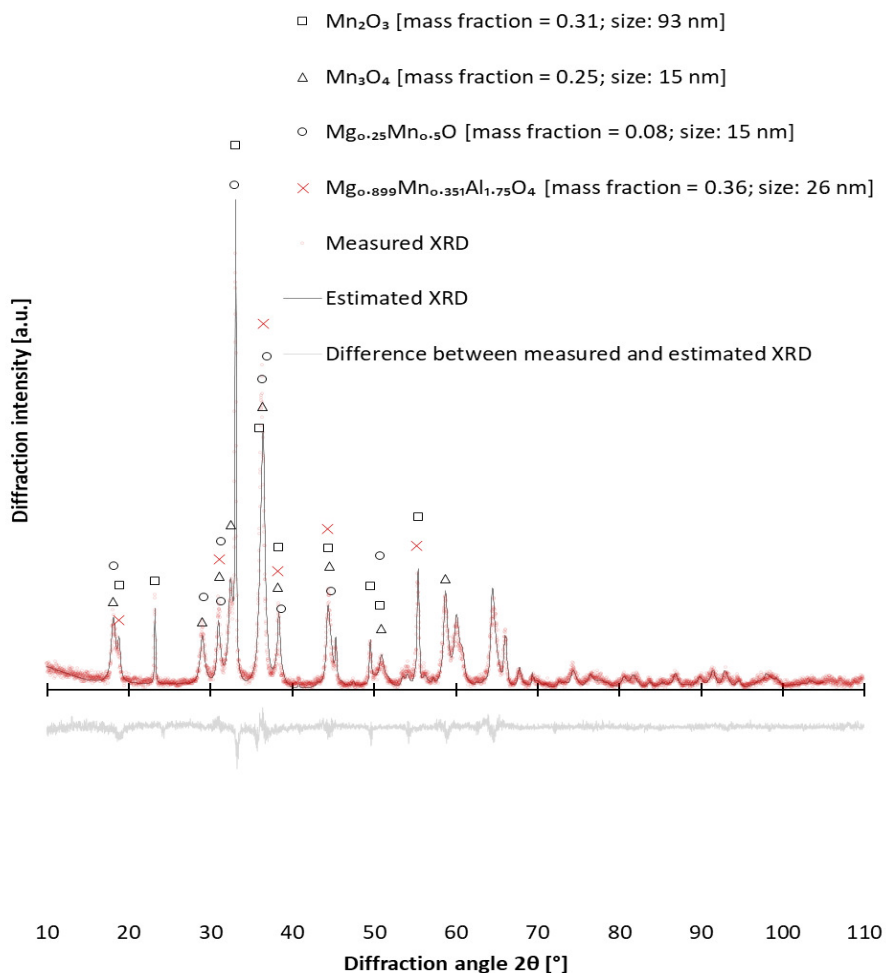


Figure D3: X-ray diffractogram of the fresh oxygen carrier 80%  $\text{Mn}_2\text{O}_3/\text{MgAl}_2\text{O}_4$  (in red circles) with the X-ray diffractogram generated by Rietveld refinement (in black) and the difference between the observed and fitted diffractogram (in grey, bottom). Peaks which have an intensity higher than 5% of the maximum peak intensity are marked and identified on the plot.



Table D3: Summary of the results for the Rietveld refinement of different materials and their phases.

Material	Phase	Lattice parameters [ $10^{-1}$ nm for a, b, and c or $^{\circ}$ for $\alpha$ , $\beta$ , and $\gamma$ ]						Crystal structure	Space group	Mass fraction	Crystallite size [nm]	Degree of crystallinity [%]	$R_{wp}$	$\chi^2$	Reference
		a	b	c	$\alpha$	$\beta$	$\gamma$								
As prepared	Mn <sub>2</sub> O <sub>3</sub>	9.356221	9.405141	9.382382	90	90	90	Orthorhombic	P c a b	0.53	167				[291]
Mn-based oxygen carrier	Mn <sub>3</sub> O <sub>4</sub>	5.747054	5.747054	9.438224	90	90	90	Tetragonal	I 41/a m d	0.08	65	76.1	0.2424	2.12	[292]
(Figure D3)	Mg <sub>0.899</sub> Mn <sub>0.351</sub> Al <sub>1.75</sub> O <sub>4</sub>	8.169781	8.169781	8.169781	90	90	90	Cubic	F d -3 m	0.17	15				[293]
	Mg <sub>0.25</sub> Mn <sub>0.5</sub> O	5.721406	5.721406	9.298237	90	90	90	Tetragonal	I 41/a m d	0.22	48				[294]



## Temperature programmed reactions

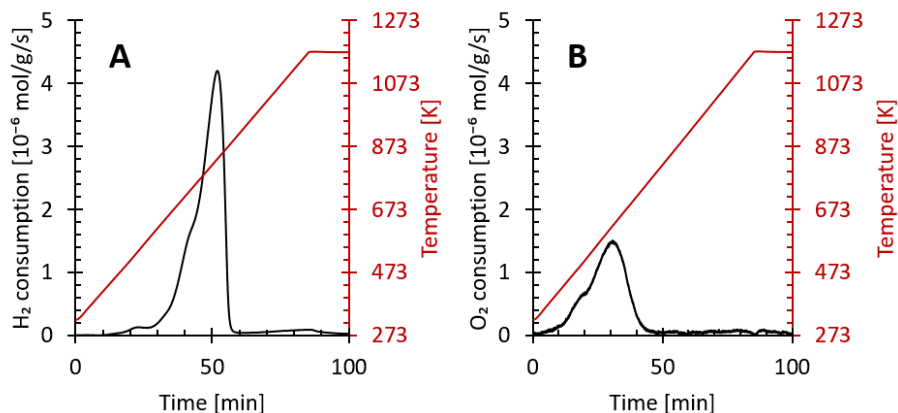


Figure D4: Temperature-programmed reactions (TPRe) with a temperature ramp of 10 K/min up to 1173 K and a total flow rate of  $45 \cdot 10^{-6}$  mol/s for the 80%  $Mn_2O_3/MgAl_2O_4$ . A:  $H_2$ -TPR under a flow of 5 mol%  $H_2$  in Ar for the determination of exchangeable oxygen atoms; B:  $O_2$ -TPO under a flow of 5%  $O_2$  in Ar for the determination of replenishable oxygen atoms in the fully reduced material.

## Redox cyclic experiments in the fixed bed reactor

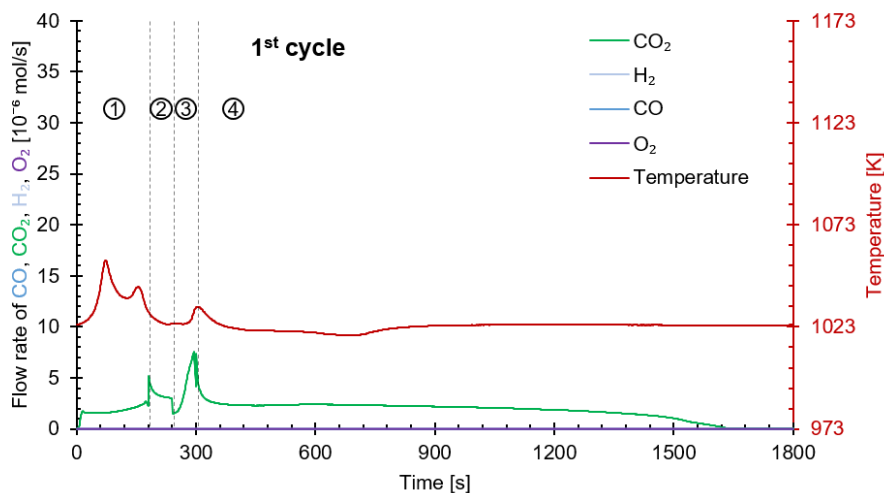


Figure D5: The first of the 30 redox cycles executed for the proof of concept experiments involving  $Mn_3O_4$ ,  $CaO$ , and  $FeO_x$  as active materials. Compared to the last

25 cycles, the reduction step lasted 180 seconds instead of 240 cycles to determine the time required for complete decarbonation of the  $\text{CaCO}_3$  in the given conditions. The vertical dashed lines indicate the change of stage (from left to right: stages 1 to 4 marked by numbers in circles).

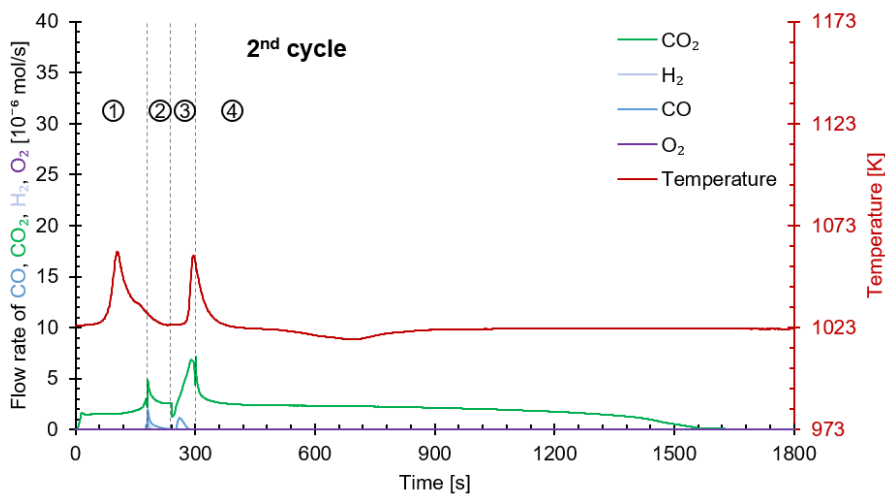


Figure D6: The second of the 30 redox cycles executed for the proof of concept experiments involving  $\text{Mn}_3\text{O}_4$ ,  $\text{CaO}$ , and  $\text{FeO}_x$  as active materials. Compared to the last 25 cycles, the reduction step lasted 180 seconds instead of 240 seconds. The vertical dashed lines indicate the change of stage (from left to right: stages 1 to 4 marked by numbers in circles).

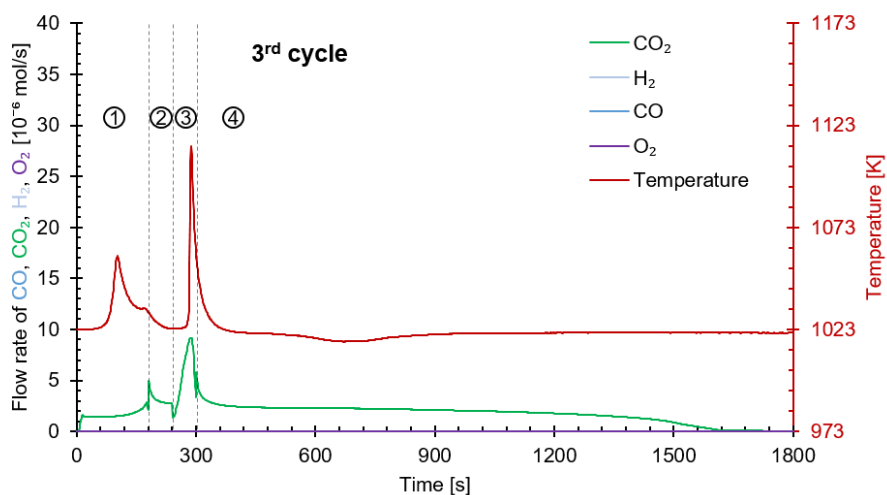


Figure D7: The third of the 30 redox cycles executed for the proof of concept experiments involving  $\text{Mn}_3\text{O}_4$ ,  $\text{CaO}$ , and  $\text{FeO}_x$  as active materials. Compared to the last 25 cycles, the reduction step lasted 180 seconds instead of 240 seconds. The vertical dashed lines indicate the change of stage (from left to right: stages 1 to 4 marked by numbers in circles).

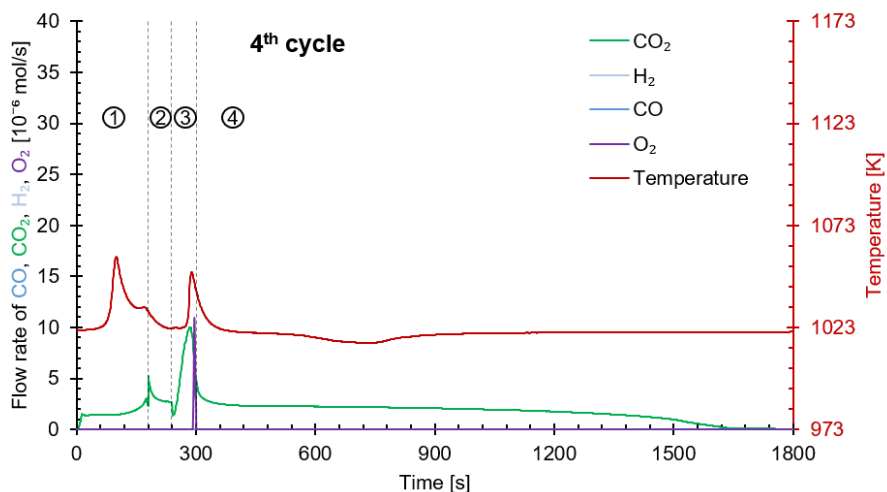


Figure D8: The fourth of the 30 redox cycles executed for the proof of concept experiments involving  $\text{Mn}_3\text{O}_4$ ,  $\text{CaO}$ , and  $\text{FeO}_x$  as active materials. Compared to the last

25 cycles, the reduction step lasted 180 seconds instead of 240 seconds. The vertical dashed lines indicate the change of stage (from left to right: stages 1 to 4 marked by numbers in circles).

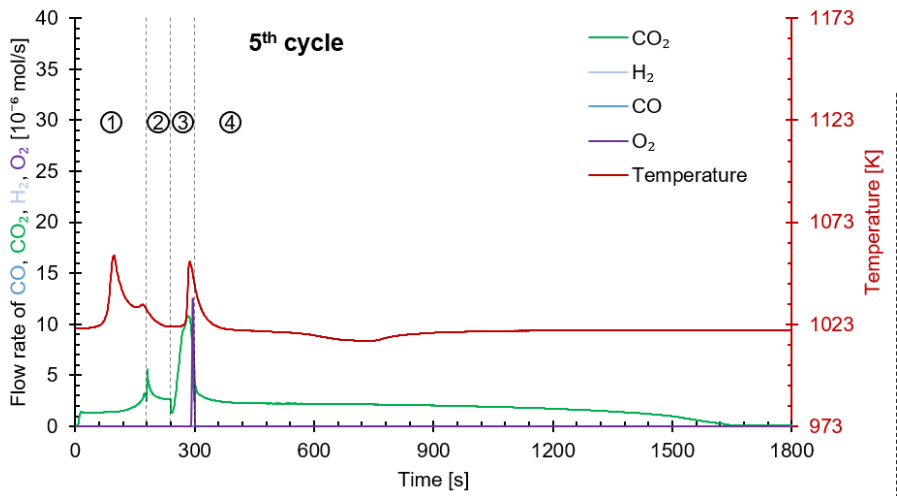


Figure D9: The fifth of the 30 redox cycles executed for the proof of concept experiments involving Mn<sub>3</sub>O<sub>4</sub>, CaO, and FeO<sub>x</sub> as active materials. Compared to the last 25 cycles, the reduction step lasted 180 seconds instead of 240 seconds. The vertical dashed lines indicate the change of stage (from left to right: stages 1 to 4 marked by numbers in circles).

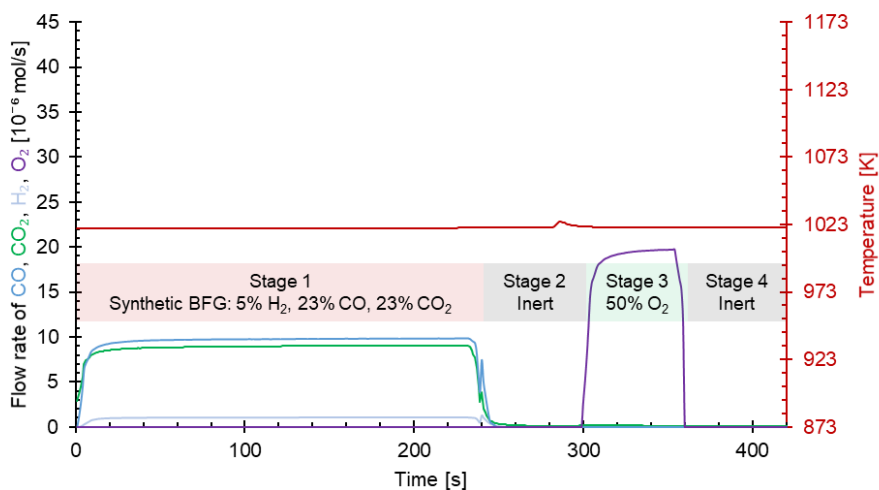


Figure D10: Experimental results showing the outlet flow rates of different components when gases were fed to an empty reactor. Total inlet flow rate during all 4 stages:  $41 \cdot 10^{-6}$  mol/s.

## Process simulations

Table D4: Aspen Plus® setup of modules, property methods, material databanks, and models.

Flowsheet setup	
Property method	<i>PR-BM</i> and <i>STEAM-TA</i> for free water method
Databank	<i>PURE36</i> , <i>INORGANIC</i> , <i>SOLIDS</i>
Solid components	C (graphite), $\text{Fe}_3\text{O}_4$ , $\text{FeO}$ , $\text{Fe}$ , $\text{CaO}$ , $\text{CaCO}_3$ , $\text{Mn}_3\text{O}_4$ , $\text{MnO}$ , $\text{MgAl}_2\text{O}_4$ , $\text{CeO}_2$
Fluid components	$\text{CO}$ , $\text{CO}_2$ , $\text{H}_2$ , $\text{H}_2\text{O}$ , $\text{CH}_4$ , $\text{O}_2$ , $\text{N}_2$
Stream class	<i>MIXCISLD</i>
Unit operation models	
Reactors	<i>RGIBBS</i> (by product distribution achieved minimisation of Gibbs free energy of selected solids and gases i.e. all possible components)
Separators	<i>SSplit</i> for solids and gases and <i>Sep</i> for separating gas mixtures
Fluid flow splitting	<i>FSplit</i>
Heat exchangers	<i>HeatX</i> (Shortcut method: 10 K minimum temperature approach and 10 K difference between hot inlet/cold outlet or hot outlet-cold inlet) and <i>Heater</i>

Mechanical operation models	
Compressor or turbine	or <i>Compr</i> (72% isentropic efficiency & 100% mechanical efficiency)

For the process simulations, the  $C_p$  data for  $\text{Fe}_3\text{O}_4$ , Fe, and CaO were taken from NIST [118] and for FeO and  $\text{CaCO}_3$  from FactSage (database: Fact-PS) [119].

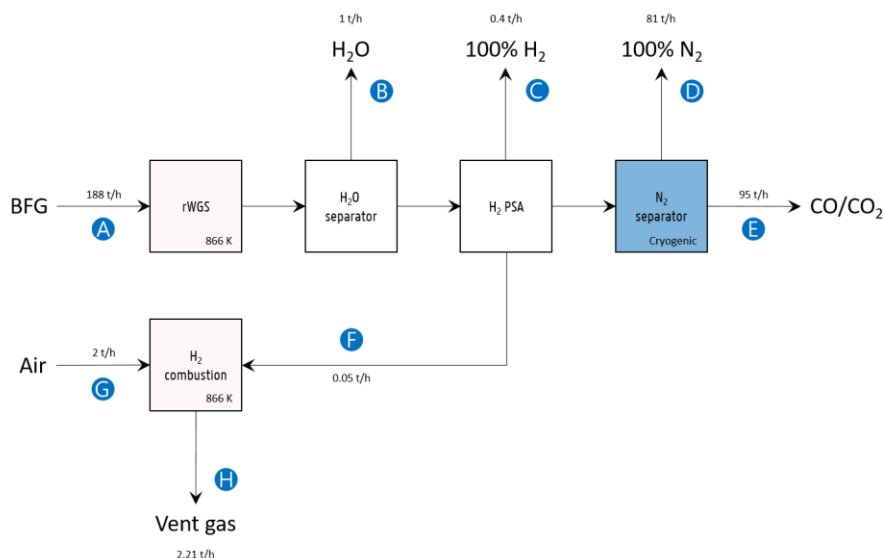


Figure D11: Block flow diagram of the process involving steady-state catalytic rWGS and downstream separation with mass flow rates. Labels: A: BFG feed to the catalytic reverse water-gas shift reaction (rWGS) block for producing a  $\text{CO}/\text{CO}_2$  product stream (E), B: a hypothetical  $\text{H}_2\text{O}$  separator (for example, a knockout drum), C: an  $\text{H}_2$  pressure swing adsorption (PSA) column for creating a 100% pure  $\text{H}_2$  stream partly for sale and partly for providing heat to the rWGS block (F), D: a pure  $\text{N}_2$  stream generated from the product stream via cryogenic distillation, G: air fed for  $\text{H}_2$  combustion, and H: outlet gas from  $\text{H}_2$  combustion.

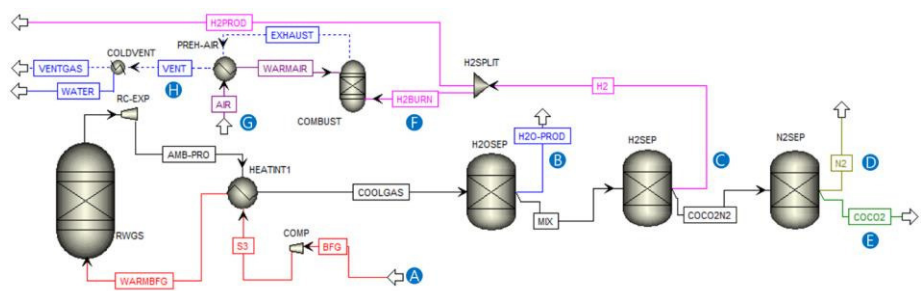


Figure D12: Aspen Plus flowsheet of rWGS with downstream separation. The alphabetical blue labels correspond to those from Figure D11.





## Techno-economic evaluation

### Estimation of the costs of fresh and spent solids and catalyst

The costs of the precursors necessary for the preparation of the oxygen carriers, 80%  $\text{Mn}_2\text{O}_3/\text{MgAl}_2\text{O}_4$  and 50%  $\text{Fe}_2\text{O}_3/\text{MgAl}_2\text{O}_4$  and the  $\text{CO}_2$  carrier 83%  $\text{CaO}/\text{CeO}_2$  were calculated by extrapolating their costs from commercial suppliers in Belgium using the relation described in equation (143) [168], where  $p(q)$  is the unit price of the precursor which is dependent on the quantity  $q$ ,  $b$  is the scale parameter and  $\gamma$  is the discount factor.

$$p(q) = b * q^\gamma$$

Figure D14, Figure D15, and Figure D16 show the retail prices used for the different precursors or raw materials used for the synthesis of the oxygen carriers and the  $\text{CO}_2$  carrier. The cost of water used in the synthesis was assumed to be 0.79 EUR<sub>2020</sub>/tonne based on the prices in the Netherlands [295], which is a conservative estimate when compared to 0.10 EUR<sub>2015</sub>/tonne made by Cormos [296].

Assuming that orders are made around 2 to 4 times a year [169], the order size for 80%  $\text{Mn}_2\text{O}_3/\text{MgAl}_2\text{O}_4$  is 500 tonnes for consumption of around 1000 tonnes/year, for 50%  $\text{Fe}_2\text{O}_3/\text{MgAl}_2\text{O}_4$  it is 1000 tonnes for consumption of around 5000 tonnes/year, and for the  $\text{CO}_2$  sorbent 83%  $\text{CaO}/\text{CeO}_2$  10000 tonnes for consumption of around 78000 tonnes/year. This corresponds to a synthesis campaign length (inclusive of 1 day for cleaning) of 4 days for 80%  $\text{Mn}_2\text{O}_3/\text{MgAl}_2\text{O}_4$ , 8 days for 50%  $\text{Fe}_2\text{O}_3/\text{MgAl}_2\text{O}_4$ , and 71 days for 83%  $\text{CaO}/\text{CeO}_2$ . Clearly, the

synthesis of the CO<sub>2</sub> sorbent would benefit from a continuous production line and its procurement would require at least 2 suppliers because of the large quantities necessary. For all the materials, the production scale is large (>150 tonnes/day) and in the same order of magnitude as the production of zeolites for fluid catalytic cracking (FCC).

In Table D5, Table D6, and Table D7, it was assumed that 5% of the material is lost during the synthesis. The USD prices from mid-2017 were converted to 2020 were converted using the web tool by U.S. Bureau of Labor Statistics [166] and a conversion factor of 1.06 USD<sub>2020</sub> per 1 USD<sub>mid-2017</sub>. Conversion of EUR to USD was carried out assuming that 0.9 EUR<sub>2020</sub> was equivalent to 1 USD<sub>2020</sub>. The selling margin was calculated as a percentage of the pre-margin costs using equation (144 [169]).

$$\text{Margin (\% of pre - margin costs)} = 60.976 * (\text{order size in tonnes})^{-0.28632}$$

The general and administrative costs amount to 5% of the subtotal and the sales, administrative, research, and distribution costs amount to 5% of the sum of the subtotal and the general and administrative costs [169].

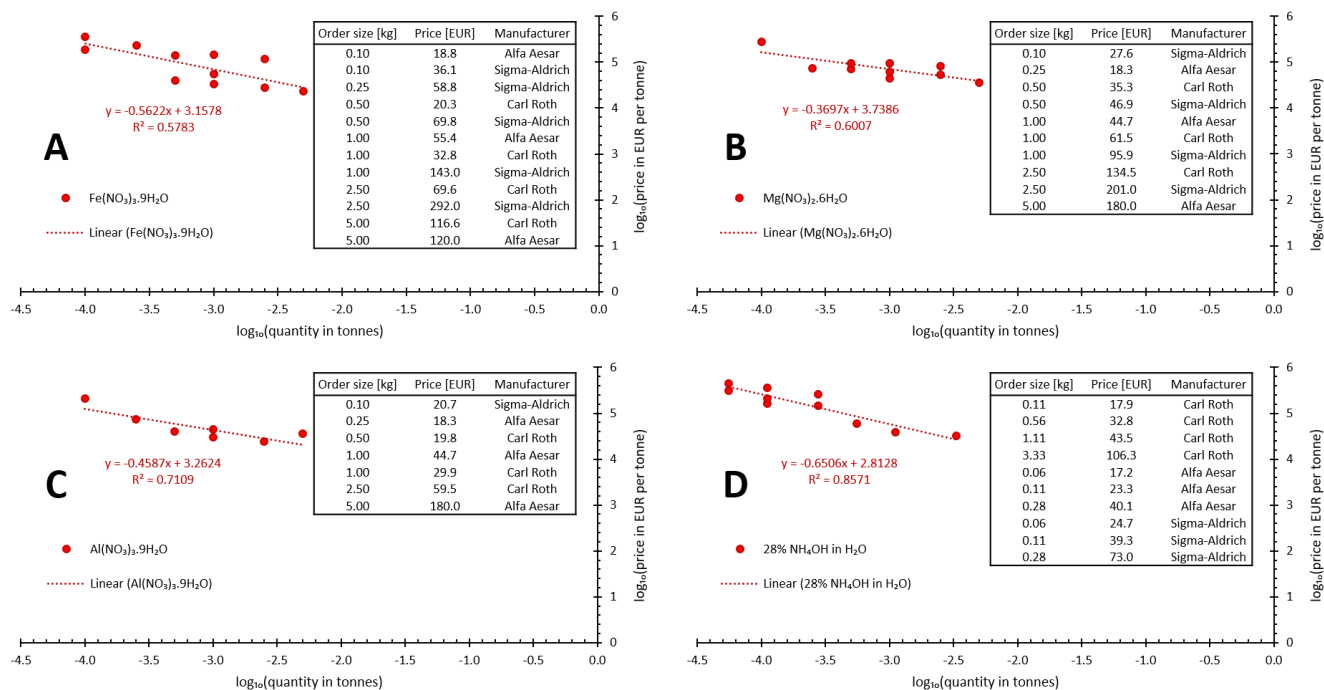


Figure D14: Fit of retail pricing data obtained from Sigma-Aldrich (Belgium), Carl Roth (Belgium), and Alfa Aesar (Germany) on 04/06/2021 and 05/06/2021 for A: iron nitrate nonahydrate, B: magnesium nitrate hexahydrate, C: aluminium nitrate nonahydrate, and D: 28%  $\text{NH}_4\text{OH}$  in  $\text{H}_2\text{O}$ , precursors for the synthesis of 50%  $\text{Fe}_2\text{O}_3/\text{MgAl}_2\text{O}_4$ . The purity of precursors was higher than 98% for all considered data points.

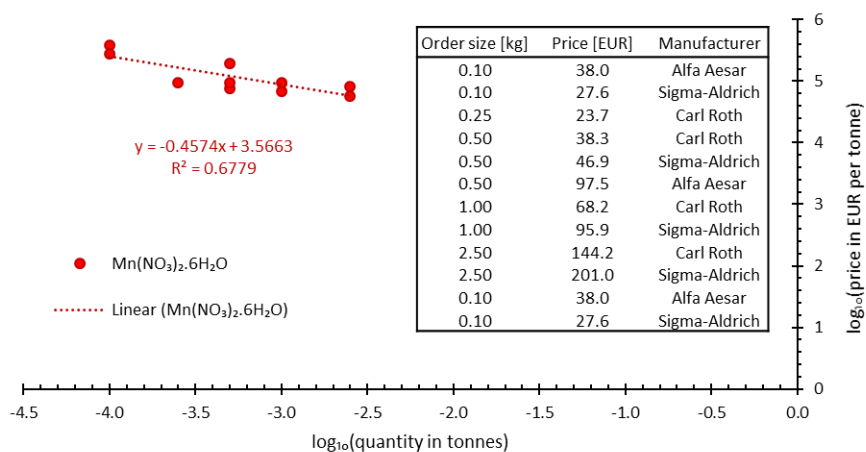


Figure D15: Fit of retail pricing data obtained from Sigma-Aldrich (Belgium), Carl Roth (Belgium), and Alfa Aesar (Germany) on 04/06/2021 and 05/06/2021 for manganese nitrate hexahydrate, precursor for the synthesis of 80%  $\text{Mn}_2\text{O}_3/\text{MgAl}_2\text{O}_4$ . The purity of the precursor was higher than 98% for all considered data points.

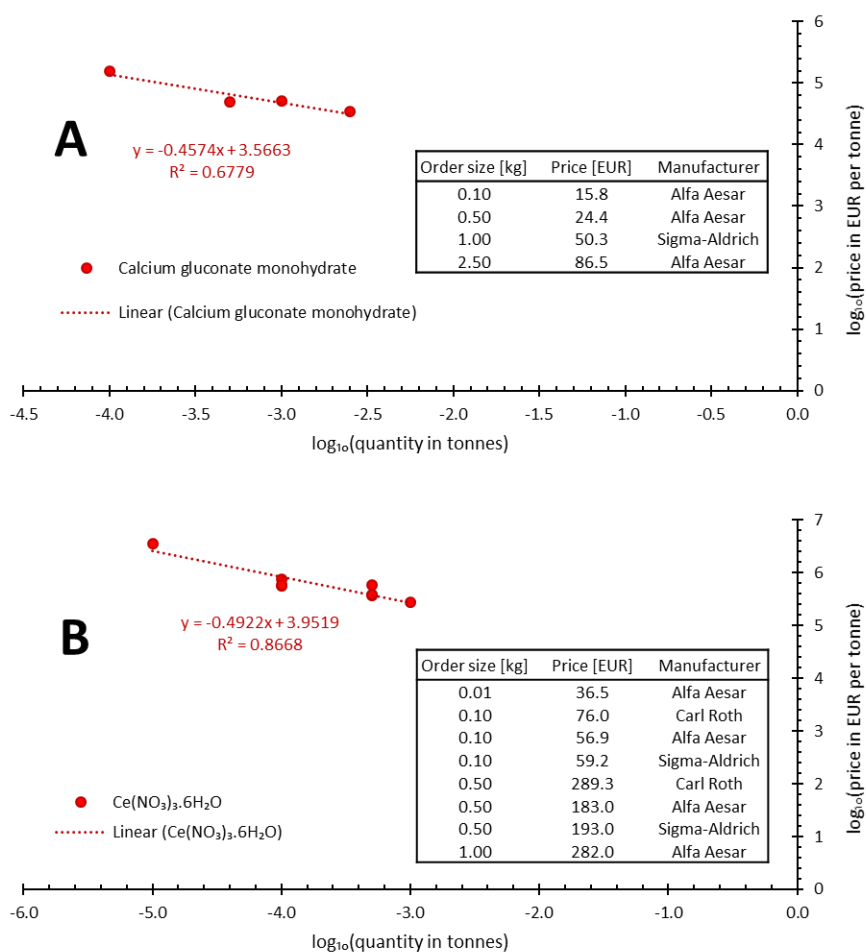


Figure D16: Fit of retail pricing data obtained from Sigma-Aldrich (Belgium), Carl Roth (Belgium), and Alfa Aesar (Germany) on 04/06/2021 and 05/06/2021 for A: calcium gluconate monohydrate and B: cerium nitrate hexahydrate, precursor for the synthesis of 83%  $\text{CaO}/\text{CeO}_2$ . The purity of precursors was higher than 98% for all considered data points.

Table D5: Cost estimation for preparing 80% Mn<sub>2</sub>O<sub>3</sub>/MgAl<sub>2</sub>O<sub>4</sub> via co-precipitation.

Material Costs			
Precursor	Cost [EUR/tonne]	kg/kg of oxygen carrier	EUR/tonne of oxygen carrier
Mn(NO <sub>3</sub> ) <sub>2</sub> ·6H <sub>2</sub> O	2.73	135.5	370
Mg(NO <sub>3</sub> ) <sub>2</sub> ·6H <sub>2</sub> O	0.44	746.4	328
Al(NO <sub>3</sub> ) <sub>3</sub> ·9H <sub>2</sub> O	1.30	93.9	122
28% NH <sub>4</sub> OH in H <sub>2</sub> O	4.69	4.2	20
H <sub>2</sub> O	18.72	0.8	15
Total	854		
Costs of synthesis steps			
Step with a brief <i>description</i>	EUR/hours	EUR/day	
Reactor, mixing <i>To mix precursors during co-precipitation</i>	191	4579	
Filter, rotary vacuum <i>To filter precipitate</i>	286	6869	
Dryer, rotary (100 – 300°C) <i>To dry the precipitate</i>	286	6869	
Kiln, continuous indirect (100 – 1290°C) <i>To calcine the material</i>	310	7441	
Scrubber for NO <sub>x</sub> emissions <i>To avoid emissions from calcination</i>	191	4579	
Total	30340		
Synthesis campaign costs			
Order size [tonnes]	500		
Cost of synthesis steps [EUR/day]	30340		
Campaign length [days]	4		
Campaign cost [EUR]	121350		
Campaign cost [EUR/tonne <sub>product</sub> ]	243		
Subtotal before Overhead and Margin			
Materials cost [EUR/tonne <sub>product</sub> ]	854		
Campaign cost [EUR/tonne <sub>product</sub> ]	243		
Subtotal [EUR/tonne <sub>product</sub> ]	1097		
Overhead and Margin			
General and administrative costs [EUR/tonne <sub>product</sub> ]		55	
Sales, administrative, research, and distribution costs [EUR/tonne <sub>product</sub> ]		58	
Margin [EUR/tonne <sub>product</sub> ]		124	
Total estimated price			
Estimated price [EUR/tonne <sub>product</sub> ]			<b>1333</b>

Table D6: Cost estimation for preparing 50% Fe<sub>2</sub>O<sub>3</sub>/MgAl<sub>2</sub>O<sub>4</sub> via co-precipitation.

Material Costs			
Precursor	Cost [EUR/tonne]	kg/kg of oxygen carrier	EUR/tonne of oxygen carrier
Fe(NO <sub>3</sub> ) <sub>3</sub> ·9H <sub>2</sub> O	2.72	16.9	46
Mg(NO <sub>3</sub> ) <sub>2</sub> ·6H <sub>2</sub> O	1.10	411.7	452
Al(NO <sub>3</sub> ) <sub>3</sub> ·9H <sub>2</sub> O	3.24	44.9	146
28% NH <sub>4</sub> OH in H <sub>2</sub> O	7.20	2.0	14
H <sub>2</sub> O	28.77	0.8	23
Total	680		
Costs of synthesis steps			
Step with a brief <i>description</i>	EUR/hours	EUR/day	
Reactor, mixing <i>To mix precursors during co-precipitation</i>	191	4579	
Filter, rotary vacuum <i>To filter precipitate</i>	286	6869	
Dryer, rotary (100 – 300°C) <i>To dry the precipitate</i>	286	6869	
Kiln, continuous indirect (100 – 1290°C) <i>To calcine the material</i>	310	7441	
Scrubber for NO <sub>x</sub> emissions <i>To avoid emissions from calcination</i>	191	4579	
Total	30340		
Synthesis campaign costs			
Order size [tonnes]	1000		
Cost of synthesis steps [EUR/day]	30340		
Campaign length [days]	8		
Campaign cost [EUR]	242700		
Campaign cost [EUR/tonne <sub>product</sub> ]	243		
Subtotal before Overhead and Margin			
Materials cost [EUR/tonne <sub>product</sub> ]	680		
Campaign cost [EUR/tonne <sub>product</sub> ]	243		
Subtotal [EUR/tonne <sub>product</sub> ]	923		
Overhead and Margin			
General and administrative costs [EUR/tonne <sub>product</sub> ]		46	
Sales, administrative, research, and distribution costs [EUR/tonne <sub>product</sub> ]		48	
Margin [EUR/tonne <sub>product</sub> ]		86	
Total estimated price			
Estimated price [EUR/tonne <sub>product</sub> ]			<b>1103</b>

Table D7: Cost estimation for preparing 83% CaO/CeO<sub>2</sub> via wet physical mixing.

Material Costs				
Precursor	Cost [EUR/tonne]	kg/kg of CO <sub>2</sub> carrier	EUR/tonne of CO <sub>2</sub> carrier	
Calcium gluconate monohydrate	7.13	10.7	77	
Ce(NO <sub>3</sub> ) <sub>3</sub> ·6H <sub>2</sub> O	0.46	141.5	65	
H <sub>2</sub> O	35.64	0.8	28	
Total	169			
Costs of synthesis steps				
Step with a brief description		EUR/hours	EUR/day	
Mixer, slurry <i>To mix precursors and the thickening solution</i>		191	4579	
Dryer, rotary (100 – 300°C) <i>To dry the formed gel</i>		286	6869	
Kiln, continuous indirect (100 – 1290°C) <i>To calcine the material</i>		310	7441	
Scrubber for NO <sub>x</sub> emissions <i>To avoid emissions from calcination</i>		191	4579	
Total		23470		
Synthesis campaign costs				
Order size [tonnes]		10000		
Cost of synthesis steps [EUR/day]		23470		
Campaign length [days]		71		
Campaign cost [EUR]		242700		
Campaign cost [EUR/tonne <sub>product</sub> ]		167		
Subtotal before Overhead and Margin				
Materials cost [EUR/tonne <sub>product</sub> ]		169		
Campaign cost [EUR/tonne <sub>product</sub> ]		167		
Subtotal [EUR/tonne <sub>product</sub> ]		336		
Overhead and Margin				
General and administrative costs [EUR/tonne <sub>product</sub> ]			17	
Sales, administrative, research, and distribution costs [EUR/tonne <sub>product</sub> ]			18	
Margin [EUR/tonne <sub>product</sub> ]			16	
Total estimated price				
Estimated price [EUR/tonne <sub>product</sub> ]			386	



The price of 21% Ni/Al<sub>2</sub>O<sub>3</sub> catalyst was obtained from Baddour et al. [169] and then converted to the equivalent price of approximately 45000 EUR/tonne using a inflation factor of 1.06 USD<sub>2020</sub> per 1 USD<sub>mid-2017</sub> and 0.9 EUR<sub>2020</sub> per 1 USD<sub>2020</sub>. It was assumed that Ni could be recovered from the spent catalyst at negligible cost and at the rate of 13770 EUR/tonne, based on the 10 year average price of nickel from 2010 to 2020 on London Metal Exchange and a conversion of USD to EUR at 0.9 EUR/USD. Using a similar approach, the value of spent iron-based oxygen carrier was estimated to be 92 EUR/tonne by assuming that the value of the spent iron-based oxygen carrier would be equal to that of iron ore. The value of spent manganese-based oxygen was assumed to be 4 EUR/tonne based on the 10 year average price of manganese ore and CNY to EUR exchange rate from 2010 to 2020 obtained from tradingeconomics.com [84]. Finally, the spent CO<sub>2</sub> carrier, 83% CaO/CeO<sub>2</sub>, is assumed to have a value of 40 EUR<sub>2020</sub>/tonne (by taking into account the inflation) [170]. Table D8 summarises the information in this paragraph.

Table D8: Price of the natural ores and the data sources.

	Cost [EUR <sub>2020</sub> /tonne]	Source
Iron ore	92	London Metal Exchange
Manganese ore	4	tradingeconomics.com [84]
Limestone	40	Anantharaman et al. [170]
Nickel	13770	London Metal Exchange

## Exergy and energy

To demonstrate the validity of the assumption that the electricity demand for cryogenic distillation can be approximated by equation (145), we have computed the energy demand using the same approach for an air separation unit for which abundant data is available in literature [224, 296, 297]. Energy transfer and Heat duty (given by equations (147) and (148)) determined by the so-called “distillation resistance” ( $\Omega$ ) (see equation (146)) as defined by Lange [159] are shown below.

Electricity demand = Energy transfer – Heat duty

$$\Omega \left( \frac{1}{^\circ\text{C}} \right) = 100 * \frac{w_{\text{N}_2}}{\text{BP}_{\text{N}_2} - \text{BP}_{\text{O}_2}} = \frac{0.77}{-183 - (-196)} = 6$$

$$\text{Energy transfer} \left( \frac{\text{GJ}}{\text{tonne}_{\text{feed}}} \right) = 1.1 * \Omega = 6.6$$

$$\text{Heat duty} \left( \frac{\text{GJ}}{\text{tonne}_{\text{feed}}} \right) = 0.57 * \Omega = 3.4$$

Based on these, the electricity required for separating  $\text{O}_2$  would be 3.2 GJ/ $t_{\text{feed}}$ , where feed is air composed of 79 mol%  $\text{N}_2$  and 21 mol%  $\text{O}_2$ . Cormos [296] reported power consumption of 225 kWh/ $t_{\text{O}_2}$ , corresponding to 3.5 GJ/ $\text{tonne}_{\text{feed}}$ . Castle [297] has shown in 2002 that, over the years, the power consumption of ASU has consistently decreased and was expected to reach 0.3 kWh/ $\text{Nm}^3$  of low pressure gaseous  $\text{O}_2$  in 2010, corresponding to 3.2 GJ/ $\text{tonne}_{\text{feed}}$ . More recently (in 2014), Banaszkiwicz et al. [224] reported a power consumption of 200 kWh/ $t_{\text{O}_2}$ , corresponding to 3.1 GJ/ $t_{\text{feed}}$ . In all cases, the value corresponds to the estimation made by equation (145) within an error margin of  $\pm 10\%$ .

To demonstrate that nullifying the carbon footprint of the proposed chemical looping process is far more facile than that of the rWGS reaction followed by downstream separation using mature technologies, equation (149) developed by House et al. [178] based on the Sherwood plot was proposed, where  $P$  is the price in \$/kg and  $C$  is the mass concentration.

$$P = 0.0208 * \left(\frac{1}{C}\right)^{0.5434}$$

For a natural gas fired power plant with a  $\text{CO}_2$  concentration of about 6.2% in the flue gas, the cost of  $\text{CO}_2$  capture from equation (149) is 94 \$/tonne. This corresponds well with the value of 72 \$<sub>2020</sub>/tonne reported by Smith et al. [190], albeit a bit overestimated, but well within the range of 54 to 103 \$<sub>2020</sub>/tonne estimated by Dieterich et al. [191] (assuming 1 EUR<sub>2020</sub> = 1.142 USD<sub>2020</sub>). Applying the same equation to the vent gas from the chemical looping combustion section of the proposed scheme, the estimated value is 30 \$/tonne.

# Appendix E

## Thermodynamics

### Catalytic reactions

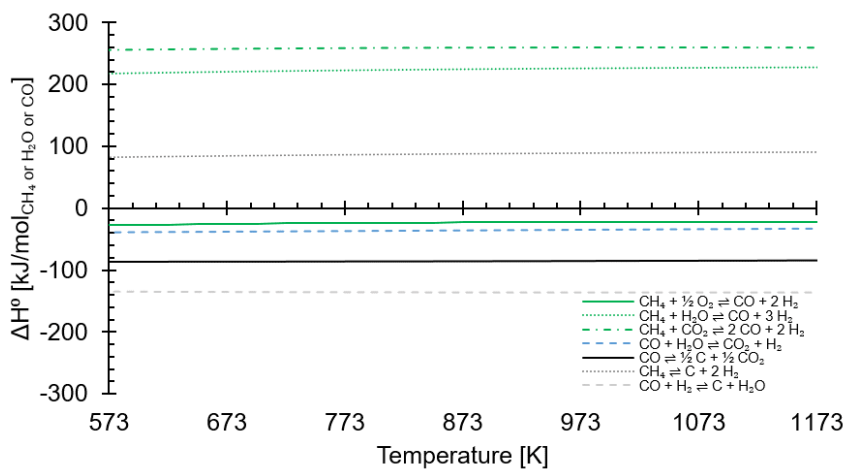


Figure E1: Standard enthalpy of several reactions that are typically catalysed during steam methane reforming using data from NIST webbook [118] and FactSage [119] for C (graphite).

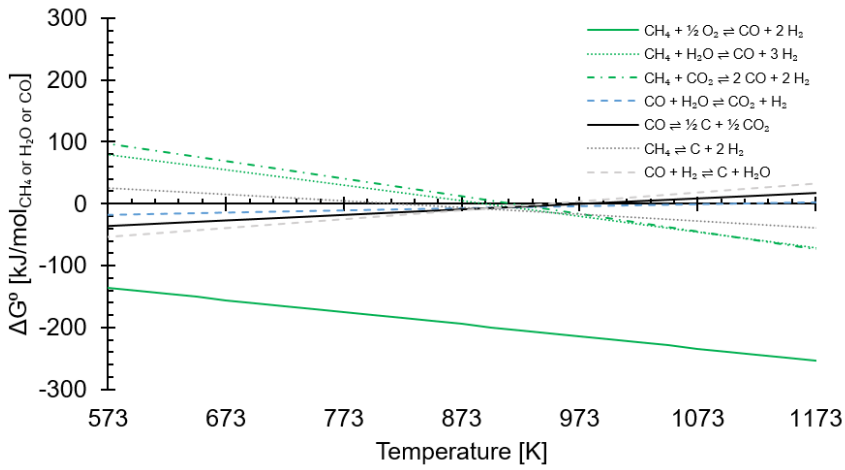


Figure E2: Standard Gibbs free energy of several reactions that are typically catalysed during steam methane reforming using data from NIST webbook [118] and FactSage [119] for C (graphite).

## Sorption enhanced reactions

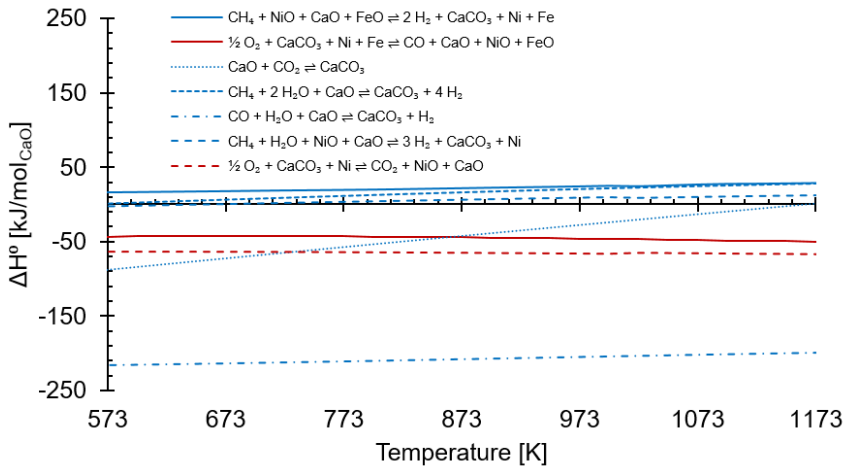


Figure E3: Standard enthalpy of the sorption enhanced reactions using data from NIST webbook [118] and FactSage [119] for CaCO<sub>3</sub>, Ni, and NiO.

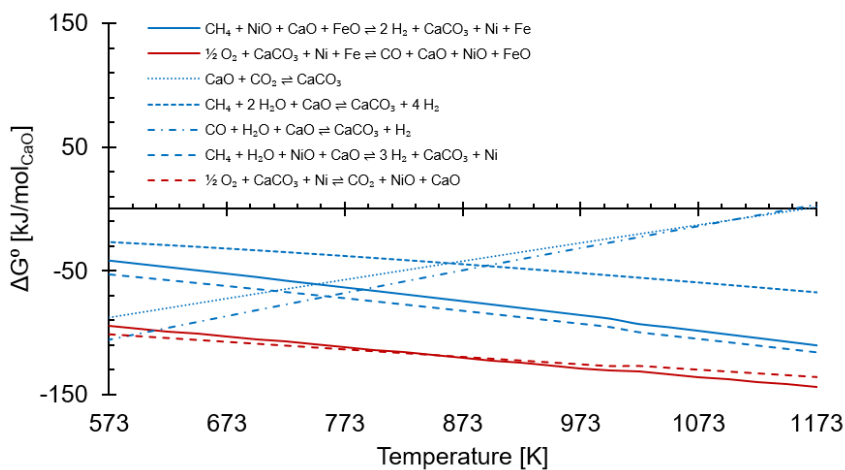


Figure E4: Standard Gibbs free energy of the sorption enhanced reactions using data from NIST webbook [118] and FactSage [119] for  $\text{CaCO}_3$ , Ni, and NiO.

## Chemical looping reverse water-gas shift reaction (CL-rWGS)

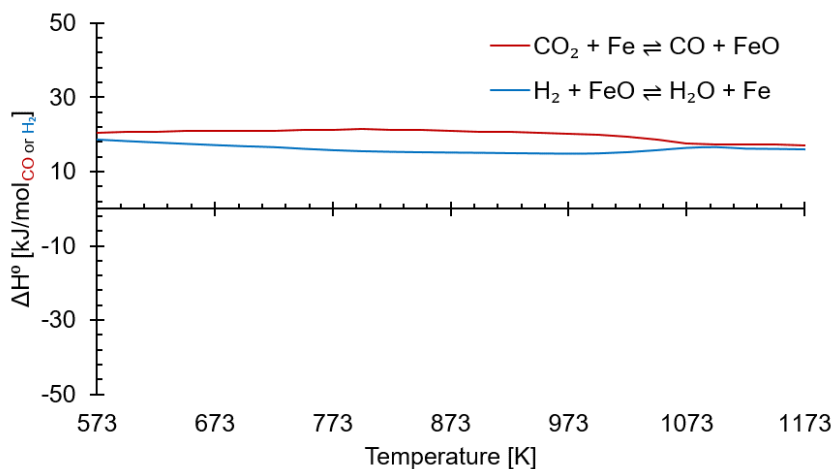


Figure E5: Standard enthalpy of the reduction and oxidation half-cycle of CL-rWGS using data from NIST webbook [118] and FactSage [119] for FeO.

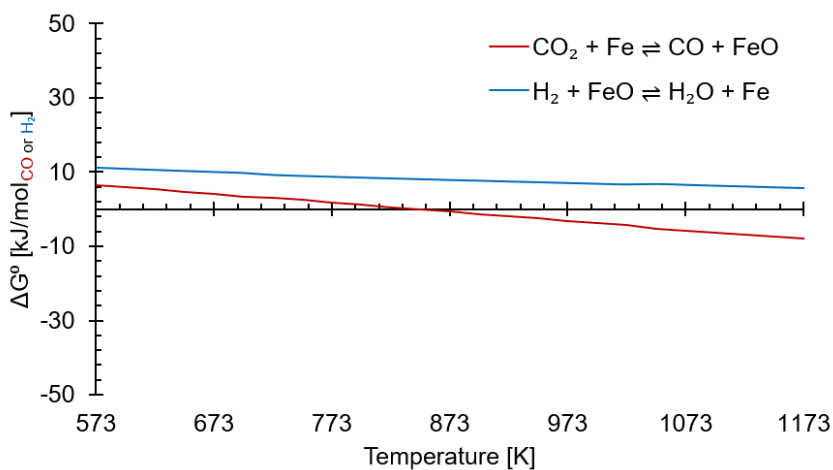


Figure E6: Standard Gibbs free energy for the reduction and oxidation half-cycle of CL-rWGS using data from NIST webbook [118] and FactSage [119] for FeO.

## Chemical looping combustion

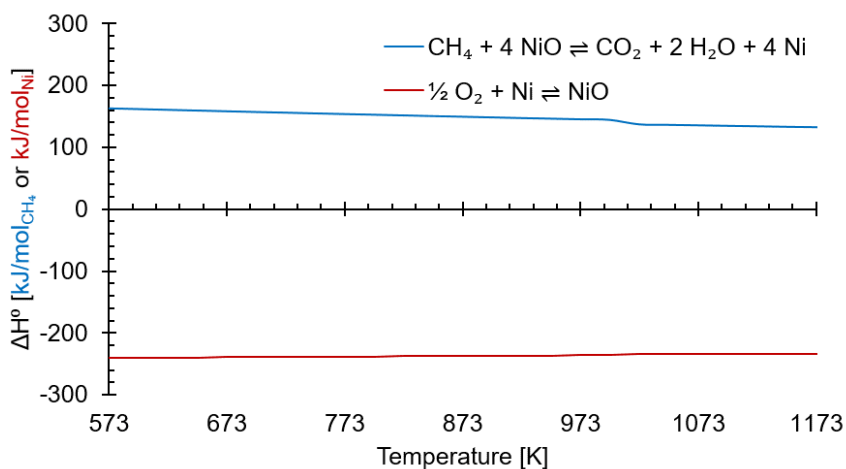


Figure E7: Standard enthalpy of chemical looping combustion half-cycles of  $\text{CH}_4$  with NiO with data from NIST webbook [118] and FactSage [119] for NiO and Ni.

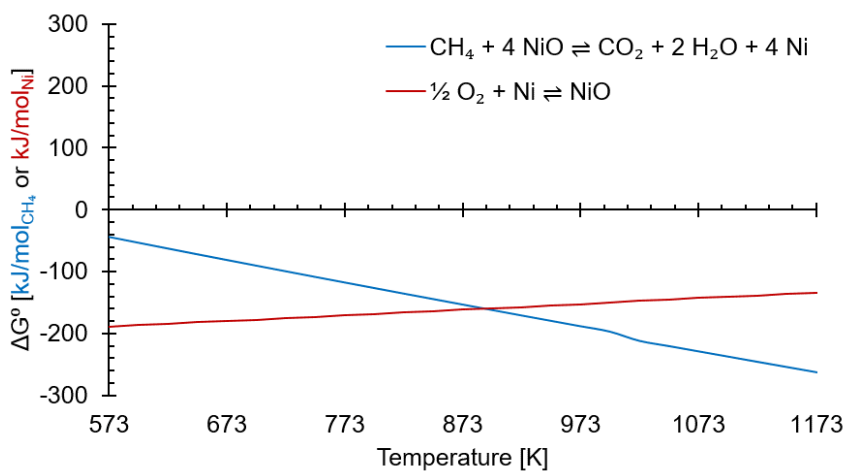


Figure E8: Standard Gibbs free energy of chemical looping combustion half-cycles of  $\text{CH}_4$  with  $\text{NiO}$  with data from NIST webbook [118] and FactSage [119] for  $\text{NiO}$  and  $\text{Ni}$ .



# Experimental section

## Shorter cycle (89 seconds) at 973 K

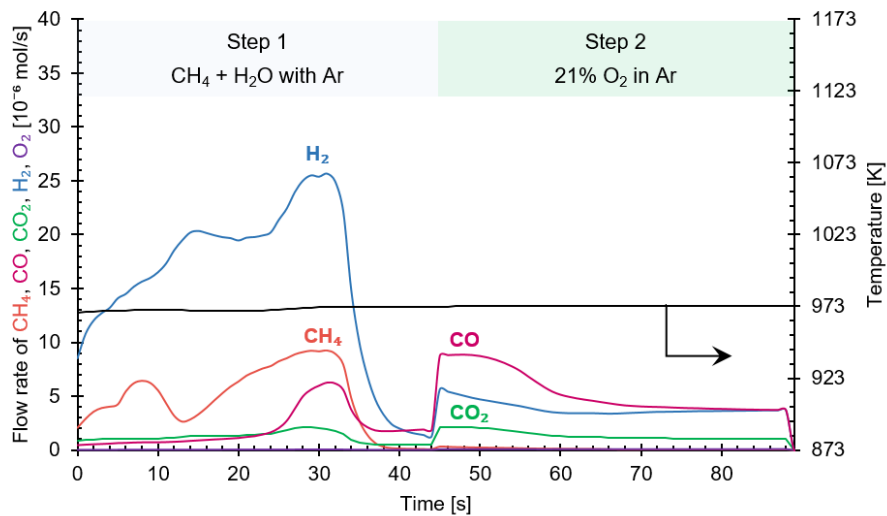


Figure E9: Shorter cycle (89 seconds) for the two-step chemical looping process to produce an  $\text{H}_2$ -rich stream in step 1 (45 seconds) and a  $\text{CO}$ -rich stream in step 2 (44 seconds) at 973 K.

# Regeneration of CO<sub>2</sub> carrier

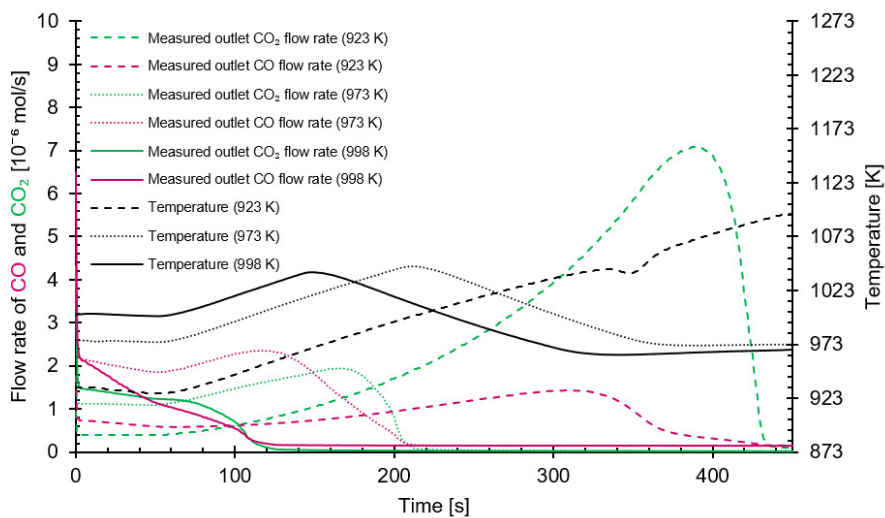


Figure E10: Decarbonation of the  $\text{CO}_2$  carrier,  $\text{CaCO}_3$ , in Ar gas flow ( $55 \cdot 10^{-6} \text{ mol/s}$ ) upon imposing a temperature ramp after the second step of the process carried out at three different temperatures (923 K – dashed lines, 973 K – dotted lines, and 998 K – solid lines).

O<sub>2</sub> post-treatment after 10 cycles

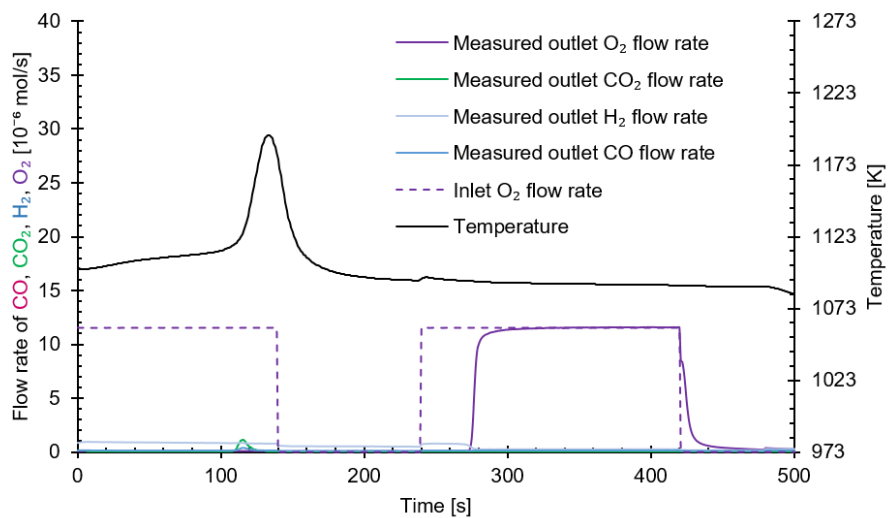


Figure E11: Outlet flow of gases during O<sub>2</sub> feed (21% O<sub>2</sub> in Ar at  $55 \cdot 10^{-6}$  mol/s) at 1073 K. The O<sub>2</sub> feed was temporarily suspended to avoid extremely high temperatures in the reactor (from 140 to 240 seconds). Note that the thermocouple is placed between the two beds. The remaining consumption of O<sub>2</sub> from 240 s onwards till its breakthrough is likely caused by the oxidation of FeO<sub>x</sub> ( $x = 0$  to 1.3) to Fe<sub>2</sub>O<sub>3</sub>.

Characterisation of materials

Table E1: Textural properties of the as prepared materials and materials after the experimental campaign from nitrogen sorption measurements at 77 K.

			Fresh		After cyclic experiments	
			40% NiO – 40% CaO – 20% CeO <sub>2</sub>	50% Fe <sub>2</sub> O <sub>3</sub> /MgAl <sub>2</sub> O <sub>4</sub> & 83% CaO/CeO <sub>2</sub> (1:1 mass)	40% NiO – 40% CaO – 20% CeO <sub>2</sub>	50% Fe <sub>2</sub> O <sub>3</sub> /MgAl <sub>2</sub> O <sub>4</sub> & 83% CaO/CeO <sub>2</sub> (1:1 mass)
BET surface area [m <sup>2</sup> /g]		8.5	23.9	13.4	14.8	
Pore volume [10 <sup>-9</sup> m <sup>3</sup> /g]		23	138	32	51	
BJH desorption pore diameter [nm]		16.6	28.7	14.5	16.4	
Particle size [nm]		130	60	101	96	

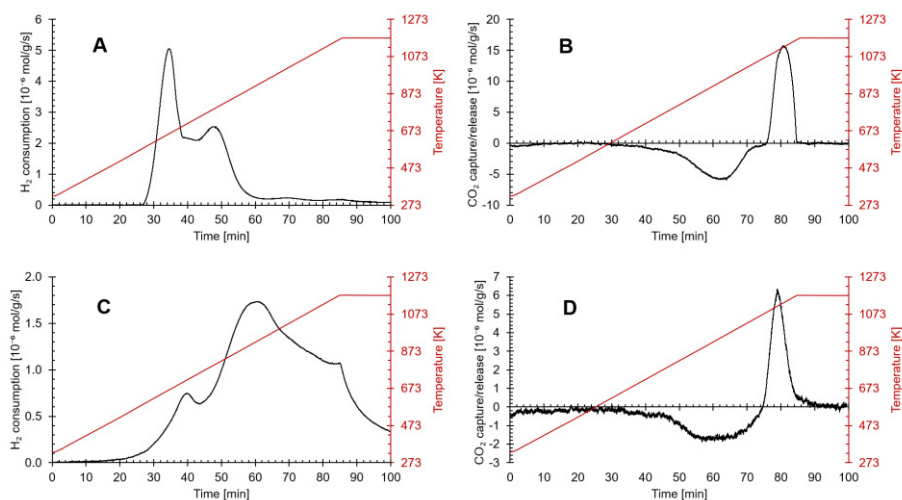


Figure E12: Temperature programmed reactions (TPRe) with a temperature ramp of 10 K/min up to 1173 K and a total flow rate of  $45 \cdot 10^{-6}$  mol/s for the multifunctional material, 40% NiO – 40% CaO – 20% CeO<sub>2</sub> (A and B) and 1:1 mass basis mixture of 50% Fe<sub>2</sub>O<sub>3</sub>/MgAl<sub>2</sub>O<sub>4</sub> and 83% CaO/CeO<sub>2</sub> (C and D) after the experimental campaign. A and C: H<sub>2</sub>-TPR under a flow of 5 mol% H<sub>2</sub> in Ar for the determination of exchangeable oxygen atoms; B and D: CO<sub>2</sub>-TPCD under a flow of 25% CO<sub>2</sub> in He (B) or 20% CO<sub>2</sub> in Ar (D) for the determination of the CO<sub>2</sub> capture and release capacity.

## Bibliography

- [1] L.C. Buelens, H. Poelman, G.B. Marin, V.V. Galvita. 110th Anniversary: Carbon Dioxide and Chemical Looping: Current Research Trends. *Industrial & Engineering Chemistry Research*. 58 (2019) 16235-57.
- [2] L. Zeng, Z. Cheng, J.A. Fan, L.-S. Fan, J. Gong. Metal oxide redox chemistry for chemical looping processes. *Nature Reviews Chemistry*. 2 (2018) 349-64.
- [3] X. Zhao, H. Zhou, V.S. Sikarwar, M. Zhao, A.-H.A. Park, P.S. Fennell, et al. Biomass-based chemical looping technologies: the good, the bad and the future. *Energy & Environmental Science*. 10 (2017) 1885-910.
- [4] G.B. Marin, V.V. Galvita, G.S. Yablonsky. Kinetics of chemical processes: From molecular to industrial scale. *Journal of Catalysis*. 10.1016/j.jcat.2021.09.014 (2021).
- [5] X. Zhu, Q. Imtiaz, F. Donat, C.R. Müller, F. Li. Chemical looping beyond combustion – a perspective. *Energy & Environmental Science*. 13 (2020) 772-804.
- [6] D.P. Hanak, E.J. Anthony, V. Manovic. A review of developments in pilot-plant testing and modelling of calcium looping process for CO<sub>2</sub> capture from power generation systems. *Energy & Environmental Science*. 8 (2015) 2199-249.
- [7] A. Lyngfelt. Chemical Looping Combustion: Status and Development Challenges. *Energy & Fuels*. 34 (2020) 9077-93.
- [8] J. Hu, V.V. Galvita, H. Poelman, G.B. Marin. Advanced Chemical Looping Materials for CO<sub>2</sub> Utilization: A Review. *Materials*. 11 (2018).
- [9] M.T. Dunstan, F. Donat, A.H. Bork, C.P. Grey, C.R. Muller. CO<sub>2</sub> Capture at Medium to High Temperature Using Solid Oxide-Based Sorbents: Fundamental Aspects, Mechanistic Insights, and Recent Advances. *Chemical Reviews*. 10.1021/acs.chemrev.1c00100 (2021).
- [10] Y. De Vos, M. Jacobs, P. Van Der Voort, I. Van Driessche, F. Snijckers, A. Verberckmoes. Development of Stable Oxygen Carrier Materials for Chemical Looping Processes—A Review. *Catalysts*. 10 (2020).
- [11] T. Gauthier, M. Yazdanpanah, A. Forret, B. Amblard, A. Lambert, S. Bertholin. CLC, a promising concept with challenging development issues. *Powder Technology*. 316 (2017) 3-17.

- [12] H. Poelman, V.V. Galvita. Intensification of Chemical Looping Processes by Catalyst Assistance and Combination. *Catalysts*. 11 (2021).
- [13] D. Cree, A. Rutter. Sustainable Bio-Inspired Limestone Eggshell Powder for Potential Industrialized Applications. *ACS Sustainable Chemistry & Engineering*. 3 (2015) 941-9.
- [14] M. Waheed, M. Yousaf, A. Shehzad, M. Inam-Ur-Raheem, M.K.I. Khan, M.R. Khan, et al. Channelling eggshell waste to valuable and utilizable products: A comprehensive review. *Trends in Food Science & Technology*. 106 (2020) 78-90.
- [15] M. Ives, R.C. Mundy, P.S. Fennell, J.F. Davidson, J.S. Dennis, A.N. Hayhurst. Comparison of Different Natural Sorbents for Removing CO<sub>2</sub> from Combustion Gases, as Studied in a Bench-Scale Fluidized Bed. *Energy & Fuels*. 22 (2008) 3852-7.
- [16] S.A. Salaudeen, B. Acharya, A. Dutta. CaO-based CO<sub>2</sub> sorbents: A review on screening, enhancement, cyclic stability, regeneration and kinetics modelling. *Journal of CO<sub>2</sub> Utilization*. 23 (2018) 179-99.
- [17] S.A. Salaudeen, S.H. Tasnim, M. Heidari, B. Acharya, A. Dutta. Eggshell as a potential CO<sub>2</sub> sorbent in the calcium looping gasification of biomass. *Waste Management*. 80 (2018) 274-84.
- [18] Y.W. Cheng, C.C. Chong, M.K. Lam, M. Ayoub, C.K. Cheng, J.W. Lim, et al. Holistic process evaluation of non-conventional palm oil mill effluent (POME) treatment technologies: A conceptual and comparative review. *Journal of Hazardous materials*. 409 (2021) 124964.
- [19] M.W. Ajiwibowo, A. Darmawan, M. Aziz. Towards clean palm oil processing: Integrated ammonia production from empty fruit bunch and palm oil effluent. *Journal of Cleaner Production*. 236 (2019) 117680.
- [20] S.S. Mahmod, A.M. Azahar, A.A.I. Luthfi, P.M. Abdul, M.S. Mastar, N. Anuar, et al. Potential Utilisation of Dark-Fermented Palm Oil Mill Effluent in Continuous Production of Biomethane by Self-Granulated Mixed Culture. *Scientific reports*. 10 (2020) 9167.
- [21] A. Akhbari, O.C. Chuen, A.A. Zinatizadeh, S. Ibrahim. Start-Up Study on Biohydrogen from Palm Oil Mill Effluent in a Pilot-Scale Reactor. *CLEAN – Soil, Air, Water*. 48 (2020).
- [22] B.S. Zainal, M.A. Ahmad, M. Danaee, N. Jamadon, N.S. Mohd, S. Ibrahim. Integrated System Technology of POME Treatment for

Biohydrogen and Biomethane Production in Malaysia. *Applied Sciences*. 10 (2020).

[23] C.C. Chong, Y.W. Cheng, K.H. Ng, D.-V.N. Vo, M.K. Lam, J.W. Lim. Bio-hydrogen production from steam reforming of liquid biomass wastes and biomass-derived oxygenates: A review. *Fuel*. 311 (2022).

[24] Y.W. Cheng, Z.S. Lee, C.C. Chong, M.R. Khan, C.K. Cheng, K.H. Ng, et al. Hydrogen-rich syngas production via steam reforming of palm oil mill effluent (POME) – A thermodynamics analysis. *International Journal of Hydrogen Energy*. 44 (2019) 20711-24.

[25] Y.W. Cheng, M.R. Khan, K.H. Ng, S. Wongsakulphasatch, C.K. Cheng. Harnessing renewable hydrogen-rich syngas from valorization of palm oil mill effluent (POME) using steam reforming technique. *Renewable Energy*. 138 (2019) 1114-26.

[26] Y.W. Cheng, C.C. Chong, S.P. Lee, J.W. Lim, T.Y. Wu, C.K. Cheng. Syngas from palm oil mill effluent (POME) steam reforming over lanthanum cobaltite: Effects of net-basicity. *Renewable Energy*. 148 (2020) 349-62.

[27] S. Santos. Iron and Steel CCS Study (Techno-Economics Integrated Steel Mill). IEA Environmental Projects Ltd. (IEAGHG) Cheltenham, 2013.

[28] worldsteel. Steel's contribution to a low carbon future and climate resilient societies. World Steel Association 2020. Press Release.

[29] M. Voll, P. Kleinschmit. Carbon, 6. Carbon Black. *Ullmann's Encyclopedia of Industrial Chemistry*. [https://doi.org/10.1002/14356007.n05\\_n05](https://doi.org/10.1002/14356007.n05_n05) (2010).

[30] Y.A. Chikri, W. Wetzels. Decarbonisation options for the Dutch carbon black industry. PBL Netherlands Environmental Assessment Agency and TNO EnergieTransitie Hague, the Netherlands, 2020.

[31] IEAGHG. Techno-Economic Evaluation of SMR Based Standalone (Merchant) Plant with CCS. IEA Environmental Projects Ltd. (IEAGHG) London, United Kingdom, 2017.

[32] IEA. The Future of Hydrogen. International Energy Agency (IEA) Paris, France, 2019.

[33] S. Tian, K. Li, J. Jiang, X. Chen, F. Yan. CO<sub>2</sub> abatement from the iron and steel industry using a combined Ca–Fe chemical loop. *Applied Energy*. 170 (2016) 345-52.



- [34] H.A.J. van Dijk, P.D. Cobden, M. Lundqvist, C.C. Cormos, M.J. Watson, G. Manzolini, et al. Cost Effective CO<sub>2</sub> Reduction in the Iron & Steel Industry by Means of the SEWGS Technology: STEPWISE Project. *Energy Procedia*. 114 (2017) 6256-65.
- [35] I. Martínez, J.R. Fernández, J.C. Abanades, M.C. Romano. Integration of a fluidised bed Ca–Cu chemical looping process in a steel mill. *Energy*. 163 (2018) 570-84.
- [36] M. Gazzani, M.C. Romano, G. Manzolini. CO<sub>2</sub> capture in integrated steelworks by commercial-ready technologies and SEWGS process. *International Journal of Greenhouse Gas Control*. 41 (2015) 249-67.
- [37] I. Wang, Y. Gao, X. Wang, R. Cai, C. Chung, S. Iftikhar, et al. Liquid Metal Shell as an Effective Iron Oxide Modifier for Redox-Based Hydrogen Production at Intermediate Temperatures. *ACS Catalysis*. 11 (2021) 10228-38.
- [38] M. Rydén, A. Lyngfelt. Using steam reforming to produce hydrogen with carbon dioxide capture by chemical-looping combustion. *International Journal of Hydrogen Energy*. 31 (2006) 1271-83.
- [39] R.J. Lee Pereira, P.A. Argyris, V. Spallina. A comparative study on clean ammonia production using chemical looping based technology. *Applied Energy*. 280 (2020).
- [40] V. Spallina, G. Motamedi, F. Gallucci, M. van Sint Annaland. Techno-economic assessment of an integrated high pressure chemical-looping process with packed-bed reactors in large scale hydrogen and methanol production. *International Journal of Greenhouse Gas Control*. 88 (2019) 71-84.
- [41] L. Yang, X. Wu, F. Liu, X. Zhang, J. He, K. Saito. Joint-use of activated carbon and carbon black to enhance catalytic stability during chemical looping methane decomposition process. *International Journal of Hydrogen Energy*. 45 (2020) 13245-55.
- [42] W. Uribe-Soto, J.-F. Portha, J.-M. Commenge, L. Falk. A review of thermochemical processes and technologies to use steelworks off-gases. *Renewable and Sustainable Energy Reviews*. 74 (2017) 809-23.
- [43] K. de Kleijne, J. James, S.V. Hanssen, R. van Zelm. Environmental benefits of urea production from basic oxygen furnace gas. *Applied Energy*. 270 (2020) 115119.

- [44] F. García-Labiano, L.F. de Diego, E. García-Díez, A. Serrano, A. Abad, P. Gayán, et al. Combustion and Reforming of Liquid Fossil Fuels through Chemical Looping Processes: Integration of Chemical Looping Processes in a Refinery. *Energy Procedia*. 114 (2017) 325-33.
- [45] L. Brody, L. Neal, V. Haribal, F. Li. Ethane to liquids via a chemical looping approach – Redox catalyst demonstration and process analysis. *Chemical Engineering Journal*. <https://doi.org/10.1016/j.cej.2021.128886> (2021).
- [46] Nitrous oxide: The unnoticed greenhouse gas. *C&EN Global Enterprise*. 99 (2021) 20-3.
- [47] H. Tian, R. Xu, J.G. Canadell, R.L. Thompson, W. Winiwarter, P. Suntharalingam, et al. A comprehensive quantification of global nitrous oxide sources and sinks. *Nature*. 586 (2020) 248-56.
- [48] J. Hu, V.V. Galvita, H. Poelman, Z. Wang, G.B. Marin, S. Kawi. Coupling CO<sub>2</sub> utilization and NO reduction in chemical looping manner by surface carbon. *Applied Catalysis B: Environmental*. 297 (2021).
- [49] V.P. Haribal, X. Wang, R. Dudek, C. Paulus, B. Turk, R. Gupta, et al. Modified Ceria for “Low-Temperature” CO<sub>2</sub> Utilization: A Chemical Looping Route to Exploit Industrial Waste Heat. *Advanced Energy Materials*. 9 (2019) 1901963.
- [50] A. Lyngfelt, A. Brink, Ø. Langørgen, T. Mattisson, M. Rydén, C. Linderholm. 11,000 h of chemical-looping combustion operation—Where are we and where do we want to go? *International Journal of Greenhouse Gas Control*. 88 (2019) 38-56.
- [51] N.V.R.A. Dharanipragada, L.C. Buelens, H. Poelman, E. De Grave, V.V. Galvita, G.B. Marin. Mg–Fe–Al–O for advanced CO<sub>2</sub> to CO conversion: carbon monoxide yield vs. oxygen storage capacity. *Journal of Materials Chemistry A*. 3 (2015) 16251-62.
- [52] Y. De Vos, M. Jacobs, I. Van Driessche, P. Van Der Voort, F. Snijkers, A. Verberckmoes. Processing and characterization of Fe-based oxygen carriers for chemical looping for hydrogen production. *International Journal of Greenhouse Gas Control*. 70 (2018) 12-21.
- [53] L.C. Buelens, A.N.V.R. Dharanipragada, H. Poelman, Z. Zhou, G.B. Marin, V.V. Galvita. Exploring the stability of Fe<sub>2</sub>O<sub>3</sub>–MgAl<sub>2</sub>O<sub>4</sub> oxygen storage materials for CO production from CO<sub>2</sub>. *Journal of CO<sub>2</sub> Utilization*. 29 (2019) 36-45.

- [54] L.C. Buelens, A. Van Alboom, H. Poelman, C. Detavernier, G.B. Marin, V.V. Galvita.  $\text{Fe}_2\text{O}_3\text{--MgAl}_2\text{O}_4$  for CO Production from  $\text{CO}_2$ : Mössbauer Spectroscopy and in Situ X-ray Diffraction. *ACS Sustainable Chemistry & Engineering*. 7 (2019) 9553-65.
- [55] W. Liu, B. Feng, Y. Wu, G. Wang, J. Barry, J.C.D.d. Costa. Synthesis of Sintering-Resistant Sorbents for  $\text{CO}_2$  Capture. *Environmental Science and Technology*. 44 (2010) 3093-7.
- [56] W. Liu, N.W.L. Low, B. Feng, G. Wang, J.C.D.d. Costa. Calcium Precursors for the Production of CaO Sorbents for Multicycle  $\text{CO}_2$  Capture. *Environmental Science and Technology*. 44 (2010) 841-7.
- [57] W. Liu, B. Feng, Y. Wu, G. Wang, J. Barry, J.C.D.d. Costa. Synthesis of Sintering-Resistant Sorbents for  $\text{CO}_2$  Capture. *Environmental Science and Technology*. 44 (2010) 3093-7.
- [58] R. Remus, M.A. Aguado-Monsonet, S. Roudier, L.D. Sancho. Best Available Techniques (BAT) Reference Document for Iron and Steel Production. Spain, 2013.
- [59] H. Lu, P.G. Smirniotis. Calcium Oxide Doped Sorbents for  $\text{CO}_2$  Uptake in the Presence of  $\text{SO}_2$  at High Temperatures. *Industrial & Engineering Chemistry Research*. 48 (2009) 5454-9.
- [60] X. Zhang, S.D. House, Y. Tang, L. Nguyen, Y. Li, A.A. Opalade, et al. Complete Oxidation of Methane on NiO Nanoclusters Supported on  $\text{CeO}_2$  Nanorods through Synergistic Effect. *ACS Sustainable Chemistry & Engineering*. 6 (2018) 6467-77.
- [61] L. Buelens. Process Concept and Materials for Carbon Dioxide Capture and Conversion: Super-dry Reforming of Methane. Department of Materials, Textiles, and Chemical Engineering. Ghent University, Ghent, Belgium, 2018. p. 285.
- [62] M. Thommes, K. Kaneko, A.V. Neimark, J.P. Olivier, F. Rodriguez-Reinoso, J. Rouquerol, et al. Physisorption of gases, with special reference to the evaluation of surface area and pore size distribution (IUPAC Technical Report). *Pure and Applied Chemistry*. 87 (2015) 1051-69.
- [63] W. Wohlleben, J. Mielke, A. Bianchin, A. Ghanem, H. Freiburger, H. Rauscher, et al. Reliable nanomaterial classification of powders using the volume-specific surface area method. *Journal of Nanoparticle Research*. 19 (2017).

- [64] A.C. Larson, R.B. Von Dreele. General Structure Analysis System (GSAS). Los Alamos National Laboratory, 2004.
- [65] B.H. Toby. EXPGUI, a graphical user interface for GSAS. *Journal of Applied Crystallography*. 34 (2001) 210-3.
- [66] S.J. Davis, N.S. Lewis, M. Shaner, S. Aggarwal, D. Arent, I.L. Azevedo, et al. Net-zero emissions energy systems. *Science*. 360 (2018).
- [67] M. Bui, C.S. Adjiman, A. Bardow, E.J. Anthony, A. Boston, S. Brown, et al. Carbon capture and storage (CCS): the way forward. *Energy & Environmental Science*. 11 (2018) 1062-176.
- [68] ArcelorMittal Climate Action Report 1. ArcelorMittal, Luxembourg, 2019.
- [69] N. Pardo, J.A. Moya, K. Vatopoulos. Prospective Scenarios on Energy Efficiency and CO<sub>2</sub> Emissions in the EU Iron & Steel Industry. Luxembourg: Publications Office of the European Union Luxembourg, 2012.
- [70] J.H. Wesseling, S. Lechtenböhmer, M. Åhman, L.J. Nilsson, E. Worrell, L. Coenen. The transition of energy intensive processing industries towards deep decarbonization: Characteristics and implications for future research. *Renewable and Sustainable Energy Reviews*. 79 (2017) 1303-13.
- [71] C.J. Laguna, J. Duerinch, F. Meinke-Hubeny, J. Valee. Carbon-free steel production: Cost reduction options and usage of existing gas infrastructure. European Parliamentary Research Service Brussels, Belgium, 2021.
- [72] IEA. Iron and Steel Technology Roadmap Towards more sustainable steelmaking. 2020.
- [73] J.P. Birat. Global Technology Roadmap for CCS in Industry: Steel sectoral report, contribution to the UNIDO roadmap for CCS (fifth draft) (Prepared for the UNIDO Global Technology Roadmap for CCS in Industry - Sectoral Experts Meeting, in Amsterdam, 24 September 2010). Maizières-lès-Metz, France, 2010.
- [74] E. Tsupari, J. Kärki, A. Arasto, E. Pisilä. Post-combustion capture of CO<sub>2</sub> at an integrated steel mill – Part II: Economic feasibility. *International Journal of Greenhouse Gas Control*. 16 (2013) 278-86.

- [75] M.-H. Chang, W.-C. Chen, C.-M. Huang, W.-H. Liu, Y.-C. Chou, W.-C. Chang, et al. Design and Experimental Testing of a 1.9MWth Calcium Looping Pilot Plant. *Energy Procedia*. 63 (2014) 2100-8.
- [76] D.P. Hanak, C. Biliyok, E.J. Anthony, V. Manovic. Modelling and comparison of calcium looping and chemical solvent scrubbing retrofits for CO<sub>2</sub> capture from coal-fired power plant. *International Journal of Greenhouse Gas Control*. 42 (2015) 226-36.
- [77] S. Tian, J. Jiang, Z. Zhang, V. Manovic. Inherent potential of steelmaking to contribute to decarbonisation targets via industrial carbon capture and storage. *Nature Communications*. 9 (2018) 4422.
- [78] C.-C. Cormos. Economic evaluations of coal-based combustion and gasification power plants with post-combustion CO<sub>2</sub> capture using calcium looping cycle. *Energy*. 78 (2014) 665-73.
- [79] A. Perejón, L.M. Romeo, Y. Lara, P. Lisbona, A. Martínez, J.M. Valverde. The Calcium-Looping technology for CO<sub>2</sub> capture: On the important roles of energy integration and sorbent behavior. *Applied Energy*. 162 (2016) 787-807.
- [80] V. Manovic, E.J. Anthony. Integration of calcium and chemical looping combustion using composite CaO/CuO-based materials. *Environmental Science and Technology*. 45 (2011) 10750-6.
- [81] J.R. Fernández, V. Spallina, J.C. Abanades. Advanced Packed-Bed Ca-Cu Looping Process for the CO<sub>2</sub> Capture From Steel Mill Off-Gases. *Frontiers in Energy Research*. 8 (2020).
- [82] H. Bahzad, K. Katayama, M.E. Boot-Handford, N. Mac Dowell, N. Shah, P.S. Fennell. Iron-based chemical-looping technology for decarbonising iron and steel production. *International Journal of Greenhouse Gas Control*. 91 (2019).
- [83] M. Ishida, D. Zheng, T. Akehata. Evaluation of a chemical-looping-combustion power-generation system by graphic exergy analysis. *Energy*. 12 (1987) 147-54.
- [84] Trading Economics (2021). "Manganese Ore." Retrieved 22/06/2021, 2021, from <https://tradingeconomics.com/commodity/manganese>.
- [85] G. Genchi, A. Carocci, G. Lauria, M.S. Sinicropi, A. Catalano. Nickel: Human Health and Environmental Toxicology. *International Journal of Environmental Research and Public Health*. 17 (2020) 679.

- [86] R. Zhai, C. Li, J. Qi, Y. Yang. Thermodynamic analysis of CO<sub>2</sub> capture by calcium looping process driven by coal and concentrated solar power. *Energy Conversion and Management*. 117 (2016) 251-63.
- [87] K. Shah, B. Moghtaderi, T. Wall. Selection of Suitable Oxygen Carriers for Chemical Looping Air Separation: A Thermodynamic Approach. *Energy & Fuels*. 26 (2012) 2038-45.
- [88] R.H. Görke, W. Hu, M.T. Dunstan, J.S. Dennis, S.A. Scott. Exploration of the material property space for chemical looping air separation applied to carbon capture and storage. *Applied Energy*. 212 (2018) 478-88.
- [89] C.L. Muhich, B.W. Evanko, K.C. Weston, P. Lichty, X. Liang, J. Martinek, et al. Efficient generation of H<sub>2</sub> by splitting water with an isothermal redox cycle. *Science*. 341 (2013) 540-2.
- [90] A.J. Carrillo, D.P. Serrano, P. Pizarro, J.M. Coronado. Thermochemical heat storage based on the Mn<sub>2</sub>O<sub>3</sub>/Mn<sub>3</sub>O<sub>4</sub> redox couple: influence of the initial particle size on the morphological evolution and cyclability. *Journal of Materials Chemistry A*. 2 (2014) 19435-43.
- [91] C.F. Patzschke, M.E. Boot-Handford, Q. Song, P.S. Fennell. Co-precipitated Cu-Mn mixed metal oxides as oxygen carriers for chemical looping processes. *Chemical Engineering Journal*. 407 (2021) 127093-107.
- [92] S. Saqline, Z.Y. Chua, W. Liu. Coupling chemical looping combustion of solid fuels with advanced steam cycles for CO<sub>2</sub> capture: A process modelling study. *Energy Conversion and Management*. 244 (2021).
- [93] I. Dincer, M.A. Rosen. Thermodynamic fundamentals. *Exergy* 2021. pp. 1-22.
- [94] J. Szargut. Exergy method: technical and ecological applications. WIT press, Southampton, 2005.
- [95] R.J. Panlener, R.N. Blumenthal, J.E. Garnier. A thermodynamic study of nonstoichiometric cerium dioxide. *Journal of Physics and Chemistry of Solids*. 36 (1975) 1213-22.
- [96] T. Gauthier, J. Bayle, P. Leroy. FCC: Fluidization Phenomena and Technologies. *Oil & Gas Science and Technology - Rev IFP*. 55 (2000) 187-207.

- [97] A. Antzara, E. Heracleous, A.A. Lemonidou. Improving the stability of synthetic CaO-based CO<sub>2</sub> sorbents by structural promoters. *Applied Energy*. 156 (2015) 331-43.
- [98] J. Adanez, A. Abad, F. Garcia-Labiano, P. Gayan, L.F. de Diego. Progress in Chemical-Looping Combustion and Reforming technologies. *Progress in Energy and Combustion Science*. 38 (2012) 215-82.
- [99] V. Galvita, T. Hempel, H. Lorenz, L.K. Rihko-Struckmann, K. Sundmacher. Deactivation of Modified Iron Oxide Materials in the Cyclic Water Gas Shift Process for CO-Free Hydrogen Production. *Industrial & Engineering Chemistry Research*. 47 (2008) 303-10.
- [100] A.M. Kierzkowska, R. Pacciani, C.R. Müller. CaO-based CO<sub>2</sub> sorbents: from fundamentals to the development of new, highly effective materials. *Chemsuschem*. 6 (2013) 1130-48.
- [101] A.N. Antzaras, E. Heracleous, A.A. Lemonidou. Hybrid catalytic materials with CO<sub>2</sub> capture and oxygen transfer functionalities for high-purity H<sub>2</sub> production. *Catalysis Today*. 369 (2020) 2-11.
- [102] H.F. Rase. Chemical reactor design for process plants. Vol. 2. John Wiley, New York, 1977.
- [103] M. Sittig. Organic chemical process encyclopedia. Noyes Development Corporation, Park Ridge, N.J., 1969.
- [104] M. Broda, C.R. Müller. Sol-gel-derived, CaO-based, ZrO<sub>2</sub>-stabilized CO<sub>2</sub> sorbents. *Fuel*. 127 (2014) 94-100.
- [105] Q. Ha, U. Armbruster, H. Atia, M. Schneider, H. Lund, G. Agostini, et al. Development of Active and Stable Low Nickel Content Catalysts for Dry Reforming of Methane. *Catalysts*. 7 (2017).
- [106] Y.A. Daza, R.A. Kent, M.M. Yung, J.N. Kuhn. Carbon Dioxide Conversion by Reverse Water-Gas Shift Chemical Looping on Perovskite-Type Oxides. *Industrial & Engineering Chemistry Research*. 53 (2014) 5828-37.
- [107] B.J. Hare, D. Maiti, Y.A. Daza, V.R. Bhethanabotla, J.N. Kuhn. Enhanced CO<sub>2</sub> Conversion to CO by Silica-Supported Perovskite Oxides at Low Temperatures. *ACS Catalysis*. 8 (2018) 3021-9.
- [108] V.V. Galvita, H. Poelman, V. Bliznuk, C. Detavernier, G.B. Marin. CeO<sub>2</sub>-Modified Fe<sub>2</sub>O<sub>3</sub> for CO<sub>2</sub> Utilization via Chemical Looping. *Industrial & Engineering Chemistry Research*. 52 (2013) 8416-26.

- [109] M. Lee, Y. Kim, H.S. Lim, A. Jo, D. Kang, J.W. Lee. Reverse Water–Gas Shift Chemical Looping Using a Core–Shell Structured Perovskite Oxygen Carrier. *Energies*. 13 (2020).
- [110] N. Utsis, M.V. Landau, A. Erenburg, M. Herskowitz. Reverse Water Gas Shift by Chemical Looping with Iron-Substituted Hexaaluminate Catalysts. *Catalysts*. 10 (2020).
- [111] M. Wenzel, L. Rihko-Struckmann, K. Sundmacher. Continuous production of CO from CO<sub>2</sub> by RWGS chemical looping in fixed and fluidized bed reactors. *Chemical Engineering Journal*. 336 (2018) 278-96.
- [112] C. George. Carbon Monoxide. in: C. Ley, (Ed.). *Kirk-Othmer Encyclopedia of Chemical Technology*. John Wiley & Sons Inc. 2001. pp. 1-27.
- [113] CORESYM: CarbOn-monoxide RE-use through industrial SYMbiosis between steel and chemical industries. Metabolic, Amsterdam, 2017.
- [114] A. Tullo. Novomer's CO<sub>2</sub> success. *C&EN Global Enterprise*. 94 (2016) 29.
- [115] A. Tullo. Lanxess launches greener polyurethanes. *C&EN Global Enterprise*. 98 (2020) 12.
- [116] C.H. Bartholomew. Mechanisms of catalyst deactivation. *Applied Catalysis A: General*. 212 (2001) 17-60.
- [117] L.C. Buelens, V.V. Galvita, H. Poelman, C. Detavernier, G.B. Marin. Super-dry reforming of methane intensifies CO<sub>2</sub> utilization via Le Chatelier's principle. *Science*. 354 (2016) 449-52.
- [118] V.K. Shen, D.W. Siderius, W.P. Krekelberg, H.W. Hatch. NIST Standard Reference Simulation Website. NIST Standard Reference Database Number 173, National Institute of Standards and Technology, Gaithersburg MD, 20899, USA, 2020.
- [119] C.W. Bale, E. Bélisle, P. Chartrand, S.A. Decterov, G. Eriksson, A.E. Gheribi, et al. FactSage thermochemical software and databases, 2010–2016. *Calphad - Computer Coupling of Phase Diagrams and Thermochemistry*. 54 (2016) 35-53.
- [120] I. Barin. *Thermochemical Data of Pure Substances* (volume 3)1995. pp. 1-1848.



- [121] K. Verbeeck, L.C. Buelens, V.V. Galvita, G.B. Marin, K.M. Van Geem, K. Rabaey. Upgrading the value of anaerobic digestion via chemical production from grid injected biomethane. *Energy & Environmental Science*. 11 (2018) 1788-802.
- [122] D. Xu, Y. Zhang, T.-L. Hsieh, M. Guo, L. Qin, C. Chung, et al. A novel chemical looping partial oxidation process for thermochemical conversion of biomass to syngas. *Applied Energy*. 222 (2018) 119-31.
- [123] J. Szargut, D.R. Morris, F.R. Steward. *Energy analysis of thermal, chemical, and metallurgical processes*. Hemisphere Publishing, New York, 1988.
- [124] P. Sun, J.R. Grace, C.J. Lim, E.J. Anthony. The effect of CaO sintering on cyclic CO<sub>2</sub> capture in energy systems. *AIChE Journal*. 53 (2007) 2432-42.
- [125] D. Spreitzer, J. Schenk. Reduction of Iron Oxides with Hydrogen—A Review. *steel research international*. 90 (2019).
- [126] H. Lu, A. Khan, S.E. Pratsinis, P.G. Smirniotis. Flame-Made Durable Doped-CaO Nanosorbents for CO<sub>2</sub> Capture. *Energy & Fuels*. 23 (2009) 1093-100.
- [127] A. Longo, S.A. Theofanidis, C. Cavallari, N.V. Srinath, J. Hu, H. Poelman, et al. What Makes Fe-Modified MgAl<sub>2</sub>O<sub>4</sub> an Active Catalyst Support? Insight from X-ray Raman Scattering. *ACS Catalysis*. 10 (2020) 6613-22.
- [128] N.V.R.A. Dharanipragada, V.V. Galvita, H. Poelman, L.C. Buelens, G.B. Marin, A. Longo. Insight in kinetics from pre-edge features using time resolved in situ XAS. *AIChE Journal*. 64 (2018) 1339-49.
- [129] J. Hu, H. Poelman, G.B. Marin, C. Detavernier, S. Kawi, V.V. Galvita. FeO controls the sintering of iron-based oxygen carriers in chemical looping CO<sub>2</sub> conversion. *Journal of CO<sub>2</sub> Utilization*. 40 (2020).
- [130] L.C. Buelens, V.V. Galvita, H. Poelman, C. Detavernier, G.B. Marin. Kinetics of Multi-Step Redox Processes by Time-Resolved In Situ X-ray Diffraction. *Chemie Ingenieur Technik*. 88 (2016) 1684-92.
- [131] Y.A. Daza, J.N. Kuhn. CO<sub>2</sub> conversion by reverse water gas shift catalysis: comparison of catalysts, mechanisms and their consequences for CO<sub>2</sub> conversion to liquid fuels. *RSC Advances*. 6 (2016) 49675-91.
- [132] W.C. Cho, C.G. Kim, S.U. Jeong, C.S. Park, K.S. Kang, D.Y. Lee, et al. Activation and Reactivity of Iron Oxides as Oxygen Carriers for Hydrogen

Production by Chemical Looping. *Industrial & Engineering Chemistry Research*. 54 (2015) 3091-100.

[133] Z. Ma, S. Zhang, Y. Lu. Activation Mechanism of  $\text{Fe}_2\text{O}_3\text{-Al}_2\text{O}_3$  Oxygen Carrier in Chemical Looping Combustion. *Energy & Fuels*. 34 (2020) 16350-5.

[134] F. Donat, C.R. Müller. A critical assessment of the testing conditions of  $\text{CaO}$ -based  $\text{CO}_2$  sorbents. *Chemical Engineering Journal*. 336 (2018) 544-9.

[135] A. Scaltsoyiannes, A. Lemonidou.  $\text{CaCO}_3$  decomposition for calcium-looping applications: Kinetic modeling in a fixed-bed reactor. *Chemical Engineering Science*: X. 8 (2020).

[136] E.L. Cussler, B.K. Dutta. On separation efficiency. *AIChE Journal*. 58 (2012) 3825-31.

[137] V. Singh, V. Galvita, M. Saeys, G.B. Marin. A method to capture and utilize  $\text{CO}_2$  and an installation for capturing and utilizing  $\text{CO}_2$ . in: W.I.P.O.I. Bureau, (Ed.). World, 2021.

[138] A. Thursfield, A. Murugan, R. Franca, I.S. Metcalfe. Chemical looping and oxygen permeable ceramic membranes for hydrogen production – a review. *Energy & Environmental Science*. 5 (2012).

[139] D. Maiti, B.J. Hare, Y.A. Daza, A.E. Ramos, J.N. Kuhn, V.R. Bhethanabotla. Earth abundant perovskite oxides for low temperature  $\text{CO}_2$  conversion. *Energy & Environmental Science*. 11 (2018) 648-59.

[140] M.T. Dunstan, A. Jain, W. Liu, S.P. Ong, T. Liu, J. Lee, et al. Large scale computational screening and experimental discovery of novel materials for high temperature  $\text{CO}_2$  capture. *Energy & Environmental Science*. 9 (2016) 1346-60.

[141] C.Y. Lau, M.T. Dunstan, W. Hu, C.P. Grey, S.A. Scott. Large scale in silico screening of materials for carbon capture through chemical looping. *Energy & Environmental Science*. 10 (2017) 818-31.

[142] J. Han. Catalytic syngas production from carbon dioxide of two emission source scenarios: techno-economic assessment. *Journal of Industrial and Engineering Chemistry*. 96 (2021) 213-8.

[143] R.M. Bown, M. Joyce, Q. Zhang, T.R. Reina, M.S. Duyar. Identifying Commercial Opportunities for the Reverse Water Gas Shift Reaction. *Energy Technology*. 9 (2021).

- [144] C. Fu, S. Roussanaly, K. Jordal, R. Anantharaman. Techno-Economic Analyses of the CaO/CaCO<sub>3</sub> Post-Combustion CO<sub>2</sub> Capture From NGCC Power Plants. *Frontiers in Chemical Engineering*. 2 (2021).
- [145] A.N. Antzara, A. Arregi, E. Heracleous, A.A. Lemonidou. In-depth evaluation of a ZrO<sub>2</sub> promoted CaO-based CO<sub>2</sub> sorbent in fluidized bed reactor tests. *Chemical Engineering Journal*. 333 (2018) 697-711.
- [146] T.R. Costa, P. Gayán, A. Abad, F. García-Labiano, L.F. de Diego, D.M.A. Melo, et al. Mn-based oxygen carriers prepared by impregnation for Chemical Looping Combustion with diverse fuels. *Fuel Processing Technology*. 178 (2018) 236-50.
- [147] P. Gayán, M.A. Pans, M. Ortiz, A. Abad, L.F. de Diego, F. García-Labiano, et al. Testing of a highly reactive impregnated Fe<sub>2</sub>O<sub>3</sub>/Al<sub>2</sub>O<sub>3</sub> oxygen carrier for a SR-CLC system in a continuous CLC unit. *Fuel Processing Technology*. 96 (2012) 37-47.
- [148] Y. De Vos, M. Jacobs, P. Van Der Voort, I. Van Driessche, F. Snijkers, A. Verberckmoes. Optimization of spray dried attrition-resistant iron based oxygen carriers for chemical looping reforming. *Chemical Engineering Journal*. 309 (2017) 824-39.
- [149] D. Bonaquist. Analysis of CO<sub>2</sub> emissions, reductions, and capture for large-scale H<sub>2</sub> production plants. Praxair and Linde United States of America, 2010.
- [150] Z. Du, C. Liu, J. Zhai, X. Guo, Y. Xiong, W. Su, et al. A Review of Hydrogen Purification Technologies for Fuel Cell Vehicles. *Catalysts*. 11 (2021).
- [151] L. Vermaak, H. Neomagus, D.G. Bessarabov. Hydrogen Separation and Purification from Various Gas Mixtures by Means of Electrochemical Membrane Technology in the Temperature Range 100-160 degrees C. *Membranes*. 11 (2021).
- [152] S. Ivanova, R. Lewis. Producing Nitrogen via Pressure Swing Adsorption. *Chemical Engineering Progress (CEP)*. (2012) 38-42.
- [153] P.S. Northrop, J.A. Valencia. The CFZ™ process: A cryogenic method for handling high- CO<sub>2</sub> and H<sub>2</sub>S gas reserves and facilitating geosequestration of CO<sub>2</sub> and acid gases. *Energy Procedia*. 1 (2009) 171-7.
- [154] J.-P. Lange. Performance metrics for sustainable catalysis in industry. *Nature Catalysis*. 4 (2021) 186-92.

- [155] European Environment Agency (2021, 11/05/2021). "Greenhouse gas emission intensity of electricity generation in Europe." Retrieved 11/06/2021, 2021, from <https://www.eea.europa.eu/data-and-maps/indicators/overview-of-the-electricity-production-3/assessment-1>.
- [156] R.P. Lively. The refinery of today, tomorrow, and the future: A separations perspective. *AIChE Journal*. 67 (2021).
- [157] R. Atlason, R. Unnthorsson. Ideal EROI (energy return on investment) deepens the understanding of energy systems. *Energy*. 67 (2014) 241-5.
- [158] D. Dunikov, D. Blinov. Extraction of hydrogen from a lean mixture with methane by metal hydride. *International Journal of Hydrogen Energy*. 45 (2020) 9914-26.
- [159] J.P. Lange. Don't Forget Product Recovery in Catalysis Research-Check the Distillation Resistance. *Chemsuschem*. 10 (2017) 245-52.
- [160] European Commission (2021, 20/05/2021). "Gas prices components for non-household consumers - annual data." Retrieved 11/06/2021, 2021, from [https://ec.europa.eu/eurostat/databrowser/view/nrg\\_pc\\_203\\_c/default/table?lang=en](https://ec.europa.eu/eurostat/databrowser/view/nrg_pc_203_c/default/table?lang=en).
- [161] M. Messagie, F. Boureima, J. Mertens, J. Sanfeliix, C. Macharis, J. Mierlo. The Influence of Allocation on the Carbon Footprint of Electricity Production from Waste Gas, a Case Study for Blast Furnace Gas. *Energies*. 6 (2013) 1217-32.
- [162] S. Redl, S. Sukumara, T. Ploeger, L. Wu, T. Olshoj Jensen, A.T. Nielsen, et al. Thermodynamics and economic feasibility of acetone production from syngas using the thermophilic production host *Moorella thermoacetica*. *Biotechnology for biofuels*. 10 (2017) 150.
- [163] S. Licht, H. Wu, C. Hettige, B. Wang, J. Asercion, J. Lau, et al. STEP cement: Solar Thermal Electrochemical Production of CaO without CO<sub>2</sub> emission. *Chemical Communications*. 48 (2012) 6019-21.
- [164] D. Sheppard, C. Hodgson (2021, 04/05/2021). "Cost of polluting in EU soars as carbon price hits record €50." *Financial Times*. Retrieved 11/06/2021, 2021, from <https://www.ft.com/content/2b965427-4fbc-4f2a-a14f-3be6019f0a7c>.

- [165] J.-P. Lange, V.L. Sushkevich, A.J. Knorpp, J.A. van Bokhoven. Methane-to-Methanol via Chemical Looping: Economic Potential and Guidance for Future Research. *Industrial & Engineering Chemistry Research*. 58 (2019) 8674–80.
- [166] U.S. Bureau of Labor Statistics (2021). "CPI Inflation Calculator." Retrieved 11/06/2021, 2021, from [https://www.bls.gov/data/inflation\\_calculator.htm](https://www.bls.gov/data/inflation_calculator.htm).
- [167] R.W. Stevens Jr., D.L. Keairns, R.A. Newby, M.C. Woods. Calcium- and Iron-Based Chemical Looping Combustion Processes. *Handbook of Chemical Looping Technology* 2018. pp. 333-76.
- [168] J.A. Schaidle, S.E. Habas, F.G. Baddour, C.A. Farberow, D.A. Ruddy, J.E. Hensley, et al. Transitioning rationally designed catalytic materials to real “working” catalysts produced at commercial scale: nanoparticle materials. *Catalysis: Volume 29. The Royal Society of Chemistry* 2017. pp. 213-81.
- [169] F.G. Baddour, L. Snowden-Swan, J.D. Super, K.M. Van Allsburg. Estimating Precommercial Heterogeneous Catalyst Price: A Simple Step-Based Method. *Organic Process Research & Development*. 22 (2018) 1599-605.
- [170] R. Anantharaman, O. Bolland, N. Booth, E. van Dorst, C. Ekstrom, E. Sanchez Fernandez, et al. European best practice guidelines for assessment of CO<sub>2</sub> capture technologies. European Commission European Union, 2011.
- [171] S. Choi, B.I. Sang, J. Hong, K.J. Yoon, J.W. Son, J.H. Lee, et al. Catalytic behavior of metal catalysts in high-temperature RWGS reaction: In-situ FT-IR experiments and first-principles calculations. *Sci Rep*. 7 (2017) 41207.
- [172] S.C. Gülen. Steam Turbine—Quo Vadis? *Frontiers in Energy Research*. 8 (2021).
- [173] T. Pröll. Fundamentals of chemical looping combustion and introduction to CLC reactor design. *Calcium and Chemical Looping Technology for Power Generation and Carbon Dioxide (CO<sub>2</sub>) Capture* 2015. pp. 197-219.
- [174] European Commission (2021, 09/06/2021). "Electricity prices components for non-household consumers - annual data (from 2007 onwards)." Retrieved 11/06/2021, 2021, from

[https://ec.europa.eu/eurostat/databrowser/view/NRG\\_PC\\_205\\_C\\_custom\\_1053782/default/table?lang=en](https://ec.europa.eu/eurostat/databrowser/view/NRG_PC_205_C_custom_1053782/default/table?lang=en).

[175] M. Kayfeci, A. Keçebaş, M. Bayat. Hydrogen production. *Solar Hydrogen Production* 2019. pp. 45-83.

[176] P. Basu, J. Butler. Studies on the operation of loop-seal in circulating fluidized bed boilers. *Applied Energy*. 86 (2009) 1723-31.

[177] D. Berstad, R. Anantharaman, R. Blom, K. Jordal, B. Arstad. NGCC post-combustion CO<sub>2</sub> capture with Ca/carbonate looping: Efficiency dependency on sorbent properties, capture unit performance and process configuration. *International Journal of Greenhouse Gas Control*. 24 (2014) 43-53.

[178] K.Z. House, A.C. Baclig, M. Ranjan, E.A. van Nierop, J. Wilcox, H.J. Herzog. Economic and energetic analysis of capturing CO<sub>2</sub> from ambient air. *Proceedings of the National Academy of Sciences of the United States of America*. 108 (2011) 20428-33.

[179] M. Keller, M. Arjmand, H. Leion, T. Mattisson. Interaction of mineral matter of coal with oxygen carriers in chemical-looping combustion (CLC). *Chemical Engineering Research and Design*. 92 (2014) 1753-70.

[180] P. Kaiser, F. Pöhlmann, A. Jess. Intrinsic and Effective Kinetics of Cobalt-Catalyzed Fischer-Tropsch Synthesis in View of a Power-to-Liquid Process Based on Renewable Energy. *Chemical Engineering & Technology*. 37 (2014) 964-72.

[181] P. Kaiser, R.B. Unde, C. Kern, A. Jess. Production of Liquid Hydrocarbons with CO<sub>2</sub> as Carbon Source based on Reverse Water-Gas Shift and Fischer-Tropsch Synthesis. *Chemie Ingenieur Technik*. 85 (2013) 489-99.

[182] Y.H. Choi, Y.J. Jang, H. Park, W.Y. Kim, Y.H. Lee, S.H. Choi, et al. Carbon dioxide Fischer-Tropsch synthesis: A new path to carbon-neutral fuels. *Applied Catalysis B: Environmental*. 202 (2017) 605-10.

[183] J. Arvola, J. Harkonen, M. Mottonen, H. Haapasalo, P. Tervonen. Combining Steel and Chemical Production to Reduce CO<sub>2</sub> Emissions. *Low Carbon Economy*. 02 (2011) 115-22.

[184] Torero consortium (2021, 20/06/2021). "Torero - Fueling a sustainable future." Retrieved 20/06/2021, 2021, from <https://www.torero.eu/>.

- [185] K.S. Sultana, D. Chen. Enhanced hydrogen production by in situ CO<sub>2</sub> removal on CaCeZrO<sub>x</sub> nanocrystals. *Catalysis Today*. 171 (2011) 43-51.
- [186] J. Blamey, E.J. Anthony. End use of lime-based sorbents from calcium looping systems. *Calcium and Chemical Looping Technology for Power Generation and Carbon Dioxide (CO<sub>2</sub>) Capture* 2015. pp. 153-69.
- [187] M. Erans, M. Jeremias, L. Zheng, J.G. Yao, J. Blamey, V. Manovic, et al. Pilot testing of enhanced sorbents for calcium looping with cement production. *Applied Energy*. 225 (2018) 392-401.
- [188] J. Bierhals. Carbon Monoxide. *Ullmann's Encyclopedia of Industrial Chemistry* 2001.
- [189] J.A. Moya, A. Boulamanti. Production costs from energy-intensive industries in the EU and third countries. European Union, 2016.
- [190] N. Smith, G. Miller, I. Aandi, R. Gadsden, J. Davison. Performance and Costs of CO<sub>2</sub> Capture at Gas Fired Power Plants. *Energy Procedia*. 37 (2013) 2443-52.
- [191] V. Dieterich, A. Buttler, A. Hanel, H. Spliethoff, S. Fendt. Power-to-liquid via synthesis of methanol, DME or Fischer–Tropsch-fuels: a review. *Energy & Environmental Science*. 13 (2020) 3207-52.
- [192] J.-P. Lange. Fuels and Chemicals Manufacturing; Guidelines for Understanding and Minimizing the Production Costs. *CATTECH*. 5 (2001) 82-95.
- [193] V. Singh, L.C. Buelens, H. Poelman, M. Saeys, G.B. Marin, V.V. Galvita. Carbon monoxide production using a steel mill gas in a combined chemical looping process. *Journal of Energy Chemistry*. 68 (2022) 811-25.
- [194] A.N.R. Bos, J.P. Lange, G. Kabra. A novel reverse flow reactor with integrated separation. *Chemical Engineering Science*. 62 (2007) 5661-2.
- [195] I.S. Metcalfe, B. Ray, C. Dejoie, W. Hu, C. de Leeuwe, C. Dueso, et al. Overcoming chemical equilibrium limitations using a thermodynamically reversible chemical reactor. *Nat Chem*. 11 (2019) 638-43.
- [196] S. Moran, K.-D. Henkel. Reactor Types and Their Industrial Applications. *Ullmann's Encyclopedia of Industrial Chemistry*. (2016) 1-49.

- [197] A. Joshi, V. Shah, P. Mohapatra, S. Kumar, R.K. Joshi, M. Kathe, et al. Chemical looping-A perspective on the next-gen technology for efficient fossil fuel utilization. *Advances in Applied Energy*. 3 (2021).
- [198] N.R. Singstock, C.J. Bartel, A.M. Holder, C.B. Musgrave. High-Throughput Analysis of Materials for Chemical Looping Processes. *Advanced Energy Materials*. 10 (2020).
- [199] V. Subramani, P. Sharma, L. Zhang, K. Liu. Catalytic Steam Reforming Technology for the Production of Hydrogen and Syngas. *Hydrogen and Syngas Production and Purification Technologies*. <https://doi.org/10.1002/9780470561256.ch2> (2009) 14-126.
- [200] C.H. Bartholomew. Carbon Deposition in Steam Reforming and Methanation. *Catalysis Reviews*. 24 (2007) 67-112.
- [201] J.R. Rostrup-Nielsen, K. Aasberg-Petersen. Steam reforming, ATR, partial oxidation: catalysts and reaction engineering. in: W. Vielstich, H.A. Gasteiger, A. Lamm, H. Yokokawa, (Eds.), *Handbook of Fuel Cells – Fundamentals, Technology and Applications*. John Wiley & Sons, Ltd. 2010.
- [202] B. Christian Enger, R. Lødeng, A. Holmen. A review of catalytic partial oxidation of methane to synthesis gas with emphasis on reaction mechanisms over transition metal catalysts. *Applied Catalysis A: General*. 346 (2008) 1-27.
- [203] L. Li, N.H. Md Dostagir, A. Shrotri, A. Fukuoka, H. Kobayashi. Partial Oxidation of Methane to Syngas via Formate Intermediate Found for a Ruthenium–Rhenium Bimetallic Catalyst. *ACS Catalysis*. 11 (2021) 3782-9.
- [204] G. Pantaleo, V.L. Parola, F. Deganello, R.K. Singha, R. Bal, A.M. Venezia. Ni/CeO<sub>2</sub> catalysts for methane partial oxidation: Synthesis driven structural and catalytic effects. *Applied Catalysis B: Environmental*. 189 (2016) 233-41.
- [205] D.P. Harrison. Sorption-Enhanced Hydrogen Production: A Review. *Industrial & Engineering Chemistry Research*. 47 (2008) 6486-501.
- [206] C. Zhao, Z. Zhou, Z. Cheng, X. Fang. Sol-gel-derived, CaZrO<sub>3</sub>-stabilized Ni/CaO-CaZrO<sub>3</sub> bifunctional catalyst for sorption-enhanced steam methane reforming. *Applied Catalysis B: Environmental*. 196 (2016) 16-26.



- [207] A.N. Antzaras, A.A. Lemonidou. Recent advances on materials and processes for intensified production of blue hydrogen. *Renewable and Sustainable Energy Reviews*. 155 (2022) 111917.
- [208] B. Balasubramanian, A. Lopez Ortiz, S. Kaytakoglu, D.P. Harrison. Hydrogen from methane in a single-step process. *Chemical Engineering Science*. 54 (1999) 3543-52.
- [209] R.K. Lyon, J.A. Cole. Unmixed combustion: an alternative to fire. *Combustion and Flame*. 121 (2000) 249-61.
- [210] J. Hu, V.V. Galvita, H. Poelman, C. Detavernier, G.B. Marin. Catalyst-assisted chemical looping auto-thermal dry reforming: Spatial structuring effects on process efficiency. *Applied Catalysis B: Environmental*. 231 (2018) 123-36.
- [211] M. Keller, J. Otomo. CO production from CO<sub>2</sub> and H<sub>2</sub> via the rWGS reaction by thermochemical redox cycling in interconnected fluidized beds. *Journal of CO<sub>2</sub> Utilization*. 40 (2020).
- [212] B. Jin, H. Poelman, C. Detavernier, Z. Liang, G.B. Marin, V.V. Galvita. Microstructured ZrO<sub>2</sub> coating of iron oxide for enhanced CO<sub>2</sub> conversion. *Applied Catalysis B: Environmental*. 292 (2021) 120194.
- [213] V.V. Galvita, H. Poelman, G.B. Marin. Combined chemical looping for energy storage and conversion. *Journal of Power Sources*. 286 (2015) 362-70.
- [214] S. Perathoner, K.M. Van Geem, G.B. Marin, G. Centi. Reuse of CO<sub>2</sub> in energy intensive process industries. *Chemical Communications*. 57 (2021) 10967-82.
- [215] D. Zeng, Y. Qiu, M. Li, L. Ma, D. Cui, S. Zhang, et al. Spatially controlled oxygen storage materials improved the syngas selectivity on chemical looping methane conversion. *Applied Catalysis B: Environmental*. 281 (2021) 119472.
- [216] J. Yang, E. Bjørgum, H. Chang, K.-K. Zhu, Z.-J. Sui, X.-G. Zhou, et al. On the ensemble requirement of fully selective chemical looping methane partial oxidation over La-Fe-based perovskites. *Applied Catalysis B: Environmental*. 301 (2022) 120788.
- [217] F. Donat, C.R. Müller. CO<sub>2</sub>-free conversion of CH<sub>4</sub> to syngas using chemical looping. *Applied Catalysis B: Environmental*. 278 (2020) 119328.

- [218] A. Löfberg, J. Guerrero-Caballero, T. Kane, A. Rubbens, L. Jalowiecki-Duhamel. Ni/CeO<sub>2</sub> based catalysts as oxygen vectors for the chemical looping dry reforming of methane for syngas production. *Applied Catalysis B: Environmental*. 212 (2017) 159-74.
- [219] M. Keller, A. Sharma. Reverse Boudouard reforming produces CO directly suitable for the production of methanol from CO<sub>2</sub> and CH<sub>4</sub>. *Chemical Engineering Journal*. 431 (2022) 134127.
- [220] S.A. Theofanidis, V.V. Galvita, H. Poelman, R. Batchu, L.C. Buelens, C. Detavernier, et al. Mechanism of carbon deposits removal from supported Ni catalysts. *Applied Catalysis B: Environmental*. 239 (2018) 502-12.
- [221] V.V. Galvita, H. Poelman, C. Detavernier, G.B. Marin. Catalyst-assisted chemical looping for CO<sub>2</sub> conversion to CO. *Applied Catalysis B: Environmental*. 164 (2015) 184-91.
- [222] P.A. Argyris, A. Wright, O. Taheri Qazvini, V. Spallina. Dynamic behaviour of integrated chemical looping process with pressure swing adsorption in small scale on-site H<sub>2</sub> and pure CO<sub>2</sub> production. *Chemical Engineering Journal*. 428 (2022) 132606.
- [223] K. Aasberg-Petersen, J.H. Bak Hansen, T.S. Christensen, I. Dybkjaer, P.S. Christensen, C. Stub Nielsen, et al. Technologies for large-scale gas conversion. *Applied Catalysis A: General*. 221 (2001) 379-87.
- [224] T. Banaszkiewicz, M. Chorowski, W. Gizicki. Comparative analysis of cryogenic and PTSA technologies for systems of oxygen production. *AIP Conference Proceedings*. 10.1063/1.4860866 (2014) 1373-8.
- [225] Renewable Energy Statistics 2019. The International Renewable Energy Agency, Abu Dhabi, 2019.
- [226] Basic data on biogas. Swedish Gas Technology Centre Ltd (SGC), Malmö, 2012.
- [227] A.R. Bodie, A.C. Micciche, G.G. Atungulu, M.J. Rothrock, S.C. Ricke. Current Trends of Rice Milling Byproducts for Agricultural Applications and Alternative Food Production Systems. *Frontiers in Sustainable Food Systems*. 3 (2019).
- [228] M. Nazar, A. Yasar, S.A. Raza, A. Ahmad, R. Rasheed, M. Shahbaz, et al. Techno-economic and environmental assessment of rice husk in comparison to coal and furnace oil as a boiler fuel. *Biomass Conversion and Biorefinery*. 10.1007/s13399-020-01238-3 (2021).

- [229] E.S. Domalski, T.L.J. Jobe, T.A. Milne. Thermodynamic data for biomass conversion and waste incineration. Colorado, United States of America, 1986.
- [230] N. Van Hung, M.C. Maguyon-Detras, M.V. Migo, R. Quilloy, C. Balingbing, P. Chivenge, et al. Rice Straw Overview: Availability, Properties, and Management Practices. in: M. Gummert, N.V. Hung, P. Chivenge, B. Douthwaite, (Eds.), Sustainable Rice Straw Management. Springer International Publishing, Cham, 2020. pp. 1-13.
- [231] B. Bhui, V. Prabu. Techno-economic evaluation of electronic waste based oxygen carriers for co-chemical looping combustion of coal and biomass integrated combined cycle power generating systems. *Energy Conversion and Management*. 236 (2021) 114075.
- [232] T.L. Bezerra, A.J. Ragauskas. A review of sugarcane bagasse for second-generation bioethanol and biopower production. *Biofuels, Bioproducts and Biorefining*. 10 (2016) 634-47.
- [233] I.L. Wiesberg, J.L. de Medeiros, R.V. Paes de Mello, J.G.S. Santos Maia, J.B.V. Bastos, O.d.Q.F. Araújo. Bioenergy production from sugarcane bagasse with carbon capture and storage: Surrogate models for techno-economic decisions. *Renewable and Sustainable Energy Reviews*. 150 (2021).
- [234] A.M. Elias, A.A. Longati, H.R. Ellamla, F.F. Furlan, M.P.A. Ribeiro, P.R.F. Marcelino, et al. Techno-Economic-Environmental Analysis of Sophorolipid Biosurfactant Production from Sugarcane Bagasse. *Industrial & Engineering Chemistry Research*. 60 (2021) 9833-50.
- [235] J.A. Ramirez, T.J. Rainey. Comparative techno-economic analysis of biofuel production through gasification, thermal liquefaction and pyrolysis of sugarcane bagasse. *Journal of Cleaner Production*. 229 (2019) 513-27.
- [236] A.K. Chandel, J.Q. Albarelli, D.T. Santos, S.P. Chundawat, M. Puri, M.A.A. Meireles. Comparative analysis of key technologies for cellulosic ethanol production from Brazilian sugarcane bagasse at a commercial scale. *Biofuels, Bioproducts and Biorefining*. 13 (2019) 994-1014.
- [237] R. Bakker, W. Elbersen, R. Poppens, J.P. Lesschen. Rice straw and Wheat straw Potential feedstocks for the Biobased Economy. NL Agency Utrecht, the Netherlands, 2013.

- [238] C. Ma, S. Zhang, R. Dong, M. Wang, W. Jia, Z. Lu. Corn Stalk Fiber-Based Biomass Brick Reinforced by Compact Organic/Inorganic Calcification Composites. *ACS Sustainable Chemistry & Engineering*. 6 (2017) 2086-93.
- [239] Y. Li, Y. Han, Y. Zhang, W. Luo, G. Li. Anaerobic digestion of different agricultural wastes: A techno-economic assessment. *Bioresource Technology*. 315 (2020) 123836.
- [240] C. Schneider, H. Hartmann. Maize as Energy Crop for Combustion Agricultural Optimisation of Fuel Supply. Technologie- und Foerderzentrum (TFZ) Straubing, Germany, 2006.
- [241] N. Hamzah, K. Tokimatsu, K. Yoshikawa. Solid Fuel from Oil Palm Biomass Residues and Municipal Solid Waste by Hydrothermal Treatment for Electrical Power Generation in Malaysia: A Review. *Sustainability*. 11 (2019) 1060.
- [242] W. Elbersen, K. Meesters, R. Bakker. Valorization of palm oil (mill) residues. Identifying and solving the challenges. NL Agency Utrecht, the Netherlands, 2013.
- [243] A.F.P. Harahap, J.R.H. Panjaitan, C.A. Curie, M.Y.A. Ramadhan, P. Srinophakun, M. Gozan. Techno-Economic Evaluation of Hand Sanitiser Production Using Oil Palm Empty Fruit Bunch-Based Bioethanol by Simultaneous Saccharification and Fermentation (SSF) Process. *Applied Sciences*. 10 (2020).
- [244] H.M. Yoo, S.W. Park, Y.C. Seo, K.H. Kim. Applicability assessment of empty fruit bunches from palm oil mills for use as bio-solid refuse fuels. *Journal of environmental management*. 234 (2019) 1-7.
- [245] Palm oil prices - International Monetary Fund. Online, 2020.
- [246] A. Lea-Langton, R.M. Zin, V. Dupont, M.V. Twigg. Biomass pyrolysis oils for hydrogen production using chemical looping reforming. *International Journal of Hydrogen Energy*. 37 (2012) 2037-43.
- [247] V. Aryan, A. Kraft. The crude tall oil value chain: Global availability and the influence of regional energy policies. *Journal of Cleaner Production*. 280 (2021).
- [248] A.A. Albuquerque, F.T.T. Ng, L. Danielski, L. Stragevitch. A new process for biodiesel production from tall oil via catalytic distillation. *Chemical Engineering Research and Design*. 170 (2021) 314-28.

- [249] P. Bajpai. Global Production of Bioethanol. Developments in Bioethanol. Springer Singapore, Singapore, 2021. pp. 177-96.
- [250] A.J.J. Straathof, A. Bampouli. Potential of commodity chemicals to become bio-based according to maximum yields and petrochemical prices. *Biofuels, Bioproducts and Biorefining*. 11 (2017) 798-810.
- [251] R.C. Costa, J.R. Sodré. Hydrous ethanol vs. gasoline-ethanol blend: Engine performance and emissions. *Fuel*. 89 (2010) 287-93.
- [252] D. Baldwin. 2018 Glycerine Structural Shift. ICIS Pan American Conference. Vantage Oleochemicals 2018.
- [253] H.J. Kim, Y. Kim, D. Lee, J.-R. Kim, H.-J. Chae, S.-Y. Jeong, et al. Coproducing Value-Added Chemicals and Hydrogen with Electrocatalytic Glycerol Oxidation Technology: Experimental and Techno-Economic Investigations. *ACS Sustainable Chemistry & Engineering*. 5 (2017) 6626-34.
- [254] L. Chen, Z. Qi, S. Zhang, J. Su, G.A. Somorjai. Catalytic Hydrogen Production from Methane: A Review on Recent Progress and Prospect. *Catalysts*. 10 (2020).
- [255] E.O. Ajala, O.A.A. Eletta, M.A. Ajala, S.K. Oyeniyi. Characterization and Evaluation of Chicken Eggshell for use as a Bio-Resource. *ARID ZONE JOURNAL OF ENGINEERING, TECHNOLOGY AND ENVIRONMENT*. 14 (2018) 26-40.
- [256] T. Tokimoto, N. Kawasaki, T. Nakamura, J. Akutagawa, S. Tanada. Removal of lead ions in drinking water by coffee grounds as vegetable biomass. *Journal of Colloid and Interface Science*. 281 (2005) 56-61.
- [257] A.E. Atabani, A.a.H. Al-Muhtaseb, G. Kumar, G.D. Saratale, M. Aslam, H.A. Khan, et al. Valorization of spent coffee grounds into biofuels and value-added products: Pathway towards integrated bio-refinery. *Fuel*. 254 (2019).
- [258] Y. Zhang, Y. Liu, Q. Yang, Q. Guo. Reaction characteristics of chemical-looping gasification for waste coffee grounds. *Huagong Xuebao (Chin Ed)*. 67 (2016) 1303-12.
- [259] C.G. Lopresto, S. Naccarato, L. Albo, M.G. De Paola, S. Chakraborty, S. Curcio, et al. Enzymatic transesterification of waste vegetable oil to produce biodiesel. *Ecotoxicology and environmental safety*. 121 (2015) 229-35.

- [260] B. Supple, R. Howard-Hildige, E. Gonzalez-Gomez, J.J. Leahy. The effect of steam treating waste cooking oil on the yield of methyl ester. *Journal of the American Oil Chemists' Society*. 79 (2002) 175-8.
- [261] P.S. Mehta, K. Anand. Estimation of a Lower Heating Value of Vegetable Oil and Biodiesel Fuel. *Energy & Fuels*. 23 (2009) 3893-8.
- [262] "WHAT A WASTE 2.0 - A Global Snapshot of Solid Waste Management to 2050." Retrieved 26/02/2022, 2022, from <https://datatopics.worldbank.org/what-a-waste/trends-in-solid-waste-management.html>.
- [263] E. Dijkgraaf, H.R.J. Vollebergh. Burn or bury? A social cost comparison of final waste disposal methods. *Ecological Economics*. 50 (2004) 233-47.
- [264] J. Cai, W. Zheng, M. Luo, C. Kuang, X. Tang. Characterization of copper (II) chemical forms and heavy metal distribution in chemical looping gasification of municipal solid waste. *J Energy Inst*. 96 (2021) 140-7.
- [265] BP. BP Statistical Review of World Energy. in: BP, (Ed.). 69th ed. BP p.l.c., London, 2020.
- [266] J. Carvill. 3 - Thermodynamics and heat transfer. in: J. Carvill, (Ed.). *Mechanical Engineer's Data Handbook*. Butterworth-Heinemann, Oxford, 1993. pp. 102-45.
- [267] J. Perez-Carbajo, P. Gomez-Alvarez, R. Bueno-Perez, P.J. Merklings, S. Calero. Optimisation of the Fischer-Tropsch process using zeolites for tail gas separation. *Physical chemistry chemical physics : PCCP*. 16 (2014) 5678-88.
- [268] G.V. Last, M.T. Schmick. *Identification and Selection of Major Carbon Dioxide Stream Compositions*. 2011.
- [269] R. Geyer, J.R. Jambeck, K.L. Law. Production, use, and fate of all plastics ever made. *Science Advances*. 3 (2017) e1700782.
- [270] C. Cimpan, A. Maul, H. Wenzel, T. Pretz. Techno-economic assessment of central sorting at material recovery facilities – the case of lightweight packaging waste. *Journal of Cleaner Production*. 112 (2016) 4387-97.
- [271] C. Areeprasert, J. Asingsamanunt, S. Srisawat, J. Kaharn, B. Inseemeeesak, P. Phasee, et al. *Municipal Plastic Waste Composition*

Study at Transfer Station of Bangkok and Possibility of its Energy Recovery by Pyrolysis. *Energy Procedia*. 107 (2017) 222-6.

[272] A. Singh, N.A. Rorrer, S.R. Nicholson, E. Erickson, J.S. DesVeaux, A.F.T. Avelino, et al. Techno-economic, life-cycle, and socioeconomic impact analysis of enzymatic recycling of poly(ethylene terephthalate). *Joule*. 5 (2021) 2479-503.

[273] R.L. Blake, R.E. Hessevick, T. Zoltai, L.W. Finger. Refinement of the hematite structure. *American Mineralogist*. 51 (1966) 123-9.

[274] G.E. Bacon, A.J.E. Welch. An X-ray examination of the spinel-type mixed oxide,  $\text{MgFeAlO}_4$ . *Acta Crystallographica*. 7 (1954) 361-3.

[275] F. Martignago, A.D. Negro, S. Carbonin. How  $\text{Cr}^{3+}$  and  $\text{Fe}^{3+}$  affect Mg-Al order-disorder transformation at high temperature in natural spinels. *Physics and Chemistry of Minerals*. 30 (2003) 401-8.

[276] G. Fiquet, P. Richet, G. Montagnac. High-temperature thermal expansion of lime, periclase, corundum and spinel. *Physics and Chemistry of Minerals*. 27 (1999) 103-11.

[277] D.L. Graf. Crystallographic tables for rhombohedral carbonates. *American Mineralogist*. 46 (1961) 1283-316.

[278] L. Desgranges, D. Grebille, G. Calvarin. Hydrogen thermal motion in calcium hydroxide:  $\text{Ca}(\text{OH})_2$ . *Acta Crystallographica Section B*. B49 (1993) 812-7.

[279] R.W.G. Wyckoff. *Crystal Structures*. Interscience Publishers, New York, USA, 1963.

[280] M.E. Fleet. The structure of magnetite. *Acta Crystallographica Section B: Structural Science, Crystal Engineering and Materials*. 37 (1981) 917-20.

[281] S.A.T. Redfern, R.J. Harrison, H.S.C. O'Neill, D.R.R. Wood. Thermodynamics and kinetics of cation ordering in  $\text{MgAl}_2\text{O}_4$  spinel up to 1600 degrees C from in situ neutron diffraction. *American Mineralogist*. 84 (1999) 299-310.

[282] R.J. Harrison, S.A.T. Redfern, H.S.C. O'Neill. The temperature dependence of the cation distribution in synthetic hercynite ( $\text{FeAl}_2\text{O}_4$ ) from in-situ neutron structure refinements. *American Mineralogist*. 83 (1998) 1092-9.

[283] G.B. Andreozzi, S. Lucchesi, H. Skogby, A. Della Giusta. Compositional dependence of cation distribution in some synthetic

(Mg,Zn)(Al,Fe<sup>3+</sup>)<sub>2</sub>O<sub>4</sub> spinels. *European Journal of Mineralogy*. 13 (2001) 391-402.

[284] E.R. Jette, F. Foote. An X-Ray Study of the Wüstite (FeO) Solid Solutions. *The Journal of Chemical Physics*. 1 (1933) 29-36.

[285] F. Martignago, G.B. Andreozzi, A.D. Negro. Thermodynamics and kinetics of cation ordering in natural and synthetic Mg(Al,Fe<sup>3+</sup>)<sub>2</sub>O<sub>4</sub> spinels from in situ high-temperature X-ray diffraction. *American Mineralogist*. 91 (2006) 306-12.

[286] P.P. Kirichok, A.P. Antoshchuk. Control of the properties of magnetic ferrite-alloys using the ions Al<sup>3+</sup>, Cr<sup>3+</sup>, Sc<sup>3+</sup>, In<sup>3+</sup>. *Izvestiya Akademii Nauk SSSR, Neorganicheskie Materialy*. 13 (1977) 1327 - 30.

[287] A. Nakatsuka, H. Ueno, N. Nakayama, T. Mizota, H. Maekawa. Single-crystal X-ray diffraction study of cation distribution in MgAl<sub>2</sub>O<sub>4</sub>–MgFe<sub>2</sub>O<sub>4</sub> spinel solid solution. *Physics and Chemistry of Minerals*. 31 (2004) 278-87.

[288] B. Lavina, F. Princivalle, A. Della Giusta. Controlled time–temperature oxidation reaction in a synthetic Mg-hercynite. *Physics and Chemistry of Minerals*. 32 (2005) 83-8.

[289] T. De Donder, P. Van Rysselberghe. *Thermodynamic Theory of Affinity. A book of principles*. Stanford University Press, Stanford, 1936.

[290] A. Navrotsky, L. Mazeina, J. Majzlan. Size-Driven Structural and Thermodynamic Complexity in Iron Oxides. *Science*. 319 (2008) 1635.

[291] S. Geller. Structure of α-Mn<sub>2</sub>O<sub>3</sub>, (Mn<sub>0.983</sub>Fe<sub>0.017</sub>)<sub>2</sub>O<sub>3</sub> and (Mn<sub>0.37</sub>Fe<sub>0.63</sub>)<sub>2</sub>O<sub>3</sub> and relation to magnetic ordering. *Acta Crystallographica Section B*. 27 (1971) 821-8.

[292] V. Baron, J. Gutzmer, H. Rundlof, R. Tellgren. The influence of iron substitution in the magnetic properties of hausmannite, Mn (super 2+) (Fe,Mn) (super 3+) <sub>2</sub> O <sub>4</sub>. *American Mineralogist*. 83 (1998) 786-93.

[293] F. Bosi, U. Hålenius, G.B. Andreozzi, H. Skogby, S. Lucchesi. Structural refinement and crystal chemistry of Mn-doped spinel: A case for tetrahedrally coordinated Mn<sup>3+</sup> in an oxygen-based structure. *American Mineralogist*. 92 (2007) 27-33.

[294] J. Yin, A.B. Brady, E.S. Takeuchi, A.C. Marschilok, K.J. Takeuchi. Magnesium-ion battery-relevant electrochemistry of MgMn<sub>2</sub>O<sub>4</sub>: crystallite size effects and the notable role of electrolyte water content. *Chemical communications (Cambridge, England)*. 53 (2017) 3665-8.



- [295] Vewin (2020, 02/2020). "Tarievenoverzicht drinkwater 2020." Retrieved 13/06/2021, 2021, from <https://www.vewin.nl/SiteCollectionDocuments/Publicaties/Cijfers/5691-VEW%20Brochure%20Tarievenoverzicht WEB.pdf>.
- [296] C.-C. Cormos. Assessment of chemical absorption/adsorption for post-combustion CO<sub>2</sub> capture from Natural Gas Combined Cycle (NGCC) power plants. Applied Thermal Engineering. 82 (2015) 120-8.
- [297] W.F. Castle. Air separation and liquefaction: recent developments and prospects for the beginning of the new millennium. International Journal of Refrigeration. 25 (2002) 158-72.



Combined chemical looping processes can help reduce CO<sub>2</sub> emissions in the metallurgical industry, among others.